ATOMIC STRUCTURE AND NON-ELECTRIC PROPERTIES OF SEMICONDUCTORS

Pressure-induced formation of thermal donor centers in silicon after oxygen ion bombardment

I. V. Antonova, V. P. Popov, and D. V. Kilanov

Institute for Physics of Semiconductors, 630090 Novosibirsk, Russia

E. P. Neustroev

Yakutia State University, 677000 Yakutsk, Russia

A. Misuk

Institute of Electronic Technology, Warsaw, Poland

(Submitted March 18, 1999; accepted for publication April 5, 1999)
Fiz. Tekh. Poluprovodn. **33**, 1153–1157 (October 1999)

This paper discusses the generation of thermal donor centers in silicon by oxygen ion implantation in the temperature range 350 to 550 °C. These donors are distributed almost uniformly over the entire thickness of the silicon crystals and well outside the region of direct penetration of the ions. It is established that implantation of Czochralski-grown silicon with oxygen ions followed by annealing accelerates the introduction of these donors into the silicon, and that application of hydrostatic pressure further accelerates the process of donor-center formation. The data indicate that this accelerated introduction of donors is associated with diffusion of radiation-induced defects from the implanted layer into the crystal bulk, and that the diffusion coefficients of these defects are 1×10^{-7} cm^2/s or larger. © *1999 American Institute of Physics.* [S1063-7826(99)00110-6]

INTRODUCTION

Ion implantation is one of the basic methods used to introduce impurities into silicon in a controllable way. The incorporation of ions into these crystals is accompanied by the generation of a considerable number of radiation-induced defects, most notably point defects, i.e., vacancies and interstitial atoms, which possess high mobilities even at room temperature.[1]

One of the many processing steps used in the fabrication of devices based on Si is thermal processing at temperatures of 350 to 550 °C. It is well known that processing of Czochralski-grown silicon (*Cz*-Si) at these temperatures leads to the introduction of donor centers (thermal donors) into the material.[2,3] When this occurs, the efficiency of thermal donor generation is found to depend strongly on the oxygen content of the silicon. At this time, the exact structure and mechanism for formation of these centers remains unclear. The most widely accepted model postulates that the thermal donors are made up of an intrinsic interstitial atom plus a chain of several interstitial oxygen atoms.[4,5]

Examination of the current literature reveals that there is no clarity regarding the question of how the processes of thermal defect formation are affected by prior irradiation. In their papers on the influence of neutron-induced doping and implantation of hydrogen ions on thermal defect formation, for example, Pflueger *et al.*[6] and Popov *et al.*[7] claimed that irradiation accelerates the formation of thermal defects. Moreover, Hallberg *et al.*[8] observed that prior irradiation by electrons accelerates the precipitation of oxygen. On the other hand, Markevich *et al.*[9], Henry *et al.*[10], and Litvinov *et al.*[11] investigated the effect of irradiation with electrons or γ-rays, and found that the irradiation either had no effect at all on the kinetics of thermal donor formation or that it actually decreased their rate of formation. It is a matter of no small interest that these latter authors were investigating cases where the radiation-induced defects are generated uniformly throughout the crystal volume, whereas ion implantation of the sort used, for example, in Ref. 7 has the peculiar feature that the same radiation-induced defects are introduced in a relatively shallow layer and accordingly conditions are created for nonuniformity in their spatial distribution. Hence, defects generated by ion implantation can affect the formation of thermal donors differently from defects generated by prior irradiation, which distributes them uniformly throughout the crystal.

Popov *et al.*[7] claimed that a variety of radiation-induced defects other than hydrogen, i.e., vacancies, intrinsic interstitial atoms, interstitial carbon atoms, or complexes of hydrogen with these centers, can also participate in the process of generating thermal donors. In this paper we will investigate how irradiating silicon with oxygen atoms affects the formation of donor centers in the temperature range 350 to 550 °C. We used ion implantation to generate radiation-induced defects in the material; our choice of oxygen atoms was moti-

 © 1999 American Institute of Physics

vated by the possibility that oxygen participates in the generation of thermal donors.

Another way to vary the concentration of intrinsic point defects in silicon crystals is to use hydrostatic pressure during thermal processing of the material. According to the data of Ref. 12, application of high pressure during thermal processing should increase the equilibrium concentration of vacancies in the crystal. This increase becomes important at pressures on the order of 1 GPa or higher. Moreover, these data[12] also indicate that the diffusion coefficients of the intrinsic defects change as well (an increase for vacancies and a decrease for interstitial atoms).

The task of this paper is to investigate the influence of irradiation by oxygen ions and the action of hydrostatic pressure on the generation of donor centers in silicon.

EXPERIMENTAL METHOD

The materials used in these studies were single crystals of *n*-type silicon grown by the Czochralski method (*Cz*-Si) and the float-zone method (*Fz*-Si). The *Cz*-Si had an oxygen concentration of $(7.5-8)\times10^{17}\,\mathrm{cm}^{-3}$ and phosphorus concentration of $(5-7)\times10^{14}\,\mathrm{cm}^{-3}$. In *Fz*-Si the oxygen concentration was less than $10^{16}\,\mathrm{cm}^{-3}$, while the concentration of phosphorus was $\sim10^{13}\,\mathrm{cm}^{-3}$. The oxygen concentrations were determined from infrared spectroscopic data based on the well-known absorption band at 1107 cm^{-1}, using the calibration coefficient $2.45\times10^{17}\,\mathrm{cm}^{-2}$. The thickness of the samples was ~450 μm for *Cz*-Si and ~350 μm for *Fz*-Si. Oxygen ions (O^+) were implanted at room temperature with energies of 200 keV in the dose range from 10^{14} to 10^{17} cm^{-2}. The projected range of O^+ ions was 0.4 μm. The thermal processing took place in air in the temperature range 200 to 750 °C for periods of up to 10 hours. Several samples were annealed under two hydrostatic pressures (0.01 and 1.2 GPa) in an argon atmosphere. The Hall effect and capacitance-voltage measurements were used in these investigations. In order to obtain the distribution of implanted centers with respect to depth into the sample, capacitance-voltage measurements were combined with etching in a 1 : 100 solution of $HF:HNO_3$, or in CP4a etch.

RESULTS

Figure 1 shows how the carrier concentration varies as a function of thermal processing time in samples of *Cz*-Si at various implantation doses of O^+ (curves *2–5*) and in a control (unirradiated) sample (curve *1*). The sizes of the data points on these curves reflect the measurement errors. It is clear from the figure that the electron concentrations of the ion-irradiated samples are increased by the thermal processing. The figure also shows that increasing the irradiation dose (to $1\times10^{16}\,\mathrm{cm}^{-2}$) increases the number of donors introduced. On this same figure we also plot the same dependences for samples subjected to thermal processing under high hydrostatic pressure (1.2 GPa), both the control sample (curve *6*) and a sample irradiated with oxygen ions (curve *7*). It is clear that application of hydrostatic pressure leads to a sizable increase in the electron concentration, both for the control and the ion-implanted samples. It is also noteworthy

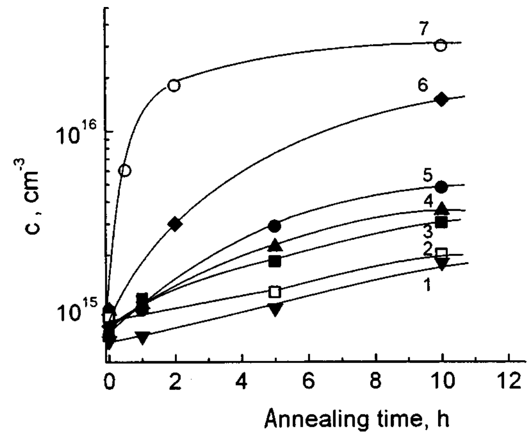

FIG. 1. Plots of the electron concentration (c) versus anneal time at 450 °C, deduced from the Hall effect measurements for crystals of *Cz*-Si implanted with O^+ at atmospheric pressure (*1—5*) and at a hydrostatic pressure of 1.2 GPa (6,7). Implantation doses, cm^{-2}: *1, 6* — 0 (controls); *2* — 1×10^{14}; *3* — 1×10^{15}; *4, 7* — 1×10^{16}; *5* — 1×10^{17}.

that the carrier concentration generated by implantation combined with pressure greatly exceeds the sum of the increases due to implantation and pressure separately.

In Fig. 2 we plot the change in average concentration of electrons in the crystal bulk as a function of irradiation dose. Annealing at atmospheric pressure (curve *1*) leads to an increase in the concentration of donor centers that saturates at an irradiation dose of $10^{16}\,\mathrm{cm}^{-2}$. Thermal processing at a pressure of 0.01 GPa (curve *2*) leads to an analogous dependence. When pressures of 1.2 GPa are applied, donors are introduced in concentrations close to the saturation concentration for all the irradiation doses (curve *3*).

Figure 3 shows typical distributions of donor-center concentrations with respect to depth for samples implanted with oxygen ions after thermal processing (450 °C, 10 hours) at vairous pressures – atmospheric 10^{-4} GPa, 0.01, and 1.2 Gpa. It is noteworthy that donor concentrations in the region of direct penetration of oxygen were considerably higher, which agrees with data well known in the literature (for example, Ref. 13). In keeping with the goals of this paper, we

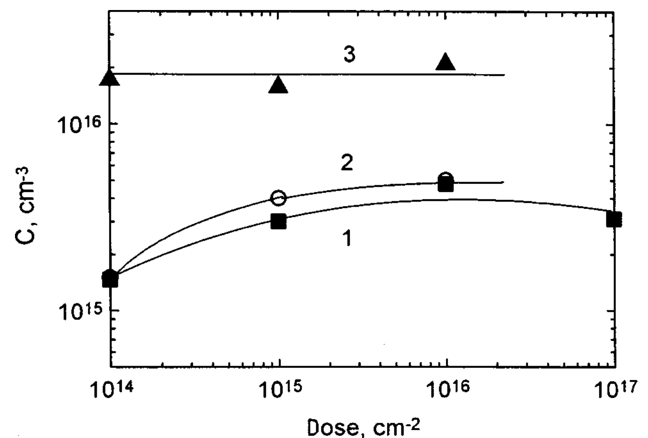

FIG. 2. Dependence of the average concentration of C donor centers on implantation dose of O^+ after annealing (450 °C, 10 h) at atmospheric pressure (*1*) and at hydrostatic pressures of 0.01 (*2*) and 1.2 GPa (*3*).

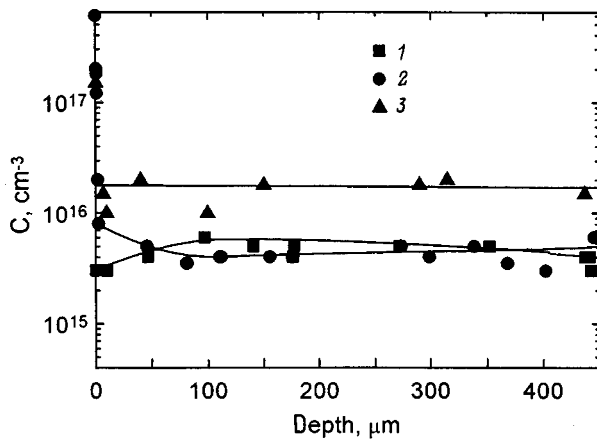

FIG. 3. Typical distributions of donor-center concentration (C) with respect to depth for samples implanted with oxygen ions at a dose of 10^{15} cm^{-2} after thermal annealing (450 °C, 10 h) at various pressures—atmospheric (*1*), 0.01 (*2*), and 1.2 GPa (*3*).

focus our attention on those regions of the crystal located outside the region of direct ion penetration. As is clear from the figure, under these processing conditions we obtain practically uniform distributions of donor-center concentrations throughout the entire crystal bulk. The same type of donor-center distribution is observed for time-dependent annealing — the distribution of charge carriers is uniform with respect to depth, with an average concentration of donor centers that increases when the anneal time is increased from 1 to 10 hours, both under hydrostatic pressure and at atmospheric pressure. It is clear from the figure that the distributions and magnitudes of the bulk carrier concentrations practically coincide for low pressure (0.01 GPa) and atmospheric pressure.

When we examined analogously irradiated samples of Fz-Si annealed (at 450 °C for 2 hours) both at atmospheric pressure and under hydrostatic pressure, we found that the carrier concentration did not change much during thermal processing . The only thing we observed was a slight increase in the concentration of carriers in the surface region at a depth of 2 to 3 μm.

Figure 4 shows how the concentration of donor centers varies for samples implanted with O^+ ions at a dose of 1×10^{16} cm^{-2} as a function of anneal temperature at atmospheric pressure and the same thermal processing time (30 min). It is clear that the accelerated introduction of donor centers takes place in the temperature range from 350 to 550 °C with a maximum at ~450 °C. Increasing the temperature beyond this point leads to recovery of the original carrier concentration. The slight increase in the concentration of donor centers at temperatures above 650 °C is most likely associated with the creation of ''new'' thermal donors.

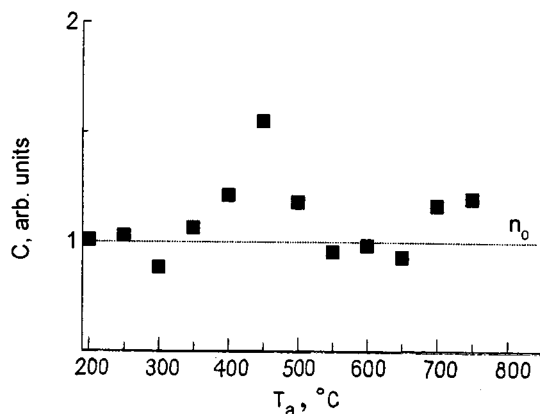

FIG. 4. Plots of the concentration of donor centers (C) for samples implanted with O^+ ions at a dose of 10^{16} cm^{-2} versus anneal temperature (T_a) at atmospheric pressure and for identical thermal processing times (30 min). n_0 is the concentration of donors in the original material.

DISCUSSION

Our results can be summarized as follows.

1) We observed no generation of donor centers in ion-implanted Fz-Si outside the region of direct penetration of ions.
2) Implantation of oxygen ions into crystals of Cz-Si with subsequent annealing leads to accelerated introduction of donor centers (compared to the original material) throughout the crystal volume.
3) Within the thermal processing times we used, donor centers were introduced uniformly throughout the crystal volume.
4) Application of hydrostatic pressure led to an increase in the rate of introduction of donor centers. In ion-implanted silicon the number of donor centers created greatly exceeded the sum of donor center concentrations introduced when pressure or irradiation were used alone.
5) At high pressures (1.2 GPa) the dependence of the electron concentration on oxygen-ion irradiation dose saturates even for the smallest doses used.

The donor centers we observed are most likely thermal donors. This is confirmed both by the temperature range in which they exist, which is the thermal-donor range, and the lack of significant changes in the number of donor centers in processed Fz-Si. This latter fact also indicates participation of oxygen in the formation of the donor centers.

The dependence of the donor-center concentration on the O^+-ion irradiation dose (Fig. 1) indicates that either incorporated ions or radiation-induced defects take part in donor-center formation. The change in the concentration of thermal donors at depths that greatly exceed the projected range of the ions strongly implies that the defects participating in the formation of donor centers have a high diffusion coefficient (D_0) in silicon. Estimates we have made show that the diffusion coefficient for the mobile component that accelerates the introduction of donor centers should be $\sim 1 \times 10^{-7}$ cm^2/s. In Ref. 7 it was shown that implanting H_2^+ ions into Cz-Si leads to accelerated formation of thermal donors at a temperature of 450 °C. In this case, these authors claimed that the rate of formation of thermal donors can be increased by participation of not only hydrogen atoms but radiation-induced defects—vacancies (V), intrinsic interstitial atoms (I), interstitial carbon atoms (C_I), or complexes of hydrogen with V or I. The diffusion coefficients for V, I and C_I can be quite large: 5×10^{-7} cm^2/s (Ref. 14), $10^{-8}-10^{-7}$ cm^2/s

(Ref. 15), and 10^{-7} cm^2/s (Ref. 16), respectively.

In contrast, the diffusion coefficient of interstitial oxygen in silicon at 450 °C is only $\sim 1\times 10^{-19}$ cm^2/s, according to data from various references.[17,18] Even when accelerated diffusion of oxygen is taken into account,[18,19] D_0 does not exceed 1×10^{-14} cm^2/s. In Ref. 20, it was claimed that oxygen molecules could have a high diffusion coefficient $D_0 \simeq 2\times 10^{-9}$ cm^2/s in silicon crystals at 450 °C. In addition, it is known[21,22]that the presence of hydrogen in the crystal lattice of silicon can affect D_0 for oxygen, due to a decrease in the activation energy for diffusion. However, the absence of accelerated formation of donor centers in Fz-Si implies that implanted oxygen probably does not play a direct role in the accelerated introduction of donor centers into the crystal bulk.

A review of the literature shows that the presence of hydrogen atoms in the starting silicon crystals can accelerate the generation of thermal donors.[23–25] The concentration of hydrogen molecules present in silicon as an uncontrolled impurity can reach 10^{14} to 10^{15} cm^{-3}.[26] For the thermal processing temperature range unde discussion here, activation of hydrogen is possible via decay of a molecule and the creation of electrically active centers of donor type with radiation defects such as H_I– Si_I and H_I–C_I.[27] The latter center can have a larger diffusion coefficient than interstitial carbon alone. It should be noted that the observed concentrations of donors exceed the initial hydrogen concentration, which rules out explaining accelerated introduction of thermal donors solely in terms of the influence of hydrogen. Nevertheless, the presence of hydrogen can have an additional accelerating effect on the formation of donor centers. Interstitial carbon, which arises from the interaction of interstitial silicon atoms with carbon in a substitutional position, also can accelerate the formation of donor centers in silicon.[16] Davies *et al.*[16] have shown that this is due to an increase in nucleation centers for thermal donors.

As for the role of vacancies in generating thermal donors, published data in the literature are ambiguous. In some papers,[28–30] it is claimed that increasing the concentration of vacancies leads to a decrease in the rate of introduction of thermal donors. At the same time, other papers report observing accelerated precipitation of oxygen when vacancies are introduced, and claim that the vacancies act as centers for nucleation of precipitates (see, e.g., Ref. 31). As for intrinsic interstitial atoms, the most widely used model of thermal donors treats them as components of the latter.[7,8] Therefore, changing the concentration of intrinsic interstitials can probably affect the rate of introduction of thermal donors as well.

Thus, our studies of the effect of oxygen-ion irradiation do not allow us to categorically exclude any of the centers we have listed from an explanation of the accelerated introduction of thermal donors, except for oxygen ions with accelerated diffusion.

Application of pressure leads to an increase in the equilibrium concentration of vacancies and a decrease in the concentration of interstitial atoms in the crystal lattice, and also to a change in the diffusion coefficients compared to their values at atmospheric pressure.[15] As shown in Ref. 15, the diffusion coefficient for interstitial atoms decreases, while the diffusion coefficient for vacancies increases. It is likely that both ion implantation and application of hydrostatic pressure saturate the bulk material with vacancy defects, which leads to an increase in the concentration of nucleation centers for thermal donors. Thus, based on the data of Ref. 15, out of all the defects listed above the best candidate for explaining the accelerated introduction of thermal donors is the vacancy.

The sizable difference in the rates of introduction of thermal donors during annealing under pressure in ion-implanted and unimplanted materials once more clearly shows that implantation creates an additional channel for accelerated formation of thermal donors. The lack of additivity of the effects of pressure and implantation is most likely due to suppression of the process of annihilation of vacancies with interstitial atoms under high pressure. In this case, the concentration of surviving defects, and accordingly their flux in the crystal, should increase. Annealing of ion-implanted silicon under pressure immediately provides a concentration of thermal defects of $\sim 2\times 10^{16}$ cm^{-3}, which corresponds to the maximum observed concentration of thermal donors in silicon. As a result, we observed saturation even for the lowest irradiation doses; i.e., increasing the dose further did not increase the concentration of thermal donors. The saturation by irradiation doses $>10^{16}$ cm^{-2} (Fig. 2) for samples annealed at atmospheric pressure is probably related to changes in the nature of the defect formation at high irradiation doses. As a result, the fraction of intrinsic defects diffusing from the implanted region into the crystal bulk during annealing changes.

In conclusion we note that these results allow us to assert that radiation-induced defects take part in the accelerated formation of thermal donors. It is likely that intrinsic point defects [vacancies and (or) intrinsic interstitial atoms] are responsible for this process. This assertion finds its confirmation in the fact that we observed accelerated formation of thermal defects during annealing under hydrostatic pressure. Both for ion implantation and for hydrostatic pressure combined with annealing, the most important indication that radiation-induced defects are involved is the increase in the concentration of centers for nucleating thermal donors.

[1] V. Privetera, S. Coffa, F. Priolo, K. K. Larsen, S. Libertino, and A. Carnera, Nucl. Instrum. Methods Phys. Res. B **120**, 9 (1996).
[2] W. Kaizer, H. Frisch, and H. Reiss, Phys. Rev. **112**, 1546 (1958).
[3] C. S. Fuller, J. H. Ditzenbergen, N. B. Hanny, and E. Buehler, Phys. Rev. **96**, 883 (1954).
[4] P. Deak, L. C. Snyder, and J. W. Corbett, Phys. Rev. B **45**, 11 612 (1992).
[5] D. Mathiot, Appl. Phys. Lett. **51**, 904 (1987).
[6] R. Pflueger, J. C. Corelli, and J. W. Corbett, Phys. Status Solidi A **91**, k49 (1985).
[7] V. P. Popov, E. P. Neustroev, I. V. Antonova, V. F. Stas, and V. I. Obodnikov, *European MRS*, Springer Meeting (1998), paper AP9.
[8] T. Hallberg and J. L. Lingstrom, J. Appl. Phys. **72**, 5130 (1992).
[9] V. P. Markevich and L. I. Murin, Fiz. Tekh. Poluprovodn. **25**, 1737 (1991) [Sov. Phys. Semicond. **25**, 1045 (1991)].
[10] A. Henry, K. Saminadayar, J. L. Pautrat, and N. Magnea, Phys. Status Solidi A **107**, 101 (1988).
[11] V. V. Litvinov, G. V. Pal'chik, and V. I. Urenev, Fiz. Tekh. Poluprovodn. **24**, 367 (1990) [Sov. Phys. Semicond. **24**, 371 (1990)].
[12] H. Park, K. S. Jones, J. A. Slinkman, and M. E. Law, J. Appl. Phys. **78**, 3664 (1995).

[13] S. Hahn, H. J. Stein, S. C. Chatas, and F. A. Ponce, J. Appl. Phys. **72**, 1758 (1992).
[14] G. D. Watkins, *Radiation Effects in Semiconductors* (Inst. of Phys., London–Bristol, 1977) [Conf. Ser. N31], p. 221.
[15] D. Eaglesham, Phys. World **4**, 41 (1995).
[16] Gr. Davies, E. C. Lightowles, R. C. Newman, and A. C. Oates, Semiconductors **2**, 524 (1987).
[17] V. M. Babich, N. I. Bletskan, and E. F. Venger, *Oxygen in Single-Crystal Silicon* (Interpress LTD, Kiev, 1997) ch. 3, p. 46.
[18] H. Takeno, Y. Hayamizu, and K. Miki, J. Appl. Phys. **84**, 3113 (1998).
[19] T. Yoneda, K. Kajiyama, F. Tohjou, Y. Yoshika, A. Ikeda, Y. Kisaka, T. Nishimura, and Y. Kido, J. Appl. Phys. **36**, 7323 (1997).
[20] U. Gözele and T. Y. Tan, Appl. Phys. A: Solids Surf. **28**(1), 31 (1982).
[21] R. C. Newman, J. H. Tucker, A. R. Broun, and S. A. McQuaid, J. Appl. Phys. **70**, 3061 (1991).
[22] L. Zhong and F. Shimura, J. Appl. Phys. **73**, 707 (1993).
[23] P. F. Lugakov and V. V. Luk'yanitsa, Fiz. Tekh. Poluprovodn. **24**, 1721 (1990) [Sov. Phys. Semicond. **24**, 1075 (1990)].
[24] V. P. Markevich and L. I. Murin, Fiz. Tekh. Poluprovodn. **30**, 262 (1996) [Semiconductors **30**, 266 (1996)].
[25] H. J. Stein and S. Hahn, J. Electrochem. Soc. **142**, 1247 (1995).
[26] Yu. V. Martynov, T. Gregorkiewicz, and C. A. J. Ammerlaan, Phys. Rev. Lett. **74**, 2030 (1995).
[27] P. Leary, R. Jones, and S. Oberg, Phys. Rev. B **57**, 3887 (1998).
[28] D. Mathiot, Mater. Sci. Forum **38–41**, 649 (1989).
[29] M. Tajiama, M. Warashina, H. Takena, and T. Abe, Appl. Phys. Lett. **65**, 222 (1994).
[30] V. P. Markevich and L. I. Murin, Fiz. Tekh. Poluprovodn. **22**, 323 (1988) [Sov. Phys. Semicond. **22**, 197 (1988)].
[31] R. Falster, M. Pagani, D. Gambaro, M. Cornara, M. Olmo, G. Ferrero, P. Pichler, and M. Lacob, Solid State Phenom. **57–58**, 129 (1997).

Translated by Frank J. Crowne

Distinctive features of molecular-beam epitaxial growth of silicon on Si (100) surfaces in the presence of arsenic

G. É. Tsirlin, V. N. Petrov, N. K. Polyakov, S. A. Masalov, and A. O. Golubok

Institute for Analytical Instrumentation, Russian Academy of Sciences, 198103 St. Petersburg, Russia

D. V. Denisov, Yu. A. Kudryavtsev, B. Ya. Ber, and V. M. Ustinov

A. F. Ioffe Physicotechnical Institute, Russian Academy of Sciences, 194021 St. Petersburg, Russia
(Submitted April 1, 1999; accepted for publication April 5, 1999)
Fiz. Tekh. Poluprovodn. **33**, 1158–1163 (October 1999)

The authors of this paper discuss their studies of the influence of background arsenic pressure on the properties of autoepitaxial layers of silicon grown on Si (100) surfaces by molecular-beam epitaxy. In these investigations the following experimental techniques were used: reflection high-energy electron diffraction (RHEED), scanning tunneling microscopy, *x*-ray photoelectron spectroscopy, and secondary ion mass spectrometry. © *1999 American Institute of Physics.* [S1063-7826(99)00210-0]

INTRODUCTION

Silicon-based devices are the semiconductor components of choice in contemporary microelectronics markets. There are many reasons for this choice: the relatively low cost of single-crystal silicon films, the existence of well-tested technologies for obtaining high-quality epitaxial layers, and the availability of post-growth processing steps to make device structures. Despite these advantages, silicon is rarely used in modern optoelectronic applications. This is because of the indirect structure of its energy bands, which prevents the emission of light during interband recombination unless a third particle participates (for example, a phonon). Since the probability of such a three-particle process is rather small, the material is optically inert.

Various attempts have been made to increase the efficiency of radiative recombination in silicon. Among them are: doping the silicon with erbium,[1] introduction of quantum dots directly into strained (Si,Ge,C)/Si heteroepitaxial systems by molecular-beam epitaxy (MBE),[2] and use of porous silicon as a medium for incorporating nanometer-sized objects.[3]

Recently we proposed a new technique for obtaining efficient luminescence from structures based on silicon.[4,5] Our approach is to create a layer of coherent nanometer-sized islands of InAs directly in a silicon matrix using MBE, using the fact that spontaneous generation of nanometer-size objects takes place during the initial stages of heteroepitaxal growth involving two systems whose lattice constants are sufficiently mismatched (see, e.g., Ref. 6).

At this time, photoluminescence (PL) has been obtained from quantum dots in the semiconductor system InAs/Si at temperatures up to room temperature. Because this PL exhibits a peak, whose exact position depends on the observation temperature, in the wavelength range 1300–1600 nm ,[7,8] this material system could be a promising source of devices for use in low-loss fiber-optic communication lines. At the same time, the PL intensity from similar structures in the InAs/GaAs system is still rather low. One reason for this is an inability to grow sufficiently high-quality samples, associated with the lack of a processing technology for making the collection of InAs quantum dots and obtaining high-quality heterojunctions during their subsequent overgrowth.

An approach that could lead to further progress in creating light-emitting structures involves the use of so-called ''stacked'' quantum dots, i.e., multilayer systems with quantum dots electrically coupled in the vertical direction. Tersoff *et al.*[9] discussed model representations that describe the formation of ordered collections of nanometer-size inclusions during multilayer heteroepitaxy of two materials with a large lattice-constant mismatch. In that paper the authors presented experimental data showing ''effective'' self-organization of $Si_{1-x}Ge_x$/Si (100) during MBE, which confirmed the physical model proposed.

In creating this kind of three-dimensional structure by MBE, the quality of the intermediate layers that make up the crystalline matrix of the system is extremely important. Layer quality directly impacts such parameters of quantum dot formation as the scatter in lateral dimensions, the degree of ordering, and the maximum number of vertically ''stacked'' layers achievable. The problem of immediate interest to us here–expitaxial growth of silicon in the presence of an increased background of arsenic pressure–unavoidably arises during growth of multilayer structures with quantum dots in systems of type (In,Ga,Al)As/Si.

In this paper we discuss our investigations of how growth conditions and background arsenic pressure affect the properties of autoepitaxial silicon layers grown on a Si (100) surface by molecular-beam epitaxy.

EXPERIMENTAL METHOD

All of our growth experiments were carried out using a Supra MBE machine (ISA Riber, France) consisting of fabrication, analysis, and annealing modules connected by a high-vacuum transport system. In all the modules of the ap-

 © 1999 American Institute of Physics

paratus, excluding the loading section, the base did not exceed 5×10^{-10} Torr. An electron-beam evaporator was used to deposit the Si. The necessary arsenic pressure was created by thermal evaporation of arsenic from an effusion source.

In order to obtain a silicon substrate with an atomically-clean structurally-ordered surface, we implemented the pre-growth preparation method described in Refs. 10 and 11. This method of chemically processing the substrate involves the following sequence of operations:

1) Washing away of organic contaminants from the surface using CCl_4 and acetone;

2) Oxidation of the top layer of silicon in boiling nitric acid and etching away the SiO_2 that forms in HF;

3) Boiling the substrate in a peroxide-ammonium solution with subsequent removal of remaining contaminants together with the oxide of silicon, again using hydrofluoric acid;

4) Creation of a thin capping layer of oxide at the surface of the freshly-cleaned silicon film by boiling in a peroxide-acid $HCl:H_2O_2:H_2O$ solution;

5) A final washing of the film with deionized water and drying with ethyl alcohol on a centrifuge.

The prepared substrates were loaded into the MBE machine with minimum exposure time in air.

Vacuum pre-growth preparation consisted of a regime of two-step thermal annealing. At the first step, the samples were held in the growth chamber at a temperature of 400 °C for 40 min, resulting in a large portion of adsorbed contaminants leaving the surface of the capping layer. This outgassing process was monitored by vacuum-meter readings. This step was followed by a high-temperature (750 °C) 30-min anneal in a weak flux of silicon atoms ($\sim10^{13}\,\mathrm{cm}^{-2}\cdot\mathrm{s}^{-1}$), which causes the oxide layer to sublime. Remaining carbon-containing compounds are removed from the surface along with the oxide. The process of removing the silicon oxide layer is monitored by examining RHEED patterns.

RHEED data reveal that substrates prepared in this way exhibit (2×2) and (7×7) surface reconstructions, which are characteristic of the Si (100) and (111) orientations, respectively. Monitoring the composition of the surface by x-ray photoelectron spectroscopy reveals that the concentrations of carbon and oxygen remaining on the surface are below the lowest levels the spectrometer can detect.

The basic parameters that determine the growth conditions during MBE are the following: the temperature (350 to 800 °C) to which the substrate is heated, the highest pressure in the fabrication chamber during deposition of Si from the electron-beam evaporator (10^{-8} Torr), rates of Si deposition (0.2 and 1.0 Å/s), and background As pressures at the substrate surface of 1.3×10^{-8} Torr (for an As source temperature of 20 °C) and 1.3×10^{-7} Torr (for an As source temperature of 300 °C). The substrates we used were n-type KEF-4.5 (100) silicon films, which were mechanically attached to an indium-free molybdenum substrate holder. The sample holder was continuously rotated during the growth. The structure of the surface during growth was monitored by an automated system for recording and processing RHEED patterns.[12] Post-growth investigations of the samples obtained involved the following measurements: analysis of the surface composition using x-ray photoelectron spectroscopy in the Surface Science Center (Riber) analysis module; study of the morphology of the sample surface at atmospheric pressure using a scanning tunneling microscope (STM) according to the methods described in Ref. 13; and profiling the element composition of the as-grown layers by secondary ion mass spectroscopy using a CAMECA ims4f setup.

Investigations by x-ray photoelectron spectroscopy were carried out *in situ* in the analysis chamber of the apparatus, with x-ray excitation supplied by unmonochromatized $MgK\alpha$ radiation (energy $\hbar\nu=1253.6$ eV, linewidth 0.8 eV). In order to record the electronic spectra, a MAC-2 (Riber) energy analyzer was used in the constant-pass energy regime ($E_{\mathrm{pass}}=10$ eV), with a resolution of 0.8 eV. The pressure of residual gases in the analysis chamber during the measurement was measured to be at a level of 2×10^{-10} Torr.

EXPERIMENTAL RESULTS

The effect of the As atmosphere on the composition of the Si surface layers was investigated by obtaining x-ray photoelectron spectra for the following group of samples: samples with a clean Si surface, i.e., either immediately after removal of the oxide or after growth of an epitaxial Si layer in the absence of As vapor; samples with an initially clean Si surface that had been left for several days in the analysis chamber and subjected to long-term exposure to the residual atmosphere; and Si structures grown in an As atmosphere.

Figure 1 shows the spectra of C $1s$ (285 eV), O $1s$ (531 eV), and As $3d$ (42 eV) lines we obtained.

For pure Si, the intensities of the $1s$-lines of carbon and oxygen in the x-ray photoelectron spectra were below the noise level of the spectrometer. After these samples were held under ultra-high vacuum in the analysis chamber (with a residual pressure of $P_{\mathrm{res}}=2\times10^{-10}$ Torr) for several days, the peaks C $1s$ and O $1s$ appeared (Fig. 1, spectra a). The source of this contamination of the initially-clean silicon surface by carbon- and hydrogen-containing compounds is the residual atmosphere.

For silicon samples grown in the presence of arsenic vapor in the growth chamber, the measurement results have a number of distinctive features. The x-ray photoelectron spectra of these structures exhibit no trace of the peaks C $1s$ and O $1s$, either for just-grown samples of Si layers or for substrates placed in the analysis chamber for a week or longer. The As $3d$ line in the spectrum indicates adsorption of As at the surface of the single-crystal Si (Fig. 1, spectra b). It is noteworthy that heating these samples to 600 °C has no effect on the spectra. Thermal desorption of As from the Si surface begins at temperatures of 650 °C or higher, as indicated by the considerable decrease in intensity of the As $3d$ peak. The departure of some of the As is accompanied by the appearance of traces of carbon and oxygen-containing contaminants on the Si surface (Fig. 1, spectra c).

In order to determine how As vapor affects the Si growth, we carried out a series of growth experiments in which we changed the growth temperature while keeping the rate of deposition of Si and the background As pressure fixed.

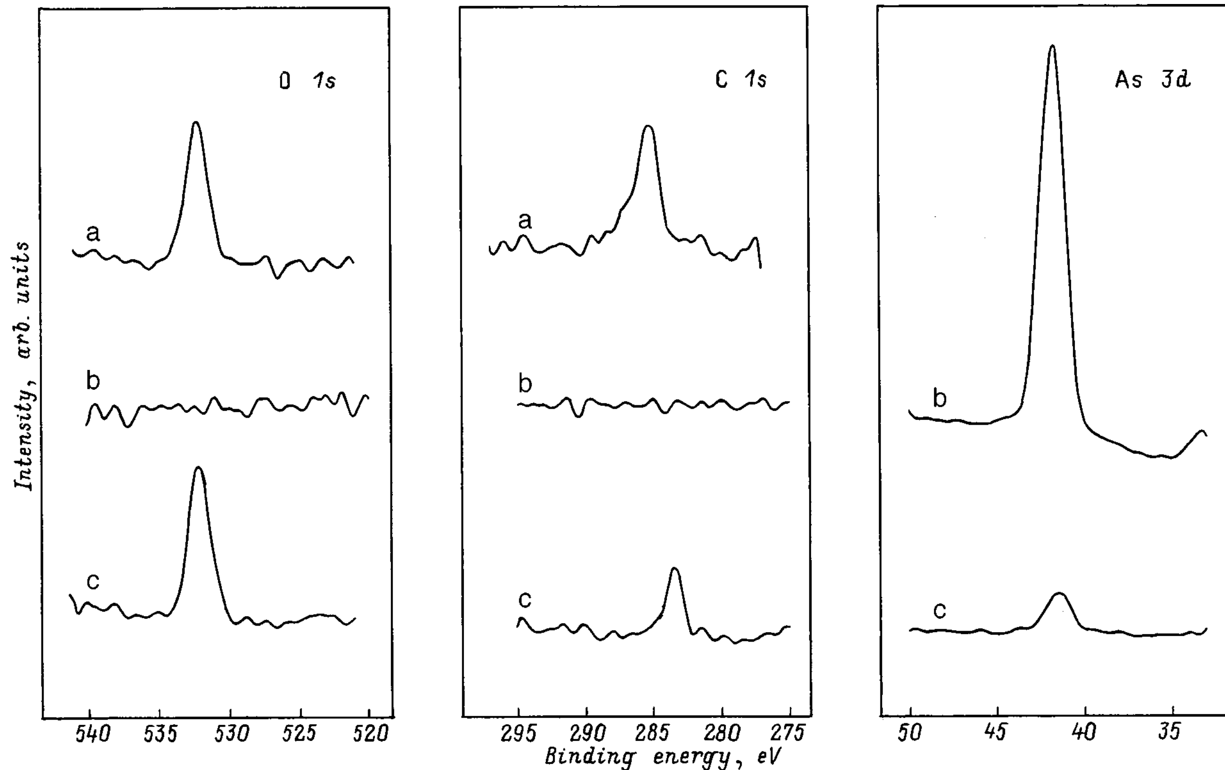

FIG. 1. *X*-ray-electronic spectra of the O 1*s*, C 1*s*, and As 3*d* lines from silicon samples (a) kept for several days in the analysis chamber after cleaning of the surface by thermal removal of the capping oxide, (b) kept for several days in the analysis chamber after deposition of a Si layer in an arsenic atmosphere, and (c) after annealing the layers at a temperature of 650 °C.

In our first series of experiments, we decreased the temperature in a stepwise manner from 800 to 350 °C. We found that layer-by-layer epitaxial growth of Si occurs over a wide range of temperatures when the As pressure is $\sim 1.0\times 10^{-8}$ Torr. Thus, we observed (2×2) diffraction patterns for both deposition rates, 0.2 and 1.0 Å/c, and substrate temperatures (T_s) ranging from 350 to 800 °C, indicating that the surface was atomically smooth and that the deposited Si had an ordered crystal structure (Fig. 2a). Increasing the background pressure of As to $\sim 1.0\times 10^{-7}$ Torr increased the lowest temperature at which epitaxial growth of Si occurred, and the (2×2) surface reconstruction was observed at temperatures above 600 °C. In the range of 600 to 500 °C, pointlike reflections appear on the fundamental lines. At 400 °C the lines disappear, and only the point reflections remain; in this case the brightness of the diffuse background increases (Fig. 2b). Decreasing the temperature further leads to disruption of the epitaxial growth, evidence for which is the absence of diffraction from the surface and a strong diffuse background that is characteristic of an amorphous layer. It should be noted that these changes are not irreversible: heating the surface to 650 °C leads to recovery of the original (2×2) surface structure of the growing layer.

From our studies of the formation of quantum-well InAs clusters on Si (100) surfaces we established that the maximum substrate temperature at which crystalline islands form on the surface was $T_s = 450$ °C.[5] Below this temperature, stable formation of quantum dots takes place. For this reason, we conducted another growth series in which we investigated the conditions for crystallization of amorphous Si layers deposited onto a relatively cold substrate (100 to 120 °C) at various As pressures. We found that at these temperatures increasing the background As pressure affected the observed diffraction pattern. The superstructural reflections decreased in brightness, while the primary lines became shorter. The presence of a direct molecular As flux led to a reconstruction of the Si surface from (2×2) to (1×1). Opening the lid of the silicon source changed the diffraction pattern considerably: the diffraction reflections disappeared, and a strong diffuse background appeared. The amorphous Si crystallized when the substrate was heated. Monitoring of the state of the surface based on diffraction patterns showed that the process of oriented crystallization of amorphous Si at a silicon surface with orientation (100) does not depend on the thickness of the deposited layer (in our case 50, 100, and 500 Å), but rather is determined by the anneal temperature. In films deposited against the background As pressure of $\sim 1.0\times 10^{-8}$ Torr, the (2×2) diffraction pattern appeared when the substrate was heated above 500 °C. Amorphous Si deposited at an As pressure of $\sim 1.0\times 10^{-8}$ Torr crystallized at higher temperatures, $620-650$ °C.

Figures 3a and 3b show STM images of portions of the Si (100) surface obtained (a) at $T_s = 350$ °C in an arsenic flux of 1.3×10^{-8} Torr (with a cold arsenic source) and (b) at $T_s = 450$ °C in an arsenic flux of 1.3×10^{-7} Torr (with an As source heated to 300 °C). The surfaces shown in Fig. 3a are characterized by the presence of indentations of pyramidal form with a crystalline structure in predominantly smooth regions. The lateral dimensions of the indentations are ~ 100 nm, their depth is 15 nm, and their average density is ~ 1

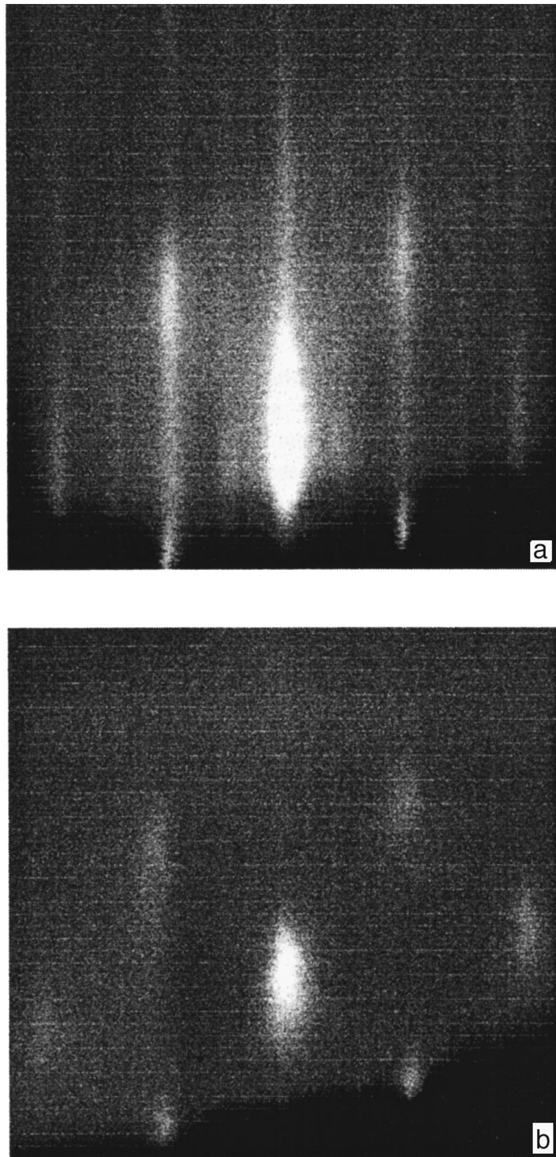

FIG. 2. RHEED patterns measured during autoepitaxial growth of silicon at a substrate temperature $T_s = 400\,^{\circ}\mathrm{C}$ in a residual pressure of 1.3×10^{-8} Torr (a) and in an arsenic flux at a pressure of 1.3×10^{-7} Torr (b).

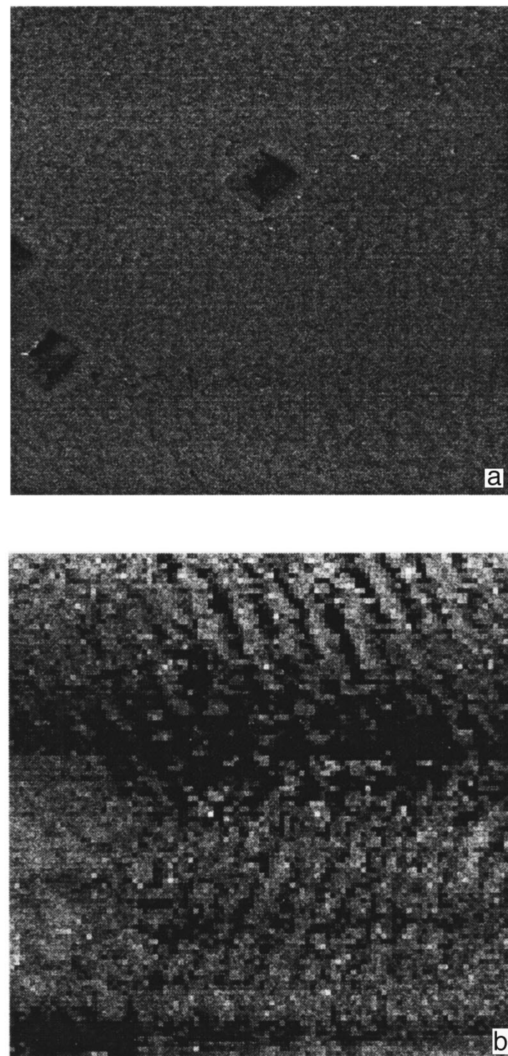

FIG. 3. STM images of portions of the surface of autoepitaxial Si (100) grown at $T_s = 350\,^{\circ}\mathrm{C}$ and a residual pressure of 1.3×10^{-8} Torr (a), and at $T_s = 450\,^{\circ}\mathrm{C}$ in an arsenic flux at a pressure of 1.3×10^{-7} Torr (b). The edges of the image are parallel to crystallographic directions [011] and $[0\bar{1}1]$.

$\times10^8\ \mathrm{cm}^{-2}$, with their sides parallel to [001] and [010]. Because the density of indentations is not large, they do not have much effect on the diffraction pattern (Fig. 2a). These morphological peculiarities are most likely associated with defects in the crystal lattice, and appear during chemical preparation of the films. When the arsenic background pressure was increased, we observed a very different picture: we saw a collection of equidistant, wire-shaped nano-objects, whose characteristic cross-sectional dimensions were 25 nm and a height of 15 nm (Fig. 3b). These objects were oriented in the [031] and $[0\bar{3}1]$ directions, which agrees with the RHEED data shown in Fig. 2b.

In Fig. 4 we show data from our studies of silicon layers grown at various growth rates and background arsenic pressures using secondary-ion mass spectroscopy. The figure shows that increasing the background arsenic pressure leads to a considerably higher probability of attachment of arsenic atoms to the growing layer. Increasing the partial pressure by an order of magnitude, for example, increases the number of incorporated As atoms by approximately two orders of magnitude, regardless of the rate of silicon deposition. Decreasing the substrate temperature also increases the probability of incorporation of arsenic into the growing layer. Changing the growth rate has a smaller effect on the concentration of As atoms in silicon. Obviously this is a consequence of the limited solubility of arsenic in a silicon host. We note that analysis of the diffraction patterns (Figs. 2a and 2b) leads to results that are in qualitative agreement with the secondary-ion mass spectroscopy data.

Thus, we have investigated several features of MBE autoepitaxial growth of silicon in an arsenic atmosphere. We have established that the temperature of crystallization of amorphous silicon deposited on a cold substrate depends on the background arsenic pressure and lies in the range 500 to 650 °C. Increasing the background arsenic pressure leads to incorporation of a larger number of As atoms into the silicon host, which is also observed when the substrate temperature

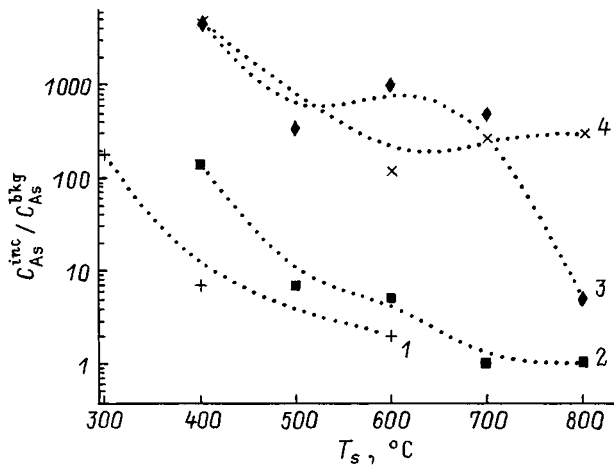

FIG. 4. Secondary-ion mass spectroscopy data on the temperature dependence of the number of As atoms incorporated into the silicon layer (C_{As}^{inc}) normalized by the background concentration in the substrate (C_{As}^{bkg}). Arsenic pressure, Torr/growth rate of Si, Å/s: *1* — 1.3×10^{-8}/0.2; *2* — 1.3×10^{-8}/1.0; *3* —1.3×10^{-7}/0.2; *4* — 1.3×10^{-7}/1.0.

is decreased. Our results indicate the need to choose technology conditions, in particular, substrate temperature and ratio of fluxes of group-III, group-IV and group-V elements, in order to address the problem of obtaining high-quality interfaces in the InAs / Si system.

We wish to thank Yu. B. Samsonenko for participating in the growth experiments. We also thank N. N. Ledentsov and N. D. Zakharov for useful discussions.

This work was carried out with the partial support of INTAS (Grant 96-0242), the scientific program ''Promising Technologies and Apparatus for Micro- and Nanoelectronics'' (project 02.04.5.1.40.E.46), and the Russian Fund for Fundamental Research (projects 98-02-18317 and 99-01-16799).

[1] G. Franzo, F. Priolo, S. Coffa, A. Polman, and A. Carnera, Appl. Phys. Lett. **64**, 2235 (1994).
[2] K. Eberl, K. Brunner, and W. Winter, Thin Solid Films **249**, 98 (1997).
[3] A. G. Gullis, L. T. Canha, and P. D. J. Calcott, J. Appl. Phys. **82**, 909 (1997).
[4] G. E. Tsyrlin, V. N. Petrov, V. G. Dubrovskii, S. A. Masalov, A. O. Golubok, N. I. Komyak, N. N. Ledentsov, Zh. I. Alferov, and D. Bimberg, Pis'ma Zh. Tekh. Fiz. Lett. **24** (8), 13 (1998) [Tech. Phys. Lett. **24**, 628 (1998)].
[5] G. E. Cirlin, V. G. Dubrovskii, V. N. Petrov, N. K. Polyakov, N. P. Korneeva, V. N. Demidov, A. O. Golubok, S. A. Masalov, D. V. Kurochkin, O. M. Gorbenko, N. I. Komyak, V. M. Ustinov, A. Yu. Egorov, A. R. Kovsh, M. V. Maximov, A. F. Tsatsul'nikov, B. V. Volovik, A. E. Zhukov, P. S. Kop'ev, Zh. I. Alferov, N. N. Ledentsov, M. Grundmann, and D. Bimberg, Semicond. Sci. Technol. **13**, 1262 (1998).
[6] N. N. Ledentsov, V. M. Ustinov, V. A. Shchukin, P. S. Kop'ev, Zh. I. Alferov, and D. Bimberg, Fiz. Tekh. Poluprovodn. **32**, 385 (1998) [Semiconductors **32**, 343 (1998)].
[7] A. F. Tsatsul'nikov, A. Yu. Egorov, P. S. Kop'ev, A. R. Kovsh, M. V. Maximov, V. M. Ustinov, B. V. Volovik, A. E. Zhukov, Zh. I. Alferov, G. E. Cirlin, A. O. Golubok, S. A. Masalov, V. N. Petrov, N. N. Ledentsov, R. Heitz, M. Grundmann, D. Bimberg, I. P. Soshnikov, P. Werner, and U. Gösele, in *Proceedings of the 24th International Conference in Physics of Semiconductors*, Jerusalem, 1998 (World Scientific, Singapore, 1999) [in press].
[8] A. Yu. Egorov, A. R. Kovsh, V. M. Ustinov, A. E. Zhukov, M. V. Maksimov, G. E. Cirlin, N. N. Ledentsov, D. Bimberg, P. Werner, and Zh. I. Alferov, J. Cryst. Growth (1999) [in press].
[9] J. Tersoff, C. Teichert, and M. G. Lagally, Phys. Rev. Lett. **76**, 1675 (1996).
[10] A. Ishisaka and Y. Shiraki, J. Electrochem. Soc. **133**, 666 (1986).
[11] V. A. Ioshkin, A. A. Orlikovskiĭ, S. R. Oktyabr'skiĭ, A. V. Kvit, and E. Yu. Dovydenko, Proceedings FTIAN (Nauka, Moscow, 1994), Vol. 8, p. 58.
[12] G. M. Gur'yanov, V. N. Demidov, N. N. Korneeva, V. N. Petrov, Yu. V. Samsonenko, and G. E. Tsyrlin, Zh. Tekh. Fiz. **67**, 111 (1997) [Tech. Phys. **67**, 956 (1997)].
[13] A. O. Golubok, S. A. Masalov, N. V. Ponomareva, V. N. Petrov, S. Ya. Tipisev, and G. E. Tsyrlin, *Surfaces: X-Ray, Synchrotron, and Neutron Investigations*, Vol. 2, 70 (1998).

Translated by Frank J. Crowne

ELECTRONIC AND OPTICAL PROPERTIES OF SEMICONDUCTORS

Detection of paramagnetic recombination centers in proton-irradiated silicon

L. S. Vlasenko, M. P. Vlasenko, and V. A. Kozlov

A. F. Ioffe Physicotechnical Institute, Russian Academy of Sciences, 194021 St. Petersburg, Russia

V. V. Kozlovskiĭ

State Technical University, 195251 St. Petersburg, Russia
(Submitted December 28, 1998; accepted for publication December 30, 1998)
Fiz. Tekh. Poluprovodn. **33**, 1164–1167 (October 1999)

The method of spin-dependent recombination was used to record electron spin resonance (ESR) spectra of recombination centers in a thin ($\sim 1\,\mu$m) surface layer of *p*-type silicon grown by the Czochralski method and irradiated by protons with energies of ~100 keV. Spectra of excited triplet states of the oxygen + vacancy complex (*A*-centers) were observed along with complexes consisting of two carbon atoms and an interstitial silicon atom ($C_S-Si_I-C_S$ complexes). The intensity of the ESR spectra of these radiation-induced defects was found to be largest at irradiation doses of $\sim 10^{13}\,cm^{-2}$, and decreased with increasing dose, which is probably attributable to passivation of the radiation-induced defects by hydrogen. © *1999 American Institute of Physics.* [S1063-7826(99)00310-5]

Irradiation of silicon with protons leads to the appearance of point defects analogous to defects that appear when silicon is irradiated with electrons, γ-rays, and neutrons.[1–6] Because of their high mobility and chemical activity, hydrogen atoms can enter into the composition of radiation-induced defects, and also can compensate for unpaired electrons at defect dangling bonds. The presence of hydrogen atoms in radiation-induced defects was established by the method of electron spin resonance (ESR) using the hyperfine structure of spectra from the hydrogen nucleus.[6] Defects in which the hydrogen atoms compensate for unpaired electrons are nonparamagnetic, and cannot be observed by ESR.

The protons used to irradiate the silicon samples used in the ESR investigations of radiation-induced defects were primarily high-energy protons (3–30 MeV), with ion currents corresponding to irradiation doses of $10^{14}-10^{16}\,cm^{-2}$. At these proton energies and irradiation doses, the radiation-induced defects are distributed in a silicon layer whose thickness ranges from 100 μm to several millimeters. The number of radiation defects induced is large enough to be recorded by ESR.[4–6]

At this time, implantation of low-energy protons (less than 150 keV) at rather low doses on the order of $10^{12}-10^{14}\,cm^{-2}$ is a widely used processing technique in semiconductor electronics. For this reason there is interest in studying the composition and microstructure of the defects that form in a thin surface layer of silicon during this irradiation. However, because of the small number of paramagnetic centers, the sensitivity to the ordinary ESR method turns out to be insufficient to record their spectra. It is, however, possible to achieve this goal by detecting the ESR spectrum via spin-dependent recombination (SDR) effects,[7–9] which have a sensitivity that is four orders of magnitude higher than traditional ESR methods. The possibility of using these methods to record ESR spectra of surface recombination centers and defects that form on a silicon surface during *x*-ray irradiation was demonstrated in Ref. 6.

In this paper we present the results of experiments in which we detected ESR spectra of radiation defects in silicon created in a thin layer near the surface irradiated by protons with energies of ~100 keV, using spin-dependent recombination.

1. EXPERIMENTAL PROCEDURE

These experiments were conducted using *p*-type Czochralski-grown silicon doped with boron, and having a resistivity $\rho \cong 40\,\Omega\cdot$cm. Samples in the form of films with dimensions $10\times3\times3$ mm were irradiated at room temperature with protons having energies of ~ 100 keV at doses ranging from 10^{12} to $10^{17}\,cm^{-2}$. The surface of the samples was processed in a polishing etch before irradiation.

The ESR spectra of paramagnetic centers was recorded using a three-centimeter band ESR spectrometer at temperatures of 4–80 K, using the spin-dependent recombination (SDR) effect.[7–9] The samples were illuminated through a window in the spectrometer resonator by a 100-W incandescent lamp. The change in sample photoconductivity as the transitions between magnetic sublevels of the recombination centers were saturated was recorded as changes in the Q-factor of the resonator of the ESR spectrometer caused by absorption of the electric contribution of the microwave field by the photoexcited carriers. In these experiments, the power of the microwave field used was as high as 400 mW.

In detecting the signals we used double modulation of the magnetic field at frequencies of 100 kHz and 100 Hz and

 © 1999 American Institute of Physics

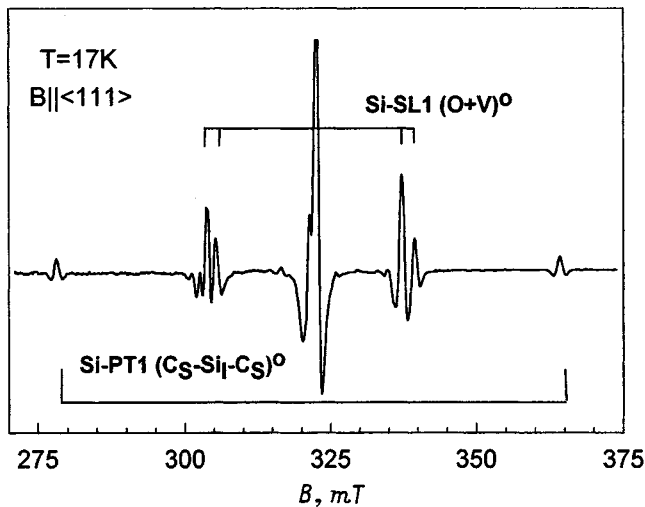

FIG. 1. SDR–ESR spectrum recorded at $T=17$ K in silicon irradiated by 100-keV protons at a dose of 10^{13} cm^{-2}.

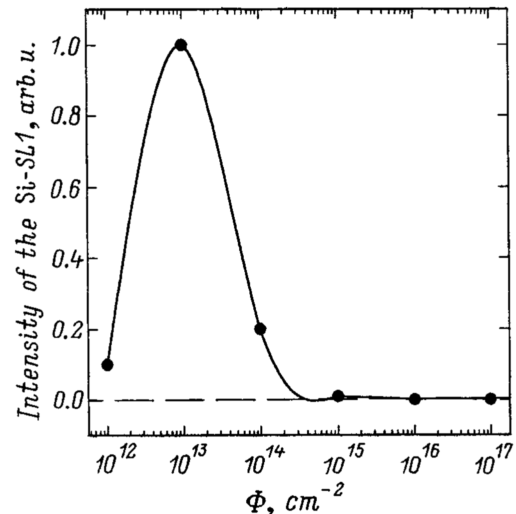

FIG. 2. Dependence of the intensity of the Si–SL1 spectrum on the proton irradiation dose Φ.

synchronous detection. This allowed us to record signals proportional to the second derivative of the absorption with respect to magnetic field and to significantly suppress the broad cyclotron resonance lines and changes in the zero level of output voltage of the synchronous detector, associated with changes in the sample resistance as the magnetic field was scanned over wide limits.

2. RESULTS AND DISCUSSION

Figure 1 shows SDR–ESR spectra of defects recorded in proton-irradiated silicon samples. Examination of the angular dependences of the positions of lines in these spectra reveals that the two groups of lines at values of the magnetic field $B \cong 305$ and 340 mT correspond to the Si–SL1 spectrum,[10] which arises from excited triplet states of a neutral A-center (an oxygen + vacancy complex). The two lines at $B \cong 278$ and 364 mT belong to the Si–PT1 spectrum,[7,8] which arises from excitation of a triplet state of a complex consisting of two carbon atoms located on neighboring lattice sites of the silicon and an interstitial silicon atom which forms bonds with these carbon atoms. Figure 1 also shows a spectral line at $B \cong 323$ mT, arising from centers with spin $S=1/2$ and a g-factor close to $g \approx 2$. This spectrum consists of poorly resolved lines and was not identified. We observed no paramagnetic recombination centers that incorporated hydrogen atoms into their composition, which would lead to hyperfine splitting of the lines caused by the hyperfine interaction with the hydrogen nuclei.

All the spectra observed in proton-irradiated silicon disappear when a surface layer of thickness $\sim 1.5\,\mu$m is removed by etching. This indicates that the paramagnetic recombination centers under study are localized in a thin layer near the irradiated surface.

We found that the samples that exhibited the most intense spectra were those irradiated with protons at a dose of $\Phi \sim 10^{13}$ cm^{-2}. As an example, in Fig. 2 we plot the dependence of the intensity of the Si–SL1 spectrum on irradiation dose. The intensity of the Si–SL1 and Si–PT1 spectra from samples irradiated by a proton dose of $\Phi \sim 10^{13}$ cm^{-2} is the same order as the intensity of these spectra from the same silicon samples irradiated by γ-rays at a dose $\Phi_\gamma \sim 10^{14}$ cm^{-2}. This allows us to make an order of magnitude estimate of the number of defects responsible for the appearance of the Si–SL1 and Si–PT1 spectra. The rate of introduction of radiation-induced defects k during γ-irradiation does not exceed 10^{-3} cm^{-1} (Ref. 1), while the number of defects in the bulk sample $V \sim 10^{-2}$ cm^{-3} is $N = k\Phi V \sim 10^8$. The ESR spectra from this number of defects is easily recorded by SDR. Increasing the irradiation dose of γ-rays to $10^{17}-10^{18}$ cm^{-2} increases the number of defects. This decreases the intensity of the SDR–ESR spectra, and the usual EPR spectrum appears.[7,8]

In proton-irradiated silicon, the decrease in intensity of the SDR–ESR spectra as the irradiation dose is increased is found to be more abrupt than for γ-irradiated silicon, and the usual ESR spectra of A-centers and carbon complexes $C_S-Si_I-C_S$ is not observed. In samples irradiated with proton doses of order 10^{17} cm^{-2}, isotropic ESR lines appear with g-factors of 2.0055, corresponding to disordered regions and dangling bonds at the silicon surface. In this case the change in the state of the irradiated surface can be observed visually as blistering of the surface, i.e., the peeling off of silicon flakes after high-dose implantation.

When the silicon is irradiated with $\sim$100-keV protons, radiation-induced defects form in a layer about $\sim 1\,\mu$m thick near the irradiated surface. For our samples this corresponds to a volume $V \sim 3 \times 10^{-5}$ cm^{-3}. The number of paramagnetic recombination centers in a sample irradiated with a dose $\Phi \sim 10^{13}$ cm^{-2}, estimated above by comparing the intensity of spectra for samples irradiated with protons and γ-rays, is on the order of $\sim 10^8$, which is considerably less than the number of implanted hydrogen atoms $N(\mathrm{H} = \Phi S \sim 3 \times 10^{12})$ (here $S \approx 0.3$ cm^2 is the area of the irradiated sample surface). This allows us to argue that most of the radiation-induced defects are passivated by hydrogen, and that they are not paramagnetic. There are two phenomena

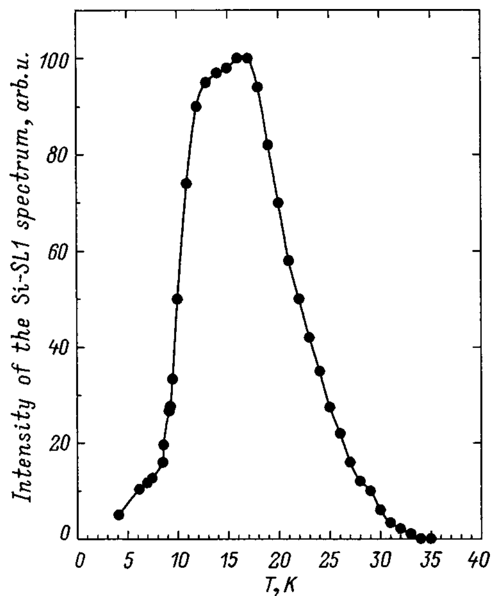

FIG. 3. Dependence of the intensity of the Si–SL1 spectrum on temperature *T*.

that limit the increase in the number of defects containing oxygen and carbon as the irradiation dose increases. First of all, the number of these defects cannot exceed the number of impurity oxygen and carbon atoms, whose concentrations in Czochralski-grown silicon is on the order of 10^{18} and $10^{17}\,\mathrm{cm}^{-3}$, respectively. The number of such atoms in a layer irradiated by protons is $\sim 3\times10^{12}-3\times10^{11}$, which is comparable to the number of implanted hydrogen atoms when the irradiation doses are on the order of $10^{13}\,\mathrm{cm}^{-2}$. The second reason why the number of, e.g., *A*-centers or carbon complexes $C_S-Si_I-C_S$, cannot increase indefinitely is that they can convert into more complicated defects.[1] Thus, it is found that the maximum number of *A*-centers and $C_S-Si_I-C_S$ complexes in a layer irradiated by protons does not exceed a value of $\sim 10^{12}$. However, the number of hydrogen atoms increases proportional to the irradiation dose Φ, and for $\Phi\sim10^{15}-10^{17}\,\mathrm{cm}^{-2}$ it can exceed by several orders of magnitude the number of *A*-centers and $C_S-Si_I-C_S$ complexes. We can thus conclude that the abrupt decrease in the intensity of the Si–SL1 spectrum (see Fig. 2) and the same decrease in the intensity of the Si–PT1 spectrum with increasing irradiation dose when $\Phi>10^{13}\,\mathrm{cm}^{-2}$ is associated with the capture of hydrogen atoms by *A*-centers and $C_S-Si_I-C_S$ complexes, which leads to passivation and disappearance of the paramagnetism of these defects.

In silicon irradiated by protons, SDR– ESR spectra are observed in the temperature range 4–35 K, and have the same temperature dependence of the line intensity. The temperature dependence of the Si–SL1 spectral intensity, which is shown in Fig. 3, is at a maximum at temperatures of 12 to 18 K. This behavior of the spectra as the temperature is varied differs significantly from the temperature dependences of Si–SL1 and Si–PT1 spectra detected by SDR when the same silicon is irradiated by 1-MeV electrons or by γ-rays. In these latter cases, the radiation-induced defects are created throughout the volume of the crystal. In this case the Si–SL1 and Si–PT1 spectra are observed in the temperature range 4–140 K; the decrease in intensity of the Si–PT1 spectrum with increasing temperature in the range 30–140 K is nonmonotonic in character and has several peaks. This difference in the temperature dependences of the ESR spectral intensity could indicate that conditions for spin-dependent recombination of photoexcited carriers generated by light in the crystal bulk are different, depending on whether the defects are uniformly distributed throughout the volume or localized near the proton-irradiated surface. In the latter case, the temperature dependence of the diffusion length for photoexcited carriers and the difference in positions of the Fermi level in the bulk of the crystal and in the skin layer, which contains the radiation-induced defects, should probably play an important role in SDR. These problems will be addressed in a separate publication.

Thus, in the course of these investigations we have recorded ESR spectra of excited triplet states of *A*-centers and carbon-containing complexes for the first time, using the method of spin-dependent recombination in a thin skin layer of silicon irradiated by protons with energies $\sim 100\,\mathrm{keV}$. Optimal conditions were established for recording SDR–ESR spectra in *p*-type Czochralski-grown silicon, corresponding to irradiation doses of $\Phi\sim10^{13}\,\mathrm{cm}^{-3}$ and an observation temperature $T\sim 12-18\,\mathrm{K}$. The abrupt decrease observed in the intensity of the spectra with increasing irradiation dose by protons above $10^{13}\,\mathrm{cm}^{-2}$ could be due to passivation of the *A*-centers and carbon complexes with hydrogen.

We wish to thank B. P. Zakharchena and R. Laĭkho for useful discussions of the results.

This work was carried out with the financial support of the Russian Fund for Fundamental Research, Project No. 97-02-18062, and with the partial support of the goal-oriented scientific-engineering program ''Promising Technology and Apparatus for Micro- and Nanoelectronics'' of the Science and Technology Ministry of the Russian Federation, Project No. 02.04.330.89.1.2.

[1] *Problems in the Radiation Processing of Semiconductors*, edited by L. S. Smirnov (Nauka, Novosibirsk, Siber. Dept. of the Sov. Acad. Sci., 1980).
[2] V. V. Kozlovski, V. N. Lomasov, and L. S. Vlasenko, Radiat. Eff. **106**, 37 (1988).
[3] *Radiation-Induced Processes in Materials Technology and Electronics Manufacturing*, edited by V. V. Kozlovskiĭ and V. S. Ivanov (Energoatomizdat, Moscow, 1997).
[4] H. Lütgemeier and K. Schnitzke, Phys. Lett. A **25**, 232 (1967).
[5] V. A. Botvin, Yu. V. Gorelinskiĭ, V. O. Sigle, and M. A. Chubisov, Fiz. Tekh. Poluprovodn. **6**, 1683 (1972) [Sov. Phys. Semicond. **6**, 1453 (1972)].
[6] Yu. V. Gorelinskiĭ and N. N. Nevinnyĭ, Pis'ma Zh. Tekh. Fiz. **13**, 105 (1987) [Sov. Tech. Phys. Lett. **13**, 45 (1987)].
[7] L. S. Vlasenko, M. P. Vlasenko, V. A. Khramtsov, and V. N. Lomasov, Zh. Éksp. Teor. Fiz. **91**, 1037 (1986) [Sov. Phys. JETP **64**, 612 (1986)].
[8] L. S. Vlasenko and V. A. Khramtsov, Pis'ma Zh. Tekh. Fiz. **11**, 909 (1985) [Sov. Tech. Phys. Lett. **11**, 375 (1985)].
[9] L. S. Vlasenko, in *Proceedings of the 20th International Conference in Physics of Semiconductors*, edited by E. V. Anastassakis and J. D. Joannopoulos (Thessaloniki, Greece, 1990), p. 714.
[10] K. L. Brower, Phys. Rev. B **4**, 1968 (1971).

Translated by Frank J. Crowne

Luminescence properties of InAs layers and $p-n$ structures grown by metallorganic chemical vapor deposition

T. I. Voronina, N. V. Zotova, S. S. Kizhayev,[*)] S. S. Molchanov, and Yu. P. Yakovlev

A. F. Ioffe Physicotechnical Institute, Russian Academy of Sciences, 194021 St. Petersburg, Russia
(Submitted February 15, 1999; accepted for publication February 18, 1999)
Fiz. Tekh. Poluprovodn. **33**, 1168–1172 (October 1999)

The luminescence properties of p- and n-type InAs layers grown by gas-phase epitaxy from metallorganic compounds at atmospheric pressure are investigated. Acceptor levels in InAs are identified with energies 350, 372, 387, and 397 meV. Optimal conditions are determined for the growth of InAs layers in a reactor of planetary type. At a growth temperature of 565 °C, InAs structures were obtained with abrupt $p-n$ junctions. The structures grown were used to make light-emitting diodes operating at wavelengths of 3.1 μm ($T=$ 77 K) and 3.7 μm ($T=$ 300 K). © *1999 American Institute of Physics.* [S1063-7826(99)00410-X]

INTRODUCTION

The growth of indium arsenide layers by metallorganic vapor-phase epitaxy (MOVPE) has been discussed in several papers, whose authors are primarily interested in investigating the electrical properties of their samples.[1–12] Iwamura *et al.* [13] investigated the process of thermal diffusion of zinc into an InAs substrate in a MOVPE reactor at low pressure. The diffusion takes place in an atmosphere of hydrogen containing tributylarsine (TBAs), with diethyl zinc (DeZn) used as a source of zinc. It was established that the dependence of the diffusion depth of Zinc on substrate temperature had a complex character, with a minimum at $T=530\,°C$. Fang *et al.*[14] investigated the effect of growth temperature on the photoluminescence (PL) of InAs grown by MOVPE at atmospheric pressure. The PL was measured at T = 10 K. For growth temperatures above 400 °C the authors observed a single peak at 415 meV [recombination of electrons at the bottom of the conduction band (E_0) with holes at the top of the valence band (E_V), or of bound excitons]. For samples grown at temperatures below 400 °C additional peaks were observed at wavelengths of 3.08 and 3.25 μm. Lacroix *et al.*[15] presented PL measurements of the properties of high-purity InAs grown at low pressure using trimethyl indium (TMI) and TBAs as sources. These authors observed in the PL spectra (380–420 meV, 1.4 K) of films grown at 540 °C intense emission peaks at 397 meV (donor-acceptor pairs), at 413 meV (excitons bound to acceptors) and at 415 meV (excitons bound to donors). Another topic of interest is the thermodynamics of layered growth. The diverse constructions of MOVPE reactors and the number of sources used lead to various results, so that at this time there is much disagreement in the literature regarding the nature of the mechanisms of InAs layer growth.

In this paper we investigate the PL properties of layers of n- and p-type InAs grown by MOVPE at atmospheric pressure in a reactor of planetary type, and also electroluminescence spectra measured from light-emitting diodes based on abrupt InAs $p-n$ junctions, with the goal of determining mechanisms for radiative transitions.

EXPERIMENT

InAs layers were grown by MOVPE at atmospheric pressure in a reactor of planetary type with a diameter of 30 cm. The graphite substrate holders were heated by a three-zone resistive heater separated from the inner volume of the chamber by a quartz bell. The gas-vapor mixture was fed in from the periphery of the bell towards the center. In order to achieve uniform growth on the surface of the substrate, the substrate holder was rotated around the central axis of the reactor and around its own axis. The sources of arsenic and indium were respectively arsine (AsH_3), diluted to 20% in hydrogen, and TMI. The temperature of the TMI evaporator was +18 °C. In all these experiments the hydrogen flux through the TMI evaporator was $600\,cm^3$/min. The rate of additional hydrogen flux was 25 liters/min. The experiments were carried out in the range of substrate temperatures 350–600 °C. The mole fraction ratios of group–III and group–V elements in the gas phase were in the range V/III = 1–40. In order to obtain p-type conductivity in the InAs, the layers were doped with zinc. The source of zinc was DeZn. The DeZn evaporator was held at a temperature of 5 °C. In these experiments we used InAs substrates oriented along the (100), (111)A, and (111)B axes. The properties of the structures grown were investigated by studying the PL excited by a GaAs diode laser (wavelength $\lambda=0.8\mu$m, emitted power $P=10$ W in pulse regime, $\tau=5\mu$s, $f=$ 500 Hz), whose light was directed onto the grown InAs layers in a ''reflection'' geometry. The test sample was held at $T=$ 77 K. The grown structures were used to make light-emitting diodes. The light-emitting structures were made by standard photolithography in the form of mesa-diodes. The diameter of the mesas was 300 μm. A continuous ohmic contact was created at the substrate. The diameter of the point contact above the epitaxial structure was 50 μm. Ohmic contacts were made by depositing gold with tellurium (for an n-type conductivity layer) and gold with zinc (for a p-type conductivity layer). For the structures obtained we measured the PL spectrum, and also the current-voltage (IV) and capacitance-voltage characteristics of the light-emitting diode structures at tem-

 © 1999 American Institute of Physics

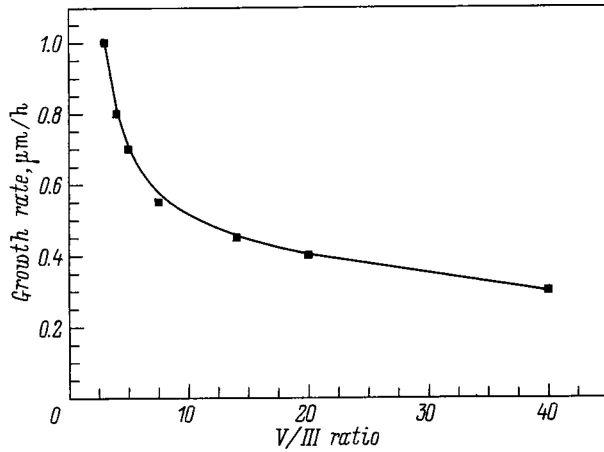

FIG. 1. Dependence of growth rate on V/III ratio for InAs layers grown at $T=565$ °C on an InAs (100) substrate.

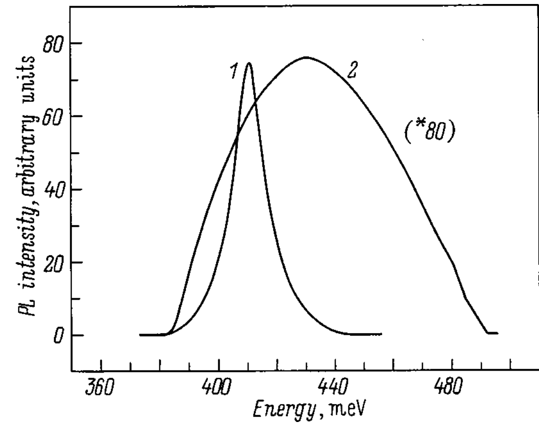

FIG. 3. PL spectra of InAs layers grown on InAs (111)B substrates at various growth temperatures, °C: *1* — 565, *2* — 350.

peratures of 77 and 300 K. The capacitance was measured by standard bridge methods at a frequency of 1 MHz. Using secondary-ion mass spectroscopy, we determined the distribution of impurities with respect to depth into the sample.

RESULTS AND DISCUSSION

InAs layers

Using the results of these experiments, we established that the rate of growth of the layers is a strong function of the V/III molar ratio in the gas phase. Figure 1 shows the dependence of the growth rate on the V/III ratio for layers grown at $T=565$ °C on InAs substrates with (100) orientation. Similar dependences were observed at other growth temperatures and on InAs substrates with (111) orientation. In Fig. 2 we plot the growth rate of the layers versus substrate temperature. Thermal decomposition of TMI is incomplete in the temperature range 350–400 °C (Ref. 16) and the growth is determined by kinetic processes at the substrate surface. The effect of surface kinetics is confirmed by the increase in growth rate with increasing substrate temperature. In the temperature range 400–570 °C the growth is determined primarily by diffusion of reagents through the boundary layer at the substrate surface. At substrate temperatures above 570 °C the growth rate begins to fall off abruptly. In our view, the reason for this decrease is the almost complete decomposition of TMI just in front of the substrate, which decreases the group-III element flux through the boundary layer at the substrate surface, thereby causing the growth rate to fall off. It should be noted that surface kinetics is found to affect growth over the entire temperature range. Evidence for this behavior is the influence of InAs substrate orientation on the growth rate and how it varies with increasing growth temperature. At 565 °C and a V/III ratio of 7.5 for layers grown on InAs substrates with orientation (111)B, the growth rate is 1.5 μm/h. On substrates with different orientation the layer growth occurs more slowly [(111)A — 0.8 μ/h, (100) — 0.5 μ/h].

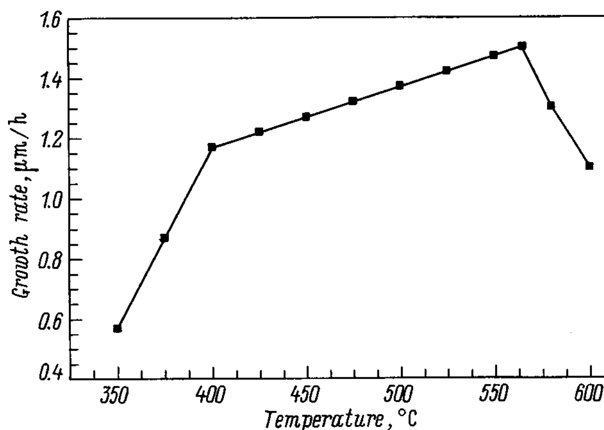

FIG. 2. Dependence of growth rate on substrate temperature for InAs layers grown with a V/III ratio of 7.5 on InAs (111)B substrates.

From galvanomagnetic measurements we established that conductivity was n-type in all the intentionally undoped layers. Depending on the growth regime, we observed different positions for the peaks in the PL spectrum. Figure 3 shows a PL spectrum from one of the purest InAs layers ($n\sim 5\times 10^{15}\,\mathrm{cm}^{-3}$), grown at 565 °C on a substrate of InAs with orientation (111)B. The layers have a mirror-smooth surface. The energy of the single peak is 408 meV, which corresponds to the width of the bandgap E_g in InAs (Ref. 17), i.e., interband radiative transitions are occurring.

The width of the PL spectrum at half-height is 11 meV, which is close to kT at 77 K. This result shows that the grown layers are structurally perfect. Secondary-ion mass spectroscopy measurements show that the concentration of background impurity atoms such as carbon and oxygen in these layers is below the threshold for detection by our measurement equipment ($\sim 5\times 10^{15}\,\mathrm{cm}^{-3}$).

Allaberenov *et al.*[17] showed that in InAs with increasing electron densuity the emission peak, which tracks the Fermi levels

$$F_{1/2}(\mu^*)=\frac{1}{4\pi}n\left(\frac{h^2}{2m^*kT}\right)^{3/2},$$

moves toward higher energies. We found that the concentration of electrons increases with decreasing growth temperature, and that the emission peak shifts toward shorter wave-

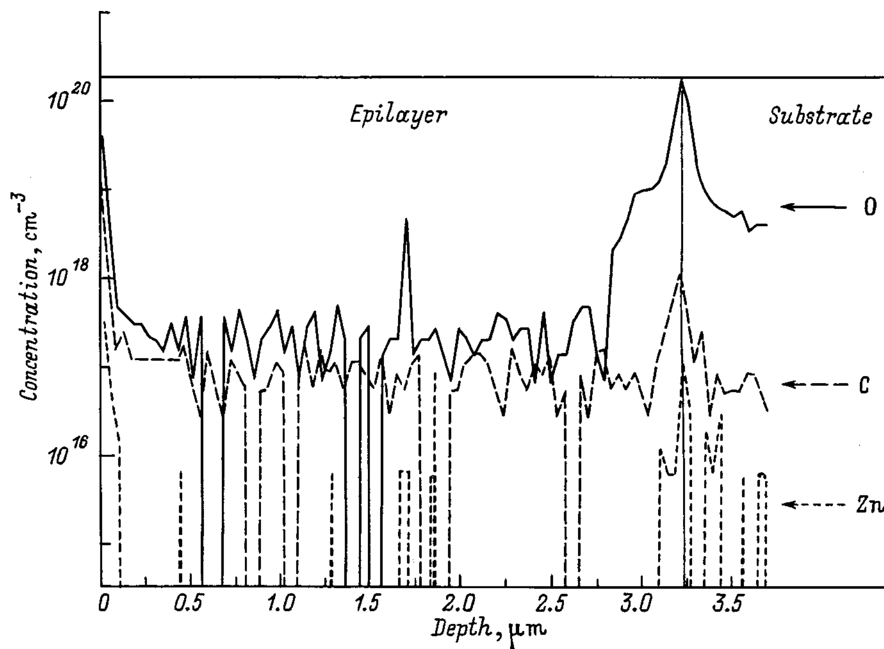

FIG. 4. Distribution of background impurities versus thickness for a sample grown at a substrate temperature of 350 °C.

lengths. The PL spectrum of a sample grown at 350° is shown in Fig. 3. The energy of the peak at $h\nu_m=$ 430 meV and the width of the spectrum at half-height for the peak at 78 meV corresponds to an electron concentration $n=4\times10^{17}\,\mathrm{cm}^{-3}$ (Ref. 17).

Using the method of secondary-ion mass spectroscopy, we established that decreasing the growth temperature leads to an increase in the concentration of background impurities in the layer. The distribution of background impurities over the thickness of the sample is shown in Fig. 4. As we have already noted, at temperatures below 400 °C TMI decomposes only partially, and carbon atoms can be incorporated into the lattice instead of indium atoms. Ito *et al.*[18] investigated the behavior of carbon in $Ga_{1-x}In_xAs$ layers grown by molecular beam epitaxy. As soon as the In content in the layer exceeded 60%, the conductivity switched from *p*- type to *n*-type. It is likely that the strength of the chemical bond between carbon and the group-III element determines the conductivity type in the layer. In GaAs, the carbon is incorporated into the sublattice of the group-V element, and hence is an acceptor impurity. The In–C bond is weaker than the Ga–C bond; therefore, in contrast to GaAs, in InAs carbon is incorporated into the group-III sublattice and is a background donor impurity.

From Fig. 4 it is clear that oxygen is present in the layer. Huang *et al.*[19] studied controlled introduction of oxygen into $In_xGa_{1-x}As$ films, and established that in InAs all the energy levels connected with oxygen are located in the conduction band. In our work, oxygen behaves as a neutral impurity and its presence in the InAs layer is most likely associated with the low growth temperature, since oxygen is found to appear in GaAs layers during low-temperature MBE growth.[20] It is obvious that increasing the growth temperature decreases the embedding level of of oxygen. Evidence for this behavior is found in secondary-ion mass spectroscopy measurements of InAs layers grown at a temperature of 565 °C.

The PL spectra of layers grown on InAs substrates with orientation (100) exhibit both interband radiative recombination and radiative transitions with the participation of acceptor levels located roughly 10 meV above the top of the valence band.

Our studies show that it is desirable to avoid the use of *p*-type substrates doped with zinc when investigating PL properties. It is clear from Fig. 4 that even at 350 °C diffusion of zinc atoms takes place from the substrate into the layer. Diffusion and the formation of $n-p$ junctions lower the PL efficiency of the grown layer.

Measurements of PL spectra of *p*-type InAs(100) substrates ($p=6\times10^{15}\,\mathrm{cm}^{-3}$) show that there is only one peak present at an energy of 350 meV, which corresponds to a recombination transition from the bottom of the conduction band to a deep acceptor level.

InAs *p*–*n* structures

In our initial attempts to make light-emitting diodes, we used structures consisting of *p*-InAs (100) substrates ($p=6\times10^{15}\,\mathrm{cm}^{-3}$, $T=77$ K) doped with zinc and *n*-type InAs layers which were not doped intentionally. The photoelectric properties of these structures were discussed in Ref. 21. Figure 5 shows the electroluminescence (EL) spectrum of an SS-100 diode at 77 K. The dominant peak corresponds to a recombination transition from the bottom of the conduction band to a deep acceptor level located approximately 35 meV above the top of the valence band. The peak with lower intensity corresponds to interband recombination. At room temperature the EL intensity is weak.

In order to obtain light-emitting diodes operating at room temperature, we grew fully epitaxial structures consisting of a *n*-InAs (111)B substrate ($n\sim3\times10^{15}\,\mathrm{cm}^{-3}$), an *n*-type layer with thickness 1 μm which was not doped intentionally, and a *p*-type layer with the same thickness. As we have already mentioned, *p*-type conductivity in InAs is obtained by doping the layers with zinc. The structures were

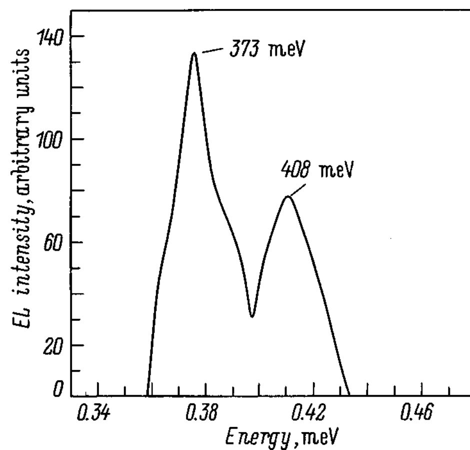

FIG. 5. EL spectrum of an SS—100 InAs diode at a temperature of 77 K.

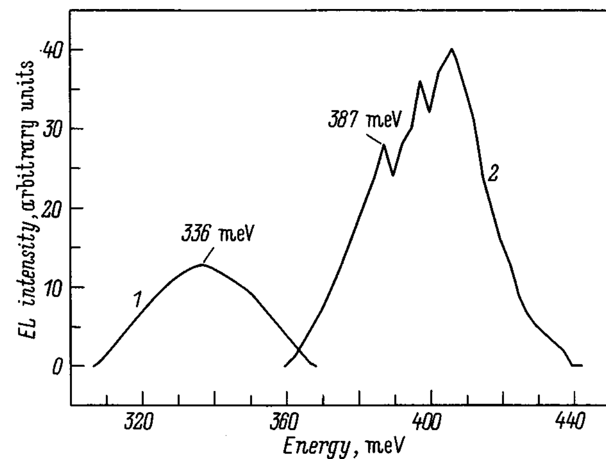

FIG. 6. EL spectra of a SS—161 diode in the pulse regime at various temperatures. *1*—$T=$ 300 K, current $I=1.5$ A. *2*—$T=77$ K, current $I=0.5$ A.

grown at a temperature of 565 °C and a V/III molar ratio of 7.5. The choice of growth temperature was made on the basis of optimal conditions for growing InAs layers and our desire to obtain abrupt $p-n$ junctions. The concentration of holes in the p-type layer was estimated from PL spectra. It increased linearly with increasing DeZn partial pressure DeZn (P_{DeZn}). $P_{\mathrm{DeZn}}=$ 0.35 Pa was sufficient to achieve a concentration $p=1\times10^{18}\,\mathrm{cm}^{-3}$. The maximum of the PL spectrum for a layer doped with zinc with a carrier concentration $p=1\times10^{18}\,\mathrm{cm}^{-3}$ corresponds to an energy of 387 meV; i.e., recombination takes place from the bottom of the conduction band to an acceptor level (E_a) located roughly 20 meV above the top of the valence band.

The I–V and capacitance–voltage characteristics were measured for diodes consisting of fully epitaxial structures with carrier concentrations at T = 77 K. They were $1\times10^{18}\,\mathrm{cm}^{-3}$ in the p-layer and $5\times10^{15}\,\mathrm{cm}^{-3}$ in the n-layer. The cutoff voltage for the forward branch of the I–V characteristic at 77 K was 0.4 V. The voltage dependence of the capacitance follows the law $1/C^2\sim V$, indicating the presence of an abrupt $p-n$ junction. The value of the capacitance lay in the interval 100–200 pF for diodes with an area of 0.1 mm^2. From capacitance-voltage characteristics we estimated the carrier concentrations in the layer to be $n=4\times10^{16}\,\mathrm{cm}^{-3}$ ($T=$ 300 K) and the width of the space-charge region to be 3×10^{-5} cm ($V=0$).

Figure 6 shows the EL spectrum of an SS–161 diode measured in the pulse regime ($\tau=5\,\mu$s, $f=$ 500 Hz) at temperatures 77 and 300 K. At T = 77 K the peak with high intensity at 408 meV corresponds to interband recombination. The two peaks with lower intensity at energies 397 and 387 meV correspond to conduction band–acceptor transitions. At room temperature the width of the EL spectrum at half-height was 35 meV. Using for the coefficient of temperature variation of E_g a value $\Delta E_g/\Delta T=2.3\times10^{-4}$ eV/K, we can compute that the maximum in the spectrum with energy 336 meV at $T=$ 300 K corresponds to a transition with $h\nu=$ 387 meV at T = 77 K.

Data on the power characteristics of an SS–161 diode operated in the cw regime are listed in Table I.

CONCLUSIONS

In this paper we have investigated the thermodynamics of growth of InAs layers in an MOVPE reactor of planetary type. At substrate temperatures below 400 °C the growth is limited by surface kinetics. In the temperature range 400–570 °C , the growth is determined by diffusion of reagents. At substrate temperatures above 570 °C , the growth rate falls off due to nearly complete decomposition of TMI in front of the substrate. We investigated the luminescence properties of InAs layers with p- and n-type conductivity. We identified acceptor levels in InAs with energies of 350, 372, 387, and 397 meV relative to the bottom of the conduction band. We established that low growth temperatures lead to an increase in the concentration of background impurities in the layer. We determined optimal conditions for growth of InAs layers in a reactor of planetary type at atmospheric pressure using trimethyl indium and arsine as sources: an InAs substrate with orientation (111)B, growth temperature 565 °C, and a V/III ratio of 7.5. Fully epitaxial structures were grown with abrupt $p-n$ junctions, and these structures were used along with standard photolithographic methods to make light-emitting diodes operating at wavelengths $\lambda=3.1\,\mu$m ($T=$ 77 K) and $\lambda=3.7\,\mu$m ($T=$ 300 K). The results which we obtained are a basis for making infrared light-emitting diodes that operate at room temperature.

This work was supported in part by the InCo–Copernicus contract 1C15-CT97-0802 (DG12-CDPF).

TABLE I.

Current, mA	Power, μW	
	$T=300$ K	$T=77$ K
50	5	93
70	5.8	105
100	7	140

*)E-mail: kijayev@vpegroup.ioffe.rssi.ru

[1] B. Baliga and K. Ghanghi, J. Electrochem. Soc. **121**, 1642 (1974).
[2] T. Fukui and Y. Horikoshi, Jpn. J. Appl. Phys. **18**, 2157 (1979).
[3] T. Fukui and Y. Horikoshi, Jpn. J. Appl. Phys. **19**, 551 (1980).
[4] T. Fukui and Y. Horikoshi, Jpn. J. Appl. Phys. **20**, 587 (1981).
[5] S. Haywood, R. Martin, N. Mason, and P. Walker, J. Cryst. Growth **97**, 489 (1989).
[6] S. Haywood, R. Martin, N. Mason, and P. Walker, J. Electron. Mater. **8**, 783 (1990).
[7] D. Partin, L. Green, D. Morelli, J. Heremans, B. Fuller, and C. Thrush, J. Electron. Mater. **20**, 1109 (1991).
[8] Y. Iwamura, H. Shigeta, and N. Watanabe, Jpn. J. Appl. Phys. **32**, 368 (1991).
[9] K. Huang, Yu Hsu, R. Cohen, and G. Stringfellow, J. Cryst. Growth **156**, 311 (1995).
[10] S. Watkins, C. Tran, R. Ares, and G. Soerensen, Appl. Phys. Lett. **66**, 882 (1995).
[11] R. Egan, T. Tansley, and V. Chin, J. Cryst. Growth **147**, 19 (1995).
[12] C. von Eichel-Streiber, M. Behet, M. Heuken, and K. Heime, J. Cryst. Growth **170**, 783 (1997).
[13] Y. Iwamura, K. Masubuchi, M. Noya, and N. Watanabe, *Abstracts of Mid-Infrared Optoelectronics Material and Devices, Second International Conference* (1998), p. 10.
[14] Z. Fang, K. Ma, R. Cohen, and G. Stringfellow, Appl. Phys. Lett. **59**, 1446 (1991).
[15] Y. Lacroix, S. Watkins, C. Tran, and M. Thewalt, Appl. Phys. Lett. **66**, 1101 (1995).
[16] N. Buchan, C. Larsen, and G. Stringfellow, J. Cryst. Growth **92**, 605 (1988).
[17] O. A. Allaberenov, N. V. Zotova, D. N. Nasledov, and L. D. Neuımina, Fiz. Tekh. Poluprovodn. **4**, 1939 (1970) [Sov. Phys. Semicond. **4**, 1662 (1970)].
[18] H. Ito and T. Ishibashi, Mater. Res. Soc. Symp. Proc. **163** 887 (1989).
[19] J. Huang, J. Ryan, K. Bray, and T. Kuech, J. Electron. Mater. **24**, 1539 (1995).
[20] C. Goo, W. Lau, T. Chong, L. Tan, and P. Chu, Appl. Phys. Lett. **68**, 841 (1996).
[21] S. S. Kizhaev, M. P. Mikhaılova, S. S. Molchanov, S. S. Stoyanov, and Yu. P. Takovlev, Pis'ma Zh. Tekh. Fiz. **24**(4), 1 (1998) [Tech. Phys. Lett. **24**, 247 (1998)].

Translated by Frank J. Crowne

Optical properties of gallium nitride bulk crystals grown by chloride vapor phase epitaxy

A. S. Zubrilov, Yu. V. Melnik, A. E. Nikolaev, M. A. Jacobson, D. K. Nelson, and V. A. Dmitriev

A. F. Ioffe Physicotechnical Institute, Russian Academy of Sciences, 194021 St. Petersburg, Russia
(Submitted October 5, 1998; accepted for publication April 5, 1999)
Fiz. Tekh. Poluprovodn. **33**, 1173–1178 (October 1999)

The optical properties of bulk crystals of gallium nitride grown by chloride vapor-phase epitaxy are investigated. It is shown that these crystals exhibit exciton luminescence bands. Analysis of the energy positions of the band maxima imply certain conclusions about the presence or absence of mechanical stresses in the bulk crystals of GaN obtained. Analysis of the luminescence spectra also reveals that the temperature dependence of the width of the GaN band gap E_g in the temperature range $T=6-600$ K is well described by the expression $E_g(T)=3.51-7.4\times10^{-4}\ T^2(T+600)^{-1}$ eV. It is estimated that values of the free electron concentration in these crystals do not exceed $10^{18}\,\mathrm{cm}^{-3}$. The optical characteristics of the bulk GaN crystals are compared analytically with literature data on bulk crystals and epitaxial layers of GaN grown by various methods. © *1999 American Institute of Physics.* [S1063-7826(99)00510-4]

1. INTRODUCTION

The creation of high-efficiency blue and green light-emitting diodes based on gallium nitride[1] and the fabrication of a violet injection laser[2] have advanced this material to the ranks of the most intensely studied semiconductors. At this time, an important factor that retards progress in developing this material is the lack of an ideal substrate material, although single crystals of GaAs, ZnO, MgO, $MgAl_2O_4$, and especially Al_2O_3 and SiC are actively used as substrates for heteroepitaxial growth of GaN.[3] The cardinal solution to the mismatch problem (with regard to crystal lattice parameters and thermal expansion coefficient) between the epitaxial layer of GaN and the substrate is obviously to use homoepitaxial methods to make device structures based on GaN. For this reason, methods for obtaining GaN substrates have been intensely pursued.[3] However, until now only a few publications have addressed the problem of obtaining and characterizing bulk single crystals of GaN,[4–10] a problem which, it must be asserted, is accompanied by serious technological difficulties.

In this paper we discuss the optical properties of bulk GaN crystals obtained by the chloride version of halide vapor-phase epitaxy (HVPE). We compare the properties of bulk GaN crystals grown in this way with structurally perfect epitaxial layers of GaN grown by the same method on substrates of $6H$-SiC, and also published data on gallium nitride.

2. TEST SAMPLES AND MEASUREMENT PROCEDURE

Samples of GaN were obtained at atmospheric pressure in a horizontal reactor placed in a multizone furnace with resistive heating. As substrates we used crystals of silicon carbide in its $6H$ polytype. Growth temperatures were in the range $T_g=950-1050\,^\circ$C. The growth rate, depending on the fabrication regime, was varied from 1 to 60 μm/h. A description of the distinctive features of this technology can be found in Refs. 6–11. In order to investigate optical properties we used single crystals of GaN with thicknesses $100-200$ μm separated from the substrate by plasma-chemical etching of the latter,[12] and also epitaxial layers of GaN with thicknesses of 1–3 μm. Prior investigations of structural properties of bulk GaN crystals using x-ray diffraction[6] showed that the samples obtained consist of block single crystals of the wurtzite polytype $(2H)$. Half-widths of rocking curves from the N-facet [i.e., from the (0002) plane] obtained in the ω-scanning regime were less than 130 arc-sec. Detailed studies of the structural properties of GaN/SiC layers obtained by chloride HVPE and published by us previously[13] also showed that they consist of bulk single crystals.

Photoluminescence (PL) of the samples was investigated in the temperature range $T=6$–600 K. At low temperatures (6–50 K) the PL was excited by a DRSh-250 mercury lamp (with UFS2 and ZhS3 filters). Comparatively low intensities were used in order to exclude the effect of concentration saturation of the optical transitions with participation of impurities and defects. The samples were placed in a helium cryostat, which allowed us to obtain a minimum sample temperature of 4.2 K. In the high-temperature range we excited the photoluminescence with a nitrogen laser for convenience (wavelength 337.1 nm), and the samples were placed in a nitrogen cryostat, where the sample temperature could be regulated from 77 to 900 K. By defocusing the laser beam we were able to decrease the excitation pulse power density to $100\ \mathrm{W/cm^2}$ (corresponding to an average pump power density of $10^{-4}\ \mathrm{W/cm^2}$), which also ensured a low level of excitation. The spectrum of the luminescence was recorded using an MDR-23 monochromator with a dispersion of 1.3 nm/mm. The spectral resolution of the apparatus was 0.1 nm or better. In order to obtain absorption spectra in the ultra-

 © 1999 American Institute of Physics

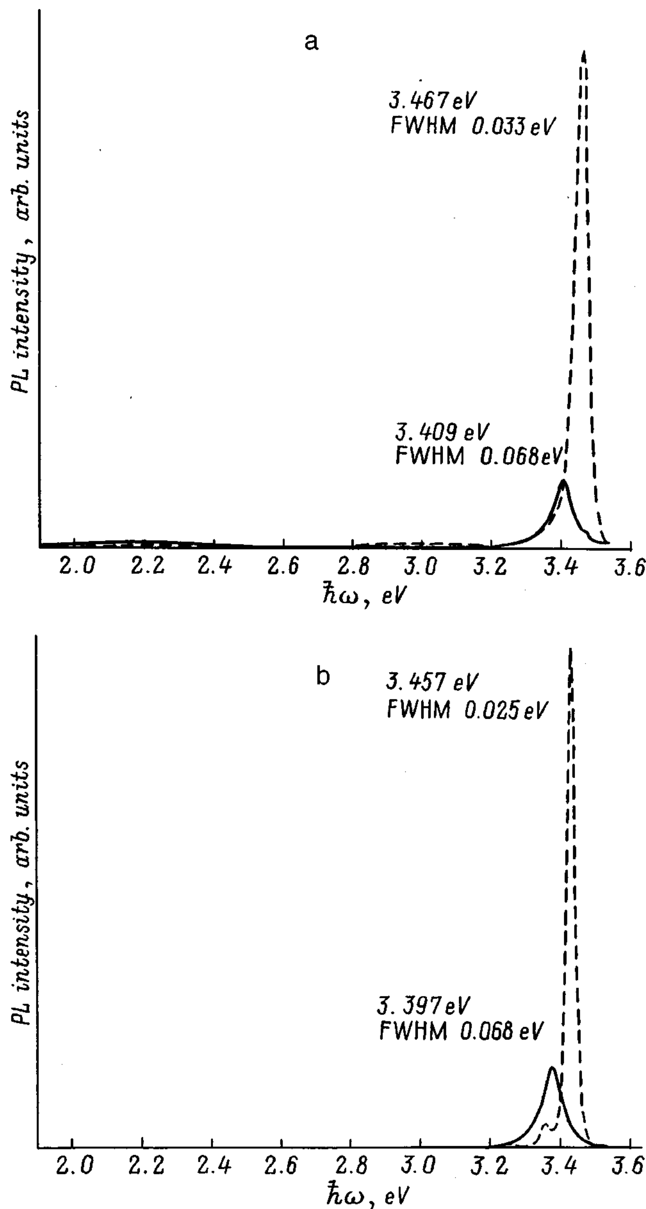

FIG. 1. Photoluminescence spectra of a bulk GaN crystal (a) and a thin (1.5 μm) epitaxial layer of GaN (b) at a temperature of 77 K (dashed curve) and 300 K (solid curve). The excitation light comes from a nitrogen laser.

violet range we used the MDR-23 monochromator and a DDS-30 deuterium lamp. Room-temperature infrared reflection spectra in the range 2.5–25 μm were measured using an IKS-29 two-beam IR spectrometer and two IPO-22 reflection attachments. As a reflection reference we used a mirror layer made of aluminum deposited on glass.

3. EXPERIMENTAL RESULTS AND DISCUSSION

During photoexcitation the GaN crystals luminesced intensely, with a luminescence that was distributed uniformly over the sample area. The luminescence spectrum of bulk GaN crystals, like that of epitaxial GaN layers, is dominated by the exciton luminescence band (Fig. 1). In the low-temperature region, the dominant band of luminescence arises from excitons bound at a neutral donor, while at high temperatures the dominant band is from recombination of free excitons.[14,15] The ratio of intensities of the "yellow" band caused by defects, with a maximum at an energy $\hbar\omega \simeq 2.2$ eV, to the intensity of the exciton peak was less than 0.01. It is important to note that for our very best GaN samples the value of the full widths at half-maximum (FWHM) of the exciton bands agreed closely with values quoted in the literature for structurally perfect epitaxial GaN layers (see, e.g., Ref. 16), which in turn indicates the rather high structural perfection of our bulk crystals. This also follows from Figs. 1a and 1b, where we compare PL spectra from our best bulk GaN crystal with that of a structurally perfect epitaxial GaN layer, also grown by us, at two temperatures 77 and 300 K. As for the positions of the exciton band maxima, it is obvious from Figs. 1a and 1b that the peaks of the bulk crystal spectra are shifted by $\sim$ 0.01 eV towards higher energies compared to those of the epitaxial GaN layer (for different samples of epitaxial GaN layers on SiC substrates with different thicknesses and technological growth regimes, this shift can have values from 0.01 to 0.02 eV). A similar shift in the PL spectra of GaN/SiC layers compared to bulk GaN crystals was reported previously by Buyanova *et al.*,[15] where it was explained by residual tensile mechanical stresses that arise along the axis of the epitaxial layer (i.e., along a plane perpendicular to the principal crystallographic axis **c**) when the samples are cooled after epitaxial growth, primarily due to differences in values of the thermal expansion coefficients of GaN and SiC.[3] The GaN layers used in Ref. 15 were obtained by metallorganic chemical vapor deposition (MOCVD) with a buffer layer, in contrast to the layers investigated by us, which may explain the somewhat lower values of residual mechanical stresses in them, and consequently the lower values of the energy shift, observed in that study,[15] in the position of the exciton lines within the layer compared to bulk material ($\sim$0.008 eV). Using the average value of the energy shift of exciton lines obtained in Ref. 17 for a biaxial mechanical stress of 1 GPa in the plane of the GaN epitaxial layer ($\sim$24 meV/GPa), we can estimate a value of $\sim$0.5 GPa for the average tensile mechanical stress in the best epitaxial layers obtained by us.

We observed the presence of both free and bound excitonic states in the low-temperature luminescence shifts. Figure 2 shows an example of low-temperature photoluminescence spectra containing the largest number of features for one of our samples of bulk GaN in the temperature range 6–45 K. At $T = 6$ K this sample exhibits a peak corresponding to an exciton bound to a neutral donor (DBE) with an energy maximum $\hbar\omega = 3.472$ eV. In addition, it is easy to see two other exciton peaks, which we assume are from an exciton bound to an acceptor (ABE) with energies $\hbar\omega = 3.449$ and 3.421 eV. On the long-wavelength side we see the first two donor-acceptor recombination peaks—a zero-phonon peak (3.263 eV) and its *LO*-phonon (energy $\sim$92 meV) replica (3.171 eV). On the short-wavelength side, in the region 3.48–3.49 eV we see a weakly expressed shoulder whose energy position corresponds to the free exciton *A* ($n = 1$).[14,15] It is clear from Fig. 2 that the donor-bound exciton line at 3.472 eV, which corresponds to the lowest binding energy ($\sim$ 4 meV), quenches most rapidly with increasing temperature. The two emission lines of the acceptor-bound

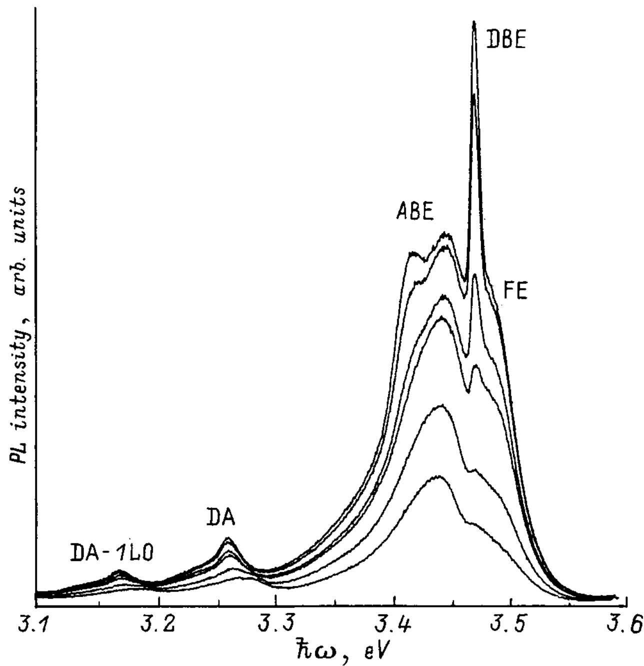

FIG. 2. Low-temperature photoluminescence spectra of a sample of bulk GaN crystal at temperatures (from top to bottom) of 6, 10, 15, 20, 30, and 45 K. Excitation light comes from a DRSh- 250 lamp.

exciton at $\hbar\omega$= 3.449 and 3.421 eV quench much more slowly, so that at $T=45$ K the predominant line for this sample is still the emission line at 3.449 eV, the most intense line in the spectrum. The emission peaks due to donor-acceptor pairs shift towards shorter wavelengths as the temperature increases, which corresponds to the decay of pairs with the lowest binding energy (i.e., the most distant pairs). The transition from donor-acceptor emission to emission via band-acceptor transitions occurs at a temperature $T\simeq 80$ K, since at $T>80$ K the observed emission is no longer described by the donor-acceptor mechanism. The energy position of an exciton bound to a neutral donor is in rather good agreement with the energy position of the donor-bound exciton published in Refs. 14 and 15 for bulk GaN without mechanical stresses (Table I). On the other hand, the donor-bound exciton appears at an energy position that is ~ 10 meV lower in the PL spectra of thin (~1μm) epitaxial layers of GaN grown by the same method in our apparatus, and not detached from a SiC substrate.[18] The energy positions of excitons bound at an acceptor (Fig. 2) are likewise close to the numbers published in Ref. 19 for mechanically unstressed bulk GaN crystals. In our view, all these results point to the absence, or at least weakness, of mechanical stresses in our samples after their removal from the substrate. At the same time, the ratio of intensities of lines from bound excitons for our samples differ somewhat from those reported in Ref. 19, e.g., for the sample in Fig. 2, the acceptor-bound exciton lines are rather intense and broad. A possible explanation for this could be stoichiometric nonuniformity of our sample, and also local electric fields which cause fluctuations in charged impurities leading to Stark shifts. We note that the more structually perfect the samples of GaN are, the weaker are the inhomogeneous broadening and acceptor-bound exciton lines and the narrower the exciton spectrum (for example, even at high temperatures the values of the FWHM for the bulk sample of GaN shown in Fig. 1a are considerably smaller— 0.033 eV at 77 K and 0.068 eV at 300 K— than for the sample shown in Fig. 2, i.e., 0.086 eV at 6 K). The temperature broadening of the exciton spectrum we obtained for the highest-quality samples of bulk GaN is well described by a linear law with a slope of 1.8×10^{-4} eV/K in the temperature range 77–600 K.

When we increased the temperature to 300 K, we observed an additional temperature- induced quenching of the luminescence spectrum for all the bands, with the bound-exciton bands decaying more rapidly than the free-exciton bands due to the considerably larger binding energy of the latter (~30 meV for the ground state of the *A*-exciton[14,20,21]). At higher temperatures ($T=500-600\,K$) the temperature-induced quenching of the exciton luminescence bands occurs more rapidly than we would expect, starting from values of the binding energy for free *A*-excitons mentioned above; therefore, we assume that nonradiative recombination processes play a dominant role.

Figure 3 shows the temperature dependence of the width of the bandgap E_g obtained by analyzing the position of the free-exciton luminescence band for bulk crystals of GaN and epitaxial GaN layers.[22] There we plot data from Ref. 23 on the temperature dependence of the band gap calculated from the optical absorption spectra of bulk crystals of GaN obtained at high pressure (Fig. 3, curve *2*). Using the standard empirical expression for the temperature dependence of the band gap of semiconductors to approximate the experimental data shown in Fig. 3 (Ref. 24).

$$E_g=E_g(0)-\gamma T^2(T+\beta)^{-1}, \qquad (1)$$

where $E_g(0)$ is the band gap at 0 K, and β and γ are em-

TABLE I. Parameters of low-temperature exciton luminescence from epitaxial layers and bulk single crystals of GaN.

Thickness, μm	Substrate	T_g, °C	Method	FE $\hbar\omega$, eV (T, K)	DBE $\hbar\omega$, eV (T, K)	ABE $\hbar\omega$, eV (T, K)	Mechanical stress	Literature
100–200	None	~1000	HVPE	3.48–3.49 (6)	3.472 (6)	3.449 (6) 3.421 (6)	None	Data from Refs.
>500	None	~1000	HVPE	3.479–3.480 (2)	3.473–3.474 (2)		None	14,15,19
2	6*H*-SiC	~1000	HVPE	3.472 (6)	3.464 (6)		Tension along layer	18
<10	6*H*- SiC	~1000	MOCVD	3.472 (2)	3.466 (2)		Tension along layer	14 and 15

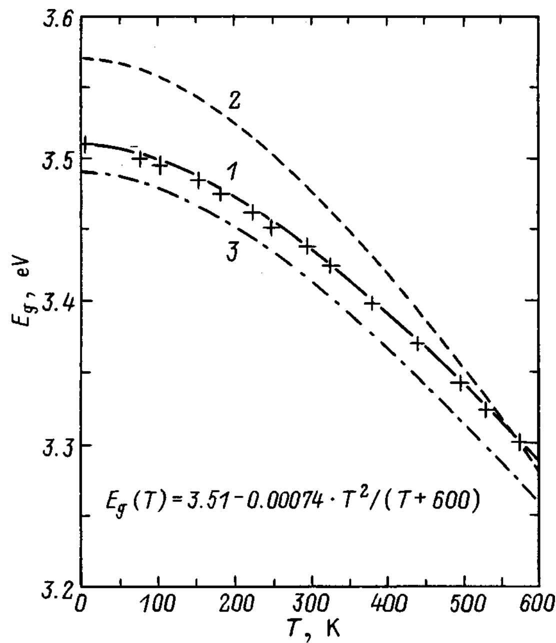

FIG. 3. Temperature dependence of the width of the optical band gap $E_g(T)$ for bulk crystals of GaN grown by chloride HVPE (*1*). For comparison we show the dependence of the energy position of the optical absorption edge for bulk crystals of GaN obtained at high pressure (Ref. 23) (*2*) and the function $E_g(T)$ obtained from the exciton luminescence data of Ref. 22 for thin (~1μm) epitaxial layers of GaN grown by MOCVD on a 6 H-SiC substrate (*3*).

pirical constants (here the parameter β is often connected with the Debye temperature), we obtain the following values for the coefficients in Eq. (1) that give us the best agreement with the experimental data (Fig. 3, curve *1*): $E_g(0)=3.51$ eV, $\gamma=7.4\times10^{-4}$ eV/K, and β=600 K. It is clear from Fig. 3 that, ignoring the effect of residual mechanical stresses, the agreement between the curves for our bulk crystals and epitaxial layers of GaN is good. On the other hand, the bulk crystals of GaN grown in Ref. 23 at high pressure (Fig. 3, curve *2*) exhibit a considerably larger value for the band gap compared to our samples of GaN. This is most likely due to the Burstein–Moss effect,[25] given the high concentration of free electrons in these crystals [on the order of $10^{20}\,\mathrm{cm}^{-3}$ (Ref. 23)]. In contrast, the concentration of free electrons is relatively low in the samples of GaN we investigated; in fact, it never exceeds the Mott limit[26] (this is confirmed by the existence of an excitonic luminescence band), an estimate for which is $n_M=(0.26/a_B)^3=7\times10^{17}\,\mathrm{cm}^{-3}$ (here $a_B=2.9$ nm is the Bohr radius of an exciton). The values reported above for the nonlinear coefficients in the temperature dependence of E_g are in satisfactory agreement with those obtained previously for epitaxial GaN layers[22] (Table II). The difference in values of the nonlinear coefficients β and γ for bulk crystals of GaN obtained at high pressure (Table II) can be qualitatively explained[23] by the temperature dependence of the Burstein-Moss effect.

The most structurally perfect of all the GaN crystals obtained by us was visually colorless and in the visible region possessed a rather high optical transparency (around 60% for a thickness of 100 μm). The value of the band gap obtained by measuring the optical absorption edge at T= 300 K (assuming a classical parabolic band and ignoring exciton effects) lies in the range 3.31–3.32 eV for various samples of GaN, which is roughly 0.13 eV lower in energy than the value expected from the photoluminescence results [as indicated by the data shown in Fig. 1a, the value of the band gap at T= 300 K should be $E_g(300\,\mathrm{K})=3.436$ eV].

TABLE II. Nonlinear coefficients of the temperature dependence $E_g(T)$ obtained for bulk crystals and epitaxial layers of gallium nitride.

Sample type	Experimental method	γ, 10^{-4} eV/K	β, K	Literature
Layer GaN/Al_2O_3	Luminescence	7.2	600	(Ref. 30)
Layer GaN/Al_2O_3	Optical absorption	9.39	772	(Ref. 23)
Layer GaN/SiC	Luminescence	7.7	600	(Ref. 22)
Bulk GaN crystal	Optical absorption	10.8	745	(Ref. 23)
Bulk GaN crystal	Luminescence	7.4	600	This work

In the infrared reflection spectrum, the lattice resonance (reststrahl band), which extends from 13.7 to 18.9 μm and whose boundaries correspond to energies for the transverse (TO) and longitudinal (LO) optical phonons,[3] is quite intense, which also attests to the relatively high structural quality of the crystals obtained (Fig. 4). In Fig. 4 we show for comparison the reflection spectrum of a structurally perfect epitaxial GaN layer on a SiC substrate (dashed curve). We note the good agreement between the two spectra in Fig. 4 in the lattice resonance (reststrahl band) of GaN, and also the appearance in the spectrum of the epitaxial layer of an additional resonance in the region 10.3−12.8 μm, which corresponds to the silicon carbide substrate.[27] Estimates of the values of the TO- and LO-phonon frequencies (560 and 730–749 cm^{-1}, respectively) from the IR reflection spectra of the bulk GaN crystals are in good agreement with results obtained previously by Raman spectroscopy,[6] and for the

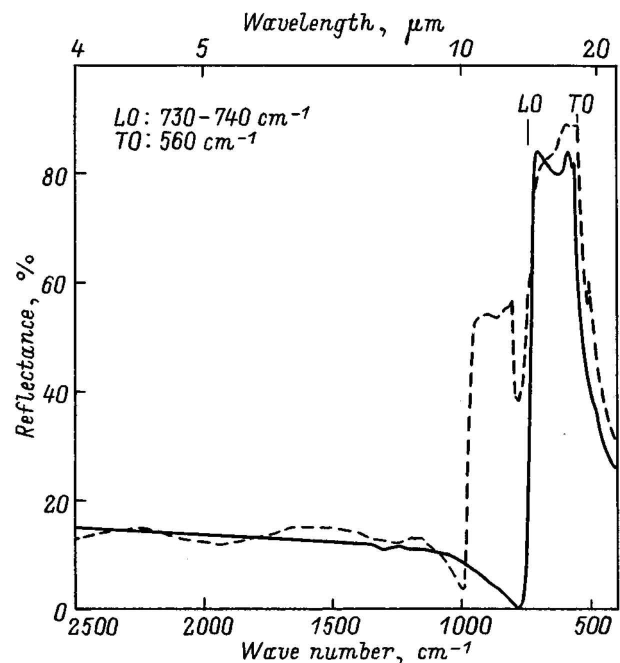

FIG. 4. IR reflection spectra for a bulk crystal of GaN (solid curve) and an epitaxial layer of GaN with thickness 3.3 μm on a SiC substrate (dashed curve). T = 300 K.

LO-phonon there is good agreement with the photoluminescence data (see the text above and Fig. 2). The location of the minimum in the reflection near the resonance, which is sensitive to the concentration of free carriers,[28] corresponds to a relatively low concentration of free electrons (less than $10^{18}\,\mathrm{cm}^{-3}$; see Ref. 29), which again agrees with luminescence data.

Thus, we have investigated several features of the optical properties of bulk GaN crystals obtained by using the chloride version of HVPE. We have established that these crystals have a bright excitonic luminescence, and that their spectra are similar to those of structurally perfect thin epitaxial layers of GaN. What differences there are primarily involve exact energy positions of excitonic bands, which in the case of bulk crystals correspond to mechanically unstressed states of gallium nitride. We have shown that the temperature dependence of the band gap for these GaN crystals in the temperature range 6–600 K can be described by the expression $E_g(T)=3.51-7.4\times10^{-4}\ T^2(T+600)^{-1}$, eV. Using photoluminescence and IR reflection, we have established that, in contrast with bulk crystals of GaN grown at high pressure, the concentration of free electrons in the bulk crystals is no more than $10^{18}\,\mathrm{cm}^{-3}$, i.e., far from degeneracy. We found that the band gap determined from the optical absorption edge for our bulk crystals is shifted (by about 0.1 eV towards lower energies) relative to the value obtained from photoluminescence measurements.

This work was financed in part by the Russian Fund for Fundamental Research (Project 97-02-18057), INTAS (Projects 96-2131 and 96-1031), and the University of Arizona, USA.

We wish to thank N. V. Seredova for technical help in these investigations.

[1] S. Nakamura, T. Mukai, and M. Senoh, Appl. Phys. Lett. **64**, 13 (1994).
[2] S. Nakamura, M. Senoh, S. Naganama, N. Iwasa, T. Yamaba, T. Matsushita, H. Kiyoku, and Y. Sugimoto, Jpn. J. Appl. Phys. **35** (1B), L74 (1996).
[3] S. Strite and H. Morkoç, J. Vac. Sci. Technol. B **10** (4), 1237 (1992).
[4] S. Porowski, J. Cryst. Growth **166**, 583 (1996).
[5] T. Detchprohm, K. Hiramatsu, A. Amano, and I. Akasaki, Appl. Phys. Lett. **61**, 2688 (1992).
[6] Yu. V. Melnik, K. V. Vassilevski, I. P. Nikitina, A. I. Babanin, V. Yu. Davydov, and V. A. Dmitriev, MRS Internet J. Nitride Semicond. Res. **2**, 39 (1997).
[7] V. V. Belkov, V. M. Botnaryuk, L. M. Fedorov, I. I. Diakonu, V. V. Krivolapchyuk, M. P. Scheglov, and Yu. V. Zhilyaev, Inst. Phys. Conf. Ser. **155**, 191 (1997).
[8] E. N. Mokhov and Y. A. Vodakov, Inst. Phys. Conf. Ser. **155**, 177 (1997).
[9] R. J. Molnar, P. Maki, R. Aggarwal, Z. L. Liau, E. R. Brown, I. Melngailis, W. Gotz, L. T. Romano, and N. M. Johnson, Mater. Res. Soc. Symp. Proc. **423**, 221 (1996).
[10] V. A. Ivantsov, V. A. Sukhoveev, V. I. Nikolaev, I. P. Nikolaev, and V. A. Dmitriev, Fiz. Tverd. Tela (St. Petersburg) **39**, 858 (1997) [Phys. Solid State **39**, 946 (1997)].
[11] Yu. V. Melnik, I. P. Nikitina, A. S. Zubrilov, A. A. Sitnikova, Yu. G. Musikhin, and V. A. Dmitriev, Inst. Phys. Conf. Ser. **142**, 863 (1996).
[12] V. E. Sizov and K. V. Vassilevski, NATO ASI, Ser. 3. High Technology, *Wide Bandgap Electronic Materials,* edited by M. A. Prelas *et al.* (Kluwer Academic Publishers, 1995) 1, p. 427.
[13] Yu. V. Melnik, I. P. Nikitina, A. E. Nikolaev, D. V. Tsvetkov, A. A. Sitnikova, and V. A. Dmitriev, Abstracts 1st Europ. Conf. on Silicon Carbide and Related Mater. (Heraklion, Greece, 1996), p. 79.
[14] B. Monemar, J. P. Bergman, I. A. Buyanova, W. Li, H. Amano, and I. Akasaki, MRS Internet J. Nitride Semicond. Res. **1**, 2 (1996).
[15] I. A. Buyanova, J. P. Bergman, and B. Monemar, Appl. Phys. Lett. **69** (9), 1 (1996).
[16] A. S. Zubrilov, Yu. V. Melnik, D. V. Tsvetkov, V. E. Bugrov, A. E. Nikolaev, S. I. Stepanov, and V. A. Dmitriev, Fiz. Tekh. Poluprovodn. **31**, 616 (1997) [Sov. Phys. Semicond. **31**, 755 (1997)].
[17] W. Rieger, T. Metzger, H. Angerer, R. Dimitrov, O. Ambacher, and M. Stutzmann, Appl. Phys. Lett. **68**, 970 (1996).
[18] D. K. Nelson, Yu. V. Melnik, A. V. Sel'kin, M. A. Jacobson, V. A. Dmitriev, K. G. Irvine, and C. H. Carter, Jr., Fiz. Tverd. Tela (St. Petersburg) **38**, 822 (1996) [Phys. Solid State **38**, 940 (1996)].
[19] B. Monemar, J. P. Bergman, H. Amano, I. Akasaki, T. Detchprohm, K. Hiramatsu, and N. Sawaki, *International Symposium on Blue Laser and Light Emitting Diodes* (Chiba Univ., Japan, 1996).
[20] S. Chichibu, T. Azurata, T. Sota, and S. Nakamura, J. Appl. Phys. **79** (5), 2784 (1996).
[21] M. A. Jacobson, V. D. Kagan, E. V. Kalinina, D. K. Nelson, A. V. Selkin, V. A. Dmitriev, K. G. Irvine, J. A. Edmond, and C. H. Carter, Jr., in *Proceedings of the 23rd International Conference Phys. Semicond.* (Berlin, Germany, 1996) p. 569.
[22] A. S. Zubrilov, V. I. Nikolaev, D. V. Tsvetkov, V. A. Dmitriev, K. G. Irvine, J. A. Edmond, and C. H. Carter, Jr., Appl. Phys. Lett. **67**, 521 (1995).
[23] H. Teisseyere, P. Perlin, T. Suski, I. Grzegory, S. Porowski, J. Jun, A. Pietraszko, and T. D. Moustakas, J. Appl. Phys. **76**, 2429 (1994).
[24] Y. P. Varshni, Physica (Amsterdam) **34**, 149 (1967).
[25] E. Burstein, Phys. Rev. **93**, 632 (1954).
[26] P. P. Edwards and M. J. Sienko, Phys. Rev. B **17**, 2575 (1978).
[27] M. F. MacMillan, R. P. Devaty, and W. J. Choyke, Appl. Phys. Lett. **62**, 750 (1993).
[28] A. S. Barker and M. Ilegems, Phys. Rev. B **7**, 743 (1973).
[29] C. Wetzel, D. Voim, B. K. Meyer, K. Pessel, S. Nilsson, E. N. Mokhov, and P. G. Baranov, Appl. Phys. Lett. **65** (8), 1033 (1994).
[30] M. Ilegems, R. Dingle, and R. A. Cogan, J. Appl. Phys. **43**, 3797 (1972).

Translated by Frank J. Crowne

The energy spectrum of lead selenide implanted with oxygen

A. N. Veĭs and N. A. Suvorova

St. Petersburg State Technical University, 195251 St. Petersburg, Russia
(Submitted March 3, 1999; accepted for publication April 13, 1999)
Fiz. Tekh. Poluprovodn. **33**, 1179–1182 (October 1999)

Single-crystal and hot-pressed samples of PbSe : O^+ were used to investigate the thermoelectric power and optical reflection spectrum and absorption of this material at 300 K. A quasilocal level associated with oxygen was identified in the valence band of PbSe : O^+. © *1999 American Institute of Physics.* [S1063-7826(99)00610-9]

It is known[1–3] that intergrain layers give rise to unusual and often irreproducible behavior when polycrystalline films of lead chalcogenides are grown on dielectric substrates (for grain sizes $\lesssim 1\,\mu$m) and annealed in an oxygen atmosphere or in air. Therefore, experimental study of the energy spectrum of oxygen in lead chalcogenides requires the use of samples doped by ion implantation and annealed in vacuum. In this case it turns out to be possible to use single crystals, thereby eliminating the influence of intergrain layers on the results of the measurements. When we performed similar experiments on PbTe,[4] we found that a quasilocal level located deep in the valence band could be associated with oxygen impurities in PbTe. We observed no other features that we could assign to oxygen in the energy spectrum of PbTe, including its band gap.

In this paper we continue the investigations started in Ref. 4. The object of our studies is lead selenide. The goal of this work is to identify localized states in the energy spectrum of oxygen-implanted PbSe that are connected with the incorporated impurity, and to establish the types of defects that generate these states. Such studies have not been done previously for PbSe : O^+.

In order to achieve these goals, in this paper we investigated the optical reflection spectrum R and absorption coefficient α of PbSe : O^+, as we did in Ref. 4. These experiments were supplemented by measurements of the thermoelectric power S made by placing a probe directly on the thin samples. All the experiments were carried out at a temperature $T=300$ K.

In these experiments we used single crystals grown by the Bridgman–Stockbarger method and polycrystalline samples prepared by hot pressing. The optical properties of the hot-pressed samples, as a multitude of experiments have shown, do not differ in any important way from the properties of single crystals. For average grain sizes of 100 μm and sample thicknesses of ~ 10 μm, the regions near grain boundaries occupy a small fraction of the surface and bulk of these samples, and therefore do not contribute to the observed optical properties. With regard to PbSe, evidence for this comes from the results of an experimental study[5] in which we conducted similar investigations and analyzed the properties of the ''original'' (i.e., unimplanted) samples (both single crystals and hot-pressed samples) that are implanted and investigated in this study.

In some of these original samples we varied the concentration of anion vacancies V_{ch}. To increase the vacancy concentration, in accordance with Refs. 5–7 we introduced tin (2 at. %), sodium via molecular impurities (up to 0.2 mole% NaSe), and superstoichiometric lead into the growth batches. All the initial samples were subjected to a homogenizing anneal in vacuum quartz cells for 100 hours at a temperature $T_a=650\,^\circ$C, and had p-type conductivity. Values of the Hall concentrations of holes p_H in these samples were $1-3 \times 10^{18}\,\mathrm{cm}^{-3}$.

As in Ref. 4, oxygen ions were implanted into the PbSe through the previously prepared optical surface by an ILU-1 implanter (ion energies of 100 keV, ion current 0.5 μA/cm^2). The dose (D) of implanted ions was varied in the range $1000-4250$ μC/cm^2. The samples were subjected to a post-implantation anneal in vacuum for 1 or 2 hours at $T_a=300\,^\circ$C. After ion implantation and annealing, the experimental samples were thinned to $3-14$ μm by mechanical grinding and polishing their back sides (i.e., the side not used for implantation).

Some of the experimental results we obtained in this work are shown in Fig. 1, where we compare them with data taken from Ref. 5 for the original samples. Comparison of the results as shown in Fig. 1 with the data of Ref. 4 shows that the changes observed in the spectra of the absorption coefficient $\alpha(\hbar\omega)$ caused by ion implantation and annealing are similar for PbSe and PbTe. As in PbTe (Ref. 4), implantation of oxygen impurities into PbSe inverts its conductivity type $p\rightarrow n$ and leads to the appearance in the α spectrum of components connected with singlet (α_1) and doublet (α_2) terms in the chalcogenide vacancy and with complexes (α_3).[8] The energy scheme for unannealed PbSe : O^+ is shown in Fig. 2.

Annealing the samples in vacuum is accompanied by reconversion of the conductivity type from electronic back to hole-like. The results of our studies of the thermoelectric power confirm this change, in that the sign of S once more becomes positive in all the samples. An important change arises in the optical absorption spectra as well. As is clear from Fig. 1, two bell-shaped features α_4 and α_5 appear in these spectra, indicating that two quasilocal levels E_4 and E_5 have appeared deep in the valence band of PbSe : O^+ annealed in vacuum (see the energy scheme shown in Fig. 2). Although the first of these features (α_4), which was ob-

 © 1999 American Institute of Physics

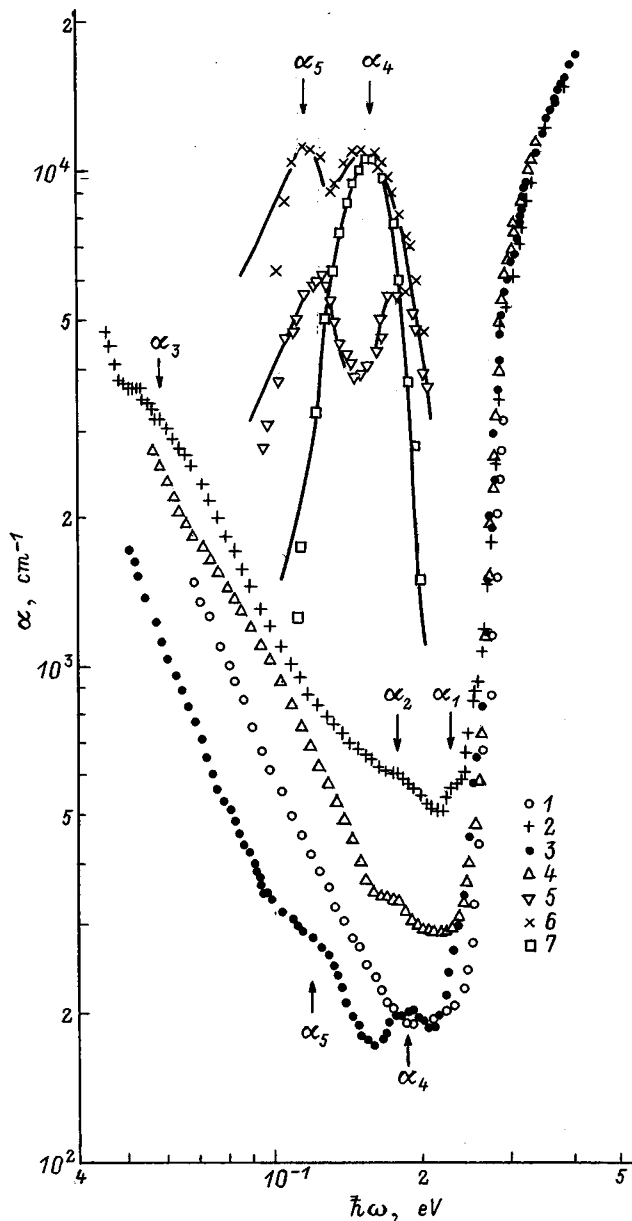

FIG. 1. Spectral dependence of the absorption coefficient α (*1– 4*) and additional absorption coefficient α_{ad} (*5–7*) in PbSe : O^+ and $Pb_{0.98}Sn_{0.02}Se$: O^+ (*6, 7*) at T=300 K. *1,7*— original samples (Ref. 5), *2–6*— samples implanted with O^+ ions, before (*2*) and after (*3–6*) annealing in vacuum. Dose of implanted ions D, μC/cm^2: *1, 7* — 0; *2* — 1000; *3, 5, 6* — 2000; *4* — 4250. The Hall concentration of holes in the initial state p_H, 10^{18} cm^{-3}: (*1–5*) — 2.8; (*6, 7*) — 3.0. Sample thickness d, μm: *1* — 9.1; *2* — 3.6; *3, 5* — 5.0; *4* — 6.9; *6* — 10.0; *7* — 4.5. For functions *5–7* the value of α_{ad} was increased by a factor of 50. The points are experiment, the curves calculations based on Eq. (1) of Ref. 8.

served previously in lead selenide,[5,7] has been assigned to anion vacancies, the second (α_5) has no analog in the literature data. This allows us to associate its presence with the action of implanted oxygen.

The energy positions of these quasilocal levels in PbSe : O^+ were determined from calculations of the frequency dependence of the additional absorption coefficient α_{ad}. The required values of the Fermi energy in these samples were estimated by studying the thermoelectric power and reflection spectra $R(\hbar\omega)$. Our analysis of these

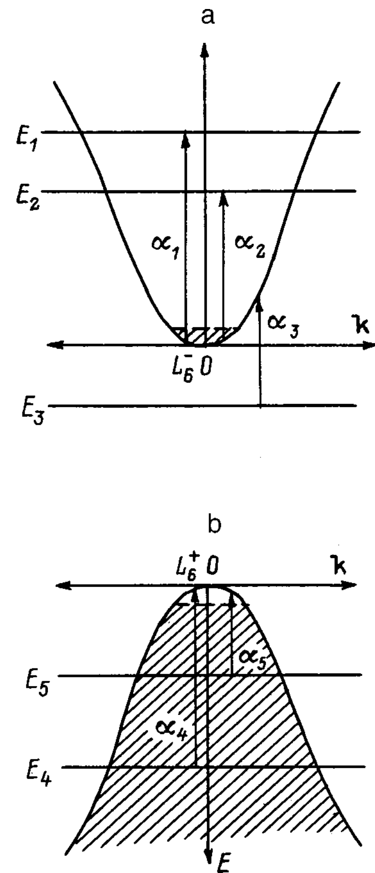

FIG. 2. Energy scheme of PbSe : O^+ before (a) and after (b) annealing in vacuum. The vertical arrows show electronic transitions between band and localized states E_1-E_5, which lead the appearance of an additional absorption band in the optical spectra.

data showed that the magnitude of p_H in all samples implanted with oxygen impurities and annealed in vacuum was in the range $2.2-2.8\times10^{18}$ cm^{-3}. Therefore, in calculating the spectra of α_{ad} we used expressions that were correct for a gas of free carriers with nondegenerate statistics.

The bands of α_{ad} were extracted from the experimental spectra and their frequency dependences calculated by using a method similar to that described in Refs. 5, 7, and 9. Some of the results obtained are shown in Fig. 1. The dots denote the experimental spectra $\alpha_{ad}=\alpha_4+\alpha_5$, the curves represent the results of calculations based on Eq. (1) of Ref. 8. It turned out that the optical charge-transfer energies of the various localized and quasilocal states in PbSe : O^+ were: $E_1^{opt}=(0.270\pm0.015)$ eV, $E_2^{opt}=(0.195\pm0.020)$ eV, $E_3^{opt}=-(0.050\pm0.005)$ eV, $E_4^{opt}=(0.200\pm0.015)$ eV, and $E_5^{opt}=(0.140\pm0.010)$ eV. Using these calculations, we also estimated half-widths of the quasilocal bands based on 0.606 of the maximum of the density functions for the resonance states: $\Gamma_{1,5}=(0.009\pm0.005)$ eV, $\Gamma_2=(0.013\pm0.008)$ eV, $\Gamma_3=0$, and $\Gamma_4=(0.017\pm0.007)$ eV. Note that the values of E_4^{opt}, E_5^{opt}, Γ_4, and Γ_5 given above were obtained by averaging data for eight samples according to the method described in Ref. 10, using the Student distribution with a confidence coefficient δ=0.95.

Comparison of the results obtained for PbSe : O^+ with known values of the optical charge-transfer energies of vari-

ous centers in lead selenide shows that the quantities $E_1^{\rm opt}-E_4^{\rm opt}$ are in good agreement with data for chalcogen vacancies and complexes.[5,7,8] At the same time, the values of $E_5^{\rm opt}$ in fact have no analogs in the literature data. This does not contradict our assertion that the α_5 bands are related to oxygen, which we inferred from qualitative analysis of the $\alpha(\hbar\omega)$ spectra. Additional evidence for this is the increase in intensity of the α_5 bands as the dose of implanted ions increases.

Certain assertions can be made regarding the nature of the center responsible for the appearance of level E_5 in the energy spectrum of PbSe:O^+, based on analysis of how the integrated absorption cross section S_5 of the α_5 bands $\{S_5=\int_0^\infty \alpha_5(\hbar\omega)d(\hbar\omega)\}$ depends on the dose of implanted ions. If level E_5 is associated with a point defect, the value of S_5 should be proportional to D. For complexes a stronger dependence of S_5 on D is characteristic.[11] It is obvious that these statements about the character of the function $S_5(D)$ are accurate only if the average value of p_H in the implanted region remains constant as the dose of implanted ions varies. As we mentioned above, this is the very situation that occurs in our samples. However, we must take into account the different thicknesses of our samples. In ion-implanted crystals the distribution of impurities with respect to depth is nonuniform; therefore, the intensity of the α_5 bands (and consequently the value of the cross section S_5) should vary not only with the dose of incorporated oxygen but also with the thickness of the samples under study.

In Ref. 12 it was shown that when lead chalcogenides are subjected to ion implantation and annealing, the distribution of impurities with respect to depth that results is close to Gaussian, differing from the latter only by the presence of an extensive ''tail'' that extends deep into the ion-implanted crystal. The concentration of impurities in the tail is considerably lower (by more than an order of magnitude) than it is at the distribution maximum. This circumstance allows us to approximate the concentration profile of the oxygen distribution in annealed PbSe:O^+ by a Gaussian. Within the framework of this assumption, we can show that the ratio of values of the experimentally measured absorption coefficient in the α_5 bands to their values in a sample that is uniformly doped with respect to depth with an oxygen concentration equal to the concentration of impurities at the maximum of the Gaussian distribution is

$$k(d)=(d\Gamma_x\sqrt{2\pi})^{-1}\int_0^d \exp\left(-\frac{(x-x_0)^2}{2\Gamma_x^2}\right)dx. \quad (1)$$

Here x_0 is the depth at which the maximum of the distribution is located, Γ_x is the half-width of the distribution based on a level of 0.606 of the maximum, and d is the thickness of the sample under study.

Note that for $d \gg x_0,\Gamma_x$ the quantity $k(d)$ turns out to be independent of either x_0 or Γ_x. Because of this circumstance, we are able to make a rather accurate comparison of the experimental data obtained from samples that are quite thick since, according to Refs. 12 and 13, the penetration depth of impurities does not exceed 1 μm in ion-implanted and vacuum-annealed lead chalcogenides. It thus follows that in order to compare data obtained from samples of varying thickness using Eq. (1) it is enough to reference the data to a single number $d^* \gg x_0,\Gamma_x$ ($S_5^*=S_5k(d^*)k^{-1}(d)$). In this paper, we choose for d^* a value of 5.0 μm. The function $S_5^*(D)$ obtained in this way for samples that do not contain sodium or tin impurities is shown in Fig. 3. These samples were chosen for analysis because the concentration of chalcogen vacancies in them in their original state, based on Ref. 5, did not exceed $2-3\times10^{18}\,{\rm cm}^{-3}$, i.e., it was not large. Therefore, even if its value changed from sample to sample, the changes would not have any effect on the concentration of centers that make up level E_5. Figure 3 shows clearly that the function $S_5^*(D)$ can be approximated by a straight line passing through the origin. This allows us to assert that level E_5 is associated with a point defect.

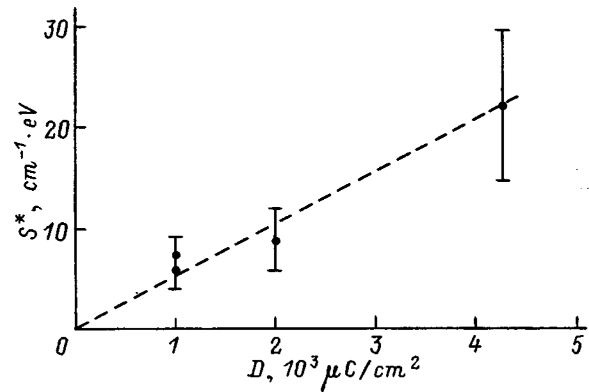

FIG. 3. Plot of the integrated absorption cross section S^* reduced by the thickness $d^*=5.0$ μm in PbSe prepared from a batch not containing Na or Sn impurities, implanted with oxygen and annealed in vacuum, versus the dose D of incorporated ions.

In conclusion we note two features in the experimental data that are common to PbTe and PbSe (Ref. 4) implanted with oxygen. First of all, the intensity of the α_5 bands, as is clear from Fig. 1, increases with increasing concentration of anion vacancies in the original samples. This result can be viewed as sufficient confirmation of what was said above regarding the connection between level E_5 and a point defect. It agrees with existing representations in which the oxygen impurities occupy positions in the chalcogen sublattice, thereby filling vacancies. Secondly, annealing of these samples in vacuum cannot completely eliminate intrinsic defects that arise during ion implantation. Evidence for the existence of such defects in annealed PbSe:O^+ are the α_4 bands associated with $V_{\rm ch}$. Usually annealing of ion-implanted lead chalcogenides in vacuum (for 25 min at $T_a=250\,^\circ$C) leads to complete elimination of all the radiation-induced defects, including $V_{\rm ch}$.[12] Apparently this feature is characteristic of all lead chalcogenides doped with oxygen ions. It could be due to the acceptor-like behavior of the impurity introduced, which is also compensated by anion vacancies.

The authors are grateful to I. O. Usov and I. B. Zakharova who carried out the ion doping and sample annealing.

[1] L. V. Neustroev and V. V. Osipov, Fiz. Tekh. Poluprovodn. **18**, 359 (1984) [Sov. Phys. Semicond. **18**, 224 (1984)].
[2] L. V. Neustroev and V. V. Osipov, Fiz. Tekh. Poluprovodn. **20**, 59 (1986) [Sov. Phys. Semicond. **20**, 11 (1986)].
[3] V. V. Teterkin, F. F. Sizov, N. O. Tashtanbaev, V. B. Orelkiĭ, and V. D. Fotiĭ, *Abstracts of Reports from the 3rd All-Union Conf. on ''Material Science of Chalcogenide Semiconductors''* (Chernovtsy, 1991), ch. 1, p. 88.
[4] A. N. Veĭs, Fiz. Tekh. Poluprovodn. **31**, 1419 (1997) [Sov. Phys. Semicond. **31**, 1225 (1997)].
[5] A. N. Veĭs and N. A. Suvorova, Fiz. Tekh. Poluprovodn. **32**, 445 (1998) [Semiconductors **32**, 397 (1998)].
[6] L. I. Vitenskiĭ, V. I. Kaĭdanov, R. B. Mel'nik, S. A. Nemov, and Yu. I. Ravich, Fiz. Tekh. Poluprovodn. **14**, 74 (1980) [Sov. Phys. Semicond. **14**, 40 (1980)].
[7] A. N. Veĭs and N. A. Suvorova, Fiz. Tekh. Poluprovodn. **30**, 2089 (1996) [Semiconductors **30**, 1089 (1996)].
[8] A. N. Veĭs, Dok. Akad. Nauk (SSSR) **289**, 1355 (1986) [Sov. Phys. Dokl. **31**, 654 (1986)].
[9] A. N. Veĭs, A. Yu. Rydanov, and N. A. Suvorova, Fiz. Tekh. Poluprovodn. **27**, 701 (1993) [Sov. Phys. Semicond. **27**, 386 (1993)].
[10] O. N. Kassandrova and V. V. Lebedev, *Processing the Results of Observations* (Nauka, Moscow, 1970).
[11] A. N. Veĭs, E. V. Glebova, and N. A. Erasova, Fiz. Tekh. Poluprovodn. **19**, 2055 (1985) [Semiconductors **19**, 1265 (1985)].
[12] L. Palmetschofer, Appl. Phys. A: Solids Surf. **34**, 139 (1984).
[13] Z. M. Dashevskiĭ, L. A. Evmen'ev, V. A. Mazur, and M. P. Rulenko, *Abstracts of Reports from the 3rd School on Current Problems in the Physics of Semimetals and Narrow-Band Semiconductors*, Tiraspol', 1987 (Kishinev, 1987), p. 92.

Translated by Frank J. Crowne

Autosolitons in an electron–hole plasma/excitons system in silicon at 4.2 K

A. M. Musaev

Kh. I. Amirkhanov Institute of Physics, Dagestan Scientific Center of the Russian Academy of Sciences, 367003 Makhachkala, Russia

(Submitted January 22, 1999; accepted for publication April 26, 1999)
Fiz. Tekh. Poluprovodn. **33**, 1183–1186 (October 1999)

Results are presented of the experimental discovery and study of auto-oscillations in an electron–hole plasma/excitons system in silicon under conditions of impact ionization of the excitons in a constant electric field. It is shown that the current auto-oscillations are due to disruption of the uniform density distribution of the electron–hole plasma and its stratification, where the latter is caused by the formation of strongly nonequilibrium structures, namely, autosolitons. The microplasma breakdown of the reverse-biased Schottky barrier is the cause of the spontaneous excitation of autosolitons. © *1999 American Institute of Physics.* [S1063-7826(99)00710-3]

Ashkinadze and Subashiev[1] reported the discovery of auto-oscillations of the density of nonequilibrium electron–hole plasma (EHP) in Si in the low-temperature region $T \simeq 4.2-15$ K under conditions of photoexcitation of electron–hole pairs in a microwave field. The appearance of auto-oscillations of the EHP density is explained by impact ionization of excitons by electrons heated in the microwave field when the condition $\omega\tau_p > 1$ is satisfied. The cause of the instability is growth of the temperature of the electrons in the microwave field with increase of their concentration. In Refs. 1 and 2 it was shown that under conditions of electron heating, when $\omega\tau_p < 1$, (equivalent to electron heating in a constant electric field) auto-oscillations do not arise.

Weman *et al.*[3] detected current auto-oscillations in photoexcited p-Si$\langle B\rangle$ at 2 K in a constant electric field. Auto-oscillations were detected only in p-Si$\langle B\rangle$ samples with concentration of thermal donor complexes $N_D \gtrsim 10^{16}$ cm^{-3} $> N_A$, where N_A is the initial boron impurity concentration in the silicon matrix. They link the physical mechanism of the auto-oscillations with critical equilibrium between impact ionization of the excitons and their degree of capture to the thermal donors.

In the present paper we report the experimental detection and study of auto-oscillations in the nonequilibrium system EHP/excitons in silicon under conditions of impact ionization of excitons in a static electric field at liquid-helium temperatures. As the results of our experiments show, the appearance of auto-oscillations is linked with a disruption of the uniformity of the plasma density distribution and stratification of the plasma caused by the appearance of a strongly nonequilibrium state—an autosoliton (AS).

In Refs. 4 and 5 it was shown that an electron–hole pair is an example of an active system with diffusion; from the general nonlinear theory of this diffusion it follows that in the region of a stable, homogeneous state of such systems an external perturbation can excite (autosolitons can also arise spontaneously near small inhomogeneities) stationary, isolated states, which do not depend on the form of the initial perturbation, but are determined by the parameters of the specific system. Such self-maintaining localized eigenstates—autosolitons of nonequilibrium systems—were detected experimentally and investigated in Refs. 6 and 7.

Our experiments were performed on samples of p-Si$\langle P\rangle$ with impurity concentration $N_D - N_A \simeq 8\times 10^{12}$ cm^{-3}, prepared in the form of rectangular parallelepipeds with dimensions $3.7\times 1.3\times 2.1$ mm. The crystallographic orientation of the sample and the configuration of the action of the electric field and photoexcitation are shown in Fig. 1. The contacts were created by melting-in a Au(Sb) alloy in vacuum on opposite faces with dimensions 3.7×1.3 mm. The face of the sample with dimensions 3.7×2.1 mm was illuminated by rectangular pulses from a monochromatic light source based on infrared GaAs diodes with photon energy $\hbar\omega \simeq 1.5$ eV $> \varepsilon_G^{\mathrm{Si}}$. The duration of the photoexcitation pulses (40 μs) ensured the setting up of a steady-state concentration of carriers and excitons. The maximum photoexcitation intensity $I_{p\max}$ corresponded to a concentration of the generated electron–hole pairs equal to 5×10^{14} cm^{-3}. Synchronously with the photoexcitation pulses, the sample was acted on by constant-electric-field pulses with a duration of 100 μs, which were delayed relative to the photoexcitation pulses by $\tau_E = 0-1.0$ ms. The pulse repetition rate of 3 Hz ensured that the temperature of the sample recovered to 4.2 K at the beginning of each pulse. Current–voltage characteristics

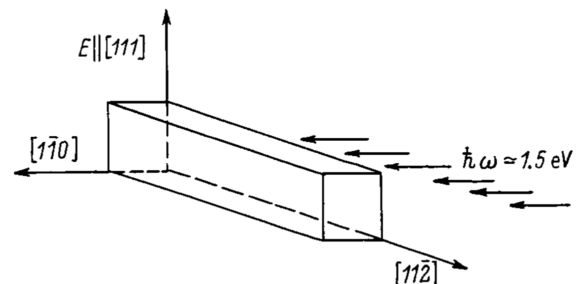

FIG. 1. Configuration of the action of an electric field and photoexcitation relative to the crystallographic axes of the sample.

 © 1999 American Institute of Physics

(CVC) were recorded by feeding a sawtooth voltage with a duration of up to 20 μs.

Figure 2 shows oscillograms of the current through the sample for different values of the photoexcitation intensity and the intensity of the applied electric field. As can be seen from the oscillograms, after feed of an electric field pulse with some delay, a conduction current pulses appears. The delay time of this pulse decreases as the electric field intensity and the photoexcitation intensity are increased. A characteristic feature of the time dependence of the conduction for $\tau_E \neq 0$ is the appearance of an initial, solitary current spike followed by the following types of oscillations: isolated pulses, relaxation oscillations, and random oscillations. With simultaneous application of the photoexcitation and electric-field pulses, the time delay between the initial peak and the subsequent peaks is absent. Figure 3 shows typical dynamic CVC's of the sample, recorded in the voltage-generator regime for various values of the delay of the sawtooth voltage pulses relative to the photoexcitation pulses (τ_E). The threshold breakdown field E_B depends both on the photoexcitation intensity I_p and on the delay time τ_E. With decrease of the photoexcitation intensity and increase of the

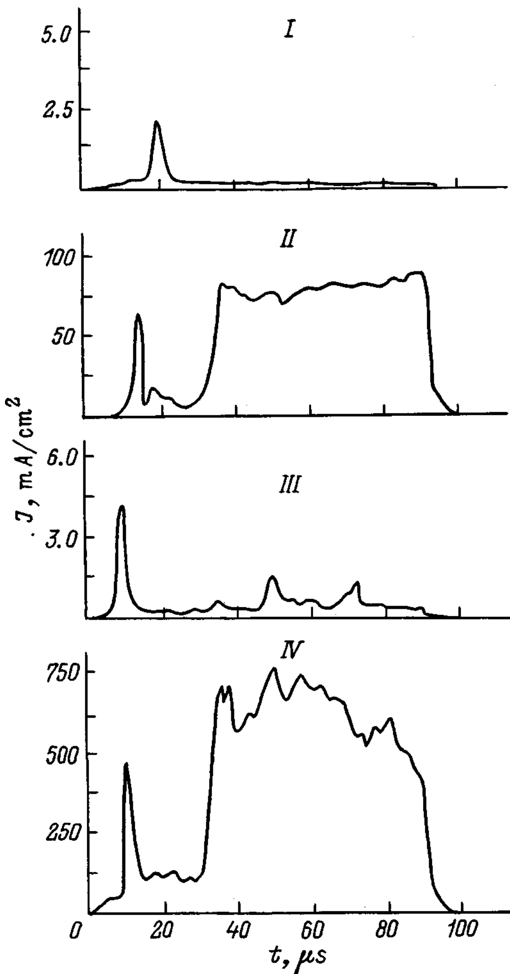

FIG. 2. Oscillograms of the current for different values of the electric field strength and the photoexcitation intensity: *I* — $E=1.5$ kV/cm, $I_p=0.05\,I_{p\max}$; *II* — $E=1.5$ kV/cm, $I_p=0.5\,I_{p\max}$; *III* — $E=2.5$ kV/cm, $I_p=0.05\,I_{p\max}$; *IV* — $E=2.5$ kV/cm, $I_p=0.5\,I_{p\max}$.

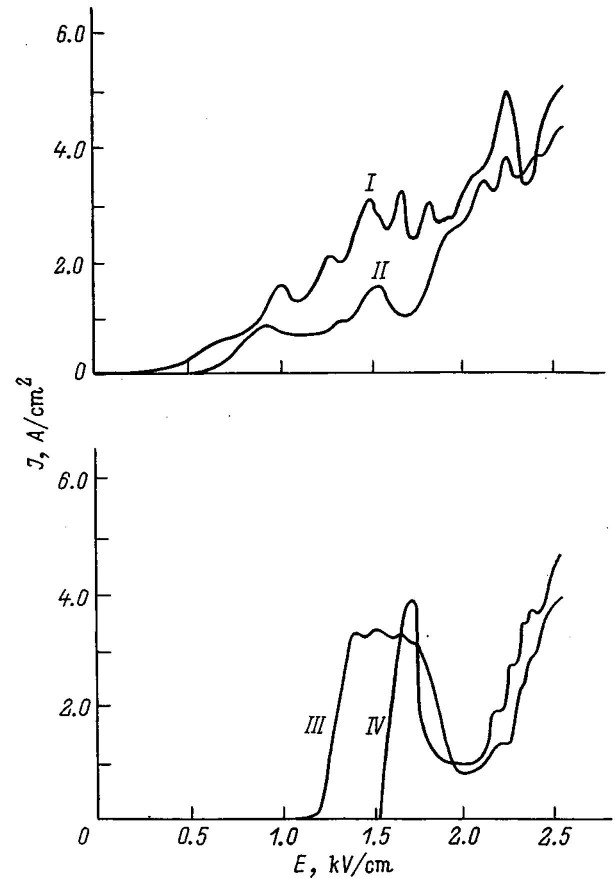

FIG. 3. Dynamic current–voltage characteristics of a sample for different values of the delay of electric field pulse relative to the photoexcitation pulse (τ_E). *I* — CVC at the time of photoexcitation; *II* — $\tau_E=1.0\,\mu$s; *III* — $\tau_E=10\,\mu$s; *IV* — $\tau_E=30\,\mu$s.

delay time τ_E, the threshold breakdown field E_B increases. Depending on the regime in which they were measured, both *S*-shaped and *N*-shaped segments of negative differential resistance are observed on the CVCs. The initial current peak is especially pronounced for large values of the delay time τ_E (Fig. 3, curves *III* and *IV*). Probe measurements for low electric field intensity reveal the presence of a stationary high-field domain on the cathode of the sample. As the field intensity is increased to its threshold value, the current oscillations arise abruptly in the sample. These phenomena were detected by the author in previous experiments on silicon samples with a Schottky barrier.[8]

To explain this phenomenon it is necessary to consider the physical processes taking place in the contact and base regions of the sample.

As is well known, almost all metals form a Schottky barrier with *n*-type silicon, with a relatively large barrier height (more than 0.5 eV). Therefore, to lower the contact potential barrier and obtain an ohmic contact, a thin, heavily doped layer is created directly at the boundary with the metal. The depleted region in this case is so thin that field emission is important, and for small biases the contact has a small resistance.[9] However, at low temperatures and moderate impurity concentrations the width of the depleted contact layer is substantial. In this case, the tunneling component of the current through the contact decreases and the current is

mainly due to generation of electron–hole pairs in the depleted region.[9] This situation is characterized by nonuniform breakdown over the area of the barrier due to the microplasma mechanism of breakdown and localization of the current on separate segments with small cross section.[10] Microplasma breakdown of the space charge region (SCR) on the cathode initiates spontaneous excitation of an autosoliton in the sample. Carrier generation in the space charge region leads to a redistribution of the voltage between the space charge region and the base of the sample, which in turn leads to impact ionization of excitons in the base region. To maintain breakdown of excitons, it is necessary that the exciton concentration exceed some critical value for the given field. This condition is satisfied because of the radial diffusion of excitons from the peripheral regions of the sample. However, the exclusion of free carriers and the decrease in the exciton concentration in the breakdown region for bounded influx of excitons into this region can lead to cessation of ionization of excitons, and the system returns to its initial state. The initial current spike observed in the CVC's and the temporal characteristics is due precisely to ionization of a bounded number of free excitons.

By absorbing the field energy the free carriers cause the temperature of the crystalline lattice to grow. This leads to thermal dissociation of bound excitons; i.e., when the lattice temperature reaches $T \geqslant 10\,\mathrm{K}$, the excitons go mainly into the free state. The lifetimes of the excitons in this case are greatly increased.[11] During breakdown, growth of the concentration of free carriers acquires an avalanche-like character. The exciton concentration in this region decreases correspondingly, forming an isolated stable localized state. Despite the abrupt growth of the concentration of free carriers in the localization region of the autosoliton, the product $N_{\mathrm{ex}} D_{\mathrm{ex}}$ in it is nearly constant due to compensation of ionized excitons by the exciton diffusion flux into this region. Stratification of the EHP density is confirmed by band measurements, and also by studies of the current density distribution in the sample as a result of splitting of the anode contact. Figure 4 shows oscillograms of the current $(I-IV)$ in regions of the sample when the anode contact is split into four equal parts. As can be seen from these figures, the autosoliton is localized in region *III* of the sample. An important factor influencing the kinetic effects of excitons at liquid-helium temperatures in Si is the nonequilibrium phonon flux.[12] Heating of free carriers in an electric field gives rise to an intense generation of nonequilibrium phonons. The large mean free path of the long-wavelength phonons at liquid-helium temperatures in Si is comparable with the dimensions of the sample. This flux is intense enough to entrain excitons with velocity close to the speed of sound, toward the surface of the sample. The abrupt change in the conduction kinetics of the ionized excitons (slope change on the curve with subsequent rapid falloff almost to zero over a short time) can be explained by the action on the excitons of the nonequilibrium phonon flux. This factor is also connected with the pulsation of autosolitons observed in our atudy. The nonequilibrium localized region is created by the increasing dependence of the exciton ionization rate v_i on the free-carrier concentration n_e, on the one hand, and by the decrease of the exciton flux into the ionization region as a consequence of the nonequilibrium phonon flux, on the other. The evolution of the electron density n_e and the exciton density N_{ex} in a static electric field is governed by the equations

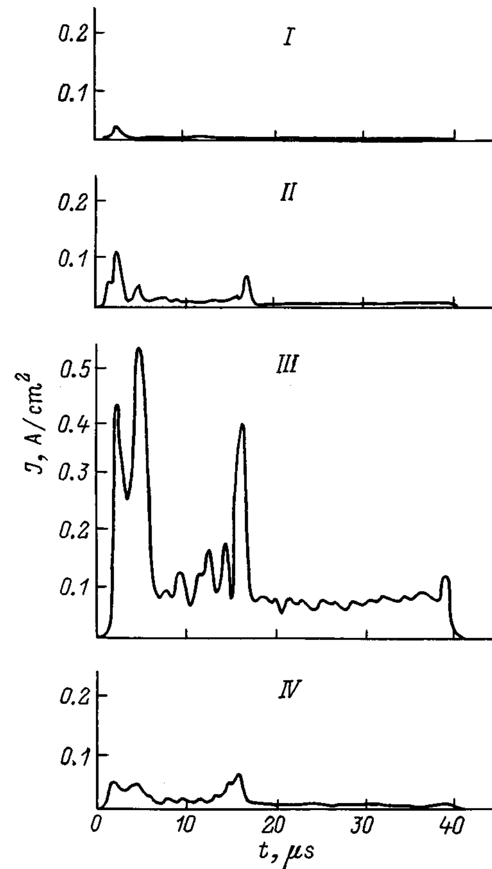

FIG. 4. Oscillograms of the current $(I-IV)$ of segments of the sample with split anode contact for $E = 2.2$ kV/cm, $\tau_E = 10\ \mu$s, and $I_p = 0.1\, I_{p\max}$.

$$\partial n_e / \partial t = -e^{-1} \operatorname{div} J_e - \gamma n_e^2 - n_e / \tau_e + \beta n_e N_{\mathrm{ex}}, \tag{1}$$

$$\partial N_{\mathrm{ex}} / \partial t = -\operatorname{div} J_{\mathrm{ex}} + \gamma n_e^2 - N_{\mathrm{ex}} / \tau_{\mathrm{ex}} - \beta n_e N_{\mathrm{ex}}, \tag{2}$$

where $\tau_e = l / v_e$ is the electron drift time, τ_{ex} is the exciton lifetime, γ is the exciton coupling coefficient, β is the impact ionization coefficient of the excitons, and J_e and J_{ex} are the electron and exciton flux densities, respectively. The exciton flux is governed by diffusion and phonon entrainment,

$$J_{\mathrm{ex}} = D_{\mathrm{ex}} \nabla N_{\mathrm{ex}} - \lambda_{ep}\, g\, N_{\mathrm{ex}}, \tag{3}$$

where D_{ex} is the exciton diffusion coefficient, and λ_{ep} is the electron–phonon interaction coefficient;

$$g \sim 1/c\, \rho [n_e\, e\, \mu\, E^2\, v/V - \lambda / b (T - T_0)], \tag{4}$$

c is the specific heat, ρ is the density, $\mu = \mu_n \simeq \mu_p$ is the carrier mobility, v/V is the volume fraction corresponding to localization of the autosoliton, λ is the thermal conductivity, b is the thickness of the sample, and T_0 is the temperature of the surrounding medium.

In the given mechanism of stratification of the electron–hole pairs the role of activator is played by the free carrier concentration (n_e), and the role of inhibitor is played by the

exciton flux, which is a function of the interaction with the phonon flux. Positive feedback via the activator is connected with the increasing dependence of the exciton ionization rate v_i on the carrier concentration n_e. The damping role of the inhibitor is determined by the fact that an increase in the free carrier concentration results in an increase in the flux of nonequilibrium phonons generated by the free carriers; these nonequilibrium phonons entrain excitons and thereby restrict their entry into the ionization region. Because of the strong dependence of the ionization rate on the exciton concentration, this circumstance in turn leads to an abrupt decrease of the carrier concentration in the ionization region. The existence of autosolitons in the given system is governed by the quantities

$$\varepsilon = l/L, \quad \alpha = \tau_e/\tau_{\mathrm{ex}},$$

where

$$l = (D_e \tau_e)^{1/2}, \quad L = (D_{\mathrm{ex}} \tau_{\mathrm{ex}})^{1/2}$$

are the diffusion lengths, and D_e and D_{ex} are the diffusion coefficients of the free carriers and excitons. The stability of the autosolitons is attributable to the fact that the autosoliton wall has a small size: $l \ll d \ll L$, where the increment of the free-carrier concentration is damped by a corresponding decrease in the exciton concentration. This damping is realized only in a certain range of variation of E: For $E > E_c$ a static autosoliton is converted, as a result of instability, into a pulsating autosoliton. The formation of pulsating autosolitons has to do with the fact that $\tau_e \ll \tau_{\mathrm{ex}}$. For $\tau_e \ll \tau_{\mathrm{ex}}$, during a fluctuation of the carrier concentration (activator) n_e with frequency on the order of $(\tau_e \tau_{\mathrm{ex}})^{-1/2}$ a fluctuation of the exciton flux (inhibitor) $\sim N_{\mathrm{ex}} D_{\mathrm{ex}}$ does not have time to vary; therefore, fluctuations of the concentration n_e grow. The system under consideration is an active system with cross diffusion and self-generation of particles. According to the classification of systems given in Ref. 4, the given model belongs to the class of $K\Omega$ systems. The $K\Omega$ phenomenon realized in the system is consistent with the existence of pulsating autosolitons, whose number and form vary periodically in time.

[1] B. M. Ashkinadze and A. V. Subashiev, JETP Lett. **46**, 357 (1987).
[2] É. M. Shakhverdiev and É. A. Sadykhov, Fiz. Tekh. Poluprovodn. **28**, 424 (1994) [Semiconductors **28**, 424 (1994)].
[3] H. Weman, A. Henry, and B. Monemar, Solid-State Electron. **32**, 1563 (1989).
[4] B. S. Kerner and V. V. Osipov, Usp. Fiz. Nauk **157**, 201 (1989) [Sov. Phys. Usp. **32**, 101 (1989)].
[5] B. S. Kerner and V. V. Osipov, Usp. Fiz. Nauk **160**, 1 (1990) [Sov. Phys. Usp. **33**, 679 (1990)].
[6] B. S. Kerner, D. P. Litvin, and V. I. Sankin, Pis'ma Zh. Tekh. Fiz. **13**, 819 (1987) [Tech. Phys. Lett. **13**, 342 (1987)].
[7] M. N. Vinoslavskiĭ, Fiz. Tverd. Tela (Leningrad) **31**, 315 (1989) [Sov. Phys. Solid State **31**, 903 (1989)].
[8] A. M. Musaev, Fiz. Tekh. Poluprovodn. **31**, 724 (1997) [Semiconductors **31**, 620 (1997)].
[9] E. H. Roderick, *Metal–Semiconductor Contacts* (Radio i Svyaz', Moscow, 1982).
[10] Z. S. Gribnikov, Fiz. Tekh. Poluprovodn. **11**, 2111 (1977) [Sov. Phys. Semicond. **11**, 1239 (1977)].
[11] R. B. Hammond and R. N. Silver, Appl. Phys. Lett. **36**, 68 (1979).
[12] V. S. Bagaev, T. I. Galkina, and N. N. Sibel'din, in *Electron–Hole Droplets in Semiconductors* [in Russian], Nauka, Moscow, 1988.

Translated by Paul F. Schippnick

Influence of indium doping on the formation of silicon–(gallium vacancy) complexes in gallium arsenide grown by molecular-beam epitaxy at low temperatures

A. E. Kunitsyn, V. V. Chaldyshev, and S. P. Vul'

A. F. Ioffe Physicotechnical Institute, Russian Academy of Sciences, 194021 St. Petersburg, Russia

V. V. Preobrazhenskiĭ, M. A. Putyato, and B. R. Semyagin

Institute of Semiconductor Physics, Siberian Branch of the Russian Academy of Sciences, 630090 Novosibirsk, Russia

(Submitted May 17, 1999; accepted for publication May 17, 1999)
Fiz. Tekh. Poluprovodn. **33**, 1187–1191 (October 1999)

Low-temperature photoluminescence (PL) studies of gallium-arsenide layers grown by molecular-beam epitaxy at low (200 °C) temperatures (*LT* GaAs) and doped with silicon or a combination of silicon and indium have been performed. The PL spectra of as-grown samples reveal a shallow acceptor-based line only. After annealing, an additional line at ~1.2 eV appears, which is attributable to $Si_{Ga}-V_{Ga}$ complexes. The activation energy of complex formation is found to be close to the activation energy of migration of gallium vacancies and is equal to 1.9 ± 0.3 eV for *LT* GaAs : Si. It is found that doping with a combination of silicon and indium leads to an increase in the activation energy of formation of $Si_{Ga}-V_{Ga}$ complexes to 2.5 ±0.3 eV. We believe that this increase in the activation energy is controlled by the gallium vacancy–indium interaction through local lattice deformations. © *1999 American Institute of Physics.* [S1063-7826(99)00810-8]

INTRODUCTION

Gallium vacancies exert a substantial influence on the properties of bulk crystals and epitaxial layers of GaAs. When gallium arsenide is doped with shallow-donor impurities (e.g., Si), the interaction of the donors with the vacancies leads to the formation of stable complexes. Such complexes degrade the efficiency of doping and can have an effect on the lifetime of the charge carriers. To elucidate and investigate $Si-V_{Ga}$ type complexes, one usually measures the photoluminescence (PL) spectra, in which a characteristic band with energy near 1.2 eV is observed.[1–3] Gallium vacancies play an especially important role in GaAs layers grown by molecular-beam epitaxy (MBE) at low (<300 °C) temperatures. The main peculiarity of this material (*LT* GaAs), which defines its unique properties, is the large arsenic excess (as high as 1.5 at.%) acquired by the layer during growth. Although a large fraction of the excess arsenic enters into the crystal in the form of antistructural defects (As_{Ga}), whose concentration reaches 10^{20} cm^{-3} (Ref. 4), the gallium-vacancy concentration is also very large, $\sim10^{18}$ cm^{-3} (Ref. 5). It is believed[6] that gallium vacancies (V_{Ga}) are the dominant compensating acceptors in *LT* GaAs, ensuring pinning of the Fermi level near the level of the deep donor As_{Ga}. In addition, it is usually assumed[7] that migration of gallium vacancies plays a key role in the transport and precipitation of excess arsenic and the formation of the system of nanosize As clusters in the *LT* GaAs matrix during annealing. It is also assumed[8,9] that diffusion of gallium vacancies leads to enhanced interdiffusion (In–Ga, Al–Ga) and smearing of the interface in isolated quantum wells and in superlattices (AlAs/GaAs and InAs/GaAs) grown by molecular-beam epitaxy at low temperatures.

We have performed a photoluminescence study of the formation of $Si_{Ga}-V_{Ga}$ complexes in *LT* GaAs : Si layers annealed at various temperatures. We have also investigated the influence of indium doping on the formation of these complexes.

SAMPLES AND EXPERIMENTAL PROCEDURE

LT GaAs layers were grown on the molecular-beam epitaxy setup ''Katun''' on substrates of polished gallium arsenide 40 mm in diameter with (100) orientation. Growth occurred at the temperature 200 °C at a rate of 1 μm/h and an arsenic pressure of 7×10^{-4} Pa. The thickness of the *LT* GaAs layer was 0.5 μm. A layer of AlAs 50 nm in thickness was also grown on the surface of the samples to prevent arsenic evaporation during annealing.

Two groups of layers were grown. The first group was doped with only the shallow donor impurity, silicon (concentration 7×10^{17} cm^{-3}), and the second, with silicon (7×10^{17} cm^{-3}) and the isovalent impurity, indium (2×10^{19} cm^{-3}).

After the growth procedure the samples were divided into several groups, one of which was held unannealed while the remaining groups were subjected to annealing at different temperatures. The samples were annealed in an atmosphere of pure hydrogen for 15 min. The annealing temperature was varied in the limits 600–850 °C.

The photoluminescence (PL) studies were performed at a temperature of 4.2 K in the spectral range 0.8–1.2 μm. An

 © 1999 American Institute of Physics

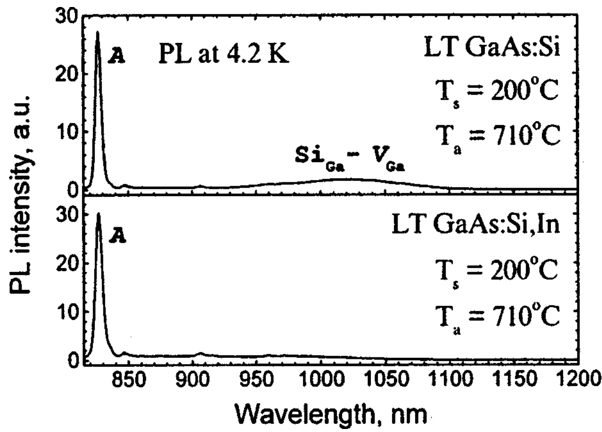

FIG. 1. Low-temperature photoluminescence spectra of *LT* GaAs : Si and *LT* GaAs : Si : In samples grown at 200 °C and annealed at 710 °C.

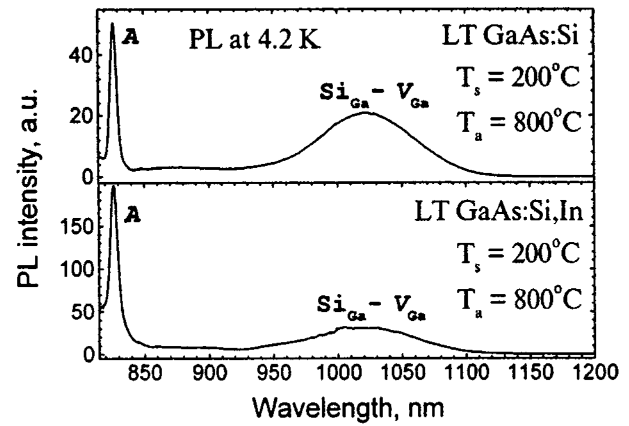

FIG. 2. Low-temperature photoluminescence spectra of *LT* GaAs : Si and *LT* GaAs : Si : In samples grown at 200 °C and annealed at 802 °C.

Ar^+ laser (the 514.5 μm line) was used to excite emission, and the signal was recorded with a FÉU-62 cooled photomultiplier.

EXPERIMENTAL RESULTS

Both the unannealed *LT* GaAs samples doped and not doped with indium were characterized by an extremely weak total photoluminescence intensity, which is due to the extremely short lifetime of the charge carriers in this material. A single line was observed in the spectra of unannealed *LT* GaAs which is associated with recombination at shallow acceptors (1.498 eV). We did not observe lines associated with recombination on free excitons, which is characteristic of *LT* GaAs (Ref. 10).

Figure 1 shows the photoluminescence spectra of *LT* GaAs samples doped and not doped with indium, annealed at 710 °C. It can be seen that in addition to the *A* line associated with shallow acceptors, a weak wide band appears in the region of 1.2 eV, which is associated with deep centers, namely, (gallium vacancy)–donor complexes (in this case $Si_{Ga}-V_{Ga}$).[1–3] It can be seen that in the indium-doped samples, the intensity of this band is much less than in the samples not doped with indium, which is evidence of a lower concentration of $Si_{Ga}-V_{Ga}$ complexes.

As the annealing temperature is raised (Fig. 2 shows photoluminescence spectra of samples of *LT* GaAs doped and not doped with indium, annealed at 800 °C), the total photoluminescence intensity increases due to intensification of the edge photoluminescence lines and due to a significant growth of the intensity of the line associated with deep centers. The increase in the intensity of the edge luminescence lines is apparently explained by an increase in the lifetime of the nonequilibrium charge carriers proportional to the extent that native lattice defects are annealed out. The intensity of the line associated with the $Si_{Ga}-V_{Ga}$ complexes, on the other hand, grows by two or three orders of magnitude, which can be explained only by an increase in the number of these complexes.

The variation in the intensities of individual photoluminescence lines in the spectra of the various samples cannot be used to judge the variation of the relative concentration of the defects responsible for the appearance of these lines since the photoluminescence intensity depends not only on the concentration of recombination centers, but also on the lifetime of the charge carriers in the investigated material. It is well known that during annealing significant changes take place in the structure of the *LT* GaAs samples associated with the formation of arsenic clusters and a decrease in the number of point defects. Clearly, in the process of such changes of the structure of the material the lifetime of the nonequilibrium charge carriers can vary over wide limits. Therefore, to determine the change in the concentration of the $Si_{Ga}-V_{Ga}$ complexes, instead of the absolute value of the intensity of the photoluminescence line associated with this defect we examined its ratio to the recombination line on shallow acceptors.

Figure 3 shows a semilog plot of the ratio of the intensity of the photoluminescence line associated with the $Si_{Ga}-V_{Ga}$ complexes to the intensity of the edge luminescence line as functions of the annealing temperature for samples of *LT* GaAs doped and not doped with indium. It can be seen that at low annealing temperatures the difference in the concentrations of the $Si_{Ga}-V_{Ga}$ complexes is quite

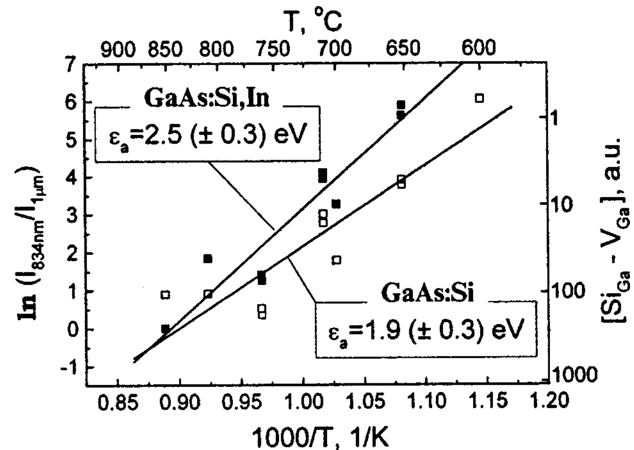

FIG. 3. Semilog plot of the temperature dependence of the ratio of the line intensity of recombination on a shallow acceptor to the intensity of the line associated with the $Si_{Ga}-V_{Ga}$ complexes.

significant while at high annealing temperatures their concentrations are roughly the same. From the slope of the line obtained by statistical processing of the results, it is possible to determine the activation energy of complex formation. For the samples not doped with indium, it is equal to 1.9 ± 0.3 eV. For the indium-doped samples the activation energy of formation of $Si_{Ga}-V_{Ga}$ complexes is equal to 2.5 ± 0.3 eV. The difference amounts to 0.6 eV, which exceeds the measurement error.

DISCUSSION OF THE RESULTS

The formation of complexes consisting of the pair gallium-vacancy and silicon in the gallium sublattice is typical of single crystals and epitaxial layers of gallium arsenide prepared by various methods. It is usually assumed[11] that the formation of (gallium vacancy)–(shallow donor) complexes in epitaxial layers occurs during crystal growth. Our studies show, however, that in the case of low-temperature molecular-beam epitaxy the concentration of $Si_{Ga}-V_{Ga}$ complexes formed during growth of the layers is small. Vigorous formation of complexes takes place during annealing of *LT* GaAs layers and intensifies as the annealing temperature is increased. This means that complex formation takes place as a consequence of migration of defects and impurities, i.e., by the mechanism characteristic of bulk single crystals.

In general, for a sufficiently high concentration of Si_{Ga} donors obtained as a result of doping, complex formation is the result of two consecutive processes: formation of a free vacancy and its migration to a lattice site at which a silicon atom is found. Motion of silicon atoms can be ignored since it is well known that the diffusion coefficient of vacancies in GaAs significantly exceeds the diffusion coefficient of substitution impurities. The activation energy of diffusion of gallium vacancies in GaAs is 1.7 ± 0.5 eV according to the data of Ref. 12, and 1.7 ± 0.3 eV according to the data of Ref. 13.

The energy of formation of gallium vacancies in GaAs is very large, 4.0 ± 0.5 eV (Ref. 12). A peculiarity of gallium arsenide grown by molecular-beam epitaxy at low temperatures is that this material contains a high concentration of gallium vacancies $\sim 10^{18}\,cm^{-3}$ (Ref. 5); i.e., the concentration of gallium vacancies in *LT* GaAs layers is comparable with the silicon concentration, and for formation of $Si_{Ga}-V_{Ga}$ complexes additional vacancies are not required.

Thus, in a layer of GaAs : Si grown by molecular-beam epitaxy at low temperatures, the concentration of gallium vacancies (V_{Ga}) and of Si_{Ga} donors is high [under conditions of a large arsenic excess, silicon atoms are embedded into the gallium sublattice (Ref. 14)]. The formation of $Si_{Ga}-V_{Ga}$ complexes, however, does not take place since the diffusion of defects and impurities at low temperatures is ''frozen.'' During annealing the gallium vacancies present in *LT* GaAs become mobile and as they diffuse they are captured by silicon atoms with subsequent formation of complexes. The activation energy of complex formation should be equal to the activation energy of migration of vacancies. According to our data, this energy for *LT* GaAs : Si layers not doped with indium is 1.9 ± 0.3 eV. This quantity is indeed in good agreement with the data for the activation energy of gallium-vacancy diffusion.[12,13]

The data plotted in Fig. 3 indicate that the activation energy of formation of $Si_{Ga}-V_{Ga}$ complexes differs significantly in the samples doped with indium from those that are not doped. It can be seen that the activation energy of formation of $Si_{Ga}-V_{Ga}$ complexes in the indium-doped samples exceeds the activation energy of the complexes in the material not doped with indium by ~ 0.6 eV. Let us consider probable reasons for this phenomenon.

Since the concentration of gallium vacancies in our experiments was not measured, we can assume that an increase in the energy of complex formation is associated with an insufficient concentration of gallium vacancies in the indium-doped material, which leads to the necessity of generation of additional gallium vacancies (V_{Ga}) for complex formation to proceed. This assumption, however, is at variance with the data obtained in our previous studies.[15] Thus, optical absorption measurements in the near-infrared show that indium-doped *LT* GaAs contains a large concentration of excess arsenic and a large concentration of antistructural defects (As_{Ga}) in comparison with the material not doped with indium. It is well known[16] that the concentration ratio As_{Ga^+}/As_{Ga^0} remains roughly constant over a wide interval of growth temperatures and flux ratios As/Ga. An increase in the number of positively charged defects in turn, should obviously be accompanied by an increase in the concentration of gallium vacancies, which, as is suggested in Ref. 6, are the main compensating acceptors. It should also be noted that despite the high concentration of shallow Si donors ($7\times 10^{17}\,cm^{-3}$), the unannealed layers were high-resistance layers, i.e., the concentration of compensating acceptors should be higher than the concentration of shallow donors. In addition, earlier studies[15] of *LT* GaAs by transmission electron microscopy showed that during annealing the indium-doped material contains a higher concentration of large arsenic clusters in comparison with *LT* GaAs not doped with indium. It is now assumed that the formation of arsenic clusters occurs as a result of diffusion of excess arsenic in the gallium vacancies. Thus, we can rightfully and confidently conclude that doping of *LT* GaAs with indium should not be accompanied by a decrease in the gallium-vacancy concentration.

A probable reason for the increase in the energy of $Si_{Ga}-V_{Ga}$ complex formation in indium-doped samples is an interaction of the gallium vacancies with the indium atoms during diffusion of vacancies in the crystal. Indeed, in the investigated samples the indium concentration exceeds the silicon concentration by more than an order of magnitude, and although indium is an isovalent impurity and electrically inactive in gallium arsenide, the difference in the size of the indium and gallium atoms leads to the appearance of local elastic deformations in the vicinity of the lattice sites occupied by indium atoms. In other words, a vacancy creates local deformations of opposite sign in the material. It is clear that such defects, which create local deformations opposite in sign, have a tendency to come together and form complexes, lowering the free energy of the material. Such complexes can have a binding energy on the order of several tens

of electron volts; however, they are less stable than defect complexes formed as a result of electrical interaction. As the annealing temperature is raised, these intermediate complexes decay, and the liberated gallium vacancy continues to diffuse about the crystal until it forms a more stable complex with a silicon donor.

CONCLUSIONS

Studies of the photoluminescence spectra at 4.2 K of GaAs layers, which have grown by molecular-beam epitaxy at low temperatures and which are doped with silicon showed that in the unannealed samples the concentration of $Si_{Ga}-V_{Ga}$ complexes is extremely small and is not detected experimentally; i.e., despite the high concentration of gallium vacancies and silicon donors, these defects virtually do not interact with one another during low-temperature molecular-beam epitaxy. Formation of $Si_{Ga}-V_{Ga}$ complexes takes place during annealing.

From the low-temperature photoluminescence data we determined the activation energy of formation of $Si_{Ga}-V_{Ga}$ complexes in *LT* GaAs layers doped with silicon. This energy is 1.9 ± 0.3 eV, which corresponds to the activation energy of diffusion of gallium vacancies.

We found that combined doping of *LT* GaAs by silicon and indium increases the activation energy of formation of $Si_{Ga}-V_{Ga}$ complexes to 2.5 ± 0.3 eV. A possible reason for this increase is an interaction between the gallium vacancies with the isovalent indium impurities due to local lattice deformations.

This work was carried out with the support of the Russian Fund for Fundamental Research (Project No. 98-02-17617) and the Russian Ministry of Science within the framework of the program ''Fullerenes and Atomic Clusters'' and ''Physics of Solid-State Nanostructures'' (Projects No. 97-2044 and No. 97-1035).

[1] E. W. Williams, Phys. Rev. **168**, 922 (1968).
[2] E. W. Williams and H. B. Bell, in *Semiconductors and Semimetals*, Vol. 8, edited by R. K. Willardson and G. C. Beer (Academic Press, New York), p. 321. G. C. Beer (Academic Press, N. Y.–London) **8**, 321 (1972).
[3] N. S. Averkiev, A. A. Gutkin, M. A. Reshchikov, and V. E. Sedov, Fiz. Tekh. Poluprovodn. **30**, 1123 (1996) [Semiconductors **30**, 595 (1996)].
[4] M. Kaminska, Z. Liliental-Weber, E. R. Weber, T. George, J. B. Kortright, F. Smith, B. Y. Tsaur, and A. R. Calawa, Appl. Phys. Lett. **54**, 1881 (1989).
[5] J. Gebauer, R. Krause-Rehberg, S. Eichler, M. Luysberg, H. Sohn, and E. R. Weber, Appl. Phys. Lett. **71**, 638 (1997).
[6] X. Liu, A. Prasad, J. Nishio, E. R. Weber, Z. Liliental-Weber, and W. Walukiewicz, Appl. Phys. Lett. **67**, 279 (1995).
[7] Z. Liliental-Weber, X. W. Lin, J. Washburn, and W. Schaff, Appl. Phys. Lett. **66**, 2086 (1995).
[8] C. Kisielowski, A. R. Calawa, and Z. Liliental-Weber, J. Appl. Phys. **80**, 156 (1996).
[9] N. A. Bert, V. V. Chaldyshev, Yu. G. Musikhin, A. A. Suvorova, V. V. Preobrazhenskii, M. A. Putyato, B. R. Semyagin, and P. Werner, Appl. Phys. Lett. **74**, 1442 (1999).
[10] N. A. Bert, A. I. Veĭnger, M. D. Vilisova, S. I. Goloshchapov, I. V. Ivonin, S. V. Kozyrev, A. E. Kunitsyn, L. G. Lavrent'eva, D. I. Lubyshev, V. V. Preobrazhenskiĭ, B. R. Semyagin, V. V. Tret'yakov, V. V. Chaldyshev, and M. P. Yakubenya, Fiz. Tverd. Tela (St. Petersburg) **35**, 2609 (1993) [Phys. Solid State **35**, 1289 (1993)].
[11] I. A. Bobrovnikova, L. G. Lavrentieva, M. P. Rusaikin, and M. D. Vilisova, J. Cryst. Growth **123**, 529 (1992).
[12] J.–L. Rouviere, Y. Kim, J. Cunningham, J. A. Rentschler, A. Bourret, and A. Ourmazd, Phys. Rev. Lett. **68**, 2798 (1992).
[13] D. E. Bliss, W. Walukiewicz, J. W. Ager, E. E. Haller, K. T. Chan, and S. Tanigawa, J. Appl. Phys. **71**, 1699 (1992).
[14] S. A. McQuaid, R. C. Newman, M. Missous, and S. O'Hagan, Appl. Phys. Lett. **61**, 3008 (1992).
[15] N. A. Bert, V. V. Chaldyshev, A. E. Kunitsyn, Yu. G. Musikhin, N. N. Faleev, V. V. Tretyakov, V. V. Preobrazhenskii, M. A. Putyato, and B. R. Semyagin, Appl. Phys. Lett. **70**, 3146 (1997).
[16] M. Luysberg, H. Sohn, A. Prasad, P. Specht, Z. Liliental-Weber, E. R. Weber, J. Gebauer, and R. Krause-Rehberg, J. Appl. Phys. **83**, 561 (1998).

Translated by Paul F. Schippnick

Oxygen and Erbium related donor centers in Czochralski grown silicon implanted with erbium

V. V. Emtsev, V. V. Emtsev, Jr., D. S. Poloskin, E. I. Shek, and N. A. Sobolev

A. F. Ioffe Physicotechnical Institute, Russian Academy of Sciences, 194021 St. Petersburg, Russia

J. Michel and L. C. Kimerling

Materials Processing Center, MIT, Cambridge, MA 02139, USA

(Submitted June 8, 1999; accepted for publication June 16, 1999)
Fiz. Tekh. Poluprovodn. **33**, 1192–1195 (October 1999)

The Hall effect measurements were conducted on Czochralski-grown silicon after implantation of erbium and two-step annealing at 700 °C and 900 °C. After the first step the formation of oxygen-related shallow donors was observed at E_c in the range 20–40 meV and erbium-related donor centers at $\approx E_c - 70$ meV and $\approx E_c - 120$ meV. Along with the same oxygen-related shallow thermal donors and donor centers at $\approx E_c - 70$ meV, other donor centers at $\approx E_c - 150$ meV are formed following the 900 °C anneal, instead of those at $\approx E_c - 120$ meV. The new donor states are of particular interest because of their possible involvement in the photoluminescence process. The obtained results for erbium-implanted silicon are compared with some fragmentary DLTS data found in the current literature on the donors with ionization energies less than 0.2 eV. © *1999 American Institute of Physics.* [S1063-7826(99)00910-2]

Studies of erbium impurity in silicon aim to produce the impurity-related centers with a strong luminescence band at 1.54 μm. This goal can be realized by investigating electrical and optical properties of Er-related centers. Implantation of Er is widely used for the doping of Si. Post-implantation annealing of Si:Er at $T \geqslant 600$ °C is needed to remove the radiation damage and activate the Er-related centers. In Si implanted with Er, many deep centers with activation energies larger than ≈0.2 eV have been studied extensively by means of DLTS (see, for example, Refs. 1–3). In contrast, the information available in the current literature about shallow donor centers is meager.[1] The purpose of this communication is to present electrical data on these centers, which are responsible for the electron conductivity of Si:Er at cryogenic and room temperatures.

Wafers of carbon-lean Czochralski-grown silicon (Cz-Si) with high oxygen contents ($\approx 10^{18}\,\mathrm{cm}^{-3}$) were used; the conversion factor for the well-known absorption band of oxygen at $1108\,\mathrm{cm}^{-1}$ was taken according to ASTM F 121-83 ($2.45\times10^{17}\,\mathrm{cm}^{-2}$). The boron concentration in the starting materials of p-type was in the range from $3\times10^{14}\,\mathrm{cm}^{-3}$ to $2\times10^{15}\,\mathrm{cm}^{-3}$. Erbium ions at 1.2 MeV were implanted in Si in doses Φ(Er) ranging from $10^{11}\,\mathrm{cm}^{-2}$ to $10^{13}\,\mathrm{cm}^{-2}$, i.e., beyond the onset of amorphization of the implanted layers. In some cases, the oxygen concentration in the samples subjected to Er implantation was increased by coimplantation of oxygen ions at 0.17 MeV. The implantation dose of oxygen was always an order-of-magnitude higher than that of the erbium, i.e., $\Phi(\mathrm{O}) = 10\Phi(\mathrm{Er})$. All samples were then annealed in two successive steps at 700 °C and 900 °C for 30 min in a chlorine-containing ambient atmosphere. Electrical measurements were taken after each annealing step. Most of the radiation damage due to ion implantation is removed at the first step. The annealing at $T = 900$ °C is used for the formation of the well-known centers with light emission at ≈1.54 μm; see, for instance, Ref. 4. This two-step annealing can be used to observe the most pronounced modifications of donor centers in the temperature range of current interest. After the first annealing step the Er-implanted layers of about 0.5 μm became n-type with the exception of those at $\Phi(\mathrm{Er}) = 10^{11}\,\mathrm{cm}^{-2}$. Under our experimental conditions, the Er peak concentration was $3\times10^{17}\,\mathrm{cm}^{-3}$ at the largest dose of $\Phi(\mathrm{Er}) = 10^{13}\,\mathrm{cm}^{-2}$. Electrical measurements of the concentration of free electrons in the implanted layers versus temperature, $n(T)$, were conducted by means of the van der Pauw technique in the temperature range from $T = 20$ K to $T = 300$ K. Analysis of the $n(T)$ curves was carried out on the basis of the relevant electroneutrality equations.

ANNEALING OF *Cz*-Si: Er AT *T*=700 °C

At $\Phi(\mathrm{Er}) = 10^{11}\,\mathrm{cm}^{-2}$ the Er-implanted layers remain p-type even for the nominally undoped Cz-Si. It allows us to estimate the total concentration of shallow donors, which is less than $3\times10^{14}\,\mathrm{cm}^{-3}$ at this low dose. Starting with $\Phi(\mathrm{Er}) = 5\times10^{11}\,\mathrm{cm}^{-2}$ the donor concentration due to the Er implantation is well in excess to overcompensate the boron acceptors available in the starting materials (see Fig. 1). Analysis of the $n(T)$ curves for Φ(Er) in the range from $5\times10^{11}\,\mathrm{cm}^{-2}$ to $10^{13}\,\mathrm{cm}^{-2}$ allowed us to separate and identify three kinds of donors with activation energies less than 0.2 eV.

The donor states of the first kind are shallow, with ionization energies less than 50 meV. They are very similar to

 © 1999 American Institute of Physics

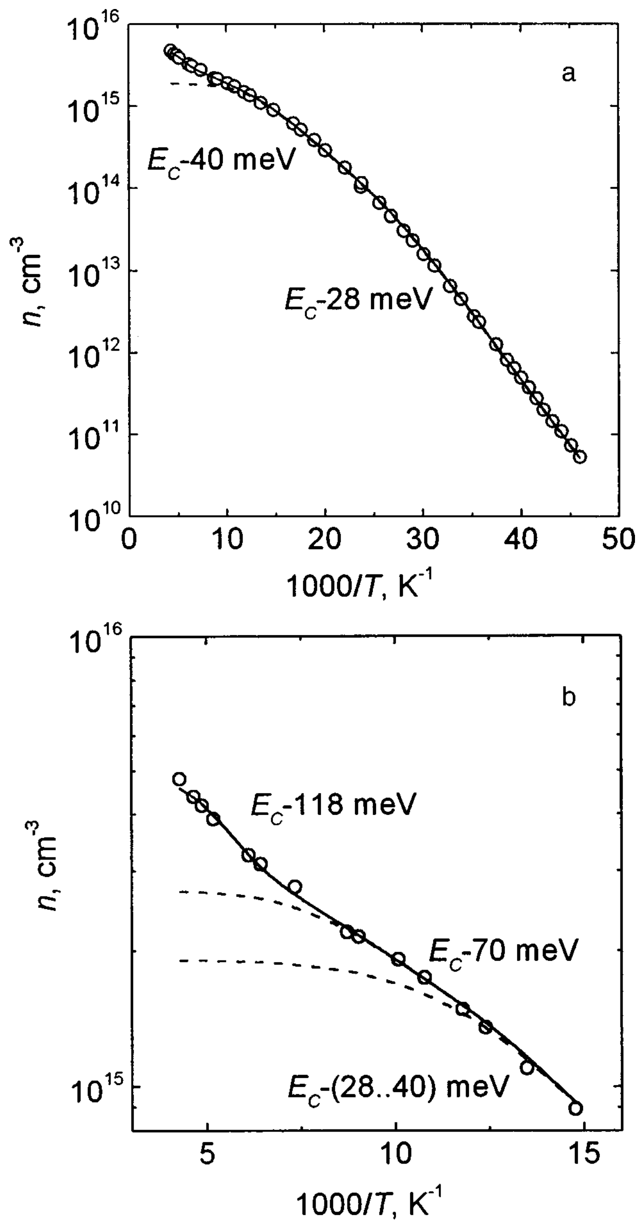

FIG. 1. Electron concentration vs reciprocal temperature for *Cz*-Si implanted with Er and annealed at $T_{ann}=700\,°C$. $\Phi(Er)=5\times10^{11}\,cm^{-2}$. The points represent experimental values; the curves denote calculated values. The $n(T)$ curve at $T\geqslant70\,K$ is shown on the expanded scale in Fig. 1b. Contributions of the donor centers at the saturation plateau are denoted by dashed lines.

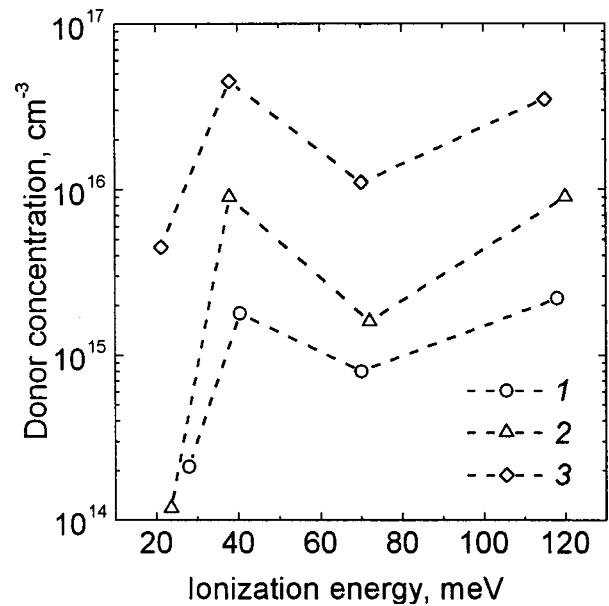

FIG. 2. Donor concentrations vs ionization energies for *Cz*-Si implanted with Er and annealed at $T_{ann}=700\,°C$. Implantation dose $\Phi(Er)$ $10^{11}\,cm^{-2}$: *1*—5; *2*—10; *3*—100. Implantation dose $\Phi(O)$, cm^{-2}: *1*, *2*—0; *3*—10^{14}. The dashed lines are shown to guide the eye only.

the oxygen-related shallow donors formed in *Cz*-Si (Ref. 5) and *Cz*-Si doped with Mg (Ref. 6) during heat treatment at $T\geqslant600\,°C-700\,°C$. In each case (Refs. 5 and 6) these small oxygen aggregates in *Cz*-Si are distributed over the ionization energy interval from ≈20 meV to ≈40 meV; the maximum of their distribution always is placed at about 40 meV. It has been found that a simplified model of two donor levels at $E_1\leqslant E_c-30\,meV$ and $E_2\approx E_c-40\,meV$ used in calculations of $n(T)$ curves can be a reasonable substitute for the real donor distribution. This is also the case for *Cz*-Si:Er. For all the samples studied by us the calculated $n(T)$ curves fit the experimental curves at $T\leqslant80\,K$ using a similar two-level model; see, for instance, Fig. 1. This leads us to conclude that the nature of the shallow donors in *Cz*-Si:Er is similar to the nature of oxygen-related shallow donors in *Cz*-Si, which originate from oxygen aggregation at high temperatures.[5,6] However, there are some distinctions in their behavior in the implanted layers, because the formation of oxygen-related donors takes place in the presence of implantation-induced native defects in sizable concentrations. These defects can serve as nucleation sites for oxygen atoms. In fact, the total concentration of shallow donors turned out to be dose-dependent (see Fig. 2). The involvement of native defects in oxygen aggregation appears to contribute to higher thermal stability of the shallow donors as well as to their larger production rate as compared to those formed under the ''pure'' heat-treatment conditions (cf. Ref. 5 and our study). The question of whether a fraction of the Er atoms, perhaps in complex form, may be included in the electrically active core of shallow donors at $E_c-(20-40)$ meV is still open.

The donor centers of the second kind are well characterized by a single ionization energy of 70±2 meV (Fig. 1). Their concentration was found to be dependent on the Er dose (see Fig. 2). Our claim that these donor centers are Er-related has been substantiated by the observation that the doping of the same material with Ho and Yb gives rise to the appearance of other donor centers at $\approx E_c-60\,meV$ and $\approx E_c-80\,meV$, respectively.[7] As in the case of *Cz*-Si:Er, the oxygen aggregation at $T=700\,°C$ also takes place in *Cz*-Si:Dy, Ho, and Yb and the formation of oxygen-related shallow donor states with ionization energies less than 50 meV is observed.[7]

Besides the two kinds of donors given above, additional donor centers at $E_c-(118\pm5)$ meV have been found in *Cz*-Si:Er (see Fig. 1). Based on the Fermi level position most reliable estimates of their concentration can be made for the samples implanted at $\Phi(Er)\leqslant10^{12}\,cm^{-2}$. At larger doses

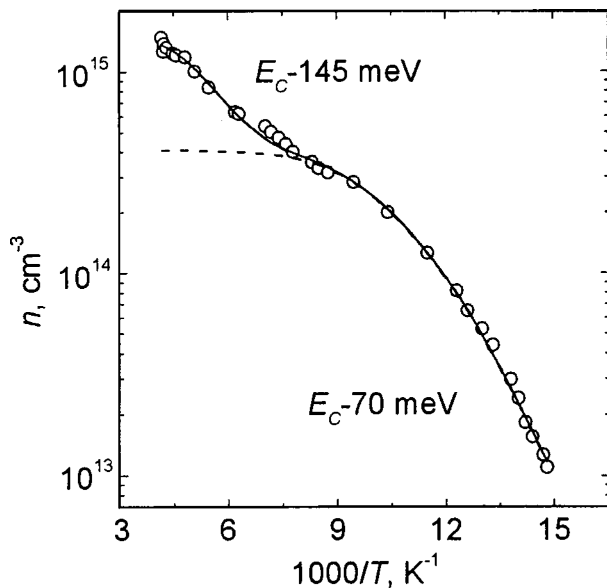

FIG. 3. Electron concentration vs reciprocal temperature for *Cz*-Si implanted with Er and annealed at $T_{ann}=900\,°C$. $\Phi(Er)=5\times10^{11}\,cm^{-2}$. The points represent experimental values; the curves denote calculated values. The contribution of donor centers at $E\approx E_c-70$ meV at the saturation plateau is shown by the dashed line.

such estimates are less accurate in energies and concentrations. Again, the position of similar donor states in *Cz*-Si:Ho and *Cz*-Si:Yb differs by $\Delta\geq15$ meV (Ref. 7) from that in *Cz*-Si:Er. Consequently, these donor centers appear to be impurity-related.

So far, DLTS measurements on *Cz*-Si:Er have provided some detailed information only for centers with activation energies greater than 0.15 eV (Ref. 3).

ANNEALING OF *Cz*-Si:Er AT *T*=900 °C

Some pronounced changes in the donor formation occur at elevated temperatures of the postimplantation annealing (see Figs. 3 and 4). First, although the formation of shallow donor states at $E_c-(20-40)$ meV has also been observed, they are formed in appreciable concentrations at heavier doses, $\Phi(Er)\geq10^{12}\,cm^{-2}$, as compared with *Cz*-Si:Er after the 700 °C anneal (cf. Figs. 1 and 3). Second, we could not detect the presence of donor states at $\approx E_c-120$ meV. Instead, new donor states at $E_c-(145\pm5)$ meV are developed in *Cz*-Si:Er annealed at $T=900\,°C$ (Fig. 3). As is seen from Figs. 2 and 5, the concentration of these new donor states is comparable to that of donors at $\approx E_c-120$ meV formed at $T=700\,°C$. This is a marked characteristic of the erbium impurity, because similar donor centers at E_c-105 meV in *Cz*-Si:Dy and *Cz*-Si:Ho were found to be stable at $T=700\,°C$ and $T=900\,°C$ (Ref. 7).

Unfortunately, some yet incomplete DLTS data on centers with activation energies less than ≈0.15 eV are available for Si:Er in Refs. 1–3. In Si:Er after implantation and annealing at $T=900\,°C$ the appearance of centers with an activation energy of about 0.15 eV has been observed by means of DLTS; see, for example, Refs. 1–3. In general, this activation energy estimated on the basis of data recorded under

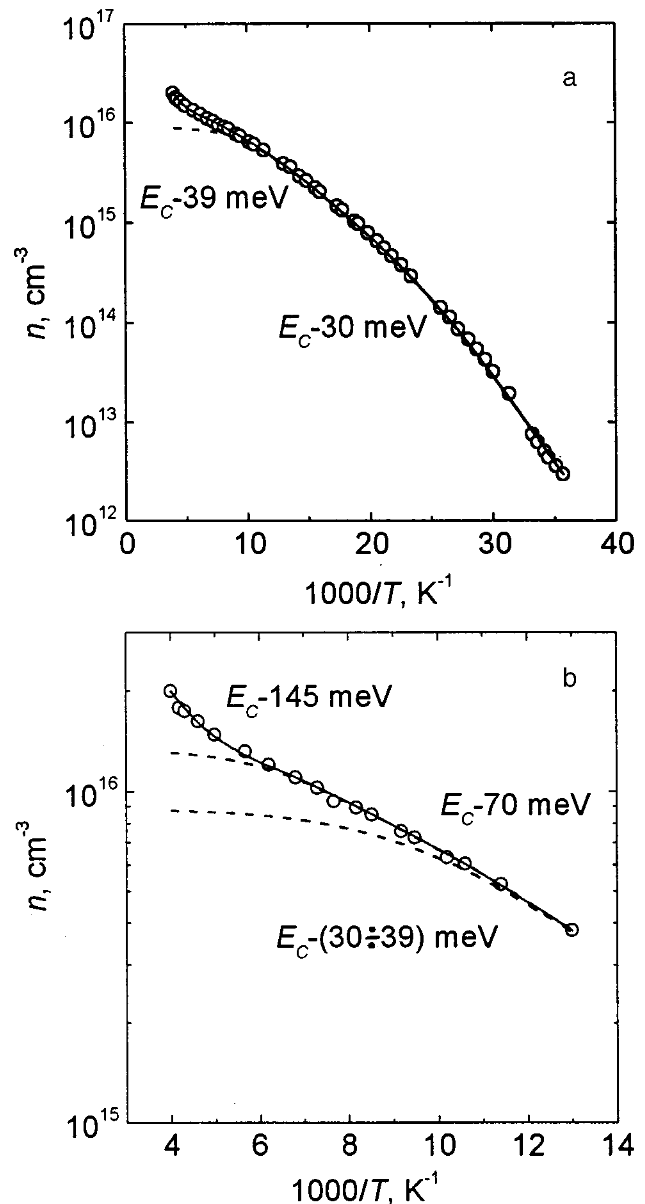

FIG. 4. Electron concentration vs reciprocal temperature for *Cz*-Si implanted with Er and annealed at $T_{ann}=900\,°C$. $\Phi(Er)=10^{12}\,cm^{-2}$. The points represent experimental values; the curves are calculated values. The $n(T)$ curve at $T\geq70$ K is shown on the expanded scale in Fig. 4b. Contributions of the donor centers at the saturation plateau are given by the dashed lines.

nonequilibrium conditions cannot be considered as the true ionization energy of these centers at equilibrium.[1] Therefore, it is still an open question whether one deals with the same centers while carrying out DLTS and Hall effect measurements. According to Refs. 2 and 3, the centers with an activation energy of 0.15 eV are formed in noticeable concentrations only in Si subjected to coimplantation with erbium and oxygen. Reportedly, in *Cz*-Si:Er without coimplantation of oxygen they are not formed at all[2] or are barely observable.[3] Under our experimental conditions, the formation of donor centers at $E_c-(145\pm5)$ meV was readily detectable in all cases, irrespective of whether coimplantation of oxygen in *Cz*-Si was used or not (see Fig. 5).

In a recent paper[8] the nonradiative decay of the excited

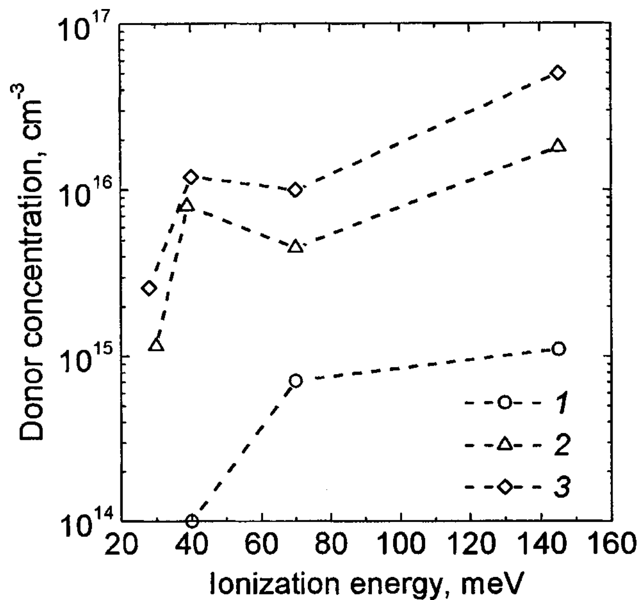

FIG. 5. Donor concentrations vs ionization energies for *Cz*-Si implanted with Er and annealed at $T_{\rm ann} = 900\,^\circ$C. Implantation dose Φ(Er), 10^{11} cm^{-2}: *1*—5; *2*—10; *3*—100. Implantation dose Φ(O), cm^{-2}: *1*, *2*—0; *3*—10^{14}. The sample implanted at $\Phi(\text{Er}) = 10^{13}$ cm^{-2} and $\Phi(O) = 10^{14}$ cm^{-2} was cut from another *Cz*-Si wafer with low oxygen concentrations (about 2×10^{17} cm^{-2}). The dashed lines are shown as an eye's guide only.

Er^{3+} ions in *Cz*-Si:P:Er at very low temperatures (at $T \leqslant 30$ K for the most part) is discussed in terms of the Auger impurity process with the energy transfer to free electrons (see also Ref. 9). In the temperature range of interest, free electrons are claimed to be released from shallow donor centers at $\approx E_c - 20$ meV (Ref. 8). However, these donor states were found to be present in a small fraction of the total concentration of shallow donors (see Fig. 5). Taking into account a more realistic donor distribution, one can estimate that in the *Cz*-Si:P:Er studied in Ref. 8 the free electron concentration at $T \leqslant 30$ K may be much less than the critical concentration, about 7×10^{14} cm^{-3}. Therefore, there is a need to put this possible channel of Er de-excitation under closer scrutiny.

In summary, three kinds of donor centers are formed in *Cz*-Si after implantation of erbium and subsequent annealing at $T = 700\,^\circ$C and $900\,^\circ$C. Shallow energy states at $E_c - (20 - 40)$ meV are attributable to oxygen-related donors. Donor centers at $\approx E_c - 70$ meV and $\approx E_c - 120$ meV appear to be Er-related. The latter ones are annealed out at $T = 900\,^\circ$C. Instead of them, new donor centers at $\approx E_c - 150$ meV are observed.

We wish to thank Dr. W. Zulehner (Wacker Siltronic, Burghausen, Germany) for providing us with silicon samples. The present work is supported in part by the CRDF (Grant 235) and the Russian Fund for Fundamental Research (Grant 99-02-17750).

[1] J. L. Benton, J. Michel, L. C. Kimerling, D. C. Jacobson, Y. H. Xie, D. J. Eaglesham, E. A. Fitzgerald, and J. M. Poate, J. Appl. Phys. **70**, 2667 (1991).

[2] S. Libertino, S. Coffa, G. Franzo, and F. Priolo, J. Appl. Phys. **78**, 3867 (1995).

[3] H. Przybylinska, W. Jantsch, Yu. Suprun-Belevitch, M. Stepikhova, L. Palmetshofer, G. Hendorfer, A. Kozanecki, R. J. Wilson, and B. J. Sealy, Phys. Rev. B **54**, 2532 (1996).

[4] J. Michel, L. J. Benton, R. F. Ferrante, D. C. Jacobson, D. J. Eaglesham, E. A. Fitzgerald, Y.-H. Xie, J. M. Poate, and L. C. Kimerling, J. Appl. Phys. **70**, 2672 (1991).

[5] V. V. Emtsev, G. A. Oganesyan, and K. Schmalz, *Solid State Phenomena,* ed. by H. Richter, M. Kittler, and C. Claeys (Scitech Publications, Ltd., Switzerland, 1996), V. **47–48**, p. 259.

[6] V. V. Emtsev, D. S. Poloskin, N. A. Sobolev, and E. I. Shek, Fiz. Tekh. Poluprovodn. **28**, 1084 (1994) [Semiconductors **28**, 624 (1994)].

[7] V. V. Emtsev, V. V. Emtsev Jr., D. S. Poloskin, N. A. Sobolev, E. I. Shek, J. Michel, and L. S. Kimerling, Fiz. Tekh. Poluprovodn. **33**, 649 (1999) [Semiconductors **33**, 603 (1999)].

[8] F. Priolo, G. Franzo, S. Coffa, and A. Carnera, Phys. Rev. B **57**, 4443 (1998).

[9] J. Palm, F. Gan, B. Zheng, J. Michel, and L. C. Kimerling, Phys. Rev. B **54**, 17 603 (1996).

This article was published in English in the original Russian journal. Reproduced here with stylistic changes by the Translation Editor.

SEMICONDUCTOR STRUCTURES, INTERFACES AND SURFACES

Electronic properties of a GaAs surface treated with hydrochloric acid

E. F. Venger, S. I. Kirillova, and V. E. Primachenko

Institute of Semiconductor Physics, National Academy of Sciences of Ukraine, 252650 Kiev, Ukraine
(Submitted June 15, 1998; accepted for publication February 18, 1999)
Fiz. Tekh. Poluprovodn. **33**, 1196–1200 (October 1999)

Processing in HCl is found to stabilize the system of surface electronic states of the (100) surface of *n*-GaAs in the temperature range 100–300 K. Distributions for the effective density of surface electronic states in the band gap of GaAs, which are obtained from the electric-field dependence of the surface photovoltage, depend on the measurement temperature. This is because the electronic states that affect the electric-field measurements are located both at the boundary between GaAs and the surface film and in the films themselves. Processing in HCl decreases the density of electronic states of both types, and also decreases the concentration of deep and shallow traps for nonequilibrium holes. These effects are even more pronounced when the processing in HCl is followed by washing in water. © *1999 American Institute of Physics.* [S1063-7826(99)01010-8]

The large density of surface electronic states on the real surface of GaAs, which prevents more widespread use of GaAs in semiconductor electronics, arises from disordering of the GaAs surface as it is oxidized in etching solutions and held in air.[1] A number of papers, notably Refs. 2–5, have shown that replacement of the oxide film on GaAs by a sulfide film leads to lowering of the density of surface electronic states and passivation of the GaAs surface with respect to oxidation. Removal of the oxide layer and passivation of the GaAs surface are also observed when GaAs is processed in a solution of HCl.[6,7] In this case, experiments conducted on the (111) surface of GaAs [Ref. 7] have shown that GaAs samples processed in HCl exhibit increased values of the photoluminescence intensity and small-signal photovoltage, which suggests that the density of surface electronic states that take part in recombination of electron-hole pairs has decreased.

In this paper we use the temperature and electric-field dependences of the surface photovoltage at high levels of electron-hole pair generation to investigate the electronic properties of the (100) surface of *n*-GaAs processed in HCl. We show that processing in HCl prevents the reconstruction of the system of surface electronic states present on a real surface with an oxide layer as the temperature is lowered in the range 100–300 K.[4,5] Moreover, processing in HCl, which removes the oxide film, followed by washing in water, which removes the film of gallium oxychloride,[6] decreases the concentration of surface electronic states at the boundary between GaAs and surface films, and also the concentration of electronic states in the films themselves. Processing in HCl, especially when followed by washing in water, also decreases the concentration of traps that capture nonequilibrium holes, which creates the photomemory of the surface potential.

EXPERIMENTAL METHOD

In this work we used samples of *n*-GaAs with electron concentrations of $1.2\times10^{17}\,\mathrm{cm}^{-3}$ and dimensions $1.5\times0.5\times0.05$ cm. Large facets of the samples were cleaved, polished, etched for 5 min in the mixture $4H_2SO_4:H_2O_2:H_2O$, and washed with distilled water. At first, we studied facets with a so-called real surface, covered with a layer of oxide roughly 20 Å thick, consisting of a mixture of As_2O_3 and Ga_2O_3.[6] Then we investigated the effect of processing the real surface in a solution of HCl (10%) for 5 min, and also processing with subsequent short-time (10 sec) washing in distilled water. Analysis of the results of synchrotron and *x*-ray photoelectron spectroscopy show[6,7] that when GaAs is processed with HCl, the film of intrinsic oxide is removed and gallium oxychloride $GaCl_xO_y$ forms at the surface. Subsequent washing with water, which removes the $GaCl_xO_y$ film, leaves a chloride coating at the surface and creates Ga–Cl bonds.

The surface potential φ_s of the GaAs surfaces under study was determined by measuring the surface (capacitor) photovoltage for a high level of electron-hole pair generation by light pulses.[4,5] The temperature and electric-field dependences of φ_s were studied as the temperature varied in the range 100–300 K.

In the majority of cases, surface potentials exhibit a photomemory effect even at room temperature.[4,5] In essence, this effect involves the following sequence of events. When an initial light pulse is used to measure the surface potential, it creates nonequilibrium holes, which are then captured at surface traps. This trapped charge then changes φ_s, and the change persists after the light pulse is gone. As a result, a second light pulse measures a changed value φ_{s2}, which differs from the value φ_{s1} measured by the first pulse. The difference $|\varphi_{s1}-\varphi_{s2}|$ defines the photomemory of the sur-

 © 1999 American Institute of Physics

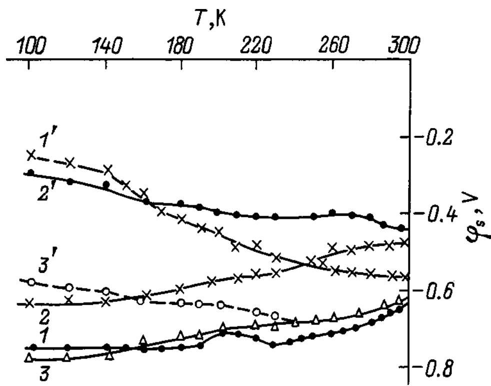

FIG. 1. Temperature dependences of the surface potential on (100) n-GaAs real surfaces (1, $1'$), HCl-processed surfaces (2, $2'$), and HCl-processed and water-washed surfaces 3, $3'$) 1–3—φ_{s1}, $1'$–$3'$—φ_{s2}.

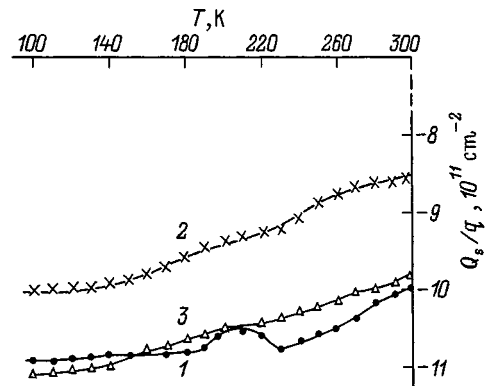

FIG. 2. Temperature dependences of the charge in the surface electronic states for real surfaces (1), HCl-processed surfaces, (2), and HCl-processed and water-washed surfaces (3).

face potential. Studies with a train of light pulses at a frequency of 1 Hz show that the trapped holes saturate the traps even after the first light pulse.

The value of φ_{s1}, which corresponds to the surface potential of a sample placed in the dark, can be obtained at a given temperature only after the traps have been emptied of their captured holes. To do this, it is necessary to wait for a certain time after the previous illumination of the sample, or heat the sample to a temperature at which the photomemory is not observed. At room temperature the time it takes the traps to capture holes is a few seconds; however, at lower temperatures it increases considerably (to hours). Therefore, in order to correctly obtain the temperature dependences of φ_{s1} and φ_{s2}, after each measurement of these quantities at a given temperature the sample must be heated to $T \geqslant 300$ K and then cooled in the dark to the next measurement temperature.

We measured the electric-field dependence of the surface potential φ_s at certain fixed temperatures in the range 290–160 K. In measuring φ_s, we first applied an external electric voltage V to the measurement capacitor, which varied in the range -400 to $+400$ V. In this case the measurements were made with the help of the second optical pulse of a train, in order to exclude the influence of photomemory effects when the first light pulse saturates the traps at the capacitor surface, and also to exclude nonequilibrium behavior of the electric voltages that deplete the GaAs of electrons.[8] The functions $\varphi_s(V)$ allow us to calculate the density of surface electronic states at fixed temperatures within the band gap near the position of the Fermi level at the surfaces under study.

EXPERIMENTAL RESULTS AND DISCUSSION

1. Figure 1 shows the temperature dependences of the surface potentials φ_{s1} (curves 1, 2, and 3) and φ_{s2} (curves $1'$, $2'$, and $3'$) for (100) n-GaAs surfaces that are real (curves 1 and $1'$), processed in HCl (curves 2 and $2'$), and both processed in HCl and washed with water (curves 3 and $3'$). The values of φ_{s1} and φ_{s2} are negative, which indicates depletion of the surface layers of electrons. The fact that the values of φ_{s2} are smaller in absolute value than the corresponding values of φ_{s1} is due to capture of holes at surface traps. While for the real and HCl-processed surfaces capture of holes occurs at room temperature, for the surfaces washed in water it begins to take place only at $T < 230$ K.

The function $\varphi_{s1}(T)$ for a real surface, as was observed previously for (100) and (111) surfaces in several other etching regimes,[4,5] is N-shaped. The N-shape disappears after processing in HCl and after processing in HCl followed by washing in water. An increase in $|\varphi_{s1}|$ observed as the temperature decreases for curves 1, 2, and 3, is caused by filling of surface electron traps with electrons as the Fermi level shifts into the conduction band. The decreasing segment of $|\varphi_{s1}|$ observed as the temperature decreases in the range 200–230 K for the real surface (curve 1) is connected with the decrease in the negative charge held in the surface electronic states, despite the shift of the Fermi level in the GaAs bulk into the conduction band. This can be explained only by assuming that as the temperature decreases, the system of surface electronic states itself reconstructs on the real surface. This reconstruction can be related to reversible structural changes at the GaAs-oxide film boundary. The reversibility and reproducibility of the function $\varphi_{s1}(T)$ are confirmed by control measurements. The N-shape of the function $\varphi_{s1}(T)$ observed at a real surface is due to competition between the mechanism that charges the surface electronic states with electrons and reconstruction of the system of surface electronic states as the temperature drops.

Each specific value of φ_{s1} corresponds to a charge Q_{sV} in the surface region, equal with opposite sign to the total charge Q_s in the surface electronic states.[4,5] Figure 2 shows the computed function $Q_s(T)$ (in units of an electron charge q) for the surfaces investigated. For a real surface, the function $Q_s(T)$, like the corresponding function $\varphi_{s1}(T)$, is N-shaped. The negative charge increases as the temperature decreases due to charging of the surface electronic states with electrons, while it decreases because of the reconstruction of the surface electronic state system, which disrupts the pinning of the Fermi level at the surface. Calculations show that for a real surface the position of the Fermi level varies in the range 0.06– 0.14 eV below the middle of the band gap E_i. Evidence for this reconstruction of the system of surface electronic states is the fact that as the temperature varies

from 230 to 200 K, the amount the Fermi level shifts into the conduction band in the GaAs bulk is 0.02 eV, while at the surface it is 0.06 eV.

The reconstruction of the system of surface electronic states and disruption of pinning of the Fermi level at a real surface can be understood by starting from the nature of the surface electronic states, which is connected with disorder. The disorder can have various origins. In particular, one reason for it could be variations in the lengths and angles of bonds between atoms in interphase cells.[9,10] This gives rise to mechanical stresses at the phase boundary as the temperature decreases, which change the degree of disorder and also lead to reconstruction of the system of surface electronic states and disruption of Fermi level pinning.

Another situation is realized for materials processed in HCl, and also those processed in HCl and washed with water. No reconstruction of the surface electronic states takes place, and the negative charge in the surface electronic states as the temperature decreases only increases due to charging of the surface electronic states with electrons (Fig. 2, curves *2* and *3*). The stability of these surfaces obviously is connected with the formation at the boundaries between GaAs and the surface films of strong Ga–Cl bonds.[6,7] The stability of the system of surface states leads to pinning of the Fermi level at the surfaces. Calculations show that in the temperature range 100–300 K the position of the Fermi level for a surface processed in HCl is pinned at an energy 0.07 ± 0.02 eV below E_i, while surfaces processed in HCl and washed with water pin the Fermi level at an energy 0.08 ± 0.01 eV below E_i.

2. The distribution of surface electronic state density in the band gap of GaAs at the surfaces under study was obtained at certain temperatures from electric-field dependences of the surface photovoltage. Calculations based on the $\varphi_s(V)$ functions obtained were analogous to those in Refs. 4 and 5. The dependences of the surface electronic state concentration on the energy of the band gap (relative to its center E_i) $N_s(E)$ at fixed temperatures 290, 260, 240, 210, 180, and 160 K for the surfaces investigated are shown in Fig. 3. Here especially we note the primary result of this paper —the dependence of the distribution of surface electronic state density on the temperature at which the measurement was made. All the functions $N_s(E)$ obtained were *V*-shaped, but their positions shifted along the E and N_s axes with changes in temperature. Analysis shows that minima of the function $N_s(E)$ are found at energies E that correspond to the position of the Fermi level at the surface at a given measurement temperature without an applied external voltage V. When a voltage V is applied to an accumulation layer of electrons in GaAs, we observe a steeper right-hand branch of the function $N_s(E)$, while when a depleting voltage V is applied the left-hand branch of $N_s(E)$ has the larger slope.

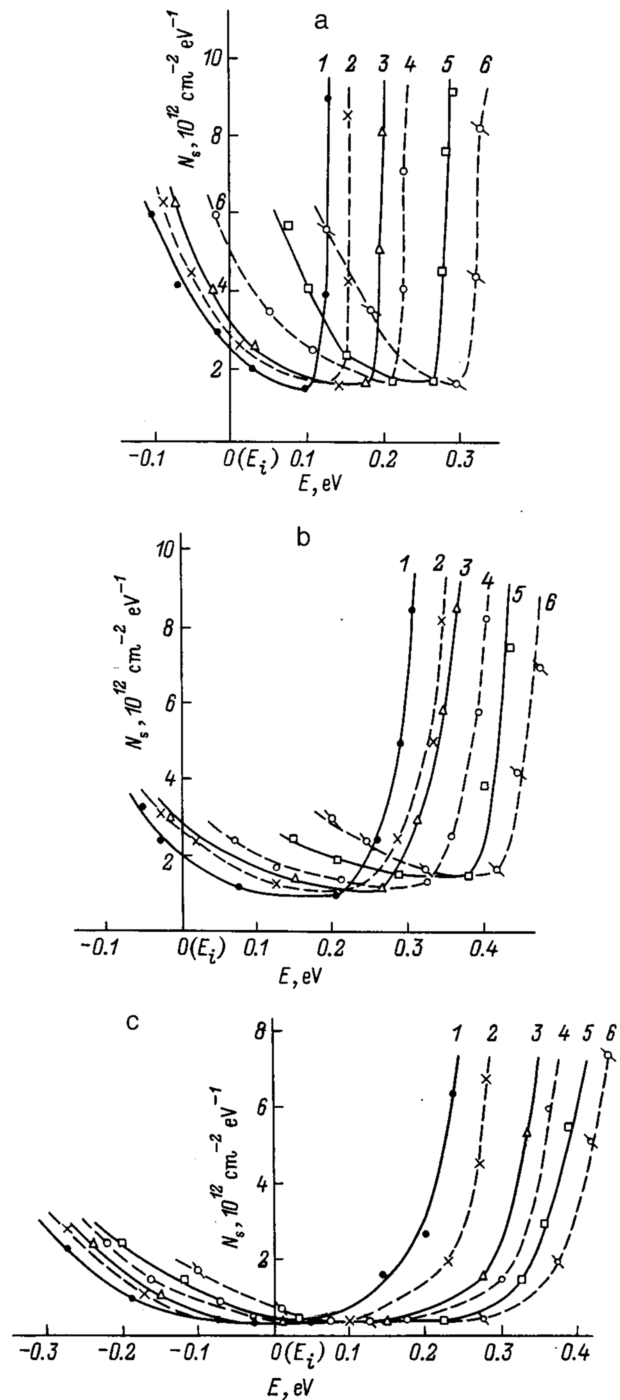

FIG. 3. Distribution of surface electronic state density with respect to energy E within the band gap of GaAs for a real surface (a), a surface processed in HCl (b), and a surface processed in HCl and washed in water (c) at temperatures, K: *1* — 290, *2* — 260, *3* — 240, *4* — 210, *5* — 180, and *6* — 160.

All the facts presented above give us reason to conclude that the density of surface electronic states measured with the help of an external electric field is an effective density. It includes in itself not only states at the boundary between GaAs and the surface film, but also electronic states of the film itself. The manifestation of this depends on the value of the electric field in the film which is capable of exchanging charge carriers between itself and the semiconductor due to the differing electric transport mechanisms.[11] When an accumulating voltage V is applied, the electric field in the film is larger, which ensures more intense electrical transfer of carriers and accounts for the fact that the right-hand branch of the function $N_s(E)$ is steeper than the left-hand branch, obtained for a depleting V.

At each measurement temperature, minimum values of

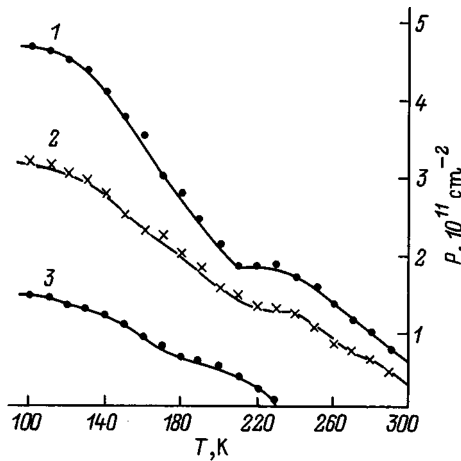

FIG. 4. Temperature dependences of the concentration of holes captured at traps for a real *n*-GaAs surface (*1*), one processed in HCl (*2*), and one processed in HCl and washed in water (*3*).

N_s were obtained at low depleting voltages. From this we may conclude that the density of surface electronic states at the GaAs-surface film boundary will not exceed these minimum values of N_s at fixed values of E. Such estimates of the densities of surface electronic states for a real surface show that at the boundary between GaAs and the oxide layer the density of surface electronic states in an energy range 0.1–0.3 eV above E_i is $1.5-1.7\times10^{12}\,\mathrm{cm}^{-2}\cdot\mathrm{eV}^{-1}$ (Fig. 3a). It is somewhat lower at the GaAs– $GaCl_xO_y$ film boundary: $1.0-1.6\times10^{12}\,\mathrm{cm}^{-2}\cdot\mathrm{eV}^{-1}$ in the range 0.1–0.4 eV above E_i (Fig. 3b). The lowest density of surface electronic states is at the GaAs-chloride layer boundary, equal to $4-5\times10^{11}\,\mathrm{cm}^{-2}\cdot\mathrm{eV}^{-1}$ in the range 0–0.3 eV above E_i (Fig. 3c).

Thus, replacing the oxide film with a film of $GaCl_xO_y$, especially one that is almost a monolayer chloride film, decreases the density of surface electronic states at the boundary of GaAs with the surface film. As we have already noted, this is associated with the lower degree of disorder at the boundary due to the formation of strong Ga–Cl bonds. Comparing Figs. 3a–3c also reveals that surfaces with $GaCl_xO_y$ films, and especially chloride films, also have lower concentrations of effective surface electronic states, because the dependences $N_s(E)$ at these surfaces are smoother than those of a real surface. This can be explained by lower disorder and the fact that the films that form after being processed with HCl, and especially after washing with water, are thinner than oxide films, in which there is a high density of electronic states that exchange carriers with the semiconductor via electrical transport mechanisms.[11]

3. Let us consider photomemory effects of the surface potential. Knowing the values φ_{s1} and φ_{s2} (Fig. 1), we can compute[4,5] the concentration of holes P captured by surface traps at a given temperature. Figure 4 shows temperature dependences $P(T)$ for real (curve *1*), HCl-processed (curve *2*), and HCl-processed and water-washed surfaces (curve *3*). It is clear that the number of captured holes increases with decreasing temperature. For cases where the traps are saturated with holes by the first light pulse, an increase in P with decreasing T indicates that the concentration of traps that capture holes increases as well. This is because the traps that participate in hole capture are located at various energies above the valence band, and as the temperature decreases, the captured holes begin to accumulate at traps that are closer and closer to the latter, due to the increasing time for reverse ejection of a hole into the band.

It is clear from Fig. 4 that all the functions $P(T)$ have a tendency to saturate near 100 K, while curves *1* and *2* have ''hollows'' in the region 220– 230 K. This gives us grounds to conclude that on real and HCl-processed surfaces there are two groups of traps: deeper traps located close to E_i, which determine the capture of holes at higher temperatures, and shallower traps located close to the valence band, which determine the capture of holes at lower temperatures. The concentrations of deep traps on a real surface with an oxide film equals $1.8\times10^{11}\,\mathrm{cm}^{-2}$, while on a HCl-processed surface with a film of $GaCl_xO_y$ it is $1.3\times10^{11}\,\mathrm{cm}^{-2}$. On a HCl processed surface washed with water with a chloride film, there are no deep traps (curve *3*). The concentrations of shallow traps on real, HCl-processed, and water-washed surfaces amount to 2.9×10^{11}, 1.9×10^{11}, and $1.4\times10^{11}\,\mathrm{cm}^{-2}$, respectively. Thus, as we go from a real to a chloridized surface upon removal of the oxide, the concentration of shallow traps decreases, while the deep traps disappear.

CONCLUSIONS

1. Processing the (100) surface of *n*-GaAs in a solution of HCl, and also subsequent washing in water, block the reconstruction of the system of surface electron traps observed at real surfaces as the temperature decreases in the range 100–300 K, leading to pinning of the Fermi level at the surface at 0.07 eV above E_i and 0.08 eV below E_i, respectively.

2. It was established that the distribution of the density of surface electronic states $N_s(E)$ in energy within the band gap of GaAs, which is *V*-shaped, depends strongly on the measurement temperature. We conclude from electric-field studies of the surface potential that an effective surface electronic state density is being determined. The smaller part of these electronic states are at the boundary between GaAs and the surface film, while the larger part is in the film itself.

3. Using the minimum values of N_s for the functions $N_s(E)$ obtained at various temperatures, we determined the energy distribution of the density of surface electronic states at the boundary between GaAs and the film surface. When the oxide layer of a real surface is replaced by a film of gallium oxychloride after processing in HCl, and also by a chloride film after additional washing in water, both the density of surface electronic states at the boundary and the effective density of surface electronic states as a whole decrease.

4. Processing the surface of GaAs in HCl decreases the concentration of deep and shallow traps for nonequilibrium holes that create photomemory of the surface potential. Processing in HCl with subsequent washing in water not only decreases the concentration of shallow traps but also completely eliminates the deep traps.

[1] V. I. Beliĭ and V. R. Belosludov, in *Current Problems in the Physical Chemistry of Semiconductor Surfaces* (Novosibirsk, 1988).
[2] C. J. Sandroff, R. N. Nottenburg, J. C. Bischoff, and R. Bhat, Appl. Phys. Lett. **51**, 33 (1987).
[3] V. N. Bessolov, M. V. Lebedev, and E. B. Novikov, Fiz. Tverd. Tela (St. Petersburg) **35**, 653 (1993) [Phys. Solid State **35**, 335 (1993)].
[4] E. F. Venger, S. I. Kirillova, V. E. Primachenko, and V. A. Chernobaĭ, Fiz. Tekh. Poluprovodn. **29**, 244 (1995) [Semiconductors **29**, 121 (1995)].
[5] E. F. Venger, S. I. Kirillova, V. E. Primachenko, and V. A. Chernobaĭ, Surfaces, Vol. 12, 59 (1996).
[6] Z. Song, S. Shogen, M. Kawasaki, and I. Suemune, Appl. Surf. Sci. **82/83**, 250 (1994).
[7] Z. H. Lu, F. Chatenoud, M. M. Dion, M. J. Graham, H. E. Ruda, I. Koutzarov, Q. Liu, C. E. Mitchell, J. G. Hill, and A. B. McLean, Appl. Phys. Lett. **67**, 670 (1995).
[8] V. E. Primachenko, O. V. Snitko, and V. V. Milenin, Phys. Status Solidi **11**, 711 (1965).
[9] Yu. A. Zarif'yants, V. F. Kiselev, S. N. Kozlov, and Yu. F. Novototskiĭ-Vlasov, Bull. Moscow State Univ., Ser. Phys., Vol. 1, 84 (1975).
[10] H. Hasegawa and H. Ohno, J. Vac. Sci. Technol. **4**, 1130 (1986).
[11] V. G. Litovchenko and A. P. Gorban', *Fundamentals of the Physics of Microelectronic MOS Structures* (Naukova Dumka, Kiev, 1978).

Translated by Frank J. Crowne

Photoconversion in heterocontacts of CdTe and its analogs with protein

Yu. V. Rud'

A. F. Ioffe Physicotechnical Institute, Russian Academy of Sciences, 194021 St. Petersburg, Russia

V. Yu. Rud'

St. Petersburg State Technical University, 195251 St. Petersburg, Russia

I. V. Bodnar' and V. V. Shatalova

Belarus State University of Information Science and Radio Engineering, 220027 Minsk, Belarus

G. A. Il'chuk

State University ''L'vov Politechnika,'' 293000 L'vov, Ukraine

(Submitted December 21, 1998; accepted for publication February 18, 1999)
Fiz. Tekh. Poluprovodn. **33**, 1201–1204 (October 1999)

Semiconductor/natural-protein photosensitive structures based on CdTe crystals and its ternary analogs have been created. The photoelectric properties of these structures in natural and linearly polarized light are examined. The wideband character of the photosensitivity of these semiconductor/protein structures is established in the range between the width of the semiconductor band gap and the energy ≈ 3.5 eV, where the latter is assumed to be the pseudogap in the band spectrum of the protein. It is shown that the natural photopleochroism of the semiconductor is reproduced in its contact with the protein. Potential applications of a new class of photosensors are discussed. © *1999 American Institute of Physics.* [S1063-7826(99)01110-2]

1. INTRODUCTION

The properties of various classes of heterocontacts (HC) are now being studied extensively, opening up entirely new and, in the initial stages of study, unexpected possibilities of these unique objects.[1] However, along with solid-state structures of the kind semiconductor/semiconductor and semiconductor/metal, an increasing amount of attention is being given to semiconductor contacts with electrolytes and substances of biological origin.[2–4] In this paper we report the results of the creation of a new class of converters consisting of contacts of cadmium telluride and its ternary analogs with natural protein.

As the semiconductor materials for creation of the heterocontacts we used crystals of CdTe and its ternary analogs from the group I–III–VI_2, which can be formally represented as the result of substitution of two atoms from the second group by atoms from the first and third groups of the periodic table (see Table I).

TABLE I. Photoelectric properties of the contacts of CdTe and its ternary analogs I–III–VI_2 with protein ($T = 300$ K).

Compound	Type of conductivity	$1/R \cdot e$, cm^{-3}	$\hbar\omega_1$, eV	S, eV^{-1}	S_u, V/W	S_i, mA/W	$\delta_{1/2}$, eV
CdTe	n	10^{16}	1.51	38	10^3	45	1.82
		10^8	1.48	90	10^4	⋯	
$CuInSe_2$	p	3×10^{17}	1.02	50	570	18	2.00
$CuInS_2$	p	2×10^{16}	1.53	60	1×10^4	7	2.02
$CuGaS_2$	p	10^7	2.48	40	3×10^3	⋯	1.84

2. EXPERIMENTAL PART

CdTe crystals were grown by two methods. One was zonal recrystallization of a melt with composition similar in stoichiometry to CdTe in the controlled vapor phase. This method made it possible to obtain electrically uniform crystals with n-type conductivity in which the Hall mobility grew as the temperature was lowered below 300 K, which is characteristic of lattice scattering. Wafers were obtained from slabs of these newly grown crystals by cleavage and therefore had specular (001) planes, which did not require further processing. The second type of sample was grown by the gas-phase method, which led to doping of the resulting CdTe crystals with iodine. The crystals obtained in this way were semi-insulating and also did not require further processing.

Crystals of the ternary compounds I–III–VI_2 were grown from melt ($CuInSe_2$, $CuInS_2$, and $AgInS_2$) or from the gas phase ($CuInS_2$ and $CuGaS_2$). The surfaces of the latter did not require processing and had orientation (112), whereas the samples obtained from melt, after being cut, were mechanically processed and then chemically polished.

As a result of a multipart study, we developed the following technique for creating a new class of photoconverters. On a glass substrate with a semitransparent metal layer (Mo, Ni, $d \cong 0.5\ \mu$,) we placed a drop of natural protein. The semiconductor wafer was placed into contact with the surface of the protein in such a way that the liquid protein was ''compressed'' between the metallized surface of the glass and the semiconductor wafer, filling the gap between them.

After completing the procedure of putting the semiconductor in contact with the substrate through the layer of pro-

 © 1999 American Institute of Physics

tein, the position of the wafer was fixed relative to the glass with the help of a dielectric lacquer. The system semiconductor/protein/metal (Fig. 1) was outfitted with electrical contacts making it possible to study photoelectric phenomena in two different geometries of illumination.

3. DISCUSSION OF THE RESULTS

The steady-state current–voltage characteristic of one of the structures is shown in Fig. 2. For all of the investigated heterocontacts in which we used crystals of *n*- and *p*-type conductivity for thicknesses of the protein layer $\cong 10 - 50\,\mu$m the current–voltage characteristics manifest a distinct rectification effect, which for different semiconductors varied in the limit 1.8–4.5 for voltages up to 5 V. The reverse characteristic, as a rule, obeys a power law with exponent close to one. The residual resistance of the structures depends strongly on the properties of the semiconductors and varies in the limits 10^3-$10^{10}\,\Omega$ at 300 K. In the course of our studies the characteristics of the structures were essentially constant and showed good reproducibility.

When heterocontacts with different semiconductors (see Table I) were illuminated, a photovoltaic effect was reproducibly observed; its sign remained unchanged for both geometries of illumination, for different positions of the light probe on the surface of the structures (diameter $\cong 0.2$ mm), and variation of the energy of the incident radiation over the entire range of photosensitivity of each of the investigated heteropairs. It is important to emphasize that the photosensitivity always predominates when the heterocontacts are illuminated from the protein-layer side. The table shows the maximum values of the voltage S_u and current S_i photosensitivity. Comparison of these data with the data known for other classes of photoconverters on crystals of similar quality[2,5–7] gives reason to believe that the new heterocontacts while still in the first stage of their development are at least as good as photoconverters presently available.

Typical curves of the spectral dependence of the relative quantum efficiency of photoconversion η for the obtained heterocontacts are shown in Fig. 3. It can be seen from the figure that the photosensitivity of the heterocontacts based on CdTe and its ternary analogs with illumination from the protein side has a wideband character, revealing a maximum value of η in the interval between the width of the band gap of the semiconductor E_G (Ref. 8) and the short-wavelength falloff of the photosensitivity near 3.5 eV. This is the "window effect," typical for ideal solid-state heterojunctions,[9] which in the given case does not require a careful choice of the semiconductor with definite lattice parameters, type of structure, etc. The appearance in all the heterocontacts of a short-wavelength boundary near 3.5 eV allows us to take this energy as the pseudogap in the energy spectrum of the protein. The long-wavelength boundary of photosensitivity of the investigated heterocontacts is movable and depends on the value of E_G in the semiconductor used in the heterocontact. The long-wavelength edge of η is exponential and its

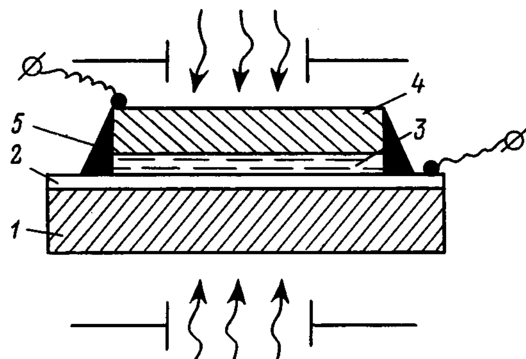

FIG. 1. Design and illumination scheme of a semiconductor/protein heterocontact (*1* — glass plate, *2* — semitransparent metal layer, *3* — layer of natural protein, *4* — semiconductor, *5* — insulating lacquer).

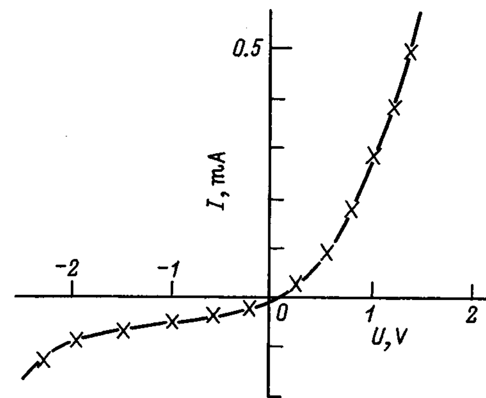

FIG. 2. Steady-state current–voltage characteristic of an *n*-CdTe/protein heterocontact at $T = 300$ K. (The transmitting direction corresponds to positive polarity of the external bias on the protein.)

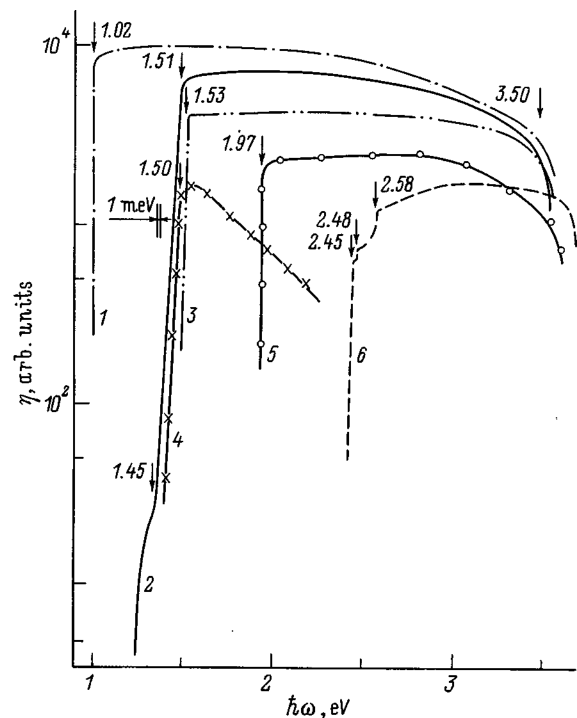

FIG. 3. Spectral dependence of the relative quantum efficiency of photoconversion of semiconductor/protein heterocontacts in natural light at $T = 300$ K. (*1* — $CuInSe_2$, *2* — CdTe, *3, 4* — $CuInS_2$, *5* — $AgInS_2$, *6* — $CuGaS_2$. Illumination from the protein side).

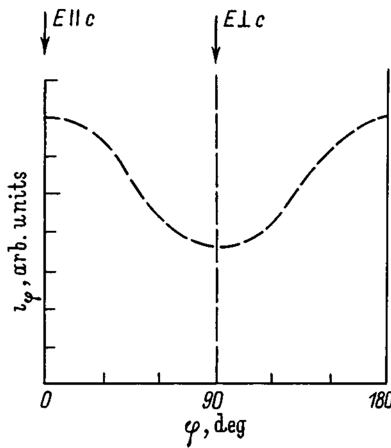

FIG. 4. Polarization indicatrix of the short-circuit photocurrent i_φ of a $CuGaS_2$/protein heterocontact at $T=300$ K. (Illumination along the normal to the (112) plane of $CuGaS_2$, $\hbar\omega=2.48$ eV).

logarithmic slope $S=\delta(\ln\hbar\omega)/\delta(\hbar\omega)$ is high, which corresponds to direct interband transitions in these semiconductors. The exponential growth of η comes to an end at $\hbar\omega_1$, which is close to the band gap E_g of the semiconductor.[8] Note that the energy $\hbar\omega_1$ also depends on the doping of the semiconductor. In the case of CdTe crystals, where growth from the gas phase is accompanied by the incorporation of an iodine impurity, for example, $\hbar\omega_1$ is shifted to 1.47–1.49 eV due to the participation in the photoconductivity of shallow-center levels. In the case of heterocontacts based on $CuGaS_2$ with orientation of the contacting plane (112), several steps show up in the long-wavelength edge of η upon illumination by natural light, which are due to splitting of the levels in the tetragonal field.[6] In the case of heterocontacts based on $CuInS_2$ (Fig. 3), we also see a pronounced short-wavelength falloff of η (curve *3*), which is characteristic of surface recombination of charge carriers. This falloff shows up in heterocontacts which are obtained using mechanically processed semiconductor surfaces, whereas when using the post-growth natural plane (112), the short-wavelength falloff disappears (Fig. 3, curve *4*). This feature was also confirmed when using heterocontacts made from CdTe and $CuInSe_2$.

As a result of changes in E_G and the state of the semiconductor surface, the FWHM (full-width at half-maximum) of the η spectra, $\delta_{1/2}$, changes. As follows from the table, the largest values of $\delta_{1/2}$ are obtained for heterocontacts made from $CuInSe_2$ and $CuInS_2$.

If the heterocontact is now illuminated on the semiconductor side, the η spectra become narrowly selective with a maximum near E_G, which is a natural consequence of the influence of strong absorption of radiation in direct-band crystals for $\hbar\omega \geqslant E_G$.

For the new class of heterocontacts based on oriented anisotropic semiconductors, one can also expect the appearance of natural photopleochroism,[10] which was obtained for the $CuGaS_2$/protein structures.

As can be seen from Fig. 4, when these structures are illuminated with linearly polarized light (LPL) along the normal to the (112) plane, the polarization indicatrix of the short-circuit photocurrent i_φ exhibits a periodic dependence,

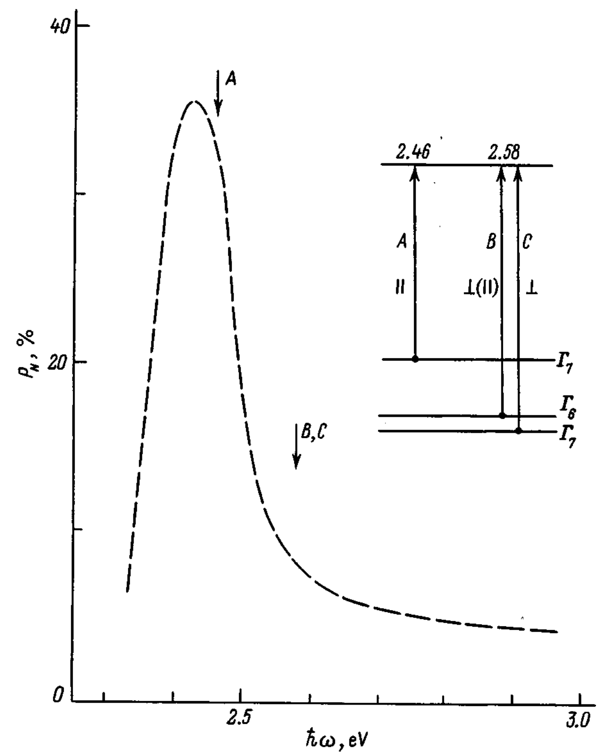

FIG. 5. Spectral dependence of the natural photopleochroism coefficient P_N of a $CuGaS_2$/protein heterostructure at $T=300$ K. The inset shows band structure and selection rules for interband transitions at the center of the Brillouin zone.

characteristic of uniaxial semiconductors, on the azimuthal angle φ between the electric field vector of the light wave **E** and the tetragonal axis **c** of the crystal

$$i_\varphi = i^{\parallel}\cos^2\varphi + i^{\perp}\sin^2\varphi, \tag{1}$$

where $i^{\parallel}$ is measured in the polarization $\mathbf{E}\parallel\mathbf{c}$, and $i^{\perp}$ is measured in the polarization $\mathbf{E}\perp\mathbf{c}$. Since the (112) plane is not coplanar with **c**, the polarization $\mathbf{E}\parallel\mathbf{c}$ in these experiments is realized only nominally. Therefore, the experimentally obtained ratio $i^{\parallel}/i^{\perp}\approx 2$ is actually even larger.

The main conclusion that should be drawn from the polarization indicatrices i_φ is that as in the case of solid-state structures,[6] the maximum photocurrent corresponds to the polarization $\mathbf{E}\parallel\mathbf{c}$ and, consequently, penetration of the linearly polarized light into the active region of the heterocontact takes place without distortions of the parameters of the incident light.

The spectral contour of the natural photopleochroism P_N of the heterocontact $CuGS_2$/protein (Fig. 5) is also similar to that established for In/$CuGaS_2$ Schottky barriers.[6] According to the selection rules for interband *A* transitions, the natural photopleochroism in $CuGaS_2$/protein structures exhibits a positive sign and reaches a maximum near the energy of the *A* transition. Transition to the short-wavelength range initiates principally the optical *B* and *C* transitions, allowed in the $\mathbf{E}\perp\mathbf{c}$ polarization, from the detached valence subbands of the valence band, which governs the decay of P_N (Fig. 5).

It follows from Fig. 5 that the maximum of P_N is shifted somewhat toward longer wavelengths relative to the energy of the *A* transitions. Taking the results of Ref. 11 into ac-

count, this fact points to the presence in the investigated $CuGaS_2$ crystals of shallow centers which give rise to an anisotropy of the photoconductivity comparable with the interband *A* transitions. The positive sign of P_N for $\hbar\omega < E_G$ suggests that the levels responsible for this absorption are formed from wave functions of the nearest free bands.

4. CONCLUSION

To summary, heterocontacts of binary II–VI semiconductors (in the case of CdTe) and their ternary analogs of the type $I-III-VI_2$ with natural protein possess a photovoltaic effect and can be used as wideband photosensors of optical light. They also make it possible to observe variations in the optical properties of proteins. A systematic feature is strikingly manifested in this new class of photoconverters which was established in the investigated crystals of various other groups. This feature can be described as follows: an increased level of complexity of the atomic composition in combination with diamond-like phases is the source of new functional dependences which lead to the creation of new devices. In the context of the above remarks, our study shows that the transition from the binary phase (CdTe) to ternary compounds endows such heterocontacts with a new functional capability, consisting in the appearance of polarization photosensitivity.

[1] Zh. I. Alferov, Fiz. Tekh. Poluprovodn. **32**, 3 (1998) [Semiconductors **32**, 2 (1998)].

[2] Yu. A. Gurevich and Yu. V. Peskov, in *Photo-electrochemistry of Semiconductors* [in Russian], Nauka, Moscow, 1983.

[3] J. Simon and J.-J. Andre, *Molecular Semiconductors: Photoelectric Properties and Solar Cells* (Springer-Verlag, Berlin, 1985).

[4] V. Yu. Rud', Yu. V. Rud', V. Ch. Shpunt, and S. Iida, Inst. Phys. Conf. Ser. No. 152 [ICTVC-11, Salford, 1997] (IOP Publishing, Ltd., 1998), p. 997.

[5] N. N. Konstantinova, V. D. Prochukhan, Yu. V. Rud', and M. A. Tairov, Fiz. Tekh. Poluprovodn. **22**(6), 1699 (1988) [Sov. Phys. Semicond. **22**, 1072 (1988)].

[6] I. V. Bodnar', V. Yu. Rud', and Yu. V. Rud', Fiz. Tekh. Poluprovodn. **28**(10), 2007 (1994) [Semiconductors **28**, 1106 (1994)].

[7] V. Yu. Rud', Yu. V. Rud', and V. Kh. Shpunt, Fiz. Tekh. Poluprovodn. **31**(1), 97 (1997) [Semiconductors **31**, 85 (1997)].

[8] *Handbook of Physical-Chemical Properties of Semiconductors* [in Russian], Nauka, Moscow, 1979.

[9] B. L. Sharma and R. K. Purohit, *Semiconductor Heterojunctions* (Pergamon Press, Oxford, 1974).

[10] F. M. Kesamanly, V. Yu. Rud', and Yu. V. Rud', Fiz. Tekh. Poluprovodn., **33**(5), 513 (1999) [Semiconductors **33**, 483 (1999)].

[11] Yu. V. Rud', Izv. vuzov SSSR: Fizika, **29**(1), 68 (1986).

Translated by Paul F. Schippnick

Fabrication and photosensitivity of $AgInSe_2$/III–VI isotypic heterojunctions

V. Yu. Rud'

St. Petersburg State Technical University, 195251 St. Petersburg, Russia

V. F. Gremenok

Institute of Solid State Physics and Semiconductors, National Academy of Sciences of Belarus, 220072 Minsk, Belarus

Yu. V. Rud' and R. N. Bekimbetov

A. F. Ioffe Physicotechnical Institute, Russian Academy of Sciences, 194021 St. Petersburg, Russia

I. V. Bodnar'

Belarus State University of Information Science and Radio Engineering, 220027 Minsk, Belarus

(Submitted February 2, 1999; accepted for publication February 18, 1999)
Fiz. Tekh. Poluprovodn. **33**, 1205–1208 (October 1999)

$AgInSe_2$ thin films on glass substrates have been prepared by pulsed laser deposition. Rectifying heterojunctions with a pronounced photovoltaic effect have been fabricated for the first time by placing such films in optical contact with layered III–VI (InSe, GaSe) semiconductors. The maximum photosensitivity of such heterostructures is $10-10^3$ V/W. It is concluded that the prepared structures can be used as wideband selective photoreceivers. © *1999 American Institute of Physics.* [S1063-7826(99)01210-7]

INTRODUCTION

Ternary semiconductor compounds of the class I–III–VI_2 and their solid solutions form a wide class of materials which have attracted attention for the purpose of creating high-efficiency photoconverters of solar energy.[1–5] They possess a high optical absorption coefficient (10^4-10^5 cm^{-1}) in the limits of the solar spectrum and higher radiation hardness in comparison with photoconverters based on silicon and gallium arsenide.[2,3] Thin-film solar cells based on the solid solutions $Cu(In,Ga)Se_2$ have already made it possible to attain efficiencies about 18% on areas of 1 cm^2 (Refs. 1 and 2). For a commercial unit consisting of 15 cells on glass substrates with dimensions $10\times10\,cm^2$, an efficiency of 13.9% has been obtained.[3] Further optimization of the parameters of such photoconverters lies along the path of detailed physicotechnological studies of the relationship between production processes and the properties of specific types of structures, and of developing numerous systems based on the wide class of ternary semiconductors I–III–VI_2.

in this paper we report the results of initial experimental studies of the photoelectric properties of isotypic heterojunctions fabricated by placing the natural cleavage faces of the layered semiconductors InSe and GaSe in optical contact with the outer post-growth surface of thin polycrystalline $AgInSe_2$ films prepared by pulsed laser evaporation.

PREPARATION OF $AgInSe_2$ FILMS

As the targets for film deposition, we used $AgInSe_2$ slabs grown by the Bridgman–Stockbarger method. In the synthesis we used ingredients with semiconductor degree of purity. The as-grown crystals were large (diameter 12 mm and length 30 mm) and homogeneous blocks, as was determined by x-ray measurements.

Films were sputtered in a vacuum of about 10^{-5} Torr with the help of a laser operating in the free lasing regime ($\lambda=1.06\,\mu m$, $t_p=10^{-3}$ s, $E_p=150-180$ J).[6] As the substrates we used chemically cleaned glass plates, whose temperature was held at $450-480\,^{\circ}C$. The thickness of the obtained layers was $0.6-0.8\,\mu m$.

The composition of the $AgInSe_2$ films was determined by microprobe x-ray spectroscopic analysis. According to the data obtained, the atomic composition corresponds to the stoichiometric formula of the compound $AgInSe_2$ and showed good uniformity over the area of the entire film (in the error limits of the method, $\pm5\%$). The films exhibited high adhesion and possessed a mirror-smooth surface. X-ray studies showed that in the diffraction patterns of ground-up crystals and of films obtained from them by evaporation in vacuum only a system of lines corresponding to chalcopyrite structure shows up. As a rule, the films had *n*-type conductivity with free-carrier concentration $\sim1.6\times10^{17}\,cm^{-3}$ and Hall mobility $\sim95\,cm^2/(V\cdot s)$ at 300 K.

EXPERIMENTAL RESULTS

Initial studies of contact phenomena showed that sputtering of layers of metals (In, Cu, Au, etc.) onto the surface of $AgInSe_2$ films does not produce rectification or a photovoltaic effect. Therefore, to obtain photosensitive structures, we examined the possibilities of placing the natural cleavage faces of layered III–VI semiconductors in optical contact with post-growth outer surfaces of sufficiently high quality

 © 1999 American Institute of Physics

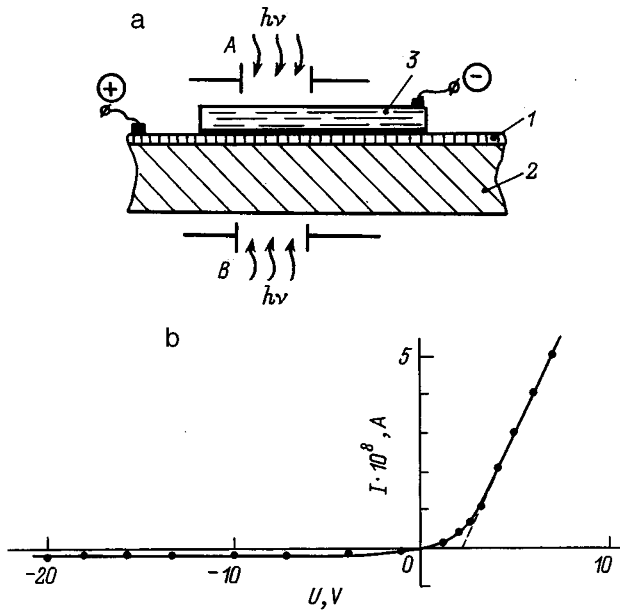

FIG. 1. a — Design of n-AgInSe$_2$/n-(In,Se, GaSe) heterojunctions and their illumination schemes (*1* — n-AgInSe$_2$ film, *2* — glass substrate, *3* — InSe or GaSe wafer); b — steady-state current–voltage characteristics of an n-AgInSe$_2$/n-GaSe heterojunction at $T=300$ K (transmitting direction corresponds to positive polarity of the external bias on the n-AgInSe$_2$ film).

of thin polycrystalline AgInSe$_2$ films prepared by pulsed laser evaporation.[7–10] Single-crystal bars of InSe and GaSe were prepared by directed crystallization of a nearly stoichiometric melt of these compounds. The InSe crystals had a free-electron concentration $n \approx 10^{14}\,\mathrm{cm}^{-3}$ and resistivity $\rho \approx 10^3\,\Omega\cdot\mathrm{cm}$ and the GaSe crystals had the corresponding values $n \approx 10^{13}\,\mathrm{cm}^{-3}$ and $\rho \approx 10^6\,\Omega\cdot\mathrm{cm}$ at $T=300$ K.

When structures are created by cleavage in air from single-crystal bars, plane-parallel wafers with high-quality mirror-smooth surfaces are obtained with area $5\times 5\,\mathrm{mm}^2$ and thickness $0.2-0.05$ mm.

The design of heterocontacts of single-crystal wafers of III–VI compounds with the outer surface of the thin polycrystalline AgInSe$_2$ films and the illumination geometries A and B used in the photosensitivity measurements are shown in Fig. 1a, and the heterojunction parameters are listed in Table I. The main results of the experiments are the following.

Isotypic heterocontacts of n-AgInSe$_2$ films with III–VI crystals of n-type conductivity reproducibly exhibit distinct rectification. The transmitting direction of these structures corresponds to the positive polarity of the external bias on the AgInSe$_2$ film. An example of a stationary current–voltage characteristic of one of these heterojunctions is shown in Fig. 1b. In the forward bias region $U > 2$ V the current–voltage characteristics obey the law

$$U = U_0 + R_0 \cdot I. \tag{1}$$

The residual resistance R_0 of the InSe-based heterojunctions is usually $\approx 10^5\,\Omega$, whereas in the case of GaSe it grows to $10^6 - 10^8\,\Omega$ at 300 K. Taking into account the electrical properties of AgInSe$_2$ films it may be assumed that the main contribution to R_0 is governed by the properties of the III–VI wafers. The cutoff voltages U_0 in the InSe structures are usually found in the limits $0.7-1.0$ V, while for the GaSe structures they increase to $1.5-1.8$ V.

The n-AgInSe$_2$/n-III–VI heterojunctions prepared by the optical contact method reveal a photovoltaic effect. The sign of the photovoltage does not depend on either the energy of the incident photons or on where the light probe (spot diameter ≈ 0.2 mm) is incident on the surface of the structures with illumination geometries A and B (Fig. 1a). Here the AgInSe$_2$ films are always charged positively, which corresponds to the rectifying direction of the structures. Typical spectral curves of the relative quantum efficiency of photoconversion η, obtained as the ratio of the photocurrent to the number of incident photons for n-AgInSe$_2$/n-InSe and n-AgInSe$_2$/n-GaSe heterojunctions in both illumination geometries are shown in Fig. 2. The maximum of η for InSe- and GaSe-based heterojunctions is observed in the region of fundamental absorption of these semiconductors,[7,8,10] which may be due to the existing relations between the electrical parameters of the contacting phases, as a result of which the active region in the heterojunctions is localized mainly in their high-resistance component—the n-III–VI compound. The long-wavelength photosensitivity edge of the heterojunctions illuminated by unpolarized light in the geometries A and B is exponential and has a steep slope (on a semilog scale) $S = \delta(\ln\eta)/\delta(\hbar\omega)$ (see Table I), which is characteristic of direct interband transitions in III–VI crystals. The narrowing of the spectral band η for illumination in the A geometry is noteworthy. It follows from the table that the FWHM (full-width at half-maximum) $\delta_{1/2}$ of the η spectra is an order of magnitude less than in the B illumination geometry. This fact has its origin in peculiarities of absorption in the AgInSe$_2$ films and the III–VI compounds. The large thickness of the InSe ($\approx 100\,\mu$m) and GaSe wafers ($\approx 50\,\mu$m) in comparison with the thickness of the AgInSe$_2$ film ($0.8\,\mu$m) is the main factor behind the increase in the short-wavelength falloff of η in comparison with the B illumination geometry.

As can be seen from the table, the maximum voltage photosensitivity S_u in the prepared heterojunctions is observed when they are illuminated from the III–VI wafer side. In this case, a narrow peak is reproducibly present in the η spectra in the region of the fundamental absorption edge, which is characteristic of the photoconductivity of layered III–VI semiconductors and is usually attributed to exciton effects.[7,11] The presence of this feature in the photosensitivity spectra of the prepared heterojunctions may be evidence

TABLE I. Photoelectric properties of n-AgInSe$_2$/n-InSe(GaSe) isotypic heterojunctions at $T=300$ K.

Type of heterojunction	Illumination from the III–VI side				Illumination from the n-AgInSe$_2$ side			
	$h\nu$, eV	$\delta_{1/2}$, meV	S, eV^{-1}	S_u, V/W	$h\nu$, eV	$\delta_{1/2}$, meV	S, eV^{-1}	S_u, V/W
n-AgInSe$_2$/ n-InSe	1.21	40	70	15	1.21	700	70	10
n-AgInSe$_2$/ n-GaSe	1.97	60	29	7×10^3	2.05	460	29	120

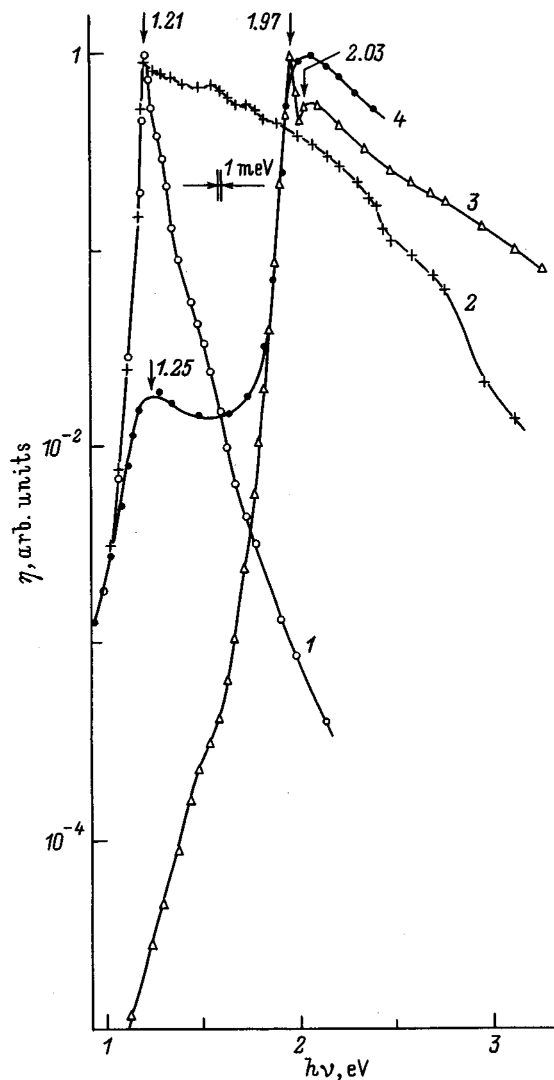

FIG. 2. Spectral dependence of the relative quantum efficiency of photoconversion of n-AgInSe$_2$/n-InSe (*1, 2*) and n-AgInSe$_2$/n-GaSe (*3, 4*) heterojunctions. *1, 3* — illumination from the side of the III–VI wafer; *2, 4* — from the n-AgInSe$_2$ side.

of the preservation of the high quality of the III–VI crystals even after formation of their contact with AgInSe$_2$.

The coincidence of the energy position of the photosensitivity maximum $\hbar\omega$ in the case of n-AgInSe$_2$/n-InSe heterojunctions in two different illumination geometries (Fig. 2, curves *1* and *2*) reflects the similarity of the widths of the band gaps (E_g) of the contacting semiconductors AgInSe$_2$ and InSe, which agrees with the data of studies of the optical absorption of these materials.[11] This explanation finds reflection in the transformation of the spectral contour η upon transition to the heterostructure n-AgInSe$_2$/n-GaSe (Fig. 2, curves *3* and *4*). For illumination in the *B* geometry the influence of absorption by the n-AgInSe$_2$ film increases and a maximum in η arises near the band gap energy of the ternary compound.

When the area of the InSe and GaSe wafers is decreased to 1×1 mm^2, the possibility arises of probing the photoelectric quality of the AgInSe$_2$ layers as a result of shifting the heterocontact along the film surface, whose area in our experiments was $\approx 20\times40$ mm^2 and in the developed technique of laser deposition is fundamentally unlimited. Experiments in which the optical contact of the same III–VI wafer was placed in optical contact with different segments of the AgInSe$_2$ film confirm the high reproducibility of the photoelectric parameters listed in the table, which testifies to the high local uniformity of photosensitivity of the laser-evaporation prepared AgInSe$_2$ films. Also note that the parameters of the prepared heterojunctions do not reveal any degradation.

When the heterojunctions are illuminated with linearly polarized light along the normal to the photoreceiver surface in the *A* and *B* geometries, photopleochroism is not observed. This is because, on the one hand, light enters the III–VI medium along its isotropic direction and, on the other, because of the polycrystalline nature of the AgInSe$_2$ thin films.

CONCLUSIONS

To sum up, a heterocontact of AgInSe$_2$ thin films with III–VI layered crystals can be used to create wideband selective photoconverters of unpolarized radiation, whose spectral range is governed by the atomic composition of the III–VI crystals. In addition, the contacts can find application in express diagnostics of the properties of AgInSe$_2$ thin films. The spectral range of the photosensitivity of n-AgInSe$_2$/n-InSe heterojunctions prepared by the optical contact method points to the possibility of applying this system to create high-efficiency thin-film solar cells. To realize this potential, in our view, requires the use of laser deposition of InSe onto the surface of AgInSe$_2$ films in a combined production cycle.

[1] T. Negami, *Abstracts of the Fifth International Conference on Polycrystalline Semiconductors – ''POLYSE'98''* (Schwabisch Gmund, Germany, 1998), p. 18.
[2] T. Negami, M. Nishitani, N. Kohara, Y. Hashimoto, and T. Wada, MRS Symposium Proceedings, Vol. 426 (1996), p. 267.
[3] B. Dimmler and H. W. Schock, Prog. Photovoltaics **4**, 425 (1996).
[4] V. Yu. Rud' and H. W. Schock, *Abstracts of the Fifth International Conference on Polycrystalline Semiconductors – ''POLYSE'98''* (Schwabisch Gmund, Germany, 1998), p. 35.
[5] Yu. V. Rud', V. F. Gremenok, V. Yu. Rud', I. V. Bodnar, S. I. Sergeev-Nekrasov, and D. D. Krivolap, *Abstracts of the Fifth International Conference on Polycrystalline Semiconductors – ''POLYSE'98''* (Schwabisch Gmund, Germany, 1998), p. 36.
[6] I. V. Bodnar, V. F. Gremenok, and E. P. Zaretskya, Thin Solid Films **207**, 54 (1992).
[7] F. Adduci, M. Ferrara, P. Fantalino, and A. Cingolani, Phys. Status Solidi A **15**, 303 (1973).
[8] N. M. Mekhtaev, Yu. V. Rud', and É. Yu. Samiev, Fiz. Tekh. Poluprovodn. **12**, 1566 (1978) [Sov. Phys. Semicond. **12**, 924 (1978)].
[9] N. N. Konstantinova, M. A. Magomedov, V. Yu. Rud', and Yu. V. Rud', Fiz. Tekh. Poluprovodn. **26**, 558 (1992) [Sov. Phys. Semicond. **26**, 317 (1992)].
[10] I. V. Bodnar, V. Yu. Rud', and Yu. V. Rud', Cryst. Res. Technol. **31S**, 261 (1996).
[11] G. L. Belen'kiĭ, Fiz. Tekh. Poluprovodn. **10**, 1206 (1976) [Sov. Phys. Semicond. **10**, 716 (1976)].

Translated by Paul F. Schippnick

Influence of atomic-hydrogen treatment on the surface properties of $n-n^+$ GaAs structures

N. A. Torkhov

Semiconductor Research Institute, 634045 Tomsk, Russia

S. V. Eremeev

V. D. Kuznetsov Siberian Physicotechnical Institute, 634050 Tomsk, Russia

(Submitted August 6, 1998; accepted for publication March 31, 1999)
Fiz. Tekh. Poluprovodn. **33**, 1209–1216 (October 1999)

Tunneling scanning electron microscopy (TSEM) has been used to study the properties of n-GaAs (100) epilayers treated in a flow of atomic hydrogen (AH). The results obtained demonstrate the effects of atomic-hydrogen treatment on the surface, which consist in etching out of the surface oxide layer, micropolishing, stabilization in relation to the alkaline environment (solution of dimethylformamide and monoethanolamine in the ratio 1:3) and oxidation, as well as a change in the surface structure due to dimer formation. It is found that treatment with atomic hydrogen leads to the formation of a thin (less than 0.05 μm), poorly conducting surface layer, which probably greatly affects the static device parameters of Schottky-barrier diodes. © *1999 American Institute of Physics.* [S1063-7826(99)01310-1]

1. INTRODUCTION

It is known that atomic hydrogen (AH), by interacting with semiconductor surfaces, has the capacity to radically alter their electrical characteristics.[1–9] Clearly, the action of atomic hydrogen on the properties of the surface and the material itself (hydrogenation) is of great practical interest. Studies that have been conducted so far show that passivation by atomic hydrogen can be used to protect the surfaces of silicon[10–12] and gallium-arsenide[13] diodes, to enhance the efficiency of silicon solar batteries,[14,15] enhance the direct and reverse current–voltage characteristics (CVC) of Schottky-barrier diodes (SBD),[16–18] and substantially improve the characteristics of silicon field-effect devices.[19]

In the present study we have used tunneling scanning electron microscopy (TSEM) to investigate the reaction of the surface of n-GaAs epitaxial layers treated in an AH flow to the standard chemical treatment used in photolithography to remove a photoresist.

2. EXPERIMENTAL PROCEDURE

Epitaxial layers of GaAs : Sn of thickness 0.5 μm, grown on n^+-GaAs : Te substrates with orientation (100), were subjected to hydrogenation. The charge-carrier concentration in the epitaxial layer was $3.5\times10^{16}\,\mathrm{cm}^{-3}$, and in the substrate, $2\times10^{18}\,\mathrm{cm}^{-3}$. After preliminary chemical cleaning, the epitaxial layers were treated with an aqueous solution of ammonium hydroxide $NH_4OH : H_2O = 1:5$ (referred to below as ''ammonia etchant'') to remove the native oxide. To protect the surface of the n-layer, the 40-mm-diam substrate was therefore convered, using a plasma-chemical technique, with a thin insulating film of SiO_2, 50 Å in thickness. An ohmic contact (OC) based on the alloy GeNi + Au was formed on the n^+-substrate side by electrochemical deposition with subsequent annealing at 450 °C for five minutes. The substrate was then divided into two wafers. The protective SiO_2 film was removed from half of the surface of each wafer using a buffered etchant. In this procedure, as studies on a MII-4 commercial interferometer showed, no steps were observed on the SiO_2–free surface boundary.

As was indicated in Ref. 18, treatment in an AH flow of an unprotected n-GaAs surface leads to an improvement of the static device characteristics of metal–semiconductor contacts when the AH-treatment temperature (T_{treat}) is raised from 100 to 150 °C, specifically, a growth of the reverse voltages (V_r) and a decrease of the ideality index (n).

The surfaces of the investigated samples were subjected to AH treatment at a temperature $T_{\mathrm{treat}} = 150\,°\mathrm{C}$ for 5 min. The residual pressure in the vacuum chamber, which was pumped out by a turbomolecular pump, was 3.7×10^{-6} Torr. The hydrogen flow-rate in all of the experiments was held at $700\,\mathrm{atm}\cdot\mathrm{cm}^3/\mathrm{h}$, and the hydrogen pressure in the vacuum chamber was held at 1.1×10^{-4} Torr. The surface of the treated wafers was oriented perpendicular to atomic-hydrogen flow. The pressure and spatial orientation of the sample relative to the effusion opening in the atomic-hydrogen generator[18] give reason to assume that the angle of incidence of the hydrogen atoms did not exceed 15° relative to the normal to the surface of the epitaxial layer. The untreated wafer in the figures and in the text is referred to as the original wafer.

The morphology and structure of the surfaces of the samples were studied with the help of a TM-2000 commercial tunneling microscope. The surfaces were scanned in air at standard temperature and pressure in the constant-current regime. The obtained TSEM images are positive, i.e., the darker areas of relief correspond to depressions, and the lighter ones, to elevations. To obtain a relatively sharp im-

 © 1999 American Institute of Physics

age, the potential difference between the needle and the surface of the original (untreated) wafer was chosen to be equal to 2–3 V.

In this work we present images of the surfaces of the investigated structures with magnifications of 2^{22} and 2^{15-16}. The 2^{22} magnification (4 194 304x) makes it possible to study the surface at the atomic level. At the magnification of 2^{15} (32 768x) the resolution of the TSEM allows one to distinguish details in the surface with dimensions less than 0.01 μm. Therefore, in view of the development of the technology of Schottky-barrier field-effect transistors with submicron-sized gates it is important to be able to examine the surface morphology at this level.

To investigate the character of the effect of AH treatment on the electrical properties of the surface region of the *n*-layer, we used another substrate with similar parameters. It was then cleaved into six wafers. Five of the wafers were subjected to AH treatment at $T_{\text{treat}} = 150\,^{\circ}\text{C}$ for 5 min. They were then etched on the *n*-layer side in the standard citric-acid etchant with different etching times. The thickness of the etched layer was determined using an MII-4 optical interferometer from the size of the step at the SiO_2–free surface boundary and was found to be equal to 0, 0.03, 0.05, 0.08, and 0.1 μm. The spread in the data did not exceed 30%. Next, to study the effect of the surface region on the reverse voltage V_r, a Schottky barrier was created on each wafer using optical photolithography. Schottky barriers of 325−μm diameter were formed by electrochemical deposition of a gold film in photoresist windows or in windows in the SiO_2. The reverse voltage was measured at a current of 10 μA. The variation in V_r over the wafer did not exceed 25%.

In the formation of the Schottky barriers by optical lithography on the original wafers we noted the appearance of a step at the SiO_2–free surface boundary. A detailed analysis of the fabrication process showed that the step appears as a result of the interaction of the surface of the *n*-GaAs layer with the dimethylformamide : monoethanolamine = 1 : 3 solution (in what follows we call it simply DM solution). In light of the fact that the DM solution is widely used in the fabrication of semiconductor devices (in particular, to remove photoresists) and in these situations it often comes into direct contact with the surface of the semiconductor, it is important to investigate its possible influence on the morphology and structure of the surface. To study the nature of the interaction of DM solution with a treated *n*-GaAs surface, the wafers were also boiled in this solution for 20 min. The surface coated with a SiO_2 film did not react with the etchant. After washing in isopropyl alcohol and drying in nitrogen, the etching rate was estimated from the magnitude of the step, measured using an optical interferometer, and the morphology and structure of the surfaces were examined using TSEM.

3. RESULTS OF EXPERIMENTS

Optical-interferometric studies of the samples treated in the DM solution revealed a difference in the size of the step *h* at the SiO_2 film–free surface boundary. Atomic-hydrogen

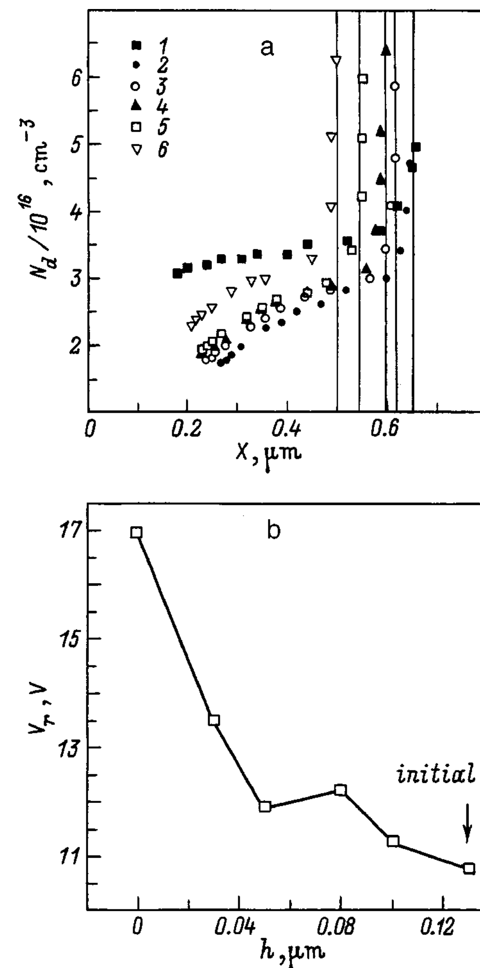

FIG. 1. Concentration profiles of an ionized shallow-donor impurity of AH-treated samples as a function of the thickness of the etched surface layer: *1* — original, *2* — after atomic-hydrogen treatment, *3* — 0.03 μm, *4* — 0.05 μm, *5* — 0.08 μm, *6* — 0.1 μm (a), and the reverse bias voltage V_r, measured at a current of 10 μA, of a diode structure treated in a flow of atomic hydrogen as a function of the thickness of the etched surface layer (b).

treatment leads to a decrease in the etching rate of *n*-GaAs. The magnitude of *h* of the original wafer, for example, was 0.08 μm, and for the treated wafer, $h = 0.05$ μm.

Figure 1 plots V_r values of diode structures as a function of the thickness of the etched surface layer after AH treatment. An inverse dependence of V_r on the thickness of the etched surface layer is clearly visible. At a thickness of the etched surface layer of about 0.1 μm the values of V_r have nearly reached the original values.

TSEM images of the surface of the epitaxial layer of the original wafer and the AH treated wafer are shown in Fig. 2 with a magnification of 2^{22}. In the image of the surface of the original wafer [Fig. 2a] periodicity is absent, and roughness in the form of islands of irregular growth, probably caused by oxidation of the surface, is visible. The shape of the surface treated in AH is smoother [Fig. 2b]. It lacks significant roughness, but to make up for it, scattered uniformly over its surface are isolated pits, which, judging from their dimensions, can be identified as vacancies. In addition, isolated ''flat'' segments are visible, occupying the space be-

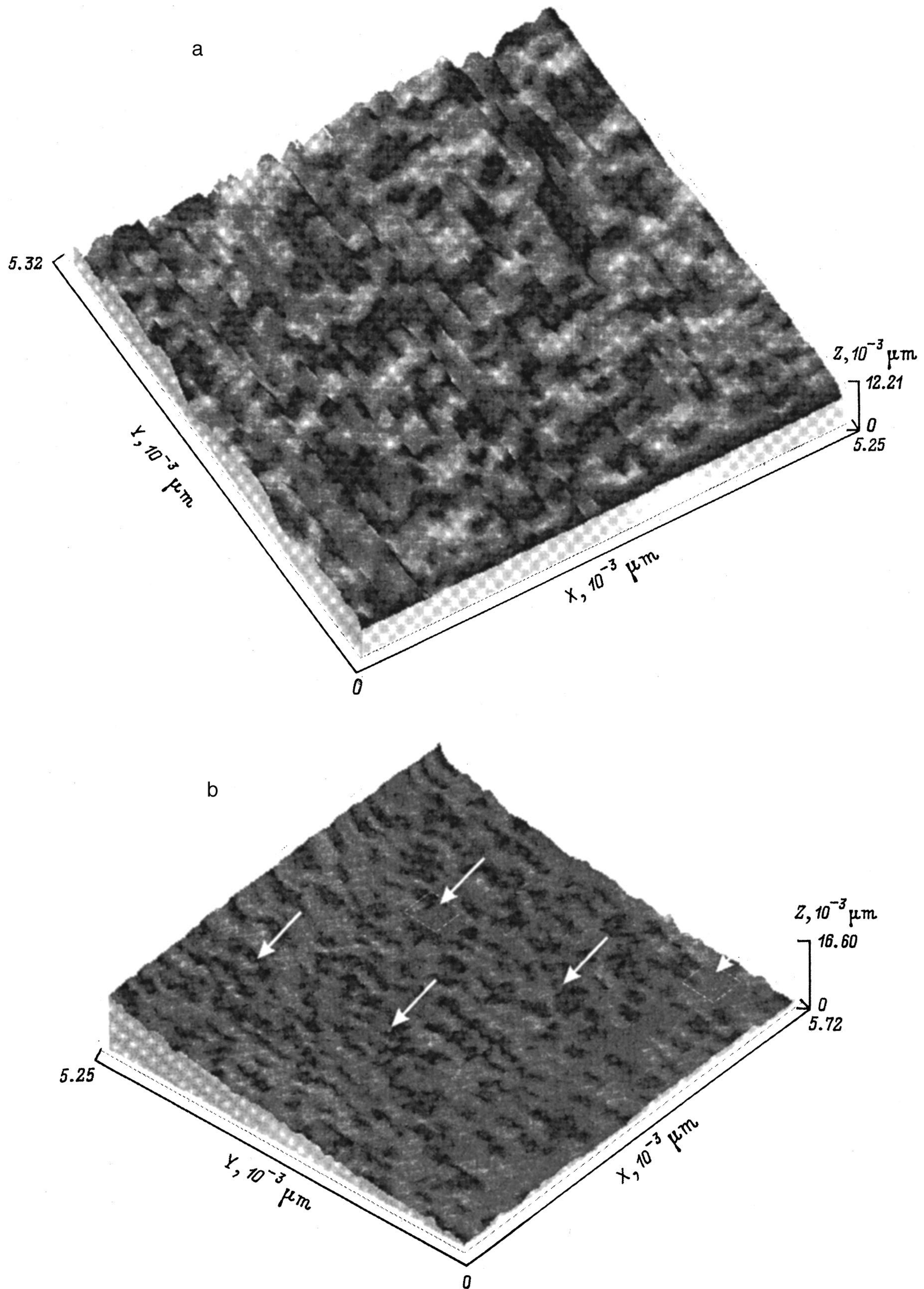

FIG. 2. Images of n-GaAs surfaces: original (a) and AH-treated (b). Magnification 2×10^{22}.

tween the vacancies. For the AH-treated surface, as our studies have shown, the appearance of such segments is completely regular and possibly attributable to a change in the electrical properties of the surface, which leads to stabilization of the tunneling current in the "flat" segments. To obtain a relatively sharp image in this case, it was necessary

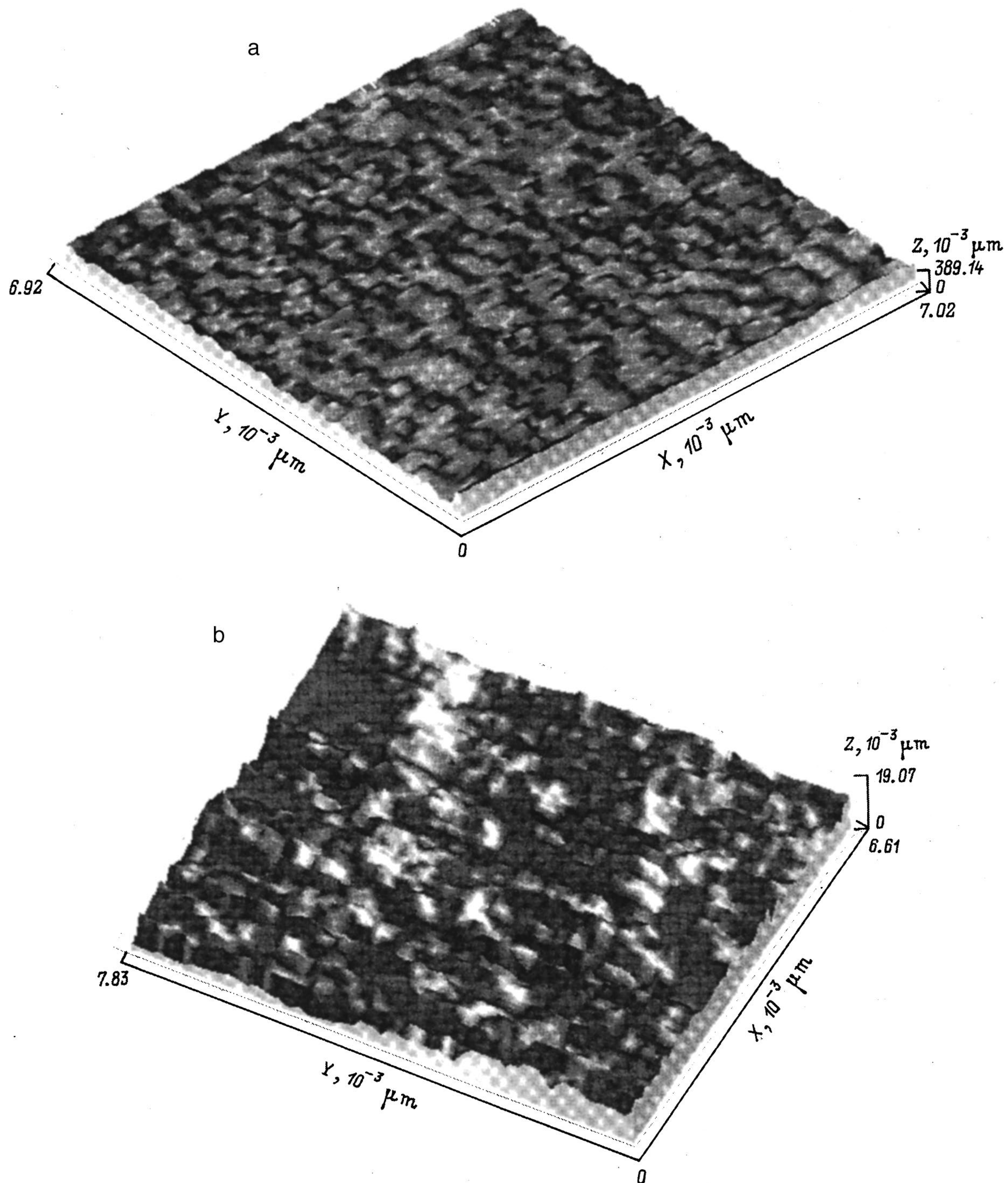

FIG. 3. Images of n-GaAs surfaces: original (a) and AH-treated (b). Magnification 2×10^{15}.

to increase the potential difference between the surface and the needle to 7–8 V. This is a direct indication of a strong lowering of the conductivity of the surface layer after AH treatment. It is clearly noticeable from a comparison of Figs. 2a and 2b that AH treatment of a GaAs (100) surface, in addition to etching away the native oxide, results in a fine polishing of the surface since the effective size of the roughnesses along the vertical (Z axis) in this case is significantly smaller. The observed surface structure after AH treatment remained unchanged for several hours.

Figure 3 shows TSEM images of the surface of the epitaxial layer of the original wafer and an AH-treated wafer with a magnification of 2^{15}.. The surface of the original wafer [Fig. 3a] reveals hilly formations with a characteristic dimension of 0.03–0.05 μm and reminiscent of a two-dimensional standing wave. The characteristic size of the roughness along the vertical is approximately 389 nm. The image of the AH-treated surface [Fig. 3b] at the given magnification differs hardly at all in its character from the original, but the effective size of the irregularities is nearly half that of the original surface. To obtain a clearer picture, the image was artificially stretched in the Z direction.

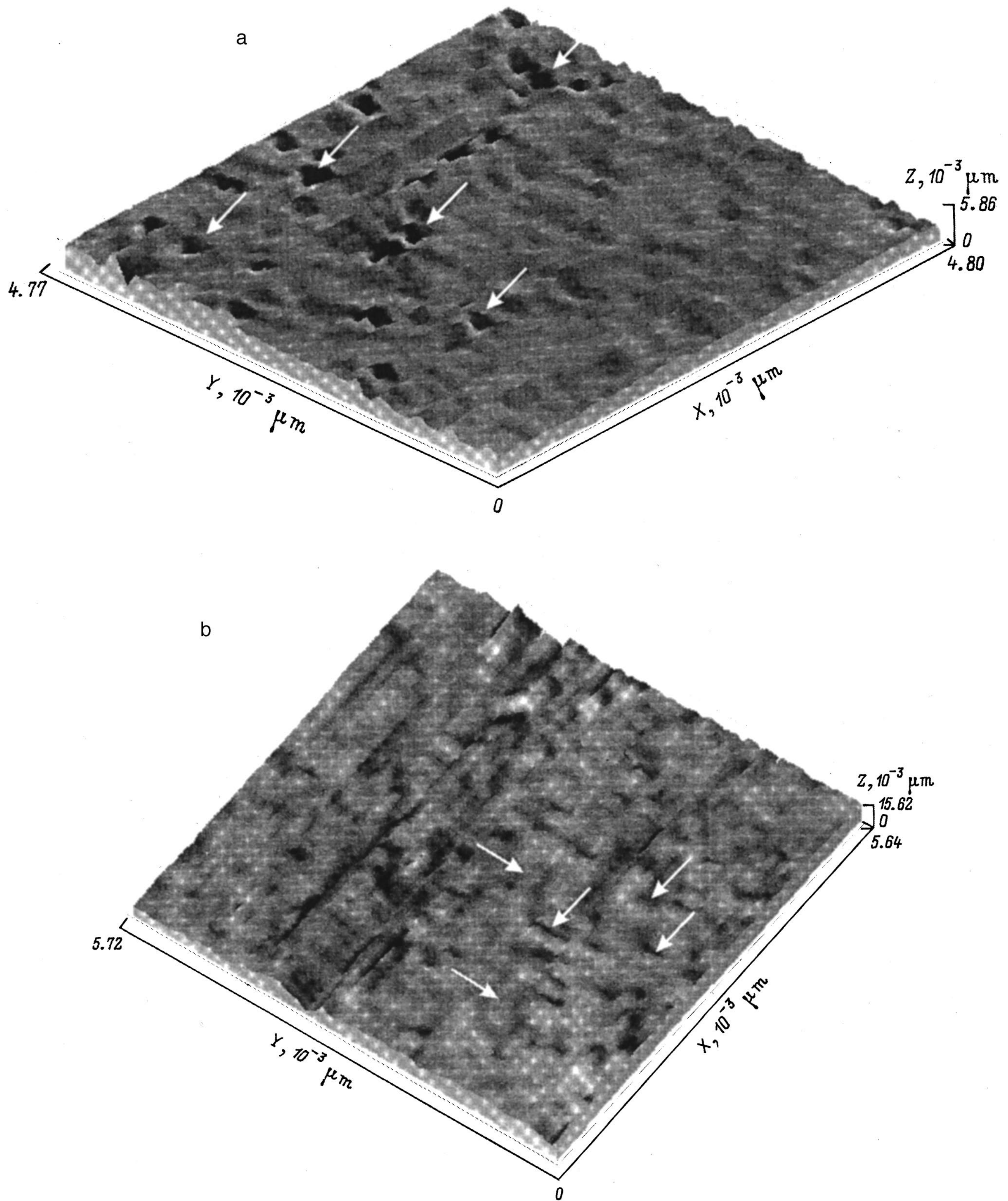

FIG. 4. Images of the original (a) and AH-treated (b) n-GaAs surface, etched with a solution of monoethanolamine : dimethylformamide = 1 : 3 for 20 min. Magnification 2×10^{15}.

Figure 4a shows an image of the original surface at a magnification of 2^{22} of samples treated with the DM solution. The presence of individual vacancies and of its clusters is clearly visible. The surface segments free of vacancies are homotypic. The surfac has a 1×1 structure. Figure 4b shows an image of a DM-treated surface that had previously been subjected to AH treatment. In this case, vacancies are essentially absent on the surface. Extended (dumbbell-like shape) formations, oriented perpendicular to one another, are visible.

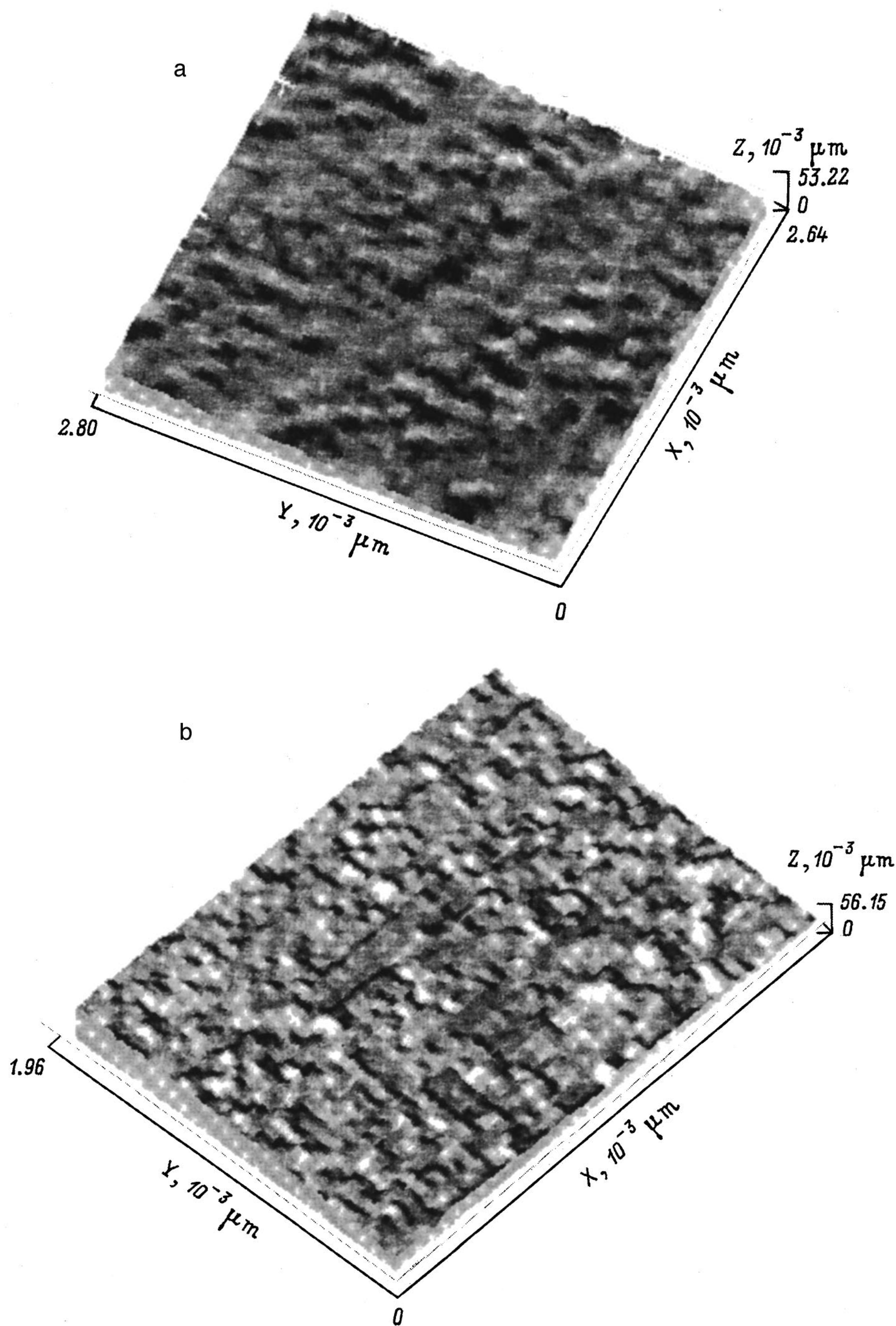

FIG. 5. Images of the original (a) and AH-treated (b) n-GaAs surface, etched with a solution of monoethanolamine : dimethylformamide = 1 : 3 for 20 min. Magnification 2×10^{22}.

Figure 5 shows TSEM images of the same surfaces as in Fig. 4, but at a magnification of 2^{15}. It can be seen that the original GaAs surface [Fig. 5a] after etching is strongly developed. Irregularities formed by individual clusters of objects of rounded shape less than 0.01 μm in size, are visible. The AH-processed surface [Fig. 5b] after treatment with the DM solution has a different morphology. The surface structure has become more uniform. In addition, the irregularities of the AH-treated surface is significantly lower. Their vertical size on the AH-treated surface [Fig. 5b] is significantly smaller than in Fig. 3a, and small differences in scale are explained by the large slope of the surface shown in Fig. 5b. The irregularities on the surface are distributed more uniformly and their shape is less rounded. Their horizontal size is 0.005–0.008 μm, on the average. Thus, treatment of the samples in a flow of atomic hydrogen leads, on the one hand, to micropolishing of the surface and, on the other, to a preservation of this effect after treatment with a solution of dimethylformamide and monoethanolamine.

4. DISCUSSION OF EXPERIMENTAL RESULTS

Our TSEM studies have shown that changes in the surface morphology are observed. As can be seen from Fig. 3, the size of the grains of the AH-treated surface is significantly smaller than on the untreated surface. Studies of the GaAs surface at significantly higher magnification (Fig. 4) revealed a change in the structure of the surface treated with

DM solution: a decrease in the number of surface dislocations, and formation of dimers (hydride phases or paired dangling bonds of surface atoms). It can be seen that dimers of the higher-lying and below-lying layers are arranged perpendicular to each other and form a structure on the *n*-GaAs surface. In their study of a silicon surface the authors of Ref. 3 showed that the state of the surface depends on the angle of incidence of the atomic hydrogen. At an angle of incidence of the atomic hydrogen exceeding 50°, for example, dimer formation is observed on the silicon surface, i.e., the H atoms do not settle on the dangling bonds, but facilitate their pairwise joining to neighboring atoms. An increase in the angle at which atomic hydrogen strikes the GaAs (100) surface, as is indicated in Ref. 2, leads to a lowering of the probability of etching-out of surface atoms, and the GaAs (100) surface remains atomically flat. It was shown in Ref. 2 that after completion of the process of cleaning with an AH flow, the dimensionality of the cells of the crystalline lattice on the surface remains 1×1. It was also shown that in this case enrichment of the surface with gallium atoms is possible, along with a breakdown of the stoichiometry due to evaporation of the arsenic atoms in the form of hydrides. In our case, the angle of incidence of the atomic hydrogen did not exceed 15°. In this case, dimer formation on the surface was also observed. In Ref. 20, similar formations on an AH-cleaned silicon surface was linked by the authors with formation of Si-dimers of the hydride phase. Dimer formation, on the one hand, can be interpreted as hydride phases of As and Ga. On the other hand, it is entirely possible that the dumbbell-like formations can form as a result of pairing of dangling bonds of neighboring surface atoms of the crystal host. According to our data, this conjecture is supported by the strict orientation of the dumbbell-like formations in the (011) and $(0\bar{1}1)$ directions. The orientation of the dumbbell-like formations was determined from the known orientation of the substrate. Each As atom on a (100) surface has two bonds with Ga atoms from the lower-lying layer, which are oriented in the $(0\bar{1}1)$ direction. Thus it may be assumed that the dangling bonds take part in pairing.

The experimental data show that AH treatment facilitates not only stabilization of the surface in relation to an alkaline environment, but also oxidation in air.

As a result of the TSEM studies, we found that AH treatment leads to the formation of a surface layer possessing poor conductivity. This is indicated by the fact that to maintain the necessary tunneling current after AH treatment the voltage between the needle and the surface had to be increased from 2–3 to 7–8 V. This is also indicated by our experiments on determining the dependence of V_r on the thickness of the etched surface layer of a semiconductor wafer treated in a flow of atomic hydrogen (Fig. 4). As was indicated above, etching was effected in this case with the standard citric-acid etchant. We found that for the thickness of the etched surface layer on the order of 0.1 μm the values of V_r approach their original values. Thus, we showed that the increase in the reverse voltages of the diode structures can be explained by the formation of a thin, poorly conducting surface layer after AH treatment.

From the available experimental data it is hard to come to any conclusion about the reasons for the decrease in the conductivity of this layer. On the one hand, it may be due to a lowering of the mobility of the majority charge carriers because of disruption of the crystal structure of the surface layer; on the other hand, it may be due to a strong lowering of their concentration and a distortion of the potential formed by the metal–semiconductor contact with the Schottky barrier. It was suggested[21] that the conductivity decreases due to the formation of a thin, semi-insulating surface layer. This suggestion was based on an interpretation of the unusual character of the behavior of the current–capacitance characteristics.

5. CONCLUSIONS

Our results demonstrate a strong dependence of the state of the surface on the means of its chemical treatment and the possibility of enhancing the surface by treatment in a flow of atomic hydrogen, which etches out the oxide layer, micropolishes the surface, and stabilizes it in relation to treatment in a solution of dimethylformamide : monoethanolamine = 1 : 3 and in relation to oxidation, and also alters the surface structure with formation of dimers.

It is found that AH treatment leads not only to a change in the surface and the properties of the surface itself, but also to the formation of a thin (<1 μm), poorly conducting surface layer, which possibly plays a defining role in the increase in V_r. Further studies are needed to explain the mechanism that lowers the conductivity of the surface layer.

We wish to thank Cand. Phys.–Math. Sci. A. V. Panin for making a tunneling microscope available for these these studies. We also thank Dr. Tech. Sci. V. G. Bozhkov and Cand. Phys.–Math. Sci. V. A. Kanadeĭ for assistance with the atomic-hydrogen treatment experiments.

[1] V. L. Gurtovoĭ, V. V. Dremov, V. A. Makarenko, and S. Yu. Shipoval, Fiz. Tekh. Poluprovodn. **29**, 1888 (1995) [Semiconductors **29**, 986 (1995)].
[2] J. Chevallier and M. Aucouturier, Annu. Rev. Mater. Sci. **18**, 219 (1988).
[3] J. A. Schaefer, V. Persch, S. Stock, Th. Allihger, and A. Goldmann, Europhys. Lett. **12**(6), 563 (1990).
[4] A. Kishimoto, I. Suemuni, K. Hamaoka, T. Koui, Y. Honda, and M. Yamanishi, Jpn. J. Appl. Phys. **29**(10), 2273 (1990).
[5] L. M. Weeglels, T. Saitoh, and H. Kanbe, Appl. Phys. Lett. **66**(21), 2870 (1995).
[6] É. M. Omel'yanovskiĭ, A. V. Pakhomov, A. Ya. Polyakov, A. V. Govorkov, O. M. Borodina, and A. S. Bruk, Fiz. Tekh. Poluprovodn. **22**(7), 1203 (1988) [Sov. Phys. Semicond. **22**, 763 (1988)].
[7] R. P. H. Chang and S. Darack, Appl. Phys. Lett. **38**(11), 898 (1981).
[8] Z. Lu, M. T. Schmidt, D. Chen, R. M. Osgood, W. M. Holber, D. V. Podlesnik, and J. Forster, Appl. Phys. Lett. **58**(11), 1143 (1991).
[9] N. Watanabe, T. Nittono, H. Ito, N. Kondo, and Y. Nanishi, J. Appl. Phys. **73**(12), 8146 (1993).
[10] S. J. Pearton, J. Electron. Mater. **14a**, 737 (1985).
[11] J. I. Pankove, M. A. Lampert, and M. L. Tarng, Appl. Phys. Lett. **32**(7), 439 (1978).
[12] J. I. Pankove and M. L. Tarng, Appl. Phys. Lett. **34**(2), 156 (1979).
[13] S. J. Pearton, E. E. Haller, and A. G. Elliot, Appl. Phys. Lett. **44**(7), 684 (1984).
[14] C. H. Seager, D. S. Ginley, and J. D. Zook, Appl. Phys. Lett. **36**(10), 831 (1980).
[15] J. I. Hanoka, C. H. Seager, D. J. Sharp, and J. K. G. Panitz, Appl. Phys. Lett. **42**(7), 618 (1983).

[16] A. Paccagnella, A. Callegari, E. Latta, and M. Gasser, Appl. Phys. Lett. **55**(3), 259 (1989).
[17] U. K. Chakrabarti, S. J. Pearton, W. S. Hobson, J. Lopata, and V. Swaminathan, Appl. Phys. Lett. **57**(9), 887 (1990).
[18] V. G. Bozhkov, V. A. Kagadeĭ, and N. A. Torkhov, Izv. Vuzov: Fizika, No. 8, 115 (1997).
[19] V. V. Aristov, S. V. Koveshnikov, S. V. Nosenko, E. B. Yakimov, and A. M. Surma, Mikroelektronika **24**(3), 198 (1995).
[20] T. Hashizume, S. Heike, M. I. Lutwyche, S. Watanabe, K. Nakajima, T. Nishi, and Y. Wada, Jpn. J. Appl. Phys. **35**(8B), L1085 (1996).
[21] Y. G. Wang and S. Ashok, J. Appl. Phys. **75**(5), 2447 (1994).

Translated by Paul F. Schippnick

Production and properties of In/$HgGa_2S_4$ Schottky barriers

V. Yu. Rud'

St. Petersburg State Technical University, 195251 St. Petersburg, Russia

Yu. V. Rud'

A. F. Ioffe Physicotechnical Institute, Russian Academy of Sciences, 194021 St. Petersburg, Russia

M. C. Ohmer

Wright Laboratory, Wright–Patterson AFB, Ohio 45433, USA

P. G. Schunemann

Lockheed Sanders, Nashua, New Hampshire 03061, USA

(Submitted March 17, 1999; accepted for publication March 31, 1999)
Fiz. Tekh. Poluprovodn. **33**, 1217–1219 (October 1999)

We have obtained In/$HgGa_2S_4$ rectifying photosensitive Schottky barriers. The sensitivity of the best structures reaches 200 V/W, and it is observed in the spectral range 0.8–3.8 eV at $T=300$ K with barrier contact side illumination. It is determined that the photosensitivity spectra of the Schottky barriers correspond to the photoluminescence of the crystals used to produce the barriers, and this correspondence is analyzed. It is concluded that the Schottky barriers can be used for monitoring the optical quality of $HgGa_2S_4$ single crystals as wide-band photodetectors. © *1999 American Institute of Physics.* [S1063-7826(99)01410-6]

One of the most important results of fundamental investigations of multicomponent diamond-like semiconductors[1,2] is the discovery of new nonlinear media, with record-high nonlinear polarizability.[2–5] Variations of the atomic composition of such materials can result in a further increase of the radiation conversion efficiency,[6] while the level of optical absorption in their transmission range is still holding back extensive use of the new materials in nonlinear optics. Such semiconductors also include the little-studied ternary compound $HgGa_2S_4$ with a thiogallate lattice.[7,8] This material holds promise for converting CO_2-laser radiation with an efficiency of up to 60%, for detecting radiation in the atmospheric transmission window 10–12 μm, and for visualizing the spectra of fast processes in the range 8–12 μm.[9,10] In the present paper, we report the results of the first investigations of the physical properties of $HgGa_2S_4$ single crystals, making it possible to obtain the first photosensitive structures based on them, and to demonstrate the new possibilities of photoelectric spectroscopy in the diagnostics of the perfection of this material.

1. The $HgGa_2S_4$ single crystals were grown by the Lockheed Sanders (USA) Company using directed crystallization of a melt close to stoichiometry of the ternary compound in a horizontal glassy carbon boat. During slow directed cooling of the melt at rates of 0.1–0.3 °C/h, the axial temperature gradient was 1–3 °C/cm, which effectively suppressed crack formation, mass transfer, and composition disturbances of the solid phase. The ingots obtained had average dimensions $10\times15\times200$ mm and a uniform bright-orange color. The cell parameters of these crystals were the same as the known parameters for $HgGa_2S_4$.[7,8]

Electrical measurements performed on single-crystal wafers which were not oriented deliberately show that such crystals possess free-electron density 10^8-10^9 cm^{-3} and resistivity 10^9-10^{10} $\Omega\cdot$cm at $T=300$ K.

2. The contact of pure indium layers, deposited by vacuum thermal sputtering, with a cleaved or polished $HgGa_2S_4$ surface shows sharp rectification, and the transmission direction in In/$HgGa_2S_4$ Schottky barriers is always obtained with positive external bias on the semiconductor.

Figure 1 shows a typical stationary current–voltage characteristic of one of the In/$HgGa_2S_4$ Schottky barriers. The rectification coefficient in the best barriers reached 15, and the reverse current increased with voltage according to a power law and did not exceed $(2-5)\times10^{-9}$ A for $U\leqslant5$ V and $T=300$ K.

When the Schottky barriers are illuminated with natural radiation, a photovoltage is generated and the semiconductor becomes positively charged, in agreement with the direction of rectification. The voltage photosensitivity of the best Schottky barriers reaches 200 V/W at $T=300$ K and dominates for barrier contact side illumination.

The typical spectral dependences of the relative quantum efficiency η of photoconversion for the barriers obtained are shown in Fig. 2. It is evident that for barrier contact side illumination photosensitivity ''arises'' at incident photon energy $\hbar\omega>0.8$ eV, and is observed in a wide spectral range up to ≈3.8 eV (Fig. 2, curves *1* and *2*). If such barriers are illuminated on the semiconductor wafer side (Fig. 2, curve *3*), then a sharp short-wavelength boundary arises in the η spectra and the photoresponse near $\hbar\omega=2.48$ eV virtually vanishes for wafer thicknesses 0.1–0.2 mm. This shows that

 © 1999 American Institute of Physics

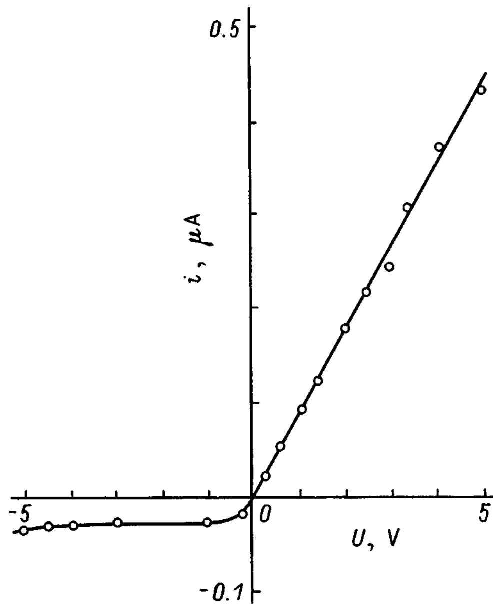

FIG. 1. Stationary current–voltage characteristic of an In/$HgGa_2S_4$ Schottky barrier at $T=300$ K. (Positive external bias corresponds to $HgGa_2S_4$).

for $\hbar\omega > 2.3$ eV optical absorption in $HgGa_2S_4$ increases rapidly, the carrier photogeneration region is localized in a thin layer near the surface, and because of the short diffusion length, the photoelectrons no longer enter the active region

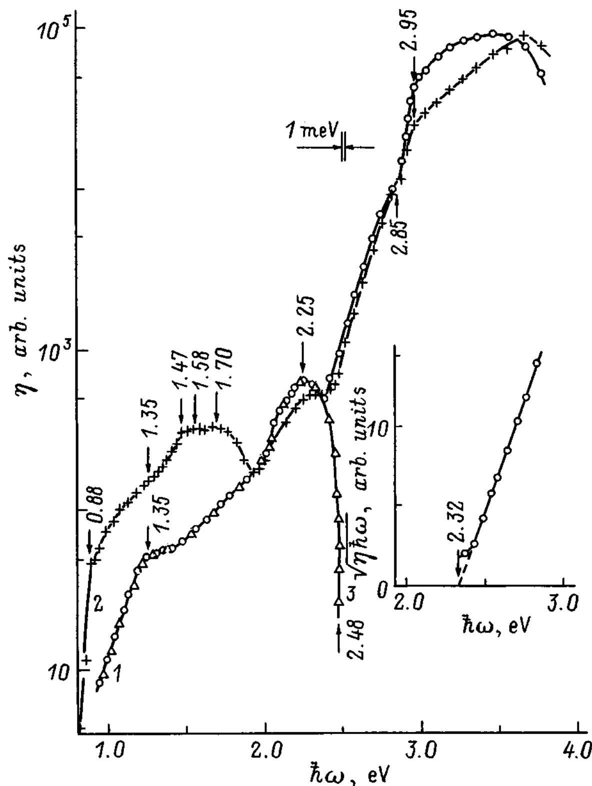

FIG. 2. Spectral dependences of the relative quantum photoconversion efficiency of In/$HgGa_2S_4$ Schottky barriers at $T=300$ K (*1*, *3*—sample 6; *2*—sample 10; *1*, *2*—barrier contact side illumination, *3*—$HgGa_2S_4$ side illumination). Inset: $(\eta\hbar\omega)^{1/2}$ versus $\hbar\omega$ for an In/$HgGa_2S_4$ Schottky barrier at $T=300$ K (sample 6, barrier contact side illumination).

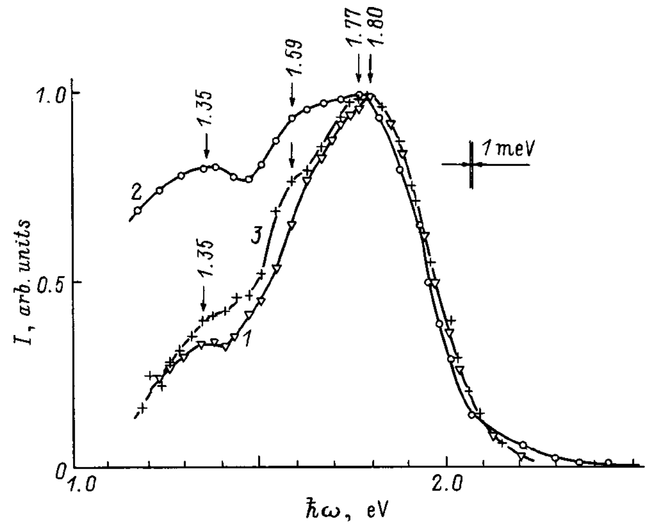

FIG. 3. Spectral dependences of the stationary photoluminescence of $HgGa_2S_4$ single crystals at $T=77$ K. (Excitation photon energy $\hbar\omega_{exc} = 2.88$ eV. *1*, *2*—Sample 6; *3*—sample 10; pump intensity P/P_0: *1*, *3*— 1, *2*—0.1.)

of the Schottky barrier and, for this reason, photosensitivity vanishes. It is important to underscore that for $\hbar\omega < 2.25$ eV the η spectra are essentially independent of the barrier illumination geometry (Fig. 2, curves *1* and *2*). This attests to a volume character of photoconductivity, and the observed differences in the long-wavelength photosensitivity and the particular features of the η spectra in the region $\hbar\omega < 2.3$ eV should be interpreted primarily as being a manifestation of the dependence of the density and nature of point lattice defects on the technological conditions under which the $HgGa_2S_4$ single crystals are obtained (Fig. 2). It is also obvious that measurements of the photosensitivity of Schottky barriers could find application for adjusting the technological process, and, correspondingly, increasing the optical quality of single crystals in their transmission range.

For all In/$HgGa_2S_4$ Schottky barriers obtained, the photosensivity for $\hbar\omega > 2.3$ eV increases sharply at the location of the short-wavelength dropoff of η, typical of substrate side illumination, with a transition to barrier contact side illumination (Fig. 2, curves *1* and *2*). From 2.3 to 2.8 eV this increase is close to a square-root law, as is indicated by the rectification of the photosensitivity spectra in the coordinates $(\eta\hbar\omega)^{1/2} - \hbar\omega$ (see the inset in Fig. 2). Extrapolating this dependence $(\eta\hbar\omega)^{1/2} \to 0$, we obtain the energy $B_1 = 2.32$ eV, which, with allowance for Refs. 10 and 11, can be correlated with indirect optical transitions in $HgGa_2S_4$. For $\hbar\omega > 2.85$ eV the increase in photosensitivity becomes nearly exponential, and it can be characterized by the slope $s = \partial(\ln\eta)/\partial(\hbar\omega) \simeq 12$ eV^{-1}, which, with allowance for Ref. 12, justifies correlating it with the onset of direct interband transitions with energy $E \simeq 2.85$ eV, which is close to the published estimate of the band gap in $HgGa_2S_4$.[13] The growth of η in the range $\hbar\omega > E_2$ up to 3.5 eV (Fig. 2, curves *1* and *2*) shows that the Schottky barriers obtained are adequate with respect to collection of the pairs photogenerated at the semiconductor surface.

3. Figure 3 shows typical photoluminescence (PL) spec-

tra of the $HgGa_2S_4$ single crystals used to produce Schottky barriers. Photoluminescence was excited by focused He–Cd laser light $\{\hbar\omega_{exc}=2.88$ eV, $P=10^{18}-10^{19}$ photons/$(cm^2\cdot s)\}$ which is strongly absorbed $HgGa_2S_4$. The PL spectra were corrected for transmission of the radiation by the optical channel and the spectral sensitivity of the photodetector; the resolution of the apparatus was not less than 1 meV.

The PL spectra at 77 K of all single crystals grown generally include several competing wide bands. The large width of the PL bands indicates that the observed radiative transitions are not elementary. The ratio of the intensities at the maxima of the PL bands for our crystals varied from sample to sample (Fig. 3, curves *1* and *2*). This correlates with the changes in the spectra η of the Schottky barriers based on the same samples. The energy position of the PL spectra, as indicated in Fig. 3, falls in the transmission range of $HgGa_2S_4$ substantially below E_1 and therefore it can be attributed to radiative transitions with the participation of levels of lattice defects.

As the pumping level decreases (Fig. 3, curves *1* and *3*), the contribution of the long-wavelength components of the photoluminescence increases and the long-wavelength wing of the PL bands shifts into the long-wavelength spectral region. This justifies attributing the observed photoluminescence to the donor–acceptor recombination.

In summary, the Schottky barriers obtained on the basis of $HgGa_2S_4$ single crystals could find application as photodetectors for natural light, and with allowance for high tetragonal compression of the crystal lattice,[4] linearly polarized light[14] in the spectral range 2.9–3.6 eV. In addition, they are ''blind'' with respect to radiation with photon energy $\hbar\omega<2.7$ eV. At the same time, it should also be underscored that investigations of the photosensitivity spectra of Schottky barriers can be used for rapid diagnostics of the optical quality $HgGa_2S_4$ single crystals in their transmission range ($\hbar\omega<2.3$ eV) and therefore for perfecting the technology of making this material which is so promising for nonlinear optics.

We thank A. A. Vaĭpolin for performing the x-ray investigations of the $HgGa_2S_4$ single crystals.

[1] N. A. Goryunova, *Crystal and Chemistry of Diamond-Like Semiconductors* (Chapman and Hall, London, 1965).
[2] V. D. Prochukhan and Yu. V. Rud', Fiz. Tekh. Poluprovodn. **12**, 209 (1978) [Sov. Phys. Semicond. **12**, 121 (1978)].
[3] N. A. Goryunova, A. A. Grinberg, S. M. Ryvkin, I. M. Fishman, G. P. Spen'kov, and I. D. Yaroshetskiĭ, Fiz. Tekh. Poluprovodn. **2**, 1525 (1968) [Sov. Phys. Semicond. **2**, 1272 (1968)].
[4] G. C. Bhar, Jpn. J. Appl. Phys. **32**, 653 (1993).
[5] M. C. Ohmer and R. Pandey, MRS Bulletin **23**, 16 (1998).
[6] B. F. Levine, Phys. Rev. B **7**, 2600 (1973).
[7] H. Hahn, G. Frank, W. Klinger, and Z. Anorg, Allgem. Chem. **279**, 241 (1955).
[8] J. A. Beun, R. Nitsche, and M. Lichtensteiger, Physica (Amsterdam) **26**, 647 (1960).
[9] S. A. Komarov, A. N. Meleshko, A. N. Pleshanov, and V. S. Solomatin, Pis'ma Zh. Tekh. Fiz. **6**, 870 (1980) [Sov. Tech. Phys. Lett. **6**, 375 (1980)].
[10] P. G. Schunemann and T. M. Pollak, MRS Bull. **23**, 23 (1998).
[11] J. J. Pankove, *Optical Processes in Semiconductors* (Prentice–Hall, New Jersey, 1971).
[12] A. A. Abdurakhimov, A. V. Lunev, Yu. V. Rud', V. E. Skoryukin, and Yu. K. Undalov, Izv. Vyssh. Uchebn. Zaved. SSSR, Fiz. No. 7, 7 (1985).
[13] *Physicotechnical Properties of Semiconductor Materials* (Nauka, Moscow, 1978).
[14] F. P. Kesamanly, V. Yu. Rud', and Yu. V. Rud', Fiz. Tekh. Poluprovodn. **30**, 1921 (1996) [Semiconductors **30**, 1001 (1996)].

Translated by M. E. Alferieff

Effect of hydrogen on the current–voltage characteristics of Pd/*p*-InGaAsP and Pd/*n*-InGaAs barrier structures

V. P. Voronkov and L. S. Khludkova

V. D. Kuznetsov Siberian Physicotechnical Institute, Tomsk State University, 634050 Tomsk, Russia
(Submitted April 8, 1999; accepted for publication April 27, 1999)
Fiz. Tekh. Poluprovodn. **33**, 1220–1223 (October 1999)

The effect of hydrogen on the current–voltage characteristics of palladium–semiconductor barrier structures based on the solid solutions $In_{0.92}Ga_{0.08}As_{0.17}P_{0.83}$ and $In_{0.53}Ga_{0.47}As$ is investigated. The hydrogen-induced kinetics of the change in the current in the structures is studied. It is shown that the response time of the structures decreases with increasing hydrogen concentration in the gas mixture. The results obtained are discussed from the standpoint of the adsorption of hydrogen atoms on the semiconductor surface. © *1999 American Institute of Physics.* [S1063-7826(99)01510-0]

The effect of hydrogen on the electric and photoelectric characteristics of palladium–semiconductor Schottky barriers has been studied rather extensively. Barrier structures based on silicon,[1,2], indium phosphide,[3,4] gallium phosphide,[5] and gallium arsenide[6,7] have been investigated experimentally. At present, there is, nonetheless, no general agreement concerning the mechanism of the hydrogen sensitivity of such structures. According to the model encountered most often in the literature, the effect of hydrogen on the characteristics of a Schottky barrier with a palladium contact is due to a change in the electron work function of palladium. At the same time, according to Ref. 4, hydrogen changes the density of surface states of the semiconductor, which changes the height of the Schottky barrier.

In the present paper we report the results of an investigation of the effect of hydrogen on the current–voltage characteristics of barrier structures based on the solid solutions $In_{0.92}Ga_{0.08}As_{0.17}P_{0.83}$ and $In_{0.53}Ga_{0.47}As$. The results obtained are discussed from the standpoint of the adsorption of hydrogen atoms in the semiconductor surface.

The barrier structures were prepared on the basis of epitaxial layers of a solid solution, which were grown by liquid-phase epitaxy on semi-insulating InP substrates. Layers of the solid solution with various compositions, degrees of doping, and type of conductivity were used to obtain the samples:

1) zinc-doped p-$In_{0.92}Ga_{0.08}As_{0.17}P_{0.83}$ layers ($E_g = 1.21$ eV, $p = 5.8\times10^{18}$ cm^{-3}),
2) n-$In_{0.53}Ga_{0.47}As$ layers ($E_g = 0.75$ eV, $n = 1.8\times10^{15}$ cm^{-3}), grown from europium-doped melts,
3) undoped n-$In_{0.53}Ga_{0.47}As$ layers ($E_g = 0.75$ eV, $n = 7.0\times10^{16}$ cm^{-3}).

The barrier contact was produced by thermal evaporation of palladium in vacuum with residual pressure 10^{-5} mm Hg. The thickness of the deposited palladium was 40 nm, and the contact area was 4×10^{-3} cm^2. No special surface treatment (other than degreasing) was performed prior to deposition. The structures were fabricated in a planar configuration. The ohmic contact to the epitaxial solid-solution layer was produced by annealing indium. The electric characteristics of the barrier structures were measured at 300 K in an airtight chamber equipped with a fan for mixing the gas mixture.

Investigation of the current–voltage characteristics (IVCs) of Pd/*p*-InGaAsP structures showed that the direct IVC branch (Fig. 1) can be described by an exponential function and can be represented in the form

$$I = AT^2 \exp\left(-\frac{\Phi_B}{kT}\right)\left(\exp\frac{qV}{nkT} - 1\right), \quad (1)$$

where A is the effective Richardson constant, Φ_B is the barrier height, and n is the nonideality coefficient. The nonideality coefficient n for the various diodes falls in the range 3.3–3.8. The barrier height estimated from the IVCs is 0.67

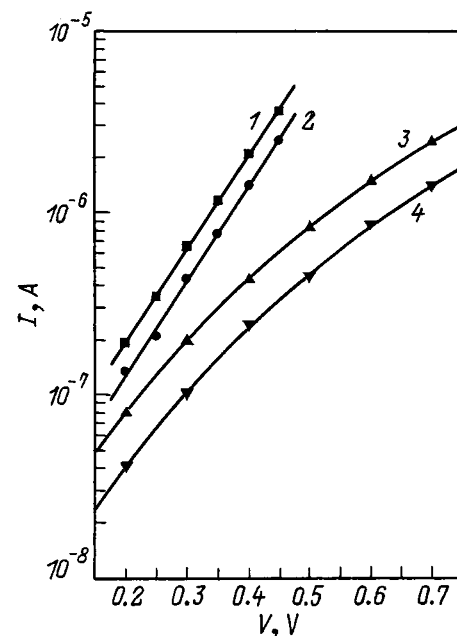

FIG. 1. Direct (*1*,*2*) and reverse (*3*,*4*) branches of the current–voltage characteristics of a Pd/*p*-InGaAsP structure without H_2 (*1*,*3*) and in air containing 0.5% H_2 (*2*,*4*).

 © 1999 American Institute of Physics

eV. In Ref. 8, for a Schottky barrier obtained by depositing gold on a solid solution Pd/*p*-InGaAsP with the same composition as ours ($E_g = 1.21$ eV), the value of Φ_B determined from the photoelectric measurements was 0.69 eV. The reverse branches of the IVCs for Pd/*p*-InGaAsP structures can be approximated by a power law with exponent 3.0–3.5.

When hydrogen was introduced into the measurement chamber, both the direct and reverse currents were observed to decrease for Pd/*p*-InGaAsP structures. In air with 0.5% hydrogen, the direct current decreases by a factor of 1.5 and the reverse current decreases by a factor of 2. Since the nonideality coefficient in a hydrogen-containing medium changes very little, the ratio of the currents in a medium with and without hydrogen can be written as

$$\frac{I_{H_2}}{I} = \exp\left(-\frac{\Delta\Phi_B}{kT}\right), \quad (2)$$

where $\Delta\Phi_B$ is the hydrogen-induced change of the barrier height. A decrease in the direct current by a factor of 1.5 (with 0.5% hydrogen) corresponds to an increase of the barrier height by 0.01 eV.

For structures based on the narrower gap solid solution n-$In_{0.53}Ga_{0.47}As$ ($E_g = 0.75$ eV) with both low ($n = 1.8 \times 10^{15}$ cm^{-3}) and high ($n = 7.0 \times 10^{16}$ cm^{-3}) charge-carrier density, the direct and reverse branches of the IVC were virtually identical and had the form of the curve described by a power-law function with an exponent of 1.3 (Fig. 2, curve *1*). This form of the IVC seems to be due to the low height of the potential barrier for electrons in a Pd/n-$In_{0.53}Ga_{0.47}As$ contact. We note that in Ref. 9 linear IVCs were obtained for a Pd/n-$In_{0.53}Ga_{0.47}As$ structure.

Hydrogen increased the direct and reverse currents of Pd/*n*-InGaAs structures, and in the process the IVC approached a linear dependence (Fig. 2, curve *2*). The sensitivity of the structure decreased somewhat with increasing applied bias. In air with 0.5% hydrogen, for example, the current (both direct and reverse) increased by a factor of 2.4 under a voltage of 0.1 V and by a factor of 1.6 under a voltage of 0.5 V. The dependences of the current increase $\Delta I = I_{H_2} - I$ in the structures on the time elasped after the introduction of hydrogen into the measurement chamber are

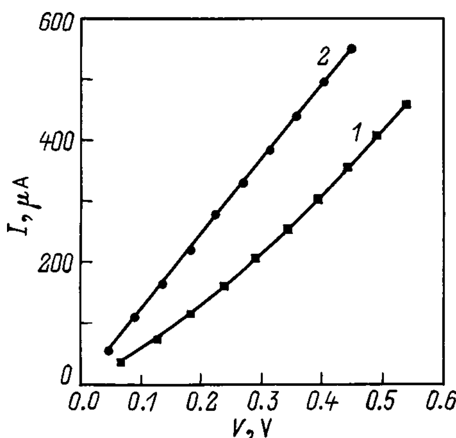

FIG. 2. Current–voltage characteristics of a Pd/*n*-InGaAs structure without H_2 (*1*) and in air with 0.5% H_2 (*2*).

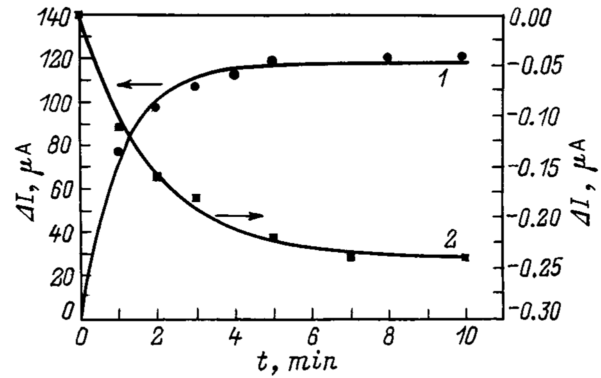

FIG. 3. Change in the current of Pd/*n*-InGaAs (*1*) and Pd/*p*-InGaAsP (*2*) structures as a function of time after hydrogen is introduced into the measurement chamber ($N_{H_2} = 0.5\%$).

shown in Fig. 3. The current was measured with a direct bias $V = 0.3$ V. The time for establishing a stationary value of the current is 5–7 min.

As follows from Eq. (2), the change $\Delta\Phi_B$ in the barrier height is proportional to the logarithm of the current ratio I_{H_2}/I,

$$\ln\frac{I_{H_2}}{I} = -\frac{\Delta\Phi_B}{kT}. \quad (3)$$

Thus, the time-dependence of $\ln(I_{H_2}/I)$ is determined by the time-dependence of the barrier height. It is known that the barrier height in structures based on III–V semiconductors is essentially independent of the electronic work function of the metal and is determined by the energy states on the semiconductor surface.[10] At the same time, it has been shown that treatment of a semiconductor surface with atomic hydrogen can change the barrier height.[11] Therefore it can be inferred that the hydrogen-induced change in the barrier height of metal–semiconductor structures is due to a change in the electronic work function of the semiconductor as a result of the adsorption of hydrogen atoms on its surface. Since the kinetics of adsorption is described, as a rule, by an exponential law, the surface characteristics of a semiconductor, such as the electric conductivity and work functions, change exponentially in time as a result of the adsorption of molecules. In Ref. 12, for example, it is shown that for adsorption of gases on germanium and silicon surfaces the kinetic curves of the electronic work function of the semiconductor (in the region of small variations of the work function) can be approximated by an exponential dependence. Taking into account the exponential character of the time-dependence of the barrier height, we can write expression (3) in the form

$$\ln\frac{I_{H_2}}{I} = -\frac{\Delta\Phi_{BST}}{kT}\left[1 - \exp\left(-\frac{t}{\tau}\right)\right]. \quad (4)$$

Let $-(\Delta\Phi_{BST}/kT) = \ln(I_{H_2ST}/I)$, where I_{H_2ST} is the stationary value of the current. We then obtain

$$\ln\frac{I_{H_2}}{I} = \ln\frac{I_{H_2ST}}{I} - \ln\frac{I_{H_2ST}}{I}\exp\left(-\frac{t}{\tau}\right). \quad (5)$$

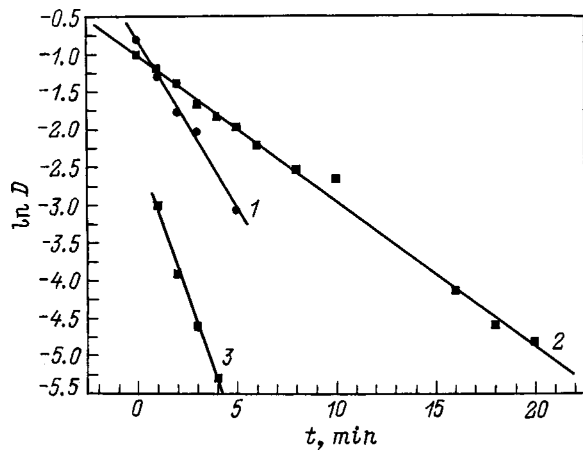

FIG. 4. The quantity characterizing the change in the current of Pd/*p*-InGaAsP (*1*) and Pd/*n*-InGaAs (*2*, *3*) structures versus time for various hydrogen concentrations in air N_{H_2}, %: *1*—0.1, *2*—0.5, *3*—1.0.

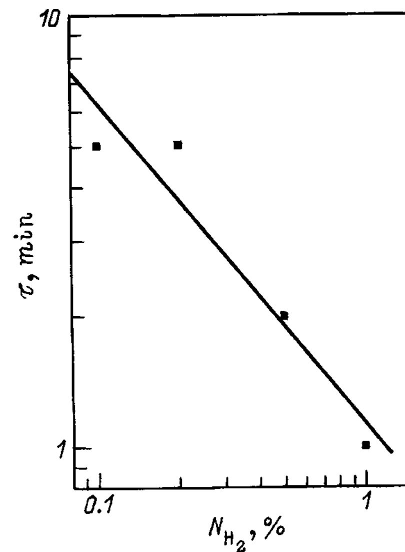

FIG. 5. The response time of a Pd/*n*-InGaAs structure versus the hydrogen concentration in air.

It thus follows that the time-dependence of I_{H_2} is linear in the coordinates $\ln D$ versus t, where

$$\ln D = \ln\left|\ln\frac{I_{H_2\mathrm{ST}}}{I} - \ln\frac{I_{H_2}}{I}\right|. \quad (6)$$

The time dependence of I_{H_2} for *p*-InGaAsP-based structures in the indicated coordinates is shown in Fig. 4 (curve *1*). The characteristic time τ appearing in the argument of the exponent is 2 min. Figure 4 also shows ln*D* versus the time for structures based on the solid solution *n*-InGaAs for various hydrogen concentrations (curves *2* and *3*). As the hydrogen concentration N_{H_2} increases from 0.1 to 1%, the characteristic time τ decreases from 5 min to 1 min. The hydrogen concentration dependence of the time τ (Fig. 5) can be approximated by a power-law function $\tau \sim N_{H_2}^{-m}$ for adsorption processes, where the exponent m is 0.7. Extrapolation of the dependence of τ on N_{H_2}, which we obtained for Pd/*n*-InGaAs structures, to lower and higher hydrogen concentrations gives good agreement with the response times for Pd/*n*-InP structures investigated in Ref. 4 (12 min for a 0.01% H_2 in nitrogen and 1.3 s for 100% H_2). In Ref. 12 a similar dependence of τ on N_{H_2} was obtained for adsorption on germanium of molecules of substances such as alcohol, acetone, and carbon monoxide. The exponent m is close to 0.5, irrespective of the type of adsorbed molecules.

Comparing the response times of barrier structures based on solid solutions and the Pd/*n*-Si structures which we investigated showed that τ is several times greater for the silicon-based structures. For a 0.5% hydrogen concentration it is 12 min. The dependence of the response time on the type of semiconductor serves as an argument in favor of the model that explains the hydrogen sensitivity of barrier structures by the interaction of hydrogen with the semiconductor surface. Another argument in favor of such a model is that the response time (especially for silicon-based barrier structures) assumes rather high values. Since the hydrogen diffusion in palladium is high ($\sim 10^7$ cm^2/s at room temperature[13]), it is difficult to imagine that the process leading to the establishment of an equilibrium state on the inner surface of palladium can last for 10 min. At the same time, it was shown that for adsorption the surface of semiconductors such as germanium and silicon is charged slowly, and the time for establishing a stationary value of the electronic work function of the semiconductor reaches 100 min.[12]

In summary, our investigations have shown that the kinetics of the hydrogen-induced change in the current in Pd/*p*-InGaAsP and Pd/*n*-InGaAs barrier structures can be described on the basis of a model of adsorption of hydrogen atoms on the semiconductor surface. It was established that the response time of the structures decreases with increasing hydrogen concentration in the gas mixture.

We thank S. V. Ponomarev for growing the epitaxial layers of the solid solutions and V. P. Germogenov for helpful discussions.

[1] G. G. Kovalevskaya, M. M. Meredov, E. V. Russu, Kh. M. Salikhov, and S. V. Slobodchikov, Zh. Tekh. Fiz. **63**(2), 185 (1993) [Tech. Phys. **38**, 149 (1993)].
[2] V. I. Gaman, P. N. Drobot, M. O. Duchenko, and V. M. Kalygina, Poverkhnost', No. 11, 64 (1996).
[3] G. G. Kovalevskaya, L. Kratena, M. M. Meredov, A. M. Marinova, and S. V. Slobodchikov, Pis'ma Zh. Tekh. Fiz. **15**(12), 55 (1989) [Sov. Tech. Phys. Lett. **15**, 478 (1989)].
[4] M. Yousuf, B. Kuliyev, B. Lalevic, and T. L. Poteat, Solid-State Electron. **25**, 753 (1982).
[5] S. V. Slobodchikov, G. G. Kovalevskaya, M. M. Meredov, E. V. Russu, and Kh. M. Salikhov, Fiz. Tekh. Poluprovodn. **28**, 1155 (1994) [Semiconductors **28**, 659 (1994)].
[6] S. V. Tikhov, V. P. Lesnikov, V. V. Podol'skiĭ, and M. V. Shilova, Zh. Tekh. Fiz. **65**(11), 120 (1995) [Tech. Phys. **40**, 1154 (1995)].
[7] V. I. Gaman, M. O. Duchenko, and V. M. Kalygina, Izv. Vyssh. Uchebn. Zaved. Fiz. No. 1, 69 (1998).
[8] J. S. Escher, L. W. James, R. Sankaran, G. A. Antypas, R. L. Moon, and R. L. Bell, J. Vac. Sci. Technol. **13**, 874 (1976).

[9] S. V. Slobodchikov, G. G. Kovalevskaya, M. M. Meredov, A. V. Pentsov, E. V. Russu, and Kh. M. Salikhov, Pis'ma Zh. Tekh. Fiz. **17**(15), 1 (1991) [Sov. Tech. Phys. Lett. **17**, 535 (1991)].
[10] S. M. Sze, *Physics of Semiconductor Devices* [Wiley, New York, 1969; Mir, Moscow, 1984, Vol. 1, Chap. 5].
[11] V. G. Bozhkov, V. A. Kagadeĭ, and N. A. Torkhov, Izv. Vyssh. Uchebn. Zaved. Fiz. No. 8, 115 (1997).
[12] V. Litovchenko, Poluprovodnikovaya tekhnika i mikroélektronika, No. 9, 92 (1972).
[13] R. M. Barrer, *Diffusion in and through Solids* [Cambridge Univeristy Press, Cambridge, 1941; Inostr. Lit., Moscow, 1948, Chap. 5, p. 246].

Translated by M. E. Alferieff

LOW-DIMENSIONAL SYSTEM

Determination of the electron mobility and density in thin semiconductor films at microwave frequencies using the magnetoplasma resonance

P. A. Borodovskiĭ and A. F. Buldygin

Institute of Semiconductor Physics, Siberian Branch of the Russian Academy of Sciences, 630090 Novosibirsk, Russia

(Submitted May 5, 1998; accepted for publication March 3, 1999)
Fiz. Tekh. Poluprovodn. **33**, 1224–1228 (October 1999)

The results of experimental and theoretical investigations of the magnetoplasma resonance at microwave frequencies ($\omega/2\pi = 8$ GHz) in AlGaAs/GaAs heterostructures and n-$Cd_xHg_{1-x}Te$ films at liquid-nitrogen temperature are reported. To explain the experimental results, an expression is derived for the conductivity $\sigma_{xx}(\omega,B)$. It is shown that the parameters of the active layer in the samples — the electron mobility and density — can be determined by comparing the computational results with the experimental dependences. © *1999 American Institute of Physics.* [S1063-7826(99)01610-5]

1. INTRODUCTION

Magnetoplasma effects in semiconductors are ordinarily investigated experimentally in the infrared range, where $\omega\tau \gg 1$ (see, for example, Ref. 1). The plasma resonance frequency $\omega_p^2 = ne^2(m^*\varepsilon_0\varepsilon_r)^{-1}$ is determined by the electron density n and does not depend on the dimensions of the sample. The measured frequency dependences of the magnetoplasma reflection of light in a magnetic field perpendicular to the plane of the sample (Faraday geometry) also makes it possible to determine the electron effective mass m^* and the momentum relaxation time τ by comparing the measured and computed dependences.

Dimensional resonances (helicons), which occur when the sample thickness is an integer multiple of half-wavelengths, can be observed in experiments at microwave frequencies. Measurement of the wavelength in the sample at resonance makes it possible to determine the carrier density. Here the sample thickness is much greater than the skin-layer depth in a zero magnetic field.

A plasma resonance in small samples (approximately 3×3 μm), fabricated using photolithography followed by etching of the AlGaAs/GaAs heterostructure with a two-dimensional electron gas (2DEG), was first observed in Ref. 2. The plasma frequency was determined by the density n_s and the diameter $2a$ of the electron disk:

$$\omega_p^2 = \pi e^2 n_s [am^*(1+\varepsilon_r)\varepsilon_0]^{-1}.$$

In a magnetic field B the resonance absorption frequency decreased from 575 GHz ($B=0$) to 120 GHz ($B=5$ T). The experiments were performed at 1.4 K temperature and the condition $\omega\tau \gg 1$ was satisfied. In subsequent works, the magnetoplasma resonances (MPRs) were also observed at low frequencies ($\omega\tau \ll 1$) in samples with sufficiently large transverse dimensions, for example, 3×4 mm (Ref. 3) and 10×11 mm.[4] It should be noted that these experiments have also been conducted at liquid-helium temperature and MPRs have been observed in quite high magnetic fields, such that $\sigma_{xy} \gg \sigma_{xx}$, where σ_{xx} and σ_{xy} are the components of the conductivity tensor of the 2DEG. The observed resonances are called edge magnetoplasmons (EMPs). A rigorous theory of EMPs has been constructed by Volkov and Mikhaĭlov.[5]

In the present paper we report the results of an experimental investigation of MPRs in thin-film samples at 77 K in magnetic fields such that the transmission of a microwave signal at frequency $\omega < \omega_p$ is determined by the diagonal component σ_{xx} of the conductivity tensor. The microwave conductivity of the sample in this case is a complex quantity when $\omega\tau \ll 1$. This occurs for sample dimensions that are small compared with the microwave wavelength ($a \ll \lambda/\sqrt{\varepsilon_r}$), so that the microwave field inside the sample depends on the permittivity $\varepsilon_0\varepsilon_r$, the transverse dimensions, and the shape of the sample. In Ref. 2, a simple theoretical model was used to determine the microwave conductivity for a sample in the form of an oblate ellipsoid (spheroid) with a small thickness δ and depolarizing factor known from electrostatics. We use similar approach here to analyze theoretically microwave transmission in a waveguide with a thin-film sample. The briefly described approximate theory of microwave measurements is applicable when

$$a \ll \lambda/\sqrt{\varepsilon_r}, \quad \omega \ll \sigma/\varepsilon_0\varepsilon_r, \quad \omega \ll (\delta^2\sigma\mu_0)^{-1},$$

where μ_0 is the magnetic permeability. The last condition imposed on the frequency means that the film thickness δ must be much less than the skin-layer depth at the microwave frequency ω of the signal.

2. CALCULATION OF THE MICROWAVE TRANSMISSION COEFFICIENTS

Before discussing the experimental results we shall establish the formulas for calculating the microwave transmis-

 © 1999 American Institute of Physics

sion coefficient. The theoretical calculation of the reflection coefficient Γ and the transmission coefficient T for a conducting film that completely covers the cross section of a rectangular waveguide with the basic type of wave H_{10} has been examined in Ref. 6. For $\gamma\delta\ll 1$ (γ is the propagation constant in a conducting medium) and the conductivity is $\sigma_s=\sigma\delta=en_s\mu$, the formulas for Γ and T have the simple form

$$\Gamma=\bar{\sigma}(2+\bar{\sigma})^{-1}, \tag{1}$$

$$T=2(2+\bar{\sigma})^{-1}, \tag{2}$$

where $\bar{\sigma}=\sigma_s Z_g$, and $Z_g=120\pi\lambda_g/\lambda$ is the characteristic impedance of the waveguide. The microwave absorption coefficient is

$$A=1-\Gamma^2-T^2=2\bar{\sigma}(2+\bar{\sigma})^{-2}. \tag{3}$$

It follows from the expression (3) that the microwave absorption is maximum for $\sigma=\sigma_s Z_g=2$. However, the microwave transmission varies monotonically as function of σ and has no minimum, since as the microwave absorption in the film increases, the reflection coefficient, correspondingly, decreases. Thus, for active conductivity (for $\omega\tau\ll 1$) the coefficient $T(B)$ for a microwave signal has no minimum.

We note that for $\omega\tau>1$ the conductivity becomes complex $\bar{\sigma}=\bar{\sigma}_{\mathrm{Re}}+i\bar{\sigma}_{\mathrm{Im}}$; the real part $\bar{\sigma}_{\mathrm{Re}}$ is determined by the microwave absorption and the imaginary part (the reactive conductivity) $\bar{\sigma}_{\mathrm{Im}}$ gives rise to a change in phase of the reflected and transmitted microwave signals. In this case, a minimum can appear in the measurement of the magnetic-field dependence of the modulus of the transmission coefficient $|T(B)|$. However, this question falls outside the scope of this work, and in what follows we shall consider the complex conductivity arising in a small sample as a result of magnetoplasma effects for $\omega\tau\ll 1$, $\omega<\omega_p$.

Using the theoretical model proposed in Ref. 2, it can be shown that the microwave conductivity of a small sample placed at the center of the cross section of a waveguide is given by

$$\sigma_{\pm}(\omega,B)=\frac{F\sigma_s}{1-i\omega\tau(\omega_p^2/\omega^2-1)\pm i\omega_c\tau}, \tag{4}$$

where the coefficient $F<1$, which takes into account the degree to which the film sample fills the cross section of the waveguide, depends on the dimensions of the sample, $\sigma_s=en_s\mu$, $n_s=n\delta$, $\mu=e/m^*\tau$, and $\omega_c=e/m^*B$ is the cyclotron frequency. According to the more accurate formula of Ref. 7, for diskotic film samples the plasma frequency is

$$\omega_p^2=3\pi e^2 n_s[8am^*\varepsilon_0(1+\varepsilon_r)]^{-1},$$

where a is the radius of the disk, and ε_r is the relative permittivity of the substrate. The signs $\pm$ in the denominator of Eq. (4) correspond to the left- and right-hand circular microwave polarizations. As is well known, a linearly polarized wave can be represented as a superposition of two waves with left- and right-hand polarizations.

The MPR effect occurs when the imaginary part in the denominator of Eq. (4) is zero, i.e., for $\omega\tau(\omega_p^2/\omega^2-1)\mp\omega_c\tau=0$. Therefore, the MPR frequency is

$$\omega=\sqrt{\omega_p^2+\omega_c^2/4}\pm\omega_c/2. \tag{5}$$

In our case, for $\omega<\omega_p$ we shall be dealing with the low-frequency branch of the MPR, for which the resonance frequency decreases as $1/B$ with increasing magnetic field, since

$$\omega=\frac{\omega_p^2-\omega^2}{\omega_c}\simeq\frac{\omega_p^2}{\omega_c}\sim\frac{1}{B}.$$

As is well known,[1] for right- and left-hand circular microwave polarizations the conductivity can be represented in the form $\sigma_{\pm}=\sigma_{xx}\mp\sigma_{xy}$. Evidently, the transmission coefficient will also have two values T_+ and T_-. In approximate calculations, we shall calculate the modulus $|T_B|$ of the transmission coefficient, substituting the conductivity $\bar{\sigma}_{xx}=(\bar{\sigma}_+ +\bar{\sigma}_-)/2$ into Eq. (1). Then

$$|T_B|=\left[\left(1+\frac{\bar{\sigma}_{\mathrm{Re}}}{2}\right)^2+\frac{\sigma_{\mathrm{Im}}^2}{4}\right]^{-1}, \tag{6}$$

$$\bar{\sigma}_{\mathrm{Re}}=F\sigma_s Z_g(1+\mu^2B^2+\alpha^2)[(1+\mu^2B^2-\alpha^2)^2+4\alpha^2]^{-1} \tag{7}$$

$$\bar{\sigma}_{\mathrm{Im}}=F\sigma_s Z_g\alpha(1-\mu^2B^2+\alpha^2)[(1+\mu^2B^2-\alpha^2)+4\alpha^2]^{-1}, \tag{8}$$

where $\alpha=\omega\tau(\omega_p^2/\omega^2-1)$, and $\mu B=\omega_c\tau$. Analysis of the formulas presented above shows that the minimum of the modulus of the transmission coefficient, i.e., the MPR, occurs in a magnetic field $B=B_m$ determined by the condition

$$\mu B_m=\alpha[2\sqrt{1+1/\alpha^2}-(1+1/\alpha^2)]^{1/2}, \tag{9}$$

$$\mu B_m\simeq\alpha \quad \text{for} \quad 1/\alpha^2\ll 1.$$

It is obvious that an MPR is observed if $\alpha\gtrsim 1$, but this does not require that $\omega\tau>1$, since $\omega\tau$ can be quite small when $\omega_p^2/\omega^2\gg 1$.

For a small sample, the fraction of the transmitted microwave power that is absorbed by the sample is small, and to observe an MPR it is desirable to record the relative change in the transmission coefficient in a magnetic field:

$$\Delta T/|T_0|=|T_B|/|T_{B=0}|-1.$$

In the absence of an MPR, i.e., for $\omega\gtrsim\omega_p$ and $\omega\tau\ll 1$, when $\alpha\ll 1$, a simple formula can be obtained for the relative change in the microwave transmission coefficient in a magnetic field:

$$\Delta T/|T_0|\simeq\frac{\bar{\sigma}_0}{2}\mu^2B^2\left[\mu^2B^2+\left(1+\frac{\bar{\sigma}_0}{2}\right)^2\right]^{-1},$$

$$\bar{\sigma}_0=F\sigma_s Z_g. \tag{10}$$

The effect of the substrate was disregarded in the derivation of the formulas for the approximate calculation of the transmission coefficient $|T|$. It was assumed that the thickness d of the substrate with permittivity $\varepsilon_0\varepsilon_r$ is much less than the wavelength ($d\ll\lambda/\sqrt{\varepsilon_r}$).

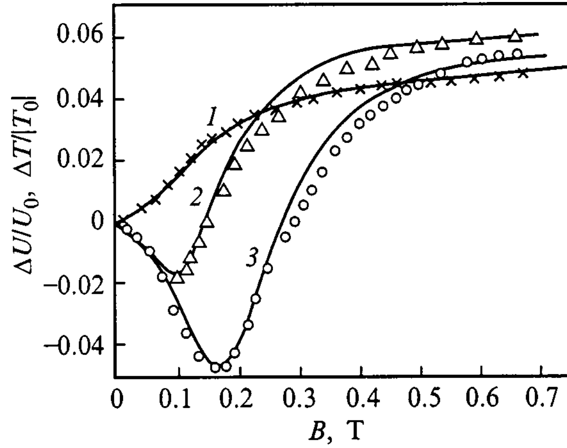

FIG. 1. Magnetic-field dependences of the microwave transmission of a waveguide with an n-AlGaAs/GaAs sample at liquid-nitrogen temperature. The numbers on the curves correspond to the sample numbers in Table I.

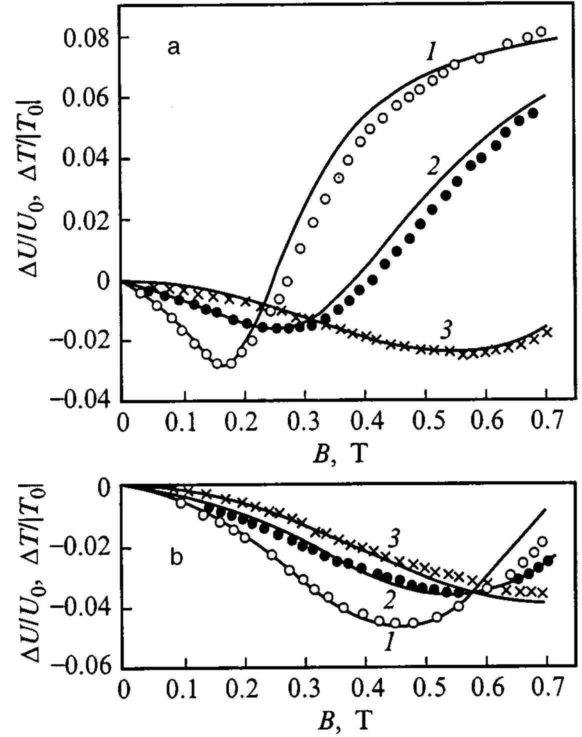

FIG. 2. Measured (symbols) and computed (solid lines) magnetic-field dependences of the microwave transmission of a waveguide containing the sample. Samples with an n-$Cd_xHg_{1-x}Te$ film (see Table I) with composition and thickness δ: a — $x=0.22$, $\delta=9$ μm; b — $x=0.23$, $\delta=10.8$ μm. Temperature T, K: *1*—80, *2*—130, *3*—150.

3. EXPERIMENTAL RESULTS

AlGaAs/GaAs heterostructures and n-CdHgTe (CHT) epitaxial films grown on GaAs substrates by molecular-beam epitaxy were used for the experiments. The dimensions of the samples in the first group were approximately 3×3 mm. The samples with an epitaxial CHT film were prepared using photolithography followed by etching to obtain 0.7×0.7-mm mesa structures separated by 0.3 mm (16 mesa structures on a 4×4-mm substrate).

For microwave measurements the samples were placed between thin mica sheets in the central part of the cross section of a rectangular waveguide (5×23 mm). The waveguide section containing the sample was placed between the poles of an electromagnet and cooled with liquid nitrogen. A similar apparatus is described in greater detail in Ref. 8. The measurements were performed at 8 GHz. The output voltage U_B of the microwave detector, proportional to the modulus $|T_B|$ of the transmission coefficient (linear detection regime), was measured with a digital voltmeter and fed simultaneously into the Y input of a recorder. The voltage from a Hall sensor, proportional to the magnetic field, was fed into the X input. Compensating the voltage U_0 from the detector at the initial point ($B=0$) and using a recorder with 1 mV/cm sensitivity, it is possible to detect reliably small changes in the transmission coefficient by scanning the magnetic field from 0 to 0.7 T (with accuracy $\Delta U/U_0\simeq10^{-3}$).

Figure 1 shows the results of measurements of $\Delta U(B)/U_0$ and the computed dependences $\Delta T(B)/|T_0|$ for three samples fabricated from AlGaAs/GaAs heterostructures with different electron densities n_s. An MPR effect is not observed in sample 1, and Eq. (10) can be used to determine the electron mobility μ and the effective conductivity $\bar{\sigma}_0=Fen_s\mu Z_g$. For the other two samples an MPR is observed (a minimum of the microwave transmission) for magnetic fields $B_m=0.09$ and 0.167 T. The plasma frequency,

$$\omega_p=\sqrt{\omega(\omega+e/m^*B_m)}, \qquad (11)$$

can be determined from the resonance condition (5) if B_m is known, and therefore the electron density n_s can be determined for the known dimensions of the sample. The parameters for which the computed dependences in Fig. 1 were determined are presented in Table I. The values $m^*/m_0=0.068$ and $\varepsilon_r=13$ were used, and the disk diameter $2a$ was assumed to be equal to the edge length of a square (see Table I for the dimensions). The values of n_s and $\omega_p/2\pi$ for sample 1 were estimated by comparing the adjustable parameter $\bar{\sigma}_0$ with the similar value of $\bar{\sigma}_0$ for sample 3, whose dimensions are approximately the same.

We did not perform Hall measurements on the experimental samples, but we can say that the values of μ and n_s in Table I agree with the certificate parameters of the structures

TABLE I.

Sample No. (structures)	Size in mm	μ, 10^4 cm^2/(V·s)	n_s, 10^{11} cm^{-2}	$\bar{\sigma}_0$	$\omega_p/2\pi$, GHz	$\omega\tau$	$\omega\tau(\omega_p^2/\omega^2-1)$
1(GA106R)	3×3	6.8	3.26	0.104	15.58	0.132	0.37
2(GA17123)	2.7×2.8	11.5	5.26	0.28	19.8	0.223	1.15
3(GA33R)	3×3.3	9.5	10.3	0.41	25	0.185	1.62

TABLE II.

	n-$Cd_{0.22}Hg_{0.78}Te$				n-$Cd_{0.23}Hg_{0.77}Te$			
T, K	μ, 10^4 $cm^2/(V \cdot s)$	n_s, 10^{11} cm^{-2}	$\bar{\sigma}_0$	ω_p/ω	μ, 10^4 $cm^2/(V \cdot s)$	n_s, 10^{11} cm^{-2}	$\bar{\sigma}_0$	ω_p/ω
80	7.2	1.5	0.42	8.35	2.9	5.57	0.54	13
130	3.7	2.36	0.39	9.925	2.24	6.74	0.48	13.75
150	2.1	4.98	0.36	14	1.8	9.88	0.52	16.375

used to prepare the samples. For example, for sample 2 the certificate parameters (Hall mobility and electron density) are $\mu_H = 1.38 \times 10^5$ $cm^2/(V \cdot)s$ and $n_s = 5.16 \times 10^{11}$ cm^{-2}, which are close to the values of μ and n_s presented in Table I. It should be noted that when the computed dependences $\Delta T(B)/|T_0|$ are fitted to the experimental dependences $\Delta U(B)/U_0$ using Eqs. (6)–(10), the value of the parameter μ is less critical than that of ω_p, so that the error in determining the electron mobility μ is greater than that for n_s.

The results of the measurements and calculations for two samples with CdHgTe (CHT) films at temperatures 80, 130, and 150 K are shown in Figs. 2a and 2b. As is well known, the electron density increases with temperature and, as one can see from Fig. 2, the MPR shifts into the range of high magnetic fields. It should be noted that the electron effective mass m^*/m_0 also changes appreciably, which was taken into account in the calculations (the data from Ref. 9 were used). The parameters obtained by comparing the experimental and the computed dependences are presented in Table II. The first sample, fabricated from an epitaxial structure with film thickness $\delta = 9$ μm, possesses at $T = 80$ K the established values of the volume density $n = n_s/\delta = 1.66 \times 10^{14}$ cm^{-3} and mobility $\mu = 7.2 \times 10^4$ $cm^2/(V \cdot s)$, close to the Hall parameters of the initial structure at liquid-nitrogen temperature: $n_H = 2.3 \times 10^{14}$ cm^{-3} and $\mu_H = 7.8 \times 10^4$ $cm^2/(V \cdot s)$. For the second sample, with film thickness $\delta = 10.8$ μm, the parameters $n = 5.15 \times 10^{14}$ cm^{-3} and $\mu = 2.9 \times 10^4$ $cm^2/(V \cdot s)$ established at 80 K differ substantially from the Hall measurements for the initial epitaxial structure: $n_H = 10^{15}$ cm^{-3} and $\mu_H = 1.2 \times 10^5$ $cm^2/(V \cdot s)$. This discrepancy could possibly be explained by the nonuniformity of the film parameters over the area, and Hall measurements directly on the experimental samples are required. At temperatures 130 and 150 K, the electron densities established from the MPR (see Table II) agree well with the values $n_s = n\delta = 6.64 \times 10^{11}$ cm^{-2} and $n_s = 9.8 \times 10^{11}$ cm^{-2} obtained from the calculation using the formulas from Ref. 9.

It should also be noted that the formulas for calculating $\Delta T(B)/|T_0|$ were obtained without allowance for the Faraday rotation and the concomitant ellipticity, which could already be substantial for film thickness on the order of 10 μm with sufficiently high electron mobility and density.

4. CONCLUSIONS

On the whole, it can be concluded that the magnetoplasma resonance method at microwave frequencies can be used as a rapid, contact-free method for determining the density and mobility of electrons in small, thin-film samples and mesa structures on high-resistance substrates.

We wish to thank A. I. Toropov, N. T. Moshegov, Yu. G. Sidorov, and V. S. Varavin for providing the thin-film semiconductor structures. We also thank V. V. Vasil'ev and T. I. Zakhar'yash for preparing samples with $Cd_xHg_{1-x}Te$ films.

[1] K. Seeger, *Semiconductor Physics* [Springer-Verlag, New York, 1973; Mir, Moscow, 1977, p. 148].
[2] S. A. Allen, Jr., H. L. Störmer, and J. C. M. Hwang, Phys. Rev. B **28**, 4875 (1983).
[3] S. A. Govorkov, M. I. Reznikov, A. P. Senichkin, and V. I. Tal'yanskiĭ, JETP Lett. **44**, 487 (1986).
[4] M. Wassermeier, J. Oshinow, J. P. Cotthaus, A. H. Mac Donald, C. T. Foxon, and J. J. Harris, Phys. Rev. B **41** 10 287 (1990).
[5] V. A. Volkov and S. A. Mikhaĭlov, Zh. Éksp. Teor. Fiz. **94**, 217 (1988) [Sov. Phys. JETP **67**, 121 (1988)].
[6] R. L. Ramey and T. S. Lewis, J. Appl. Phys. **39**, 1747 (1968).
[7] R. P. Leavitt and J. W. Little, Phys. Rev. B **34**, 2450 (1986).
[8] P. A. Borodovskiĭ, A. F. Buldygin, and S. A. Studenikin, Avtometriya, No. 4, 59 (1966).
[9] G. L. Hansen and J. L. Schmit, J. Appl. Phys. **54**, 1963 (1983).

Translated by M. E. Alferieff

Modeling of the electron distribution in AlGaAs/GaAs (δ-Si) structures grown on vicinal surfaces

V. M. Osadchiĭ

Institute of Semiconductor Physics, Siberian Branch of the Russian Academy of Sciences, 630090 Novosibirsk, Russia

(Submitted February 2, 1999; accepted for publication March 3, 1999)
Fiz. Tekh. Poluprovodn. **33**, 1229–1231 (October 1999)

The potential and electron density distributions in AlGaAs/GaAs (δ-Si) structures grown on vicinal surfaces are calculated. It is shown that a lateral superlattice can form in the structures. The optimal technological parameters for obtaining a superlattice are estimated.
© *1999 American Institute of Physics.* [S1063-7826(99)01710-X]

Low-dimensional structures with vicinal interfaces, which make it possible to obtain δ-layered, laterally modulated doping in the structures and thereby to influence the charge-carrier transport, have recently been studied.[1,2] It is of interest to investigate the effect of the technological parameters on the distribution of the potential and the density of two-dimensional electrons in such structures. We have accordingly performed model calculations of these distributions in an AlGaAs/GaAs (δ-Si) structure with a GaAs vicinal boundary. The δ-doped layer was treated as a periodic system of charged filaments, separated by distance d, with linear charge density N and located at a distance t (spacer thickness) from the potential well in GaAs (Fig. 1). Strictly speaking, a self-consistent system of equations, including the Poisson and Schrödinger equations, must be solved to determine the potential in such a structure. This is a difficult problem in the two-dimensional case. We confined our attention to solving the two-dimensional Poisson equation in the Thomas–Fermi approximation,[3] since it is known that this approach gives for a δ-doped quantum well a potential that is very close to that obtained in self-consistent calculations.[4] The Poisson equation was solved numerically, taking into account the electric neutrality of the system. To avoid singularities in the potential from the filaments, the latter were treated as having a finite thickness on the order of atomic dimensions. The computational results changed very little when the thickness of the filament was increased severalfold.

As expected, the calculations showed that the potential and electron density distributions in the GaAs well along the heterojunction is periodic. The maximum density occurs at a coordinate along the boundary corresponding to the position of the filament and the minimum density occurs midway between two filaments. The degree of modulation of the density, i.e., the difference between the maximum and minimum values, is large in structures with extremely small spacer thickness. As the spacer thickness increases, the degree of modulation decreases appreciably. For example, for a structure with period $d = 16$ nm and spacer thickness $t = 10$ nm there is virtually no modulation of the distribution, since here the electron gas in a GaAs well is located at a distance from the filaments comparable to the distance between the filaments. The degree of modulation increases with the period of the system of filaments.

The dependence of the electron density distribution in the GaAs well on the charge density on a filament is interesting (Fig. 2). The degree of modulation of the potential increases with the charge, which at first increases the modulation of the density. However, large N causes overlapping of the two-dimensional electron gas (2DEG) in the GaAs well,

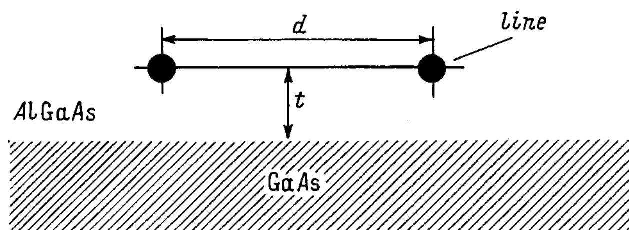

FIG. 1. Schematic representation of the simulated structure.

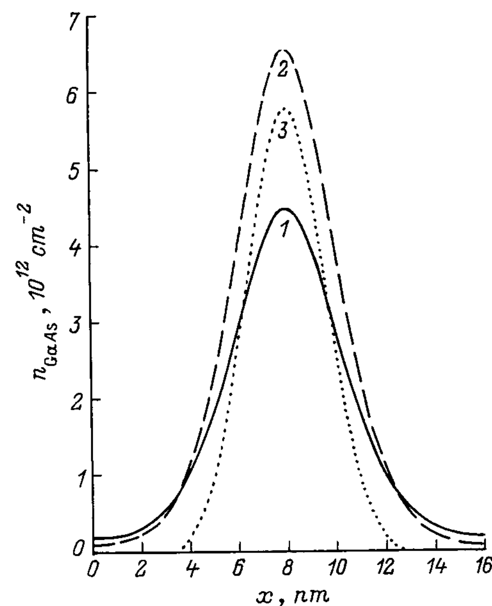

FIG. 2. Density distribution of an electron gas in a GaAs well for linear charge density on the filament, N, cm^{-1}: *1*—4×10^6, *2*—6×10^6, *3*—8×10^6. Spacer thickness $t=3$ nm.

 © 1999 American Institute of Physics

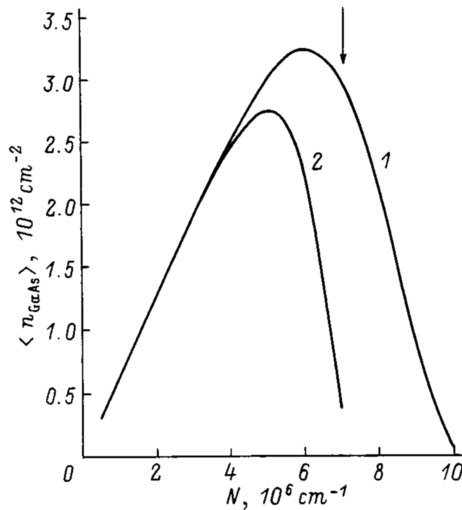

FIG. 3. Average electron density $\langle n_{\mathrm{GaAs}}\rangle$ in a GaAs well versus the charge N on a filament for a 16-nm period and a 3-nm (*1*) and 5-nm (*2*) spacer thicknesses. The arrow indicates for curve *1* the density N_1, above which the gas in GaAs decomposes into a system of one-dimensional channels.

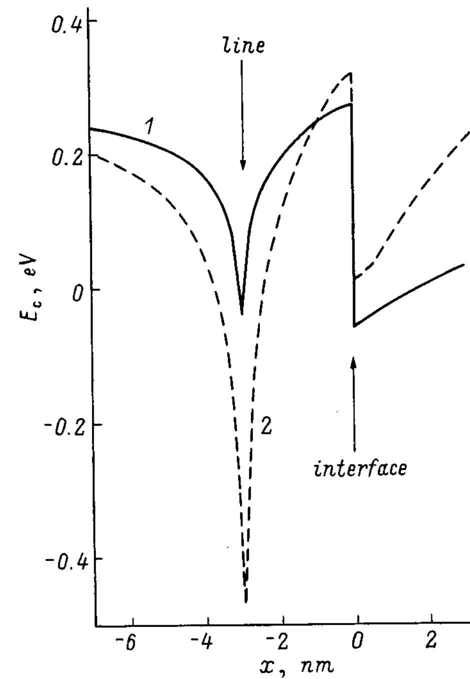

FIG. 4. Profile of the conduction band edge E_c perpendicular to the heterojunction for a structure with a 16-nm period, spacer thickness 3 nm, and filament charges 4×10^6 cm^{-1} (*1*) and 10^7 cm^{-1} (*2*). E_c is measured from the position of the Fermi level.

and the gas decomposes into a system of isolated one-dimensional channels — quantum wires. Such systems could be interesting from the standpoint that the transverse motion in them is quantized, and the conductivity along these channels can be high.[5] The density N at which a transition occurs to a system of one-dimensional channels depends on the spacer thickness. For $t=2$ nm and $d=16$ nm the overlapping of the 2DEG occurs when $N>4\times10^6$ cm^{-1}, and for $t=3$ nm it occurs when $N>6\times10^6$ cm^{-1}. For $t=1$ nm overlapping of the 2DEG occurs at least at $N=5\times10^5$ cm^{-1}. When the period of the system of filaments is large, decomposition of the 2DEG into a system of quantum wires starts at a larger spacer thickness for the same charge density on the filament: for $d=32$ nm and $t=5$ nm this occurs even for $N=5\times10^5$ cm^{-1}. It is obvious that the conductivity in such structures should be anisotropic, especially with a transition to a system of quantum wires.

Figure 3 shows the density of the electron gas in a GaAs well, averaged over the period $d=16$ nm, as a function of the linear charge density on a filament. These dependences are nonmonotonic, in contrast to the dependences for ordinary structures with modulated doping. This is explained by the characteristic features of the screening of the potential of a charged filament by the electron gas. As our numerical calculations showed, the screening of the filament charge by electrons is weaker than the screening of planar charge. As the charge on a filament increases, the potential well around it becomes deeper (Fig. 4) and increasingly larger number of electrons are confined in the potential well around the filament. For filament period $d=16$ nm, the 2DEG density reaches high values — about 3×10^{12} cm^{-2}. For a spacer with $t=3$ nm, decomposition into a system of one-dimensional channels already occurs soon after the maximum, and at the maximum itself we have a high degree of density modulation (Fig. 2, curve *2*). As the spacer thickness increases, the 2DEG density decreases (Fig. 3, curve *2*).

In summary, we have simulated the potential distribution and electron density distribution in AlGaAs/GaAs (δ-Si) structures grown on vicinal surfaces. The computational results show that a lateral superlattice can form. For a 16-nm lattice period the optimal parameters are a linear charge density $(5-6)\times10^6$ cm^{-1} on the filaments and spacer thickness 3–5 nm. The two-dimensional electron gas density is about 3×10^{12} cm^{-2} with a large modulation amplitude. For high charge densities of the filaments, the two-dimensional electron gas decomposes into a system of one-dimensional channels — quantum wires.

This work was supported by the Russian Fund for Fundamental Research (Project No. 96-02-19371a).

[1] V. I. Kadushkin, V. A. Kul'bachinskiĭ, E. V. Bogdanov, and A. V. Senichkin, Fiz. Tekh. Poluprovodn. **28**, 1889 (1994) [Semiconductors **28**, 1042 (1994)].
[2] V. I. Kadushkin and E. L. Shanina, Fiz. Tekh. Poluprovodn. **30**, 1676 (1996) [Semiconductors **30**, 876 (1996)].
[3] L. D. Landau and E. M. Lifshitz, *Quantum Mechanics. The Nonrelativistic Theory* [Pergamon Press, New York; Nauka, Moscow, 1974, p. 302].
[4] Z. D. Kvon and A. G. Pogosov, Fiz. Tekh. Poluprovodn. **25**, 138 (1991) [Sov. Phys. Semicond. **25**, 82 (1991)].
[5] H. Sakaki, Jpn. J. Appl. Phys. **19**, L735 (1980).

Translated by M. E. Alferieff

Effect of the configuration of a quantum wire on the electron–phonon interaction

O. V. Kibis*)

Novosibirsk State Technical University, 630092 Novosibirsk, Russia

(Submitted July 13, 1998; accepted for publication March 15, 1999)
Fiz. Tekh. Poluprovodn. **33**, 1232–1234 (October 1999)

The dissipation of the electric current on acoustic phonons in a one-dimensional conductor is of an activational character. The activation energy of phonon scattering of an electron depends on the spatial configuration of the conductor. For this reason, electron scattering by phonons can be substantially weakened and the phonon contribution to the resistance thereby can be decreased by choosing an appropriate form of the conductor. © *1999 American Institute of Physics.* [S1063-7826(99)01810-4]

One of the high-priority problems in modern semiconductor physics is to develope structures with prescribed values of the electrical parameters, most importantly the conductivity. It is known that the conductivity of real structures is limited by scattering by lattice defects and by phonons. Modern technologies make it possible to eliminate defects of the crystal structure, while in order to decrease phonon scattering it is necessary to develop a method for controlling the electron–phonon interaction. Previous investigations[1,2] have shown that the matrix elements of the electron–phonon interaction can be substantially decreased and the phonon scattering mechanism can therefore be substantially suppressed by creating artificial crystal structures with prescribed parameters of the electron energy spectrum or by manipulating the electron energy spectrum in two- and three-dimensional systems by means of external perturbations (quantizing magnetic field, static deformation of the crystal, and others).

A qualitatively different (and substantially more effective) method of decreasing scattering by phonons can be implemented in one-dimensional conducting structures (quantum wires) with a nonlinear configuration. The physical factor responsible for the effect of the configuration of a quantum wire (QW) on the phonon scattering of electrons is that the potential of any elementary interaction in a solid (electron–electron, electron–photon, electron–phonon, and so on) is three-dimensional, while the translational motion of an electron in a QW is one-dimensional. By prescribing the electron trajectory in three-dimensional space by means of the configuration of the QW it is possible to change qualitatively the effective interaction potential. This was first noted in Ref. 3. Subsequent investigations[4,5] have shown that the configuration of the wire influences very critically the electron–electron and electron–photon interaction processes. In this sense, the electron–phonon interaction also should not be ruled out. As will be shown below, electron scattering by acoustic phonons can be greatly weakened by making an appropriate choice of the form of the QW.

Real QWs are conducting channels which are embedded in a three-dimensional crystal. For this reason, phonon scattering in QWs is due to the interaction with three-dimensional phonons and the electron–phonon interaction potential at the point $\mathbf{r}$, in general, has the form

$$U(\mathbf{r},\mathbf{q},t)=\widetilde{U}(\mathbf{q})\exp(i\,\mathbf{q}\cdot\mathbf{r})\exp[-i\widetilde{\varepsilon}(\mathbf{q})t/\hbar], \tag{1}$$

where $\mathbf{q}$ is the three-dimensional phonon wave vector, $\widetilde{\varepsilon}(\mathbf{q})$ is the phonon energy, and the explicit form of the function $\widetilde{U}(\mathbf{q})$ depends on the choice of the specific model of the electron–phonon interaction. The electron wave function in a one-dimensional rectilinear conductor is

$$\psi_k(s,t)=\sqrt{1/L}\,\exp(i\,k\,s)\exp[-i\varepsilon(k)t/\hbar], \tag{2}$$

where k is the wave number corresponding to the motion of an electron along the QW, s is the coordinate measured along the QW, L is the length of the QW, and $\varepsilon(k)=\hbar^2k^2/2m$ is the electron energy. In accordance with the standard quantum-mechanical relations, the lifetime $\tau(k)$ for an electron in the state k in the presence of the perturbation (1) is determined by the expression

$$\frac{1}{\tau(k)}=\sum_{\mathbf{q}}\frac{1}{\tau(k,\mathbf{q})}, \tag{3}$$

where

$$\frac{1}{\tau(k,\mathbf{q})}=\frac{2\pi}{\hbar}\sum_{k'}\{1-f[\varepsilon(k')]\}\times\{|U^{(-)}_{k'k}(\mathbf{q})|^2\delta[\varepsilon(k')-\varepsilon(k)-\widetilde{\varepsilon}(\mathbf{q})]+|U^{(+)}_{k'k}(\mathbf{q})|^2\delta[\varepsilon(k')-\varepsilon(k)+\widetilde{\varepsilon}(\mathbf{q})]\} \tag{4}$$

determines the electron lifetime $\tau(k,\mathbf{q})$ in the state k in the presence of an interaction with the phonon $\mathbf{q}$. Here $f[\varepsilon(k)]$ is the Fermi–Dirac distribution function

$$U^{(\pm)}_{k'k}(\mathbf{q})=\frac{\widetilde{U}^{(\pm)}(\mathbf{q})}{L}\int_{-L/2}^{L/2}\exp\{i[q_xx(s)+q_yy(s)+q_zz(s)]\}\exp[i(k-k')s]ds \tag{5}$$

is the matrix element of the electron–phonon interaction potential (1) for a transition of an electron from the state k into the state k', the signs $\pm$ in the matrix element correspond to phonon emission and absorption, and $x(s)$, $y(s)$, and $z(s)$ are the Cartesian coordinates of the point s on the one-dimensional conductor. We shall consider a QW embedded

 © 1999 American Institute of Physics

in a three-dimensional isotropic elastic continuum, characterized by density ρ and longitudinal sound velocity v_l, such that the Fermi velocity of the electrons in the QW satisfies $v_F \gg v_l$. We shall use the deformation potential method to describe the interaction of electrons with acoustic phonons, so that the expression (1) assumes the form

$$U(\mathbf{r},\mathbf{q},t) = \Xi \operatorname{div} \mathbf{u}(\mathbf{q}), \tag{6}$$

where Ξ is the deformation potential constant, and $\mathbf{u(q)}$ is the deformation vector of the elastic medium for a phonon with wave vector $\mathbf{q}$. For the interaction potential (6) $\tilde{U}^{(-)}(\mathbf{q})$ is given by

$$\tilde{U}^{(-)}(\mathbf{q}) = \left[\frac{\hbar n(q) q}{2V\rho v_l}\right]^{1/2} \Xi, \tag{7}$$

where $n(q)$ is the phonon occupation number, described by the Bose–Einstein function, and V is the volume of the three-dimensional elastic continuum. The quantity $\tilde{U}^{(+)}(\mathbf{q})$, corresponding to phonon emission, is obtained from Eq. (7) by formally replacing $n(q)$ with $n(q)+1$. With Eqs. (4)–(7) the expression (3) becomes

$$\frac{1}{\tau(k)} = \frac{\pi \Xi^2}{\rho v_l L^2 V} \sum_{\mathbf{q}} \sum_{k'} q\{1 - f[\varepsilon(k')]\} |J(k,k',\mathbf{q}|^2 \times \{n(q)\delta[\varepsilon(k') - \varepsilon(k) - \tilde{\varepsilon}(\mathbf{q})] + [n(q)+1]\delta[\varepsilon(k') - \varepsilon(k) + \tilde{\varepsilon}(\mathbf{q})]\}, \tag{8}$$

where

$$J(k',k,\mathbf{q}) = \int_{-L/2}^{L/2} \exp\{i[q_x x(s) + q_y y(s) + q_z z(s)]\} \exp\{i(k-k')s\} ds.$$

Since the Fermi surface in a QW consists of only two points, dissipation of the electric current in the QW occurs as a result of the scattering of electrons from one Fermi point into the other. It is obvious that in a rectilinear QW, such scattering processes are due to the interaction of electrons with phonons whose wave vector $q \geq 2k_F$. Since the energy of such phonons satisfies $\tilde{\varepsilon}(\mathbf{q}) \geq \tilde{\varepsilon}(2k_F)$ and is substantially different from zero for a prescribed value of the Fermi wave vector k_F, electron scattering by acoustic phonons in a QW is an inelastic process, in contrast to scattering by acoustic phonons in two- and three-dimensional systems. This results in a qualitatively different picture of current dissipation in a QW at low temperatures

$$T \ll \tilde{\varepsilon}(2k_{\mathrm{F}})/K_{\mathrm{B}}, \tag{9}$$

where $\tilde{\varepsilon}(2k_{\mathrm{F}}) = 2\hbar v_l k_{\mathrm{F}}$, and K_B is Boltzmann's constant. The scattering probability due to absorption of a phonon (the process 1 in Fig. 1) is exponentially small, since at low temperatures (9) there are few phonons with energy $\tilde{\varepsilon}(\mathbf{q}) \geq \tilde{\varepsilon}(2k_{\mathrm{F}})$. The scattering probability due to emission of a phonon (the process 2 in Fig. 1) is exponentially small because of the Pauli principle, since at temperatures corresponding to the inequality (9) the region of thermal broadening of the Fermi–Dirac distribution function near the Fermi

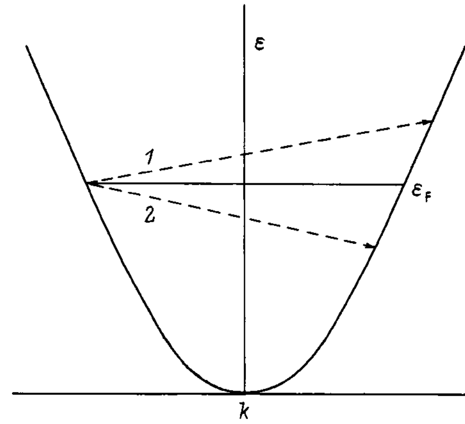

FIG. 1. Electron–phonon scattering processes near the Fermi energy ε_{F} in a rectilinear quantum wire: *1*—with phonon absorption, *2*—with phonon emission.

level is much smaller than the minimum energy $\tilde{\varepsilon}(2k_{\mathrm{F}})$ of the emitted phonon. Therefore, when the condition (9) holds, the probability of phonon scattering of an electron satisfies

$$W \propto \exp\left(-\frac{2\hbar v_l k_{\mathrm{F}}}{K_{\mathrm{B}} T}\right). \tag{10}$$

It follows from the relation (10) and the preceding qualitative arguments that phonon scattering of electrons in a QW is of an activational character, and the activation energy of the phonon mechanism of scattering in a rectilinear QW is

$$\varepsilon_{a0} = 2\hbar v_l k_{\mathrm{F}}. \tag{11}$$

Using Eq. (8) to calculate the electron lifetime $\tau(k_{\mathrm{F}})$ at the Fermi level in a rectilinear QW for the scattering processes shown in Fig. 1, we obtain the expression

$$\frac{1}{\tau(k_{\mathrm{F}})} = \frac{4\Xi^2 m K_{\mathrm{B}} T k_{\mathrm{F}}}{\pi \rho v_l^2 \hbar^3} \exp\left(-\frac{\varepsilon_{a0}}{K_{\mathrm{B}} T}\right), \tag{12}$$

if the condition (9) is satisfied. This expression is in complete agreement with the qualitative analysis. The activation energy of phonon scattering can be substantially increased by changing the configuration of the QW. This will expand the temperature range in which the phonon contribution to the resistance is exponentially small. As a specific example, we shall consider a QW in the form of a helix. Since the curvature of such a QW is the same at all points, the wave vector of the electron along the helical QW is a conserved quantity just as the wave vector of an electron along a rectilinear QW. Under this circumstance, the relation (8), written for a rectilinear QW, remains in force for a helical QW, where

$$x(s) = R\cos(2\pi s/l), \quad y(s) = R\sin(2\pi s/l), \quad z(s) = sh/l,$$

R is the radius of the helix, h is the pitch of the helix, and $l = \sqrt{4\pi^2 R^2 + h^2}$ is the length of the helix. Calculating for a helical QW the electron lifetime at the Fermi level using Eq. (8), we find for $K_{\mathrm{B}} T \ll \varepsilon_a$ and $K_{\mathrm{B}} T \ll h v_l / R$

$$\frac{1}{\tau(k_{\mathrm{F}})} = \frac{4\Xi^2 m K_{\mathrm{B}} T k_{\mathrm{F}}}{\pi \rho v_l^2 \hbar^3} \left(\frac{l}{h}\right)^3 \exp\left(-\frac{\varepsilon_a}{K_{\mathrm{B}} T}\right), \tag{13}$$

where the activation energy of phonon scattering of an electron in a helical QW (the energy of a phonon which transfers an electron from one Fermi point into another on the helical QW) is

$$\varepsilon_a = \frac{2\hbar v_l k_F l}{h}. \tag{14}$$

Comparing the activation energies (11) and (14), we obtain

$$\frac{\varepsilon_a}{\varepsilon_{a0}} = \frac{l}{h}. \tag{15}$$

It follows from the relations (13)–(15) that to increase the lifetime $\tau(k_F)$ at the Fermi level and to obtain the associated increase in conductivity the values of the parameters h/l and R of the helical QW must be small. Specifically, at liquid-helium temperatures and $k_F \simeq 10^6$ cm^{-1}, $v_l \simeq 10^6$ cm/s, $R \simeq 10^{-6}$ cm, and $h/l \simeq 10^{-2}$ it follows from Eqs. (12) and (13) that the phonon-scattering-induced transport electron relaxation time at the Fermi level in a helical QW is tens of orders of magnitude greater than the relaxation time in such rectilinear QW.

The single-electron approximation was used in the derivation of the basic relations obtained in this paper. This approximation is valid if the electronic system can be treated as a Fermi gas. At the same time, it is known that the formation of an electron liquid in a one-dimensional conductor (Tomonaga–Luttinger liquid) leads to an energy spectrum of elementary excitations of the electronic system that is qualitatively different from that of a Fermi gas (see, for example, the review in Ref. 6). Thus, it is necessary to formulate a criterion of applicability of the single-electron approximation in the problem solved in the present paper. For the helical QW considered here, the single-electron approximation certainly holds for the electron–phonon processes shown in Fig. 1, if the energy (14) of such phonons is much higher than the characteristic electron–electron interaction energy $e^2/\epsilon r$, where ϵ is the dielectric constant of the medium, and $r = \pi/k_F$ is the distance between the electrons. This criterion can be written explicitly as

$$\frac{e^2}{2\pi\hbar v_l \epsilon l}\,\frac{h}{l} \ll 1,$$

and it holds, in particular, for the parameter values used to obtain the previous estimate of $\tau(k_F)$ in a helical QW. The conclusion that the phonon dissipation of current in a helical QW is strongly suppressed therefore remains valid when the electron–electron interaction is taken into account.

*)E-Mail: Oleg.Kibis@nstu.ru; Fax: 7–3832–460209

[1] O. V. Kibis and M. V. Éntin, Fiz. Tekh. Poluprovodn. **28**, 584 (1994) [Semiconductors **28**, 352 (1994)].
[2] O. V. Kibis, Fiz. Tekh. Poluprovodn. **32**, 730 (1998) [Semiconductors **32**, 657 (1998)].
[3] O. V. Kibis, Phys. Lett. A **166**, 393 (1992).
[4] O. V. Kibis, Fiz. Tverd. Tela (Leningrad) **34**, 3511 (1992) [Sov. Phys. Solid State **34**, 1880 (1992)].
[5] O. V. Kibis and D. A. Romanov, Fiz. Tverd. Tela (St. Petersburg) **37**, 129 (1995) [Phys. Solid State **37**, 69 (1995)].
[6] E. Abrahams, Physica B **197**, 435 (1994).

Translated by M. E. Alferieff

Inelastic scattering of hot electrons by neutral donors in heavily silicon-doped GaAs/AlAs quantum wells

I. A. Akimov,*) V. F. Sapega, D. N. Mirlin, B. P. Zakharchenya, V. M. Ustinov, A. E. Zhukov, and A. Yu. Egorov

A. F. Ioffe Physicotechnical Institute, Russian Academy of Sciences, 194021 St. Petersburg, Russia

A. A. Sirenko

Department of Physics, Pennsylvania State University, University Park, PA 16802, USA
(Submitted March 17, 1999; accepted for publication March 18, 1999)
Fiz. Tekh. Poluprovodn. **33**, 1235–1239 (October 1999)

The energy and momentum relaxation of hot electrons in *n*-type GaAs/AlAs quantum wells is studied. Hot photoluminescence due to the recombination of hot electrons with holes bound on Si acceptors is observed in structures with a high level of doping with silicon. Using the method of magnetic depolarization of hot photoluminescence, the probability of scattering of hot electrons is found to decrease substantially with increasing temperature in the range 4–80 K. This effect is shown to be due to the ionization of donors. It is established that the probability of inelastic scattering by neutral donors is several times greater than the probability of quasielastic electron–electron scattering. © *1999 American Institute of Physics.* [S1063-7826(99)01910-9]

1. INTRODUCTION

It is known that the main mechanism of scattering of hot electrons in lightly or moderately doped bulk GaAs and structures with GaAs/AlAs quantum wells (QWs) is inelastic scattering by optical phonons.[1,2] It has been shown that as the dopant density (acceptors) increases in *p*-type structures ($N_A \geqslant 10^{18}$ cm^{-3}), an additional scattering process due to the inelastic interaction of hot electrons with neutral acceptors appears.[3] This is valid for bulk GaAs and for a GaAs/AlAs QWs.

A Mott transition occurs in bulk *n*-type GaAs with donor density $N_D \approx 5\times10^{16}$ cm^{-3}, causing the semiconductor to be degenerate at low temperatures. The degeneracy in *n*-type samples occurs much earlier than in *p*-type structures, because the ionization energy of donors is lower than that of acceptors. The main mechanism of scattering of hot electrons in silicon-doped bulk *n*-GaAs with silicon densities $N_{\mathrm{Si}} \geqslant 7\times10^{17}$ cm^{-3} is inelastic scattering by coupled phonon–plasmon modes.[4] In QWs size quantization increases the binding energy of electrons on donors. As a result, the Mott transition shifts to higher impurity densities. This makes it possible to investigate a system containing a large number of mutual donors and not an electron gas.

The main objective of the present work is to study the scattering of hot electrons in QWs heavily doped with silicon (*n*-type conductivity).

2. EXPERIMENTAL RESULTS

2.1. Hot photoluminescence in *n*-type quantum wells

The experimental GaAs/AlAs structures were grown by molecular-beam epitaxy on (100) substrates. The well width in each structure was 40 Å, and the barrier width was 80 Å (in what follows 40 Å /80 Å) with 80 periods. The central part of the wells (∼20 Å) was doped with silicon, while the regions adjoining the interfaces remained undoped. The silicon density for different samples varied in the range $N_{\mathrm{Si}} = 4\times10^{10} - 4\times10^{11}$ cm^{-2}. Moreover, a similar structure 50 Å /80 Å with silicon density 5×10^{11} cm^{-2} was also investigated. The samples were placed in a helium cryostat with a variable holder temperature. To obtain magnetic fields up to 7.5 T, a superconducting magnet was placed in the cryostat. A Kr^+ laser with photon energy $\hbar\omega_{\mathrm{exc}} = 1.92$ eV as well as a dye laser (DCM dye) pumped with an Ar^+ laser were used to excite the hot carriers. The pumping density on the sample was $P \leqslant 100$ W/cm^2. DFS-24 and SPEX-1877 spectrometers, equipped with a cooled FÉU-79 photomultiplier and a multichannel detector (CCD camera), respectively, were used to detect the luminescence.

In *n*-type structures with silicon density $N_{\mathrm{Si}} > 10^{11}$ cm^{-2}, we observed low-temperature donor–acceptor luminescence shifted in the spectra in the direction of energies lower by 25 meV from the excitonic line. The donor–acceptor luminescence vanishes as temperature T increases to 50–60 K. This is evidently due to the ionization of the neutral Si donors. In the same samples with $N_{\mathrm{Si}} > 10^{11}$ cm^{-2}, we observe high-frequency luminescence near the exciting laser line, whose spectrum at $T = 9$ K and $N_{\mathrm{Si}} = 1.6\times10^{11}$ cm^{-2} is shown in Fig. 1 (solid line). For comparison, the hot photoluminescence (HPL) spectrum at the same temperature in a strongly doped *p*-type QW with beryllium density $N_{\mathrm{Be}} = 1\times10^{12}$ cm^{-2} (dashed line) is also shown in Fig. 1. The narrow peaks with photon energy $\hbar\omega_{\mathrm{lum}} = 1.89$ eV correspond to Raman scattering of light and are not discussed below.

The observed luminescence in *n*-type QWs possesses the following properties.

a) As follows from Fig. 1, the form of the spectrum is

 © 1999 American Institute of Physics

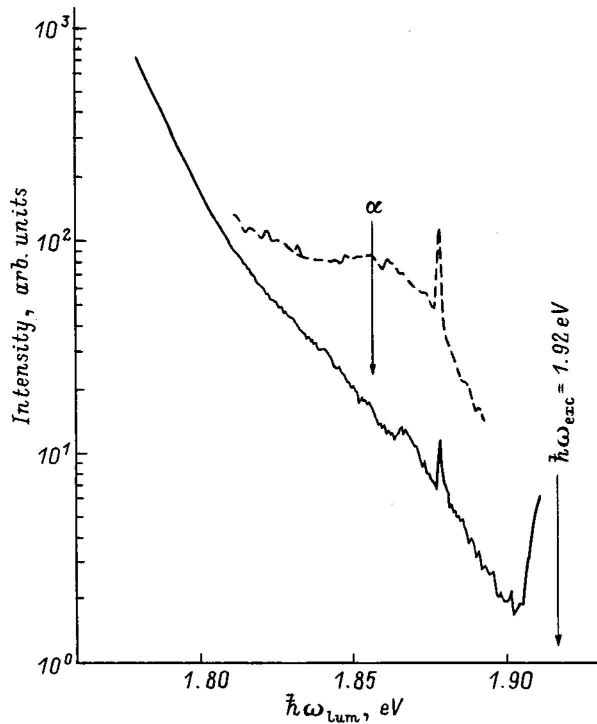

FIG. 1. Hot photoluminescence spectra of n-type QWs doped with silicon to density $N_{Si}=1.6\times10^{11}$ cm^{-2} (solid line) and p-type QWs doped with beryllium to density $N_{Be}=1\times10^{12}$ cm^{-2} (solid line) with excitation photon energy $\hbar\omega_{exc}=1.92$ eV. $T=9$ K. The point α corresponds to the energy of the radiation of hot electrons from the point of creation into the ground state of the acceptor.

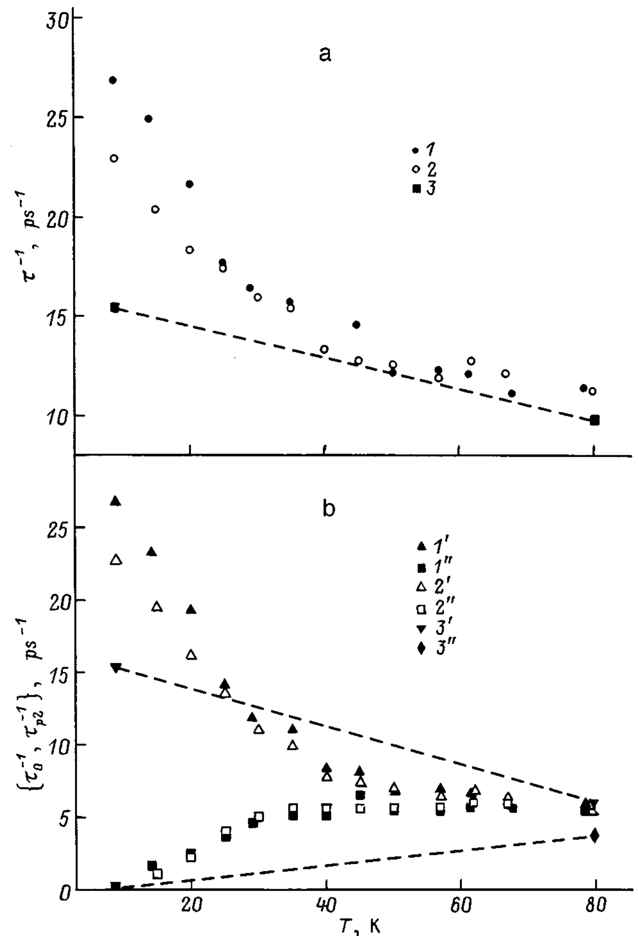

FIG. 2. a — Temperature dependence of the scattering probability τ^{-1} for samples with densities N_{Si}, 10^{11} cm^{-2}: *1*—1.6, *2*—4, *3*—5. b— Temperature dependences of the escape probability τ_0^{-1} (inelastic collisions) (*1′–3″*) and relaxation probability τ_{p2}^{-1} (elastic collisions) of the momentum anisotropy (*1″–3″*) for structures with densities N_{Si}, 10^{11} cm^{-2}: *1′,1″*—1.6; *2′,2″*—4; *3,3″*—5.

similar to that of the HPL spectrum in strongly doped p-type QWs.

b) The intensity varies quadratically with the power density of the exciting light.

c) With linear and circular polarization of the exciting light the luminescence is linearly and circularly polarized, respectively; the sign of the charge of the recombining carriers, which was determined from the change in the Stokes parameters in a magnetic field,[1] is negative and therefore corresponds to electrons.

In p-type structures, HPL is due to the recombination of hot electrons from the first conduction subband with holes bound on acceptors (transitions of the type $1e\rightarrow A^0$).[1,2] Therefore, it follows from the properties a)–c) listed above that in the QWs investigated, for $N_{Si}>10^{11}$ cm^{-2}, HPL corresponding to the same optical transitions as in p-type QWs is observed near the excitation line. The point is that silicon in GaAs is an amphoteric impurity, and at hot doping levels it can become not only a donor but also an acceptor.[5] This makes it possible to investigate recombination radiation of hot electrons with holes at Si acceptors in the presence of a large number of Si donors. In the structures investigated, the donor density is higher than the acceptor density, $N_D>N_A$ (n-type).

2.2. Probability of scattering of hot electrons

We used the method of depolarization of HPL in a magnetic field (Faraday geometry) to measure the probability of scattering of hot electrons. The magnetic-field dependence of the linear polarization is described by the Lorentz formula[1]

$$\frac{\rho(B)}{\rho(0)}=\frac{1}{1+(2\omega_c\tau)^2}, \tag{1}$$

where $\rho(B)$ is the degree of linear polarizaiton in a magnetic field B, $\omega_c=eB/m_cc$ is the cyclotron frequency, and τ^{-1} is the probability of scattering of a hot electron. The scattering probability τ^{-1} can therefore be found from the half-width of the depolarization curve. The polarization of HPL was measured at the point of the spectrum marked by α in Fig. 1a. This point corresponds to recombination radiation of photoexcited electrons which have not undergone energy relaxation after being created (we call it below the recombination of electrons from the creation point). The kinetic energy of the electrons corresponds to approximately 140 and 180 meV for samples with 40 and 50-Å-wide wells.

Figure 2a shows the scattering probability τ^{-1} versus the temperature T in 40 Å /80 Å samples with densities $N_{Si}=1.6\times10^{11}$ cm^{-2} and 4×10^{11} cm^{-2}. It is evident that τ^{-1} depends strongly on T. At low temperature ($T=9$ K) the

electron scattering probability is 27 and 23 ps^{-1} with $N_{\mathrm{Si}}=1.6\times10^{11}$ cm^{-2} and 4×10^{11} cm^{-2}, respectively. As the temperature is raised, the probability τ^{-1} gradually decreases to 12 ps^{-1} at $T\simeq80$ K for each sample.

We also observed that the linear polarization of the HPL $\rho(B=0)$ decreases with increasing temperature. This means that the anisotropy of the momentum distribution of hot electrons at the creation point, which determines the value of $\rho(B=0)$, decreases. The point is that over the lifetime of electrons in this energy state (creation point), which is determined by the inelastic scattering mechanisms, isotropization of the momentum distribution can occur. This is valid in the presence of elastic collisions, which result in momentum relaxation of electrons without a change in the electron energy. Thus, the higher the probability of elastic scattering mechanisms compared with inelastic mechanisms, the lower the degree of linear polarization of the HPL of electrons from the creation point. Hence it follows that the decrease in $\rho(B=0)$ with increasing T is due to an increase in the role of elastic collisions. To distinguish the mechanisms of elastic and inelastic scattering of hot electrons, we write the scattering probability as

$$\tau^{-1}=\tau_0^{-1}+\tau_{p2}^{-1}, \tag{2}$$

where τ_0 is the escape time of an electron from the initial energy state, and τ_{p2} is the relaxation time of the momentum anisotropy as a result of elastic scattering processes. In turn, the linear polarization of the HPL of electrons from the creation point depends on τ_0 and τ_{p2} as[1]

$$\rho(B=0)\propto\frac{\tau_{p2}}{\tau_0+\tau_{p2}}. \tag{3}$$

Using Eqs. (1)–(3) and the fact that the escape probability τ_0^{-1} is limited from below by the probability $\tau_{0,e-LO}^{-1}$ of scattering of hot electrons by polar optical phonons, we calculated the temperature dependences of τ_0^{-1} and τ_{p2}^{-1}, which are shown in Figs. 2b by the points $1',2'$ and $1'',2''$, respectively. It follows from Fig. 2 that the decrease in the total scattering rate τ^{-1} with increasing T is due to a strong decrease of the escape probability τ_0^{-1}. For both samples, the escape probability changes from the maximum value $\tau_0^{-1}\approx\tau^{-1}$ at $T\approx9$ K, approaching $\tau_0^{-1}\approx6-7$ ps^{-1} at $T\approx80$ K, corresponding to the probability of scattering by polar optical phonons $\tau_{0,e-LO}^{-1}$.[2] The escape probability minus $\tau_{0,e-LO}^{-1}$, shown in Fig. 3, can be described by an activation dependence, and at high temperatures it decreases with T (see linear section marked by the arrow in Fig. 3) as

$$\tau_0^{-1}-\tau_{0,e-LO}^{-1}\propto\exp(E/k_BT), \tag{4}$$

where E is the activation energy. A fit to the experimental results (solid and dashed curves in Fig. 3) gives $E\approx13$ meV. This value is in good agreement with the computed ioinization energy of donors in such structures.[6] Moreover, it follows from Fig. 2b that the contribution of elastic scattering mechanisms, whose probability is determined by τ_{p2}^{-1}, is essentially absent at $T\approx9$ K and increases with temperature.

We obtained similarly the values of the scattering probabilities τ^{-1} (Fig. 2a) and τ_0^{-1} and τ_{p2}^{-1} (Fig. 2b) in a 50 Å/80 Å sample with density $N_{\mathrm{Si}}=5\times10^{11}$ cm^{-2} at temperatures 9 and 80 K. It is evident that the qualitative temperature dependences of τ^{-1}, τ_0^{-1}, and τ_{2p}^{-1} are the same as those obtained for the 40 Å /80 Åstructures.

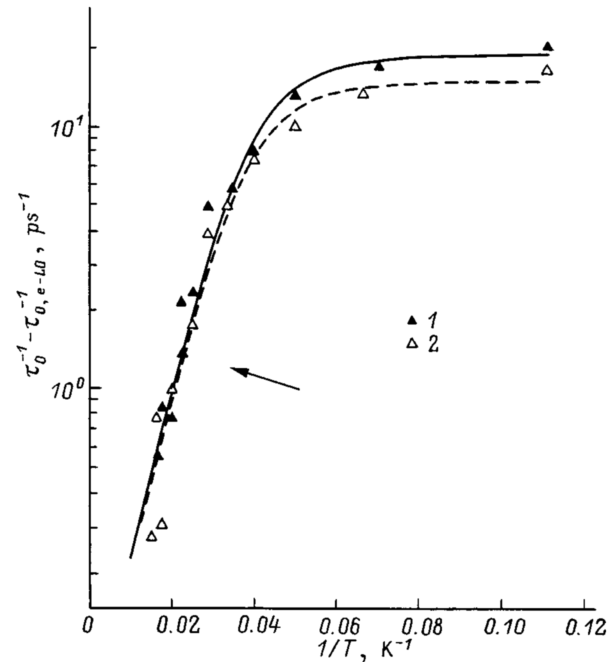

FIG. 3. Escape probability minus $\tau_{0,e-LO}^{-1}$ versus $1/T$ for samples with $N_{\mathrm{Si}}=1.6\times10^{11}$ (*1*) and 4×10^{11} cm^{-2} (*2*). At high temperatures (arrow) the dependence is described by $\ln(\tau_0^{-1}-\tau_{0,e-ph}^{-1})\propto E/T$, $E\sim150$ K ~13 meV.

We compared the results obtained with the results for heavily doped p-type QWs. It was found that in p-type QWs with the same density τ^{-1} ($T\approx9$ K) is several times less than in n-type QWs. In p-type structures τ^{-1} does not depend on temperature in a wide range from 9 to 150 K.

Therefore, in heavily silicon-doped QWs the decrease of τ^{-1} with increasing temperature, which is due to the strong variation of τ_0^{-1}, occurs as a result of ionization of Si donors. At low temperatures ($T\approx9$ K) the main mechanism for scattering of hot electrons in such structures is inelastic scattering by neutral donors D^0 with scattering probability $\tau_{e-D^0}^{-1}=\tau_0^{-1}-\tau_{0,e-LO}^{-1}$. The high value of the probability for scattering of an electron by an impurity in n-type QWs as compared with p-type structures seems to be explained by the large Bohr radius of localized electrons at donors, which results in a higher effective scattering cross section. A temperature increase results in the ionization of donors and therefore a decrease of the escape probability τ_0^{-1}, which approaches the value of the scattering probability by polar optical phonons $\tau_{0,e-LO}^{-1}$ and is described by the activational dependence (4). It should be noted that a large change in the probabilities of scattering of hot electrons occurs at temperatures from 10 to 50 K. We observed the donor–acceptor luminescence to vanish in the same range; i.e., the conclusion that the change in the scattering processes with increasing T is due to ionization of donors is confirmed.

It is obvious that at low temperatures one would expect the probability of scattering by neutral donors should increase with the impurity density. However, it is evident from

our experimental results (Fig. 2) that this is not so. For the sample with $N_{\rm Si}=1.6\times10^{11}$ cm^{-2}, the probability for scattering of hot electrons by Si donors is at a maximum and $\tau^{-1}_{e-D^0}\approx 20$ ps^{-1}. An increase of the silicon density to 4×10^{11} and 5×10^{11} cm^{-2} decreases $\tau^{-1}_{e-D^0}$ to 16 and 9 ps^{-1}, respectively. We attribute this result to the fact that at high doping levels silicon is more likely to be an acceptor. The maximum possible density of uncompensated donors in bulk GaAs corresponds to $N_D^{\max}\approx 6\times10^{18}$ cm^{-3} (Ref. 5). As follows from our results, in the QWs investigated $N_D^{\max}\approx 2\times10^{11}$ cm^{-2}. A further increase of the silicon density does not result in a larger number of donors. In contrast, it intensifies the degree of compensation. The number of neutral donors at low temperature in this case decreases, and we observe a decrease of $\tau^{-1}_{e-D^0}$.

We shall now consider the mechanisms due to elastic collisions, to which the scattering probability τ^{-1}_{p2} corresponds. We found (Fig. 2b) that in all samples the contribution of elastic interactions is negligible ($\tau^{-1}_{p2}\approx 0$) at low temperatures ($T\approx 9$ K). Since this holds in structures with high silicon density ($N_{\rm Si}=4\times10^{11}-5\times10^{11}$ cm^{-2}), where as a result of compensation the number of neutral donors is less than the number of charged Si centers even at $T\approx 9$ K, we can assume that the elastic scattering of electrons by charged impurities $\rm Si^+$ and $\rm Si^-$ is negligible for any T. Nonetheless, raising the temperature increases the importance of elastic collisions, which become substantial together with inelastic processes. It is obvious that as T is raised, the ionization of Si donors increases the number of free electrons. The increase in τ^{-1}_{p2} with temperature is therefore due primarily to the appearance of quasielastic scattering by free electrons. At high temperatures ($T\approx 80$ K), when it can be assumed that virtually all donors are ionized, the probability of electron–electron scattering is comparable to the electron–phonon interaction. In Ref. 7 it was shown that scattering of hot electrons by electron–hole ($e-h$) plasma causes the electron–plasmon and electron–phonon scattering probabilities to be identical at plasma density $n_{2D}\approx 10^{11}$ cm^{-2} in QWs and $n_{3D}\approx 10^{17}$ cm^{-3} in bulk GaAs, respectively. It follows from a theoretical calculation for bulk GaAs (Ref. 8) that the electron–electron interaction plays the main role in the scattering of hot electrons by $e-h$ plasma. In our case, electron–electron scattering at $T\approx 80$ K becomes comparable to scattering by phonons at approximately the same densities n_{2D} of the electron gas.

3. CONCLUSIONS

It was found that at low temperatures the main energy relaxation process for hot electrons in *n*-type QWs is inelastic scattering of electrons by neutral donors — $e-D^0$ scattering. A temperature increase results in the ionization of donors and vanishing of $e-D^0$ scattering. Electron–phonon scattering becomes the main energy relaxation process. Moreover, an increase in temperature gives rise to quasielastic electron–electron interaction, which results in appreciable momentum relaxation.

The degree of compensation of the structure which we are studying can be estimated from the temperature dependence of the scattering probability of hot electrons in heavily silicon-doped QWs.

This work was supported by the Russian Fund for Fundamental Research (Grants Nos. 99-02-18298, 96-15-96393, 96-15-96392) and the Volkswagon Foundation (Grant No. I/70958).

*)E-Mail: akimov@dnm.ioffe.rsi.ru; Fax (812) 2471017

[1] B. P. Zakharchenya, D. N. Mirlin, V. I. Perel', and I. I. Reshina, Usp. Fiz. Nauk **136**, 459 (1982) [Sov. Phys. Usp. **25**, 143 (1982)]; D. N. Mirlin, I. Ya. Karlik, L. P. Nikitin, I. I. Reshina, and V. F. Sapega, Solid State Commun. **37**, 757 (1981).

[2] D. N. Mirlin, B. P. Zakharchenya, I. I. Reshina, A. V. Rodina, V. F. Sapega, A. A. Sirenko, V. M. Ustinov, A. E. Zhukov, and A. Yu. Egorov, Fiz. Tekh. Poluprovodn. **30**, 699 (1996) [Semiconductors **30**, 377 (1996)].

[3] I. I. Reshina, D. N. Mirlin, V. I. Perel, A. Yu. Dobin, A. G. Agranov, and B. Ya. Ber, Solid State Commun. **103**, 151 (1997).

[4] C. L. Peterson and S. A. Lyon, Phys. Rev. Lett. **65**, 760 (1990).

[5] Y. G. Chai, R. Chow, and C. E. C. Wood, Appl. Phys. Lett. **39**, 800 (1981).

[6] C. Malhiot, Yia-Chung Chang, and T. C. McGill, Phys. Rev. B **26**, 4449 (1982).

[7] J. A. Kash, Phys. Rev. B **48**, 18 336 (1993).

[8] J. F. Young and P. J. Kelly, Phys. Rev. B **47**, 6316 (1993).

Translated by M. E. Alferieff

Momentum relaxation time and temperature dependence of electron mobility in semiconductor superlattices consisting of weakly interacting quantum wells

S. I. Borisenko

V. D. Kuznetsov Siberian Physicotechnical Institute,Tomsk State University, 634050 Tomsk, Russia

(Submitted January 22, 1999; accepted for publication March 23, 1999)
Fiz. Tekh. Poluprovodn. **33**, 1240–1245 (October 1999)

Formulas are derived for the longitudinal and transverse electron momentum relaxation times in a superlattice consisting of weakly interacting quantum wells in the approximation of a bulk-semiconductor scattering potential. Scattering by impurity ions, neutral atoms, and volume-type longitudinal acoustic and polar optical phonons is studied. A numerical analysis is performed of the longitudinal and transverse momentum relaxation times for scattering by impurity ions and neutral atoms as a function of the electron energy, temperature, density of the electron gas, and quantum well width. © *1999 American Institute of Physics.*
[S1063-7826(99)02010-4]

As is well known, scattering mechanisms play an important role in the electric and optical properties of semiconductors and structures based on them. The present paper is devoted to the calculation and numerical analysis of the tensor of the reciprocal momentum relaxation time and mobility of electrons in semiconductor superlattices (SLs) consisting of weakly interacting quantum wells (QWs) based on heterostructures. Such SLs are of interest because of the unique properties of the electron energy spectrum and the possibility of using the SLs in infrared-range photodetectors[1–5] and microwave generators.[6–9] Formulas are derived for calculating the longitudinal and transverse electron momentum relaxation times in such SLs for the basic scattering mechanisms, and a numerical analysis is performed of the energy dependence of the relaxation time and temperature dependence of the mobility for scattering by impurity ions and neutral atoms. The following basic approximations were made in deriving the formulas: The electron gas in the quantum wells is almost two-dimensional, i.e., the width of the lower conduction miniband is much less than the average electron energy, the wave function of the lower miniband can be represented as a Bloch sum over wave functions of the ground state of infinitely deep QWs, and the potentials of the scattering centers in bulk semiconductors and SLs are essentially the same. These approximations together with the results obtaind by other authors[10–14] show that the formulas derived are acceptable not only for qualitative but also quantitative analysis. The latter is valid if the period of the SL is sufficiently large and size quantization of the phonon spectrum can be disregarded[12,14] and if the anisotropy of the scattering potentials, which arises primarily as a result of the difference in the dielectric constants of the layers of the SL which correspond to QWs and barriers, can also be disregarded.[11]

1. ELECTRON MOMENTUM RELAXATION TIME TENSOR

The tensor of the reciprocal of the relaxation time for electrons in the bottom miniband was calculated using the nonequilibrium correction $f_{1\mathbf{k}}$ for the equilibrium distribution function f_0 given by

$$f_{1\mathbf{k}}=e\frac{\partial f_0}{\partial E}\sum_i \tau_i F_i v_i, \tag{1}$$

where τ_i are the diagonal components of the relaxation time tensor, F_i and v_i are, respectively, the electric field intensity and electron velocity vectors in a Cartesian coordinate system, and E is the electron energy. As is well-known, for composite SLs consisting of weakly interacting QWs

$$E=\frac{\hbar^2(k_x^2+k_y^2)}{2m^*}+\frac{\Delta}{2}(1-\cos qd), \tag{2}$$

where m^* is the effective mass corresponding to the free motion of electrons along the layers of the SL, Δ is the width of the bottom miniband, corresponding to electron motion along the axis of the SL parallel to the z axis, $d=a+b$ is the SL period, a and b are the QW and barrier widths, respectively, and k_x, k_y, and $q=k_z$ are the components of the wave vector. In the two-dimensional electron gas approximation ($\Delta \ll k_0 T$), and using Eqs. (1) and (2) and the symmetry of the SL in the plane of the layers, the following expressions can be obtained for the transverse ($\tau_\perp=\tau_x=\tau_y$) and longitudinal ($\tau_\parallel=\tau_z$) components of the relaxation time tensor:

$$\frac{1}{\tau_\perp(E)}=\frac{4m^*V}{\pi d\hbar^3}\int_0^1\frac{W(2k_\perp x)}{\sqrt{1-x^2}}x^2dx, \tag{3}$$

$$\frac{1}{\tau_\parallel(E)}=\frac{2m^*V}{\pi d\hbar^3}\int_0^1\frac{W(2k_\perp x)}{\sqrt{1-x^2}}dx, \tag{4}$$

where $E=\hbar^2k_\perp^2/2m^*$, $k_\perp=\sqrt{k_x^2+k_y^2}$, $V=SL$ is the volume of a SL of thickness $L=Nd$, and N is the number of periods in the SL. The function W is related to the total probability $P_{\mathbf{kk}'}$ of an electron making a transition from the state $\mathbf{k}$ into the state $\mathbf{k}'$ in a definite type of scattering by the formula

$$P_{\mathbf{kk}'}=\frac{2\pi}{\hbar}W(|\mathbf{k}'_\perp-\mathbf{k}_\perp|)\,\delta[E(\mathbf{k}')-E(\mathbf{k})], \tag{5}$$

 © 1999 American Institute of Physics

where $W(|\mathbf{k}'-\mathbf{k}|)=|U_{\mathbf{k}'\mathbf{k}}|^2$, and $U_{\mathbf{k}'\mathbf{k}}=U(|\mathbf{k}'-\mathbf{k}|)$ is the matrix element of the scattering operator $\hat{U}(\mathbf{r})$ in the basis of Bloch-type envelope wave functions $\tilde{\psi}_{\mathbf{k}}(\mathbf{r})$:

$$U(\mathbf{k}'-\mathbf{k})=\frac{1}{V}\int \tilde{\psi}^*_{\mathbf{k}'}\hat{U}(\mathbf{r})\tilde{\psi}_k d\mathbf{r}, \tag{6}$$

$$\tilde{\psi}_{\mathbf{k}}(r)=\frac{1}{\sqrt{S}}\exp[i(k_x x+k_y y)]\psi_q(z). \tag{7}$$

For the SL considered here, a Bloch sum over wave functions of the ground state of infinitely deep QWs was taken as the function describing electron motion along the axis of the SL:

$$\psi_q(z)=\frac{1}{\sqrt{L}}\exp(iqz)u_q(z)$$

$$=\frac{1}{\sqrt{N}}\sum_{n=-N/2}^{N/2}\exp(iqdn)\varphi(z-dn), \tag{8}$$

$$\varphi_q(z)=\sqrt{\frac{2}{a}}\cos\left(\frac{\pi}{a}z\right)\left[-\frac{a}{2}<z<\frac{a}{2}\right],$$

$$\varphi_q(z)=0\left[z<-\frac{a}{2},\quad \frac{a}{2}<z\right]. \tag{9}$$

It should be noted that using the approximations described above, according to Eq. (5), the scattering probability does not depend on the longitudinal wave vector.

1.1. Scattering by impurity atoms and neutral atoms

For scattering by impurity atoms and neutral atoms the scattering operator has the form

$$\hat{U}(\mathbf{r})=U(\mathbf{r})=\sum_{\alpha} U(\mathbf{r}-\mathbf{R}_\alpha), \tag{10}$$

where $U(\mathbf{r}-\mathbf{R}_\alpha)$ is the interaction energy of an electron with an ion or neutral atom located at the point $\mathbf{R}_\alpha$. Using Eqs. (6)–(10), we have

$$U(\mathbf{k})=\sum_{\alpha} U_\alpha(\mathbf{k}), \tag{11}$$

where

$$U_\alpha(\mathbf{k})=\frac{1}{V}\sum_n \exp(-i\mathbf{k}_n\cdot\mathbf{R}_\alpha)S_n(q)U(\mathbf{k}_n), \tag{12}$$

$$S_n(q)=\frac{1}{q}\int_{-d/2}^{d/2}\exp(i2\pi nz/d)u_q^*(z)u_0(z)dz, \tag{13}$$

$$U(\mathbf{k})=U(k_\perp,q)=\int_V \exp(-i\mathbf{k}\cdot\mathbf{r})U(\mathbf{r})d\mathbf{r}, \tag{14}$$

$$\mathbf{k}_n=(\mathbf{k}_\perp,q+2\pi n/d).$$

Using a uniform distribution of scattering centers over the volume of the SL or the volume of the QW, we obtain the following expression for the desired function $W(k_\perp)$ with the formulas presented above:

$$W(k_\perp)=\frac{N_i d}{\pi V}\int_0^\infty |S(q)|^2|U(k_\perp,q)|^2 dq, \tag{15}$$

where N_i is the density of scattering centers and

$$S(q)=\frac{\pi^2\sin(aq/2)}{(aq/2)[\pi^2-(ad/2)^2]}. \tag{16}$$

For scattering by a screened Coulomb ion potential, we have in the approximation of isotropic and uniform permittivity

$$|U(k_\perp,q)|^2=\frac{e^4}{\varepsilon_0^2\varepsilon_s^2(k_\perp^2+q^2+\alpha_s^2)^2}, \tag{17}$$

where ε_s is the static permittivity, and α_s^{-1} is the Debye screening length for the static field. For a SL in the two-dimensional electron gas approximation

$$\alpha_s^2=\alpha_{s0}^2\frac{N_c}{n+N_c}, \tag{18}$$

where $\alpha_{s0}^{-1}=(ne^2/\varepsilon_0\varepsilon_s k_0 T)^{-1/2}$ is the Debye screening length of a bulk semiconductor for a nondegenerate electron gas, n is the electron density in the SL, and $N_c=m^*k_0T/\pi d\hbar^2$ is the effective density of states of the two-dimensional electron gas in the bottom miniband. For elastic scattering by neutral atoms, according to the theory of Ref. 15, extended to the case of a two-dimensional electron gas,

$$|U(k_\perp,q)|^2=\frac{30\pi r_0\hbar^4}{m^*}(k_\perp^2+q^2+\alpha_s^2)^{-1/2}, \tag{19}$$

where r_0 is the effective Bohr radius.

1.2. Scattering by phonons

As is well known, the operator representing the interaction of an electron with phonons for a separate allowed branch in a bulk semiconductor can be written as

$$\hat{U}(\mathbf{r})=\hat{U}^+(\mathbf{r})+\hat{U}^-(\mathbf{r}), \tag{20}$$

where

$$\hat{U}^\pm(\mathbf{r})=\sum_{\mathbf{Q}} A^\pm(\mathbf{Q})e^{\mp i\mathbf{Q}\cdot\mathbf{r}} \tag{21}$$

are operators corresponding to creation and annihilation of phonons during scattering and $\mathbf{Q}$ is the phonon wave vector. Substituting the expression (21) into Eq. (12) and equating $\mathbf{R}_\alpha$ to zero, we obtain

$$W(k_\perp)=W^+(k_\perp)+W^-(k_\perp), \tag{22}$$

where

$$W^\pm(k_\perp)=|U^\pm(\mathbf{k})|^2=\left(\frac{d}{\pi}\right)^2\left|\int_0^\infty S(q)A^\pm(k_\perp,q)dq\right|^2. \tag{23}$$

1.2.1. Acoustic phonons

For scattering of electrons by longitudinal acoustic phonons in a volume-type SL (Ref. 14), we use in the deformation potential approximation for the average value of the operators $A^{\pm}$ the standard formula

$$A^{\pm}(\mathbf{Q})=\mp iQD\sqrt{\frac{\hbar}{2\rho V\omega_L(\mathbf{Q})}\left[N_L(\mathbf{Q})+\frac{1}{2}\pm\frac{1}{2}\right]},\quad (24)$$

where D is the deformation-potential constant, ρ is the density of the crystal, $\omega_L=v_LQ$ and v_L are, respectively, the frequency and velocity of longitudinal long-wavelength acoustic phonons, and $N_L(\mathbf{Q})$ is the thermodynamically equilibrium number of phonons, described by the Bose–Einstein distribution function. For $\hbar\omega_L\ll k_0T$

$$A^{\pm}(\mathbf{Q})=A=i\frac{D}{v_L}\sqrt{\frac{k_0T}{2\rho V}}.\quad (25)$$

Using Eqs. (22), (23), and (25), we obtain for the desired function

$$W(k_\perp)=2\left(\frac{Ad}{\pi}\right)^2\left|\int_0^\infty S(q)dq\right|^2=4\frac{k_0T}{\rho V}\left(\frac{Dd}{v_La}\right)^2.\quad (26)$$

1.2.2. Optical polar phonons

For scattering of electrons by longitudinal optical polar phonons of the volume type[12,13] we use for the average value of the operators $A^{\pm}(\mathbf{Q})$ the well-known formula corresponding to a screened optical potential and the high-temperature approximation

$$A^{\pm}(\mathbf{Q})=\mp A(\mathbf{Q})=\mp i\frac{eP_L}{\omega_L^{\mathrm{PO}}}\sqrt{\frac{k_0T}{2\varepsilon_0V}}\frac{Q}{Q^2+\alpha_\infty^2},\quad (27)$$

where ω_L^{PO} is the frequency of long-wavelength longitudinal optical polar phonons, p_L is the oscillator strength, and α_∞^{-1} is the Debye screening length for the high-frequency field, which differs from α_s^{-1} by the fact that in Eq. (18) the static permittivity ε_s is replaced by the high-frequency permittivity ε_∞. As is well known, the following relation holds for III–V semiconductors:

$$\frac{P_L^2}{\omega_L^2}=\frac{1}{\varepsilon^*}=\frac{1}{\varepsilon_\infty}-\frac{1}{\varepsilon_s}.\quad (28)$$

Using Eqs. (23) and (27), we obtain the following expression for the desired function:

$$W(k_\perp)=2\left(\frac{d}{\pi}\right)^2\left|\int_0^\infty S(q)A(k_\perp,q)dq\right|^2.\quad (29)$$

1.3. Electron momentum relaxation time

Using the formulas obtained for the function $W(k_\perp)$, we represent the components of the tensor of the reciprocal of the momentum relaxation time for individual scattering mechanisms in the form

$$\frac{1}{\tau_i(E)}=\frac{1}{\tau_0(E)}G_i(E),\quad (30)$$

where

$$\tau_0(E)=(ak_\perp)\tau(E),\quad (31)$$

$\tau(E)$ is the relaxation time in a bulk semiconductor, and $G_i(E)$ is a dimensionless function, whose parameters, in general, are the QW width, the SL period, and the free charge-carrier density.

1.3.1. Impurity ions

For scattering by impurity ions, using Eqs. (3), (4), and (15)–(17), we obtain for the functions $G_i(E)$ the integral expressions

$$G_\perp(E)=\frac{\pi^4}{2F(\eta)}\int_0^\infty\frac{dx\sin^2x}{A(x,\gamma,\beta_s)(\gamma^2x^2+\beta_s^2)^{1/2}},\quad (32)$$

$$G_\parallel(E)=\frac{\pi^4}{2F(\eta)}\int_0^\infty\frac{dx(2\gamma^2x^2+2\beta_s^2+1)\sin^2x}{A(x,\gamma,\beta_s)(\gamma^2x^2+\beta_s^2)^{3/2}},\quad (33)$$

$$A(x,\gamma,\beta_s)=x^2(\pi^2-x^2)(\gamma^2x^2+\beta_s^2+1)^{3/2},$$

where $\gamma=1/ak_\perp$, $\beta_s=\alpha_s/2k_\perp$, and the function $F(\eta)=\ln(1+\eta)-\eta/(1+\eta)$, which depends on the parameter $\eta=(2k_\perp/\alpha_{s0})^2$, is known from the theory of Coulomb scattering in bulk semiconductors.

1.3.2. Neutral impurity atoms

For scattering by neutral impurity atoms, using Eqs. (3), (4), (15), (16), and (19), we can write the functions $G_i(E)$ as a pair of integrals

$$G_\perp(E)=\frac{4}{\pi}\int_0^1\frac{x^2}{\sqrt{1-x^2}}g(E,x)dx,$$

$$G_\parallel(E)=\frac{2}{\pi}\int_0^1\frac{1}{\sqrt{1-x^2}}g(E,x)dx,\quad (34)$$

where

$$g(E,x)=\frac{3\pi^4}{2}\int_0^\infty\frac{dy\sin^2y}{y^2(\pi^2-y^2)^2(\gamma^2y^2+x^2+\beta_s^2)^{1/2}}.\quad (35)$$

1.3.3. Acoustic phonons

For scattering by acoustic phonons, using Eqs. (3), (4), and (26), we found the functions $G_i(E)$ to be constant:

$$G_\perp(E)=G_\parallel(E)=4\pi\frac{d}{a}.\quad (36)$$

1.3.4. Polar optical phonons

Using Eqs. (3), (4), and (29), we can represent the functions $G_i(E)$ for scattering by polar optical phonons in the form of Eqs. (34), where

$$g(E,x)=\pi^3\left(\frac{d}{a}\right)\left|\int_0^\infty\frac{dy\sin y(\gamma^2y^2+x^2)^{1/2}}{y(\pi^2-y^2)(\gamma^2y^2+x^2+\beta_\infty^2)}\right|^2,$$

$$\beta_\infty=\alpha_\infty/2k_\perp.\quad (37)$$

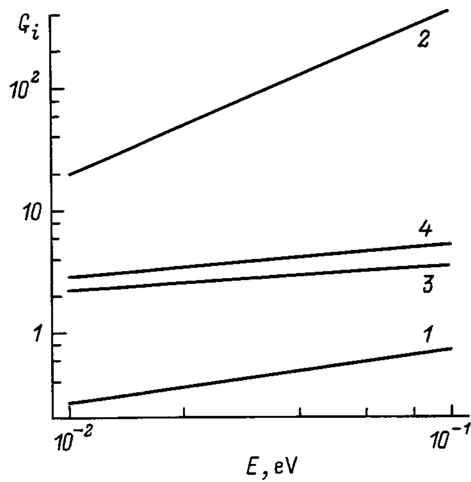

FIG. 1. Dimensionless function G_i versus the energy for $T=100$ K. $a=b=5$ nm, $n=10^{15}$ cm^{-3} for scattering: *1*, *2*—by impurity ions and *3*, *4*—by neutral atoms. *1*, *3*—Transverse component of the tensor, *2*, *4*—longitudinal component of the tensor.

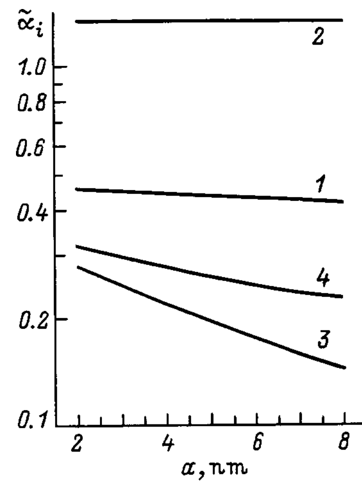

FIG. 2. $\tilde{\alpha}_i$ versus the quantum well width at $T=100$ K for $b=5$ nm and $n=10^{15}$ cm^{-3}. The numbers on the curves have the same meaning as in Fig. 1.

2. MOBILITY TENSOR

Using Eqs. (1) and (2), we can represent the diagonal components of the mobility tensor $\hat{\mu}$, written in principal axes, in the standard form

$$\mu_\perp=\frac{e\langle\tau_\perp\rangle}{m^*},\quad \mu_\parallel=\frac{e\langle\tau_\parallel\rangle}{\langle m_\parallel\rangle},\tag{38}$$

where $\langle\tau_\perp\rangle$ and $\langle\tau_\parallel\rangle$ are the energy-averaged transverse and longitudinal relaxation times, $\langle m_\parallel\rangle$ is the average longitudinal effective mass,

$$\langle\tau_\perp\rangle=\frac{1}{n}\int_0^\infty\left(-\frac{\partial f_0}{\partial E}\right)\tau_\perp(E)\rho_c(E)EdE,\tag{39}$$

$$\langle\tau_\parallel\rangle=[1-\exp(-n/N_c)]^{-1}\int_0^\infty\left(-\frac{\partial f_0}{\partial E}\right)\tau_\parallel(E)dE,\tag{40}$$

$$\frac{1}{\langle m_\parallel\rangle}=\frac{\Delta\rho_c}{4m_\parallel n}[1-\exp(-n/N_c)].\tag{41}$$

In Eqs. (39)–(41), $\rho_c=m^*/\pi d\hbar^2$ is the density of states in the bottom conduction miniband in the two-dimensional electron gas approximation, $N_c=k_0T\rho_c$ is the effective density of states in the bottom miniband, and $m_\parallel=2\hbar^2/\Delta^2d^2$ is the longitudinal effective mass at the miniband bottom. For a nondegenerate electron gas, which corresponds to satisfying the condition $n\ll N_c$, in the power-law approximation for the relaxation time as a function of the energy and temperature

$$\tau_i(E)=\tau_{0i}(k_0T)^{\beta_i}E^{\alpha_i+1/2},\tag{42}$$

the expressions for the average relaxation times (39) and (40) and for the average longitudinal effective mass (41) assume the form

$$\langle\tau_i\rangle=\tau_{0i}(k_0T)^{\alpha_i+\beta_i+1/2}\Gamma(\alpha_i+\delta_i),\tag{43}$$

$$\frac{1}{\langle m_\parallel\rangle}=\frac{\Delta}{4k_0T}\frac{1}{m_\parallel}\sim T^{-1},\tag{44}$$

where $\Gamma(n)$ is the gamma function, $\delta_\perp=5/2$, and $\delta_\parallel=3/2$. Using Eqs. (38), (43), and (44), we obtain for the temperature dependence of the mobility

$$\mu_i\sim T^{\gamma_i},\tag{45}$$

where $\gamma_i=\alpha_i+\beta_i+\chi_i$, $\chi_i=1/2$, and $\chi_\parallel=-1/2$.

For a degenerate electron gas with $n\gg N_c$ we obtain, instead of Eqs. (43) and (44), formulas that depend on the reduced Fermi level ξ, or electron density $n=\rho_c\xi$,

$$\langle\tau_i\rangle=\tau_i(\xi)\sim T^{\beta_i}\xi^{\alpha_i+1/2}\sim T^{\beta_i}n^{\alpha_i+1/2},\tag{46}$$

$$\frac{1}{\langle m_\parallel\rangle}=\frac{\Delta}{4\xi}\frac{1}{m_\parallel}\sim n^{-1}.\tag{47}$$

According to Eqs. (46) and (47), we obtain the following expression for the temperature and electron density dependence of the mobility:

$$\mu_i\sim T^{\beta_i}n^{\alpha_i+\chi_i}.\tag{48}$$

3. NUMERICAL ANALYSIS FOR SCATTERING BY IMPURITY IONS AND NEUTRAL ATOMS

Since analytic expressions could not be obtained for the formulas describing scattering by impurity ions and neutral atoms, we analyzed numerically for these scattering mechanisms the energy dependence of the relaxation time and temperature dependence of the mobility. The analysis was made in the temperature range $50<T<300$ K for a composite SL with the parameters $a=b=5$ nm, $m^*=0.1m_0$, potential barrier height $V_{SL}=0.4$ eV, $\varepsilon_s=\varepsilon_\infty=10$, and $n=10^{15}$ cm^{-3}, which are characteristic of SLs used in infrared-range photodetectors.[1,2] According to numerical calculations,[16] the energy spectrum of this SL in the QW has two minibands of width $\Delta_1=1.6$ meV and $\Delta_2=18.5$ meV, separated in energy by 210 meV. These data substantiate the validity of the approximation, used in the calculations presented above, of a two-dimensional electron gas and a single miniband approximation for the SL.

The analysis associated with the numerical calculation of the functions $G_i(E)$ showed the following.

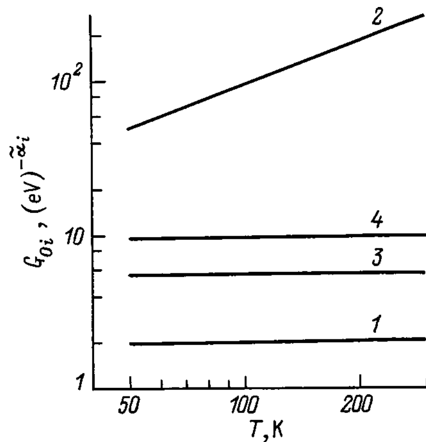

FIG. 3. G_{0i} versus the temperature for $a=b=5$ nm and $n=10^{15}$ cm^{-3}. The numbers on the curves have the same meaning as in Fig. 1.

1. For scattering by impurity ions and neutral atoms the functions $G_i(E)$ show a strong energy dependence, similar to a power-law dependence (see Fig. 1). In other words,

$$G_i(E) \approx G_{0i}(T) E^{\tilde{\alpha}_i}. \tag{49}$$

2. The exponent $\tilde{\alpha}_i$ in this dependence is essentially independent of temperature and the electron density in the range $n<10^{16}$ cm^{-3}. For scattering by neutral atoms it depends appreciably on the QW width a (see Fig. 2).

3. As the temperature increases, the quantity $G_{0\parallel}$ for scattering by impurity ions (Fig. 3, curve *2*) increases almost linearly, while $G_{0\perp}$ depends very weakly on temperature (Fig. 3, curve *1*). For scattering by neutral atoms this dependence is also very weak for both components (see Fig. 3, curve *3* and *4*).

4. For scattering by impurity ions, $G_{0\parallel}$ was found to be several orders of magnitude greater than G_{0i}, and it increases with decreasing electron density (Fig. 4, curve *2*). For $G_{0\perp}$ this dependence is weak. For scattering by neutral atoms, $G_{0\parallel}$ and $G_{0\perp}$ are of the same order of magnitude and are virtually independent of electron density (see Fig. 4).

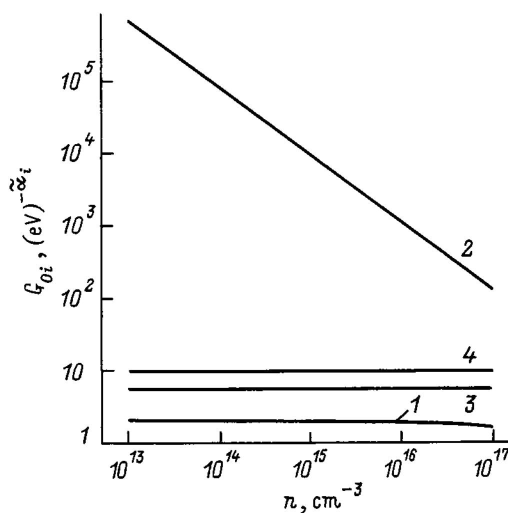

FIG. 4. G_{0i} versus the electron density at $T=100$ K for $a=b=5$ nm. The numbers on the curves have the same meaning as in Fig. 1.

TABLE I. Exponents in the energy and temperature dependences of the momentum relaxation time and mobility of electrons in a superlattice.

Scattering mechanism	$\alpha_0+\beta_0$	$\tilde{\alpha}_i$ $i=\perp$	$\tilde{\alpha}_i$ $i=\parallel$	$\tilde{\beta}_i$ $i=\perp$	$\tilde{\beta}_i$ $i=\parallel$	γ $i=\perp$	γ $i=\parallel$
Impurity ions	1.5	0.4	1.4	0	0.9	1.6	−1.3
Neutral atoms	0	0.2	0.3	0	0	0.3	−0.8
Acoustic phonons	−1.5	0	0	0	0	−1.0	−2.0

Note: The exponents refer to the transverse ($i=\perp$) and longitudinal ($i=\parallel$) components of the tensor.

On the basis of the above analysis, the dependence of the functions G_i on temperature and energy can be represented in the form

$$G_i \sim T^{\tilde{\beta}_i} E^{\tilde{\alpha}_i}, \tag{50}$$

Then, using Eqs. (31) and (45), the temperature-dependence of the mobility for a nondegenerate electron gas assumes the form (45), where $\alpha_i=\alpha_0-\tilde{\alpha}_i$, $\beta_i=\beta_0-\tilde{\beta}_i$, and α_0 and β_0 are the exponents in the energy and temperature dependences of the relaxation time in a bulk semiconductor. The temperature-average values of $\tilde{\alpha}_i$, $\tilde{\beta}_i$, and γ_i, calculated with the above-indicated parameters of the SL and corresponding to the three basic scattering mechanisms, are presented in Table I. It follows from the table that a strong change in the temperature-dependence of the mobility in the SL under study, in contrast to its constituent bulk semiconductors, should be expected for the longitudinal component. In the extrinsic conductivity range, determined by scattering by impurity ions and neutral atoms, this dependence for the longitudinal mobility is of a qualitatively different character than in bulk semiconductors, since it should decrease with increasing temperature.

[1] K. K. Choi, B. F. Levine, C. G. Bethea, J. Walker, and R. J. Malik, Appl. Phys. Lett. **50**, 1814 (1987).
[2] B. F. Levine, A. Y. Cho, J. Walker, D. L. Sivco, and D. A. Kleinman, Appl. Phys. Lett. **52**, 1481 (1988).
[3] B. F. Levine, S. D. Gunapala, and R. F. Kopf, Appl. Phys. Lett. **58**, 1551 (1991).
[4] H. Lobentanzer, W. Konig, W. Stolz, K. Ploog, LT. Elsaesser, and R. J. Bauerle, Appl. Phys. Lett. **53**, 572 (1988).
[5] X. Zhou, P. K. Bhattocharaya, G. Hugo, S. C. Hong, and E. Gulari, Appl. Phys. Lett. **54**, 856 (1989).
[6] A. Sibille, J. F. Palmier, H. Wang, and F. Mollot, Phys. Rev. Lett. **64**, 52 (1990).
[7] C. Waschke, H. G. Roskos, and R. Schwedler, Phys. Rev. Lett. **70**, 3319 (1993).
[8] A. A. Ignatov, K. F. Renk, and E. P. Dodin, Appl. Phys. Rev. Lett. **70**, 1996 (1993).
[9] Yu. V. Kopaev and S. N. Molotkov, JETP Lett. **59**, 800 (1994).
[10] A. Ya. Shik, Fiz. Tekh. Poluprovodn. **7**, 261 (1973) [Sov. Phys. Semicond. **7**, 187 (1973)].
[11] J. R. Meyer, D. J. Arnold, C. A. Hoffman, and F. J. Bartoli, J. Appl. Phys. **74**, 6676 (1993).
[12] I. Dharssi and P. N. Butcher, J. Phys.: Condens. Matter **2**, 119 (1990).
[13] B. L. Gelmont, M. Shur, and M. Stroscio, J. Appl. Phys. **77**, 657 (1995).
[14] N. Bannov, V. Aristov, and V. Mitin, Solid State Commun. **93**, 483 (1995).
[15] C. Erginsoy, Phys. Rev. **79**, 1013 (1950).
[16] S. I. Borisenko and K. F. Karavaev, Fiz. Tekh. Poluprovodn. **32**, 607 (1998) [Semiconductors **32**, 544 (1998)].

Translated by M. E. Alferieff

Determination of the density of states in quantum wells and quantum dot arrays by the capacitance-voltage method

V. Ya. Aleshkin,*) N. A. Bekin, M. N. Buyanova, and A. V. Murel'

Institute of Physics of Microstructures, Russian Academy of Sciences, 603600 Nizhny Novgorod, Russia

B. N. Zvonkov

Physicotechnical Scientific-Research Institute at the Nizhegorod State University, 660036 Nizhny Novgorod, Russia

(Submitted February 8, 1999; accepted for publication April 2, 1999)
Fiz. Tekh. Poluprovodn. **33**, 1246–1252 (October 1999)

The possibility of determining the electronic density of states in quantum wells and quantum dot arrays in heterostructures from the capacitance-voltage curve is investigated. In heterostructures fluctuations of the composition and geometrical dimensions play an important role. It is shown that to reconstruct the exact density of states from the measured capacitance-voltage curve is impossible, because this problem is ill-posed from the mathematical point of view. An approximate method is proposed for solving the problem, involving the determination of a ''reduced'' density of states. It is shown that the reduced density of states is close to the true density if the characteristic energy scale governing the variation of the latter is much greater than the thermal energy kT. The proposed method is used to find the density of states in the conduction band of a quantum well in an $In_{0.22}Ga_{0.78}As/GaAs$ heterostructure.
© *1999 American Institute of Physics.* [S1063-7826(99)02110-9]

INTRODUCTION

Capacitance-voltage curves (C–V method) are currently used not only to determine the concentration profile of a doping impurity, but also to find discontinuities of the energy bands at heterojunctions[1] and to investigate the spectra of electrons and holes in quantum wells[2–4] and quantum dots.[5,6] The electron spectra in quantum wells and arrays of quantum dots (we use the generic term ''planar states'' for both cases) are usually found by comparing the calculated dependence of the capacitance on the applied voltage, $C(V)$, for an ''ideal'' (free of fluctuations) structure with the observed curve (see, e.g., Refs. 3, 4, and 7); simple estimates have been used for the same purpose in Ref. 5). The parameters of the electronic states in quantum wells and quantum dots can then be determined from the condition of best fit of these curves.

In real structures, however, owing to fluctuations of the composition of semiconductors and fluctuations of their geometrical dimensions, the density of planar states can differ appreciably from the density of the ideal structure. This disparity bears important information about the quality of the structure. By the same token, it is one of the causes of errors in determining the parameters of the electronic spectrum by the above-indicated method. It seems natural to inquire whether the electronic density of planar states could be found directly from the measured $C(V)$ curve.

In this paper we show that the exact density of planar states $G(\varepsilon)$ cannot be reconstructed from the measured capacitance-voltage curve. However, a ''reduced'' density of states $\tilde{G}(\varepsilon)$ can be determined from the $C(V)$ curve. The reduced density of states is close to the real one if the energy scale of variation of the latter is much greater than kT, where k is the Boltzmann constant, and T is the temperature at which $C(V)$ is measured. The proposed method of reconstructing the reduced density of states is used for an $In_{0.22}Ga_{0.78}As/GaAs$ heterostructure with a broad (72 Å) quantum well. The density-of-states curves reconstructed from $C(V)$ measurements for this structure exhibit good agreement with data obtained from photoluminescence measurements.

The analogous problem of finding the density of surface states at an insulator-semiconductor interface has been solved for MIS structures.[8] In solving this problem, however, the authors have assumed that the density of surface states varies only slightly within the kT scale. For structures containing quantum dots and quantum wells this condition can break down over a wide range of temperatures. Moreover, even for the density of surface states this assumption is not always valid. In these cases the proposed method will give a more accurate value of the density of surface states than the customary approach.[8]

THEORY

We consider a Schottky contact to an n-type semiconductor containing planar states. We direct the x axis into the depth of the semiconductor and place the origin on its surface. Let $x=x_1$ in the plane in which the planar states are situated. We introduce several simplifying assumptions. First, we consider the semiconductor to be uniformly doped. Second, we assume that the lengths of the wave function of the planar states in the x direction are much smaller than the characteristic lengths of the space-charge regions, so that the charge density of the planar states can be regarded as pro-

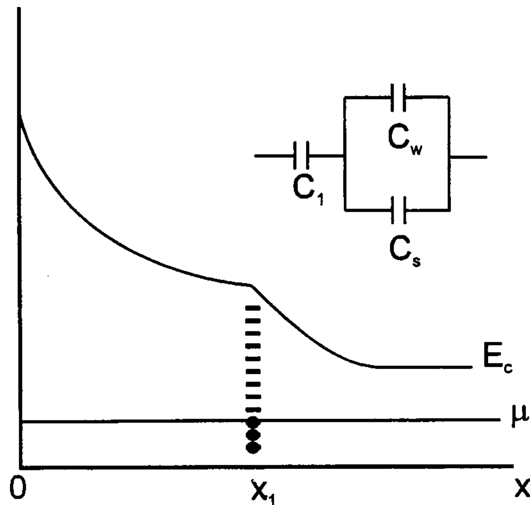

FIG. 1. Band diagram of the Schottky contact to a semiconductor containing planar states, showing the conduction band E_c and the level of the chemical potential μ. Inset: equivalent circuit of the Schottky barrier.

portional to the Dirac delta function $\delta(x-x_1)$. Finally, we assume that the frequency of the external applied voltage is either much higher (high frequency) or much lower (low frequency) than the charge-transfer frequency of the planar states.

Let a large negative voltage be applied to the Schottky barrier, so that all electrons are expelled from the region $0<x<x_1$ by the electric field (see Fig. 1). We set the electric potential in the bulk of the semiconductor equal to zero. When the applied voltage is changed by a small increment dV, the potential in the plane $x=x_1$ also changes by an increment du, where

$$dV=du+x_1 dE, \tag{1}$$

where dE is the increment of the electric field in the region $x<x_1$.

Since there are no electrons in this region, the charge in the semiconductor can change only for $x \geqslant x_1$. Consequently, the following relations are valid for dE:

$$dE_0=-\frac{4\pi}{\chi}(dQ_w+dQ_s), \quad dE_\infty=-\frac{4\pi}{\chi}dQ_s, \tag{2}$$

where the subscripts 0 and ∞ correspond to low frequencies and high frequencies, respectively, χ is the dielectric permittivity of the semiconductor, and dQ_w and dQ_s are the charge increments of the planar states and the semiconductor, respectively, in the region $x>x_1$.

Equations for the reciprocal specific capacitance (reciprocal of the capacitance per unit area) of the Schottky barrier at low and high frequencies can be obtained from Eqs. (1) and (2):

$$\frac{1}{C_0(V)}=\frac{dV}{dQ_0}=\frac{1}{C_1}+\frac{1}{C_w+C_s}, \tag{3}$$

$$\frac{1}{C_\infty(V)}=\frac{dV}{dQ_\infty}=\frac{1}{C_1}+\frac{1}{C_s},$$

where C_1 is the specific capacitance of the semiconductor layer $0<x<x_1$, C_w is the specific capacitance of the planar states, and C_s is the specific capacitance of the semiconductor $x>x_1$,

$$C_1=\frac{\chi}{4\pi x_1}, \quad C_w=-\frac{dQ_w}{du}, \quad C_s=-\frac{dQ_s}{du}. \tag{4}$$

The charges Q_w and Q_s are completely determined by the potential in the plane $x=x_1$, so that C_w and C_s are functions of u and not of the total voltage V. Consequently, the low-frequency capacitance can be represented by the equivalent circuit[3,8] shown in the inset in Fig. 1. It is obvious from Eq. (3) that the high-frequency capacitance can be regarded as C_1 and C_s connected in series.

To find the electronic charge on the planar states, it is necessary to integrate the product of the density of states and the distribution function over the energy. In order for the density of planar states to be independent of the voltage u, it is convenient to choose the bottom of the conduction band in the plane $x=x_1$ as the reference energy level.

This electronic charge can then be written in the form

$$Q_w(u)=-e\int_{-\infty}^{\infty}\frac{G(\varepsilon)}{1+(1/g)\exp[(\varepsilon-eu-\mu)/kT]}d\varepsilon, \tag{5}$$

where $G(\varepsilon)$ expresses the energy dependence of the density of planar states, μ is the chemical potential relative to the bottom of the conduction band in the bulk of the semiconductor, $-e$ is the electron charge, and g is the spin degeneracy factor. If Coulomb effects do not have any bearing on the filling of states, as is the case, for example, in quantum wells, then $g=1$. Otherwise (as in the case of quantum dots), $g>1$ (see the Appendix).

Differentiating (5) with respect to u, we find an equation for $C_w(u)$:

$$C_w(u)=\frac{e^2}{kT}\int_{-\infty}^{\infty}G(\varepsilon) \times\frac{(1/g)\exp[(\varepsilon-eu-\mu)/kT]}{\{1+(1/g)\exp[(\varepsilon-eu-\mu)/kT]\}^2}d\varepsilon. \tag{6}$$

The $C_w(u)$ curve can be obtained from the experimentally determined $C_0(V)$ and $C_\infty(V)$ curves. We shall discuss below how this can be done.

Can $G(\varepsilon)$ be determined from the known function $C_w(u)$ by solving Eq. (6) exactly? The answer is no, unless $T=0$ and the amplitude of the alternating voltage is infinitely small. Then $C_w(u)=e^2G(\mu+eu)$. We first discuss the physical reason for the negative answer. It is evident from Eq. (6) that planar states whose energies differ from the chemical potential [which is $\mu+eu$ in the energy reference frame (5)] by an amount smaller than, or of the same order as kT contribute to the capacitance C_w. It is therefore clearly impossible for the structure of the density of states on an energy scale much smaller than kT to be extracted from the function $C_w(u)$. Consequently, the only quantity that can be

deduced from $C_w(u)$ is $\widetilde{G}(\varepsilon)$, which is obtained from $G(\varepsilon)$ by averaging over the energy in a scale of the order of kT with a certain weighting function.

From the mathematical point of view Eq. (6) is an example of an ill-posed problem,[9] because an inverse operator does not exist for an integral operator with a kernel of the kind in Eq. (6). Indeed, the function $\exp(it\varepsilon)$ is an eigenfunction of an integral operator with the kernel (6), corresponding to the eigenvalue

$$\lambda(t)=\frac{\pi t}{\sinh(\pi kTt)}\exp(it\widetilde{\mu}),\quad \widetilde{\mu}=\mu+kT\ln(g). \tag{7}$$

The quantity $\lambda(t)$ vanishes as t tends to infinity, a consequence of the "insensitivity" of this integral operator to rapidly oscillating functions. It is a well-known fact that operators with null eigenvalues do not have inverse operators.

To find an approximate solution of Eq. (6), we can construct an approximate inverse operator (Green's function), in which the contribution of harmonics with $|t|\geqslant t_{\max}\sim 1/kT$ is suppressed. As a result, the function $G(\varepsilon)$ is obtained instead of $\widetilde{G}(\varepsilon)$. Constructing the Fourier transform, from Eq. (6) we obtain

$$G(t)=C_w(t)\frac{\exp(-it\widetilde{\mu})\sinh(\pi tkT)}{e^2\pi tkT},$$

$$G(t)=\int_{-\infty}^{\infty}G(\varepsilon)\exp(-it\varepsilon)d\varepsilon. \tag{8}$$

Equation (8) can be used to find the expression for $\widetilde{G}(\varepsilon)$

$$\widetilde{G}(\varepsilon)=\frac{1}{ekT}\int_{-\infty}^{\infty}C_w(u)F\left(\frac{\varepsilon-\widetilde{\mu}-eu}{kT}\right)du, \tag{9}$$

where $F(\alpha)$ is the approximate Green's function of Eq. (6),

$$F(\alpha)=\frac{1}{\pi}\int_0^{\infty}\frac{\sinh(\pi x)}{\pi x}\cos(\alpha x)\cdot\sigma(\beta x)dx,$$

$$\sigma(\beta x)=\exp(-\pi\beta x^2). \tag{10}$$

Here the function $\sigma(\beta x)$ is introduced for regularization, cutting out the contribution of higher harmonics to the Green's function, $\beta\sim 1/\sqrt{t_{\max}kT}$. Figure 2 shows the $F(\alpha)$ curves for three values of β: $\beta=0.3$, 0.2, 0.15.

It is evident from the figure that the frequency and the amplitude of the oscillations of $F(\alpha)$ increase as β decreases. They tend to infinity as β tends to zero, the amplitude increasing exponentially as β decreases. It is therefore impossible to make β too small, because, on the one hand, to do so would produce errors in the calculations and, on the other hand, the result would be strongly influenced by errors of measurement of $C(V)$.

We note that in the determination of the density of surface states in MIS structures a function of the density of states with an argument equal to $\mu+eu$ is taken outside the integral analogous to (6) (Ref. 8). This operation converts Eq. (6) from an integral equation to an algebraic equation, but information is lost about the variations of the density of states on a scale of the order of kT.

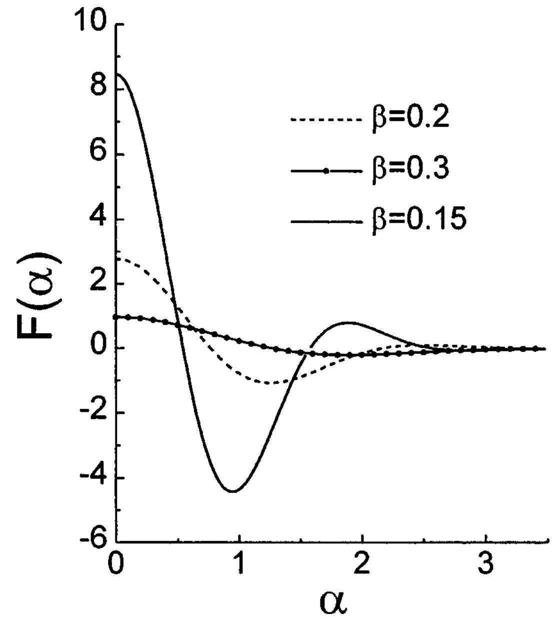

FIG. 2. Approximate Green's function of Eq. (6) for three values of β.

By a procedure analogous to that in MIS structures the function $C_w(u)$ can be extracted from $C_0(V)$ or from $C_\infty(V)$ or by using both characteristics directly.[8] If the capacitance C_1 is known, this problem reduces to the determination of the function $u(V)$. Thus, the function $C_s(u)$ is known for a uniformly doped semiconductor:

$$C_s(u)=\sqrt{e^2\chi}\left\{N_cF_{1/2}\left(\frac{\mu+eu}{kT}\right)-\frac{N_d}{1+g_d\exp[(\mu-E_d+eu)/kT]}\right\}\times(8\pi kT)^{-1/2}\left\{N_c\left[F_{3/2}\left(\frac{\mu+eu}{kT}\right)-F_{3/2}\left(\frac{\mu}{kT}\right)\right]-N_d\ln\left[\frac{g_d+\exp[(\mu-E_d+eu)/kT]}{g_d+\exp[(\mu-E_d)/kT]}\right]\right\}^{-1/2}. \tag{11}$$

In Eq. (11) N_c is the effective density of states in the conduction band, N_d is the density of uncompensated donors, E_d is the donor ionization energy, g_d is the donor spin degeneracy factor, and F_j denotes the Fermi–Dirac integrals.[10] Equation (11) can be obtained by a single integration of the Poisson equation in the region $x>x_1$.

If $C_0(V)$ is used to find $C_w(u)$, a differential equation for the function $u(V)$ can be obtained from Eqs. (1)–(3):

$$\frac{du}{dV}=1-\frac{C_0(V)}{C_1}, \tag{12}$$

which can then be integrated to give

$$u(V)=u_o+\int_{V_0}^{V}\left[1-\frac{C_0(V')}{C_1}\right]dV'. \tag{13}$$

The constant $u_0=u(V_0)$ can be evaluated by setting V_0 equal to a large negative quantity such that all electrons are

expelled from planar states; i.e., $C_w(u_0)=0$. At such voltages $1/C^2$ is a linear function of V, whose slope is governed by the number density N_d. Choosing an arbitrary point V_0 on this segment, we find $C_s(u_0)$ from Eq. (3). Equation (11) can be used to find u_0 from $C_s(u_0)$. Once the function $u(V)$ has been determined, $C_w(u)$ can be found from Eq. (3), taking (11) into account.

When $C_\infty(V)$ is used to find $C_w(u)$ (probably the right choice for working with quantum dots at low temperatures), the function $C_s(V)$ is determined from Eq. (3) and can then be used to seek $u(V)$ with the aid of Eq. (11). Dividing Eq. (1) by du and taking (2) and (4) into account, we find $C_w(u)$ (Ref. 8)

$$C_w(u)=C_1\left[\left(\frac{du}{dV}\right)^{-1}-1\right]-C_s(u). \tag{14}$$

If both the functions $C_\infty(V)$ and $C_0(V)$ are known, the quantity C_w can be determined from (3) for each value of V (Ref. 8):

$$C_w=\left(\frac{1}{C_0}-\frac{1}{C_1}\right)^{-1}-\left(\frac{1}{C_\infty}-\frac{1}{C_1}\right)^{-1}, \tag{15}$$

and the function $u(V)$ can be found by one of the means discussed above.

We now discuss how to find C_1. Several methods are available for its determination. We shall look at the two simplest ones. In heterostructures having sufficiently long departure times of electrons from planar states (e.g., in quantum dot arrays), the required function is probably simplest to determine by measuring $C_0(V)$ and $C_\infty(V)$. Calculating u according to Eq. (13), we can choose C_1 so that the function $C_\infty(V)$ obtained from (3) using (11) best fits the experimentally observed curve.

In a uniformly doped structure the law of conservation of momentum of the charge distribution can be used to determine C_1 (Ref. 1). The coordinate x_1 can then be written in the form

$$x_1=\int_{x_0}^{x_2}[N_d-\hat{n}(x)]x\,dx \Bigg/ \int_{x_0}^{x_2}[N_d-\hat{n}(x)]dx, \tag{16}$$

where $\hat{n}(x)$ and x are the number density and coordinate obtained from $C_0(V)$ by means of the Schottky equation.[11] Without an external voltage the potentials of the x_0 and x_2 planes must be identical. In such a structure, for low bias voltages, when the space-charge region of the Schottky barrier is not in contact with the space-charge region around the planar states, $1/C^2$ depends linearly on V. At high voltages, when all electrons are expelled from the planar states, it is again linear. The requirement of equality of the potentials in the x_0 and x_2 planes can be met if the voltages corresponding to passage of the space-charge region through these planes are chosen anywhere in the indicated linear segments at low and high voltages.

Figure 3 shows the results of determining the density of states of a quantum well in GaAs from the calculated dependence $C_0(V)$ at three temperatures. The density of states of the quantum well is chosen in the form

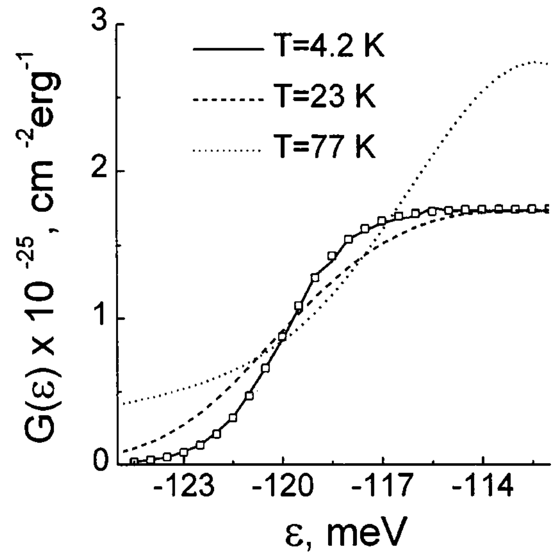

FIG. 3. True density of states (points) and curves reconstructed from Eq. (9) for three temperatures: $T=4.2$ K, $\gamma\gg kT=0.36$ meV; $T=23$ K, $\gamma\sim kT$ meV; $T=77$ K, $\gamma\ll kT=6.6$ meV.

$$G(\varepsilon)=\frac{m_c}{2\pi\hbar^2}\left[1+\tanh\left(\frac{\varepsilon+\varepsilon_0}{\gamma}\right)\right], \tag{17}$$

where m_c is the electron mass in the conduction band of GaAs, $\varepsilon_0=120$ meV, and $\gamma=2$ meV. The donor density in GaAs is assumed to be $3\times10^{16}\,\mathrm{cm}^{-3}$, and $x_1=0.13\,\mu$m. Making use of Eq. (17) and solving the Poisson equation, we calculate the function $C(V)$ and then determine $\tilde{G}(\varepsilon)$ form it (setting $\beta=0.2$). It is evident form the figure that $\tilde{G}(\varepsilon)$ is close to $G(\varepsilon)$ if the characteristic scale of $G(\varepsilon)$ is much greater than kT ($\gamma\gg kT$).

Note the considerable sensitivity of the method to the accuracy of determination of x_1. Calculations show that an error of a fraction of one percent for x_1 induces double-digit percent errors in determining the density of states for quantum wells in the plateau region. This fact probably rules out the possibility of determining the density of states with high accuracy on the plateau in quantum wells (i.e., of finding the effective mass). However, the method is far less sensitive to errors of x_1 in the region of a small density of states. We therefore assume that the given method can be used to investigate the structure of the density of states in this region (i.e., in the vicinity of the edge of the band).

EXPERIMENT AND DISCUSSION

An experiment has been performed on an $In_{0.22}Ga_{0.78}As/GaAs$ heterostructure. The structure was grown by metal-organic vapor-phase epitaxy (MOVPE) at atmospheric pressure using an n-GaAs substrate (carrier density $n\sim10^{18}\,\mathrm{cm}^{-3}$). The $In_{0.22}Ga_{0.78}As$ quantum well had a width of 72 Å and was situated at a distance of 0.17 μm from the surface of the semiconductor. The composition of the solid solution was determined from photoluminescence data. The GaAs epitaxial layer was doped with donors at a density of $8.5\times10^{16}\,\mathrm{cm}^{-3}$. The upper contact was a spray-deposited Au disk of diameter 1 mm. The $C(V)$ curves were measured

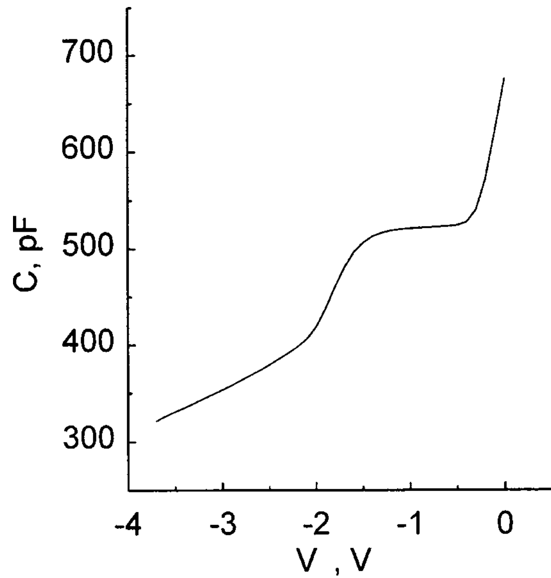

FIG. 4. Experimental capacitance-voltage curve of an $In_{0.22}Ga_{0.78}As/GaAs$ heterostructure with a broad (72 Å) quantum well. $T = 4.2$ K, frequency 1 MHz.

at liquid-helium temperature at frequencies of 1 MHz, 10 kHz, and 1 kHz. The observed C(V) curves for all three frequencies coincided within error limits dictated by the measurement error and corresponded to the low-frequency capacitance $C_0(V)$. A measured $C(V)$ curve is shown in Fig. 4.

Figure 5 shows the $\tilde{G}(\varepsilon)$ curve for this structure and the function $G_1(\varepsilon) = 6\times 10^{26}\exp(\varepsilon/\varepsilon_0)\,\mathrm{cm}^{-2}\cdot\mathrm{erg}^{-1}$, $\varepsilon_0 = 16$ meV. It is clearly evident in the figure that for $\varepsilon < -90$ meV these functions are nearly identical, and for $\varepsilon > -90$ meV the reconstructed density of states increases more rapidly with increasing energy than $G_1(\varepsilon)$. We note that the $\tilde{G}(\varepsilon)$ does not have the characteristic plateau observed for the two-dimensional density of states (the horizontal arrow indicates the calculated position of this plateau). The reason for the absence of the plateau is that the energy scale of the density of states is quite large (16 meV), so that even without an applied voltage the electron-filled states fall below this plateau. Consequently, the density of states determined from $C(V)$ is far from its counterpart in the ideal quantum well.

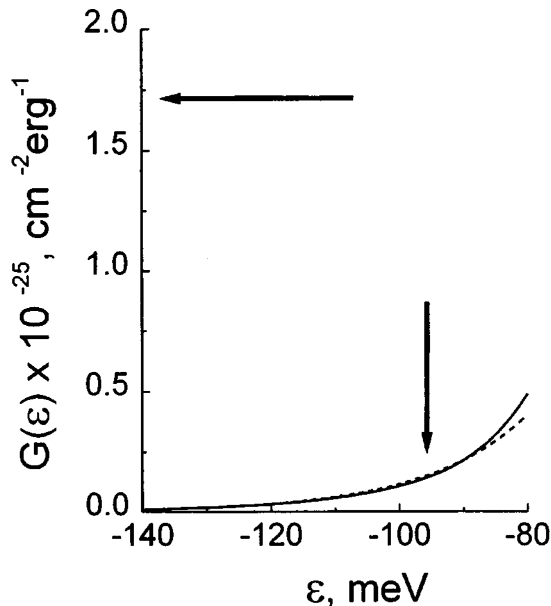

FIG. 5. Reconstructed electronic density of states $\tilde{G}(\varepsilon)$ (solid curve) in the quantum well of the $In_{0.22}Ga_{0.78}As/GaAs$ heterostructure. The dashed curve represents the function $G_1(e) = 6\times 10^{26}\exp(\varepsilon/\varepsilon_0)$ cm,$^{-2}$erg^{-1}, $\varepsilon_0 = 16$ meV. The vertical arrow indicates the energy of electrons in the quantum well at the maximum of the photoluminescence line. The horizontal arrow indicates the density of states of the ''ideal'' quantum well.

The full width at half-maximum (FWHM) of the photoluminescence peak is ~ 5 meV at $T = 4.2$ K (the diameter of the luminescent spot is $\sim 100\,\mu$m), as is fairly typical of such structures. The vertical arrow in Fig. 5 indicates the energy of electrons responsible for the main photoluminescence contribution at 77 K. It is evident that this energy lies at the beginning of a sharp rise in the density of two-dimensional states. The main factor responsible for the deviation of density of states in our structures from the ideal is fluctuations of the composition of the quantum well.[12] Clearly, the parts of the solid solution layer comprising the deepest wells for both electrons and holes, i.e., the parts with an above-average indium content, contribute to the photoluminescence. Consequently, the average depth of the quantum well for electrons must be smaller than inferred from the photoluminescence observations, consistent with the results shown in Fig. 5. We note that the scale of decay of the combined density of states in the vicinity of E_g for such structures, measured by means of the photoconductivity, amounts to several tens of meV (Ref. 13).

We wish to thank I. A. Sherishevskiĭ and V. I. Shashkin for helpful discussions.

This work has received financial support from the Russian Fund for Fundamental Research (RFFI Grant 98-02-16625), the Scientific=FETechnical Center ''Physics of Solid State Nanostructures'' (Grants 97-1069 and 97-1070), and the U.S. Civilian Research and Development Foundation for the Independent States of the Former Soviet Union (CRDF, BRHE Program).

APPENDIX

A statistical approached developed for multiply charged centers[14] can be used to find the charge density in a quantum dot array. Let us consider a single quantum dot. We denote by W_n the probability of finding n electrons in it, and by N the maximum number of electrons that can exist in it. We assume that the temperature is low enough that the population of excited states can be disregarded. The following relation holds in this case:

$$\frac{W_n}{W_{n-1}} = g_n \exp\left(\frac{\mu - \varepsilon_n}{kT}\right), \tag{A1}$$

where g_n is the number of ways for the nth electron to be situated in the quantum dot, and ε_n is the change in the

energy of the quantum dot when the nth electron is added to it. Using Eq. (18) and the fact that the sum of W_n over all possible n is equal to unity, we find

$$W_n=\frac{\Pi_{i=1}^{n} g_i \exp[(\mu-\varepsilon_i)/kT]}{1+\Sigma_{n=1}^{N}\Pi_{i=1}^{n} g_i \exp[(\mu-\varepsilon_i)/kT]}. \tag{A2}$$

To determine the electronic charge on the quantum dot, it is appropriate to introduce the probability of at least n electrons being situated in it:

$$w_n=\sum_{i=n}^{N} W_n=\frac{1}{1+\gamma_n \exp[(\varepsilon_n-\mu)/kT]}, \tag{A3}$$

$$\gamma_n=\frac{1+\sum\limits_{n'=0}^{n-2}\prod\limits_{i=n'}^{n-1}(1/g_i)\exp[(\varepsilon_i-\mu)/kT]}{g_n\left\{1+\sum\limits_{n'=n+1}^{N}\prod\limits_{i=n+1}^{n'} g_i \exp[(\mu-\varepsilon_i)/kT]\right\}}. \tag{A4}$$

If the distance between energy levels is much greater than kT, we have

$$w_n\approx\frac{1}{1+(1/g_n)\exp[(\varepsilon_n-\mu)/kT]}. \tag{A5}$$

The average electronic charge of the quantum dot can now be written in the form

$$q=-e\sum_{n=0}^{N} w_n=-e\int d\varepsilon\sum_{n=0}^{N}\delta(\varepsilon-\varepsilon_n)w(\varepsilon)$$

$$=-e\int d\varepsilon G_{\mathrm{QD}}(\varepsilon)w(\varepsilon), \tag{A6}$$

where $G_{\mathrm{QD}}(\varepsilon)$ is the density of states in the quantum dot, and

$$w(\varepsilon)=\frac{1}{1+[1/g(\varepsilon)]\exp[(\varepsilon-\mu)/kT]},$$

$$g(\varepsilon_n)=g_n, \quad w(\varepsilon_n)=w_n. \tag{A7}$$

Summing (A6) over the array of quantum dots, we obtain Eq. (5). We note that $g=2$ for the ground state and the first excited state in self-organized dots of the heteropair GaAs/InAs, and $g=4$ for higher excited states.[6] Because of strong spin-orbit interaction for all hole states in these dots, $g=2$ (this result can be demonstrated using group theory). Since the energy in Eq. (9) is determined to within an amount of the order of kT, we can assume without incurring large error that $g=2$ for such structures.

[*)]E-mail: aleshkin@ipm.sci-nnov.ru; Fax: (8312)675553

[1] H. Kroemer, W. Y. Chen, J. S. Harris, and D. D. Edwall, Appl. Phys. Lett. **36**, 295 (1980).
[2] X. Letartre, D. Stievenard, and E. Barbier, J. Appl. Phys. **69**, 7912 (1991).
[3] V. Ya. Aleshkin, E. V. Demidov, B. N. Zvonkov, A. V. Murel', and Yu. A. Romanov, Fiz. Tekh. Poluprovodn. **25**, 1047 (1991) [Sov. Phys. Semicond. **25**, 631 (1991)].
[4] P. N. Brounkov, S. G. Konnikov, T. Benyattou, and G. Guillot, Phys. Low-Dimens. Semicond. Struct. **10/11**, 197 (1995).
[5] G. Medeiros-Rebeiro, D. Leonard, and P. M. Petroff, Appl. Phys. Lett. **66**, 1767 (1995).
[6] M. Fricke, A. Lorke, J. P. Kotthaus, and G. Medeiros-Ribeiro, and P. M. Petroff, Europhys. Lett. **36**, 197 (1996).
[7] D. N. Bychkovskiĭ and O. V. Konstantinov, Fiz. Tekh. Poluprovodn. **28**, 1257 (1994) [Semiconductors **28**, 715 (1994)].
[8] E. H. Nicollian and J. R. Brews, *MOS (Metal Oxide Semiconductor) Physics and Technology* (Wiley, New York, 1982), Chap. 8.
[9] A. N. Tikhonov and V. Ya. Arsenin, *Solutions of Ill-Posed Problems* (Halsted Press, New York, 1977).
[10] V. I. Fistul', *Heavily Doped Semiconductors* (Plenum Press, New York, 1969).
[11] S. M. Sze, *Physics of Semiconductor Devices*, 2nd ed. (Wiley–Interscience, New York, 1981).
[12] I. A. Avrutskiĭ, O. P. Osaulenko, V. G. Plotnichenko, and Yu. N. Pyrkov, Fiz. Tekh. Poluprovodn. **26**, 1907 (1992) [Sov. Phys. Semicond. **26**, 1069 (1992)].
[13] I. A. Karpovich, V. Ya. Aleshkin, A. V. Anshon, N. V. Baĭdus', L. M. Batukova, B. N. Zvonkov, and S. M. Plankina, Fiz. Tekh. Poluprovodn. **26**, 1886 (1992) [Sov. Phys. Semicond. **26**, 1057 (1992)].
[14] V. L. Bonch-Bruevich and S. G. Kalashnikov, *Physics of Semiconductors* [in Russian], Nauka, Moscow, 1990.

Translated by James S. Wood

AMORPHOUS, GLASSY AND POROUS SEMICONDUCTORS

Role of impurities in the formation of silicyne (long-chain silicon): theory and experiment

A. I. Mashin,*) A. F. Khokhlov, S. K. Ignatov, and A. A. Shchepalov

N. I. Lobachevskiĭ Nizhegorod State University, 603600 Nizhny Novgorod, Russia

A. G. Razuvaev

Scientific-Research Institute of Chemistry at the Nizhegorod State University, 603600 Nizhny Novgorod, Russia

Fiz. Tekh. Poluprovodn. **33**, 1253–1259 (October 1999)

The short-range order structure of amorphous silicon prepared by various methods is investigated by electron diffraction analysis. The influence of impurities in the as-prepared films and those irradiated with neon, oxygen, and carbon ions at doses up to 1×10^{16} cm^{-2} on the character of structural transformations and the formation of interatomic silicon multiple bonds during annealing are investigated. The structure of films annealed at 500 °C is found to depend on the type of impurities and the nature of their chemical bond with silicon atoms. In particular, oxygen (>0.2 at. %), unlike hydrogen and carbon, acts as an inhibitor for the formation of silicyne. Good agreement is also noted between the experimentally determined short-range order parameters and those calculated by the nonempirical Hartree-Fock method. © *1999 American Institute of Physics.* [S1063-7826(99)02210-3]

INTRODUCTION

We have previously[1–3] published experimental data indicating that elemental silicon, like carbon, is capable of forming new allotropic forms. The new material, silicyne, consists of long linear chains (up to 100 atoms) of silicon atoms in the sp hybrid state. The probable formations in this case are polyene $(-\mathrm{Si}{\equiv}\mathrm{Si}-\mathrm{Si}{\equiv}\mathrm{Si}-\mathrm{Si}{\equiv}\mathrm{Si}-)_n$ or cumulene $(=\mathrm{Si}=\mathrm{Si}=\mathrm{Si}=\mathrm{Si}=\mathrm{Si}=\mathrm{Si}=)_n$ chains of silicon atoms. The chemical bond between atoms is established by sp hybridized (σ-bond) and p nonhybridized (π-bond) atomic orbitals. Some of the silicon atoms ($\approx 10-15$ at. %) exist in the sp^2 hybridized state. These atoms, like bridges, bind the silicon chains into a three-dimensional ordered network. We have obtained the new amorphous material (silicyne) by high-temperature (≈ 500 °C) vacuum annealing of tetrahedral amorphous silicon. The as-prepared films of amorphous silicon must have certain properties for this operation. In our work, in particular, we have prepared tetrahedral coordinated amorphous silicon by various methods capable of yielding both hydrogenated (*a*-Si:H) and hydrogen-free (*a*-Si) amorphous silicon, including the irradiation of crystalline silicon with inert gas ions. Only in certain cases, however, has vacuum annealing of the prepared amorphous silicon films resulted in the formation of silicyne. This fact, coupled with the lack of detailed investigations of the postanneal short-range order structure of amorphous silicon, possibly explains why linear chains of silicon atoms had not been discovered earlier.

The objective of the present study is to ascertain the necessary conditions for obtaining elemental silicon with an atomic structure other than tetrahedral. To achieve this goal, we have recruited the latest methods of physics and quantum chemistry, along with our own experimental data.

EXPERIMENTAL PROCEDURE

The basic films of amorphous silicon were prepared by the decomposition of silane in an rf glow discharge, electron-beam evaporation, ion-plasma sputtering, and vacuum sublimation of silicon. For the structural measurements silicon films of thickness 70–80 nm were deposited on a freshly cleaved NaCl chip. The deposition rate did not exceed 0.15 nm/s. The resulting amorphous silicon had a tetrahedral structure.

To modify the structure of the film and investigate the influence of impurities on the structural modifications, the amorphous silicon was irradiated with ions and then subjected to thermal annealing.

Irradiation by neon, carbon, and oxygen ions with energies up to 40 keV at doses in the range 10^{14} ions/cm^2 to 10^{16} ions/cm^2 took place with the target at room temperature. In none of the cases did the ion current density exceed 1 μA/cm^2.

Isothermal annealing was performed in a vacuum $\sim10^{-5}$ Torr. The anneal time was 20–30 min. The anneal temperatures were 350 °C, 500 °C, and 700 °C.

Transmission electron diffraction patterns were recorded by means of an ÉMR-102 recording electron diffraction camera. The electron scattering intensity was converted to the radial distribution function of the electron density by the standard Fourier transform procedure[4] and by optimization

 © 1999 American Institute of Physics

of the information functional.[5] The short-range order parameters were calculated from the area and positions of the maxima of the radial distribution function of the electron-density by a procedure similar to the one used in Ref. 6.

The spectral composition of the films was investigated by Auger electron spectroscopy on a PHI-545 spectrometer with a sensitivity threshold ≈ 0.1 at. %.

The amorphous silicon films for the nonstructural experiments had a thickness of 500–700 nm and were deposited on single-crystalline silicon or fused quartz substrates.

THEORETICAL APPROXIMATION

Quantum-chemical calculations have been performed by the nonempirical Hartree–Fock method in basis 6-311G(d) [RHF/6-311G(d)]. The correlation energy was taken into account by second-order Møller–Plesset perturbation theory [MP2/6-311G(d)]. The geometry was optimized by the gradient method. The stationary points of the surface potential energy were characterized by calculating the vibration frequencies. We have confined the present study to clusters of atoms existing only in the singlet spin state. The results of calculations of states having a higher order of multiplicity will be published in subsequent papers. PC Gamess-4.5.1 software[7] was used for all the calculations.

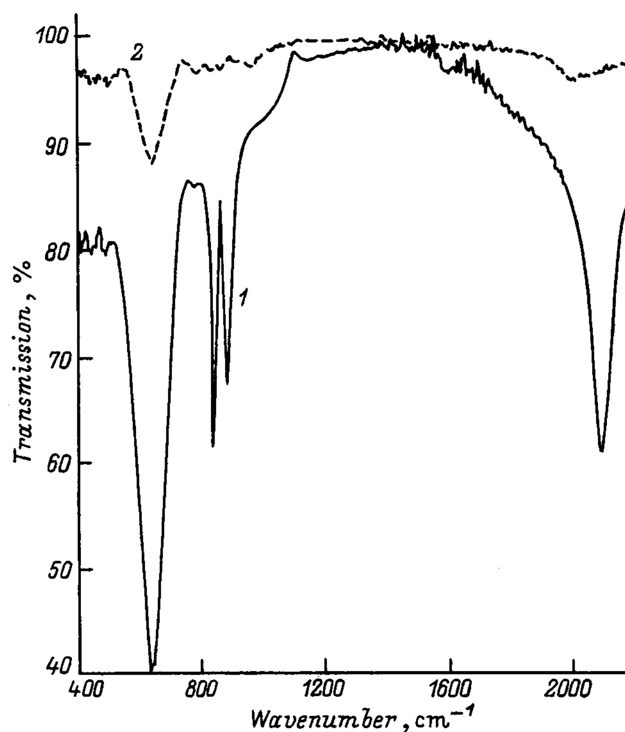

FIG. 1. Infrared transmission spectra of *a*-Si:H. (*1*) Before annealing; (*2*) after annealing at 500 °C.

RESULTS AND DISCUSSION

We have investigated the anneal-induced structural modification in *a*-Si:H films prepared by silane decomposition in a glow discharge at a substrate temperature $T_s = 50\,°C$. The film thickness was 70 nm. This material differs significantly from the *a*-Si:H investigated in our earlier work.[1] Its hydrogen content attains 40 at. %. The films have a high density of voids, which contain a large fraction of hydrogen both in their interior and on their surface.[8] As should be expected, the infrared (IR) transmission spectrum of such films (Fig. 1) differs from the customary investigated material (with $T_s = 250-300\,°C$) by the presence of absorption maxima in the interval $845-890\,cm^{-1}$, which correspond to $Si-H_2$ bonds and (or) polymer $(-SiH_2)_n$ chains. The short-wavelength absorption peak normally observed at $2000\,cm^{-1}$ is shifted to $2100\,cm^{-1}$. The shift is caused by Si–H or $Si-H_2$ bonds situated on the surfaces of the voids and not by Si–H bonds dissolved in the bulk of the material. It must also be noted that the IR spectrum of our investigated *a*-Si:H films contains weak absorption peaks near $950-1000\,cm^{-1}$ and $780\,cm^{-1}$. They are usually identified with vibrations of C–H and Si–C bonds, respectively.

A 20-min anneal at 500 °C leads to partial hydrogen evaporation. According to Ref. 8, not one, but two hydrogen evaporation peaks are observed for heavily hydrated amorphous silicon films. Their positions depend on the thickness of the film, but in every case the first hydrogen evaporation maximum occurs at a temperature below 400 °C, and the second occurs at 500–600 °C. Only at temperatures above 900 °C can the total evaporation of hydrogen be expected. Consequently, after annealing at 500 °C the hydrogen concentration in the films decreases, but not all the way to zero. This result is clearly evident from the IR transmission spectra of *a*-Si:H films annealed at 500 °C. It is a well-known fact that vibrational spectroscopy is not entirely a quantitative method, but it can be used effectively to detect the presence of impurity atoms and to determine the configurations in which they can be found. It is evident from Fig. 1 that the intensities of all the hydrogen-related absorption peaks drop considerably after annealing. This is particularly true of the absorption peaks associated with vibrations of bonds of the $Si-H_2$ types. Moreover, the absorption maximum in the vicinity of $2100\,cm^{-1}$ shifts toward $2000\,cm^{-1}$, so that mainly hydrogen in the form of Si–H bonds is left in the silicon film, where they propagate throughout the entire volume of the amorphous material. Weak absorption peaks corresponding to C–H and Si–C bonds can also be seen in this spectrum. Thus, according to IR spectroscopy data, in analyzing the structural modifications we must take into account not only the presence of Si in our films, but also hydrogen in monohydride (Si–H) and dihydride ($Si-H_2$) configurations, as well as carbon bonded to hydrogen or silicon. Our Auger spectral analysis of the investigated *a*-Si:H films has confirmed the presence of carbon in them at the sensitivity threshold level (≈ 0.1 at. %) of the instrument used in our work. No other impurities have been detected.

According to our measurements, *a*-Si:H films deposited at a substrate temperature of 50 °C have an almost-tetrahedral short-range order structure. Electron-density distribution curves with similar short-range order parameters have been observed by us previously[1] and by other researchers[6] in instrument-quality *a*-Si:H films. The first coordination number k_1 for the films investigated here is equal to 3.4 ± 0.2. The somewhat lower value of k_1 relative to our previous data[1] is attributable to a higher content of micro-

TABLE I. Results of Auger spectral analysis of amorphous silicon films.

Method of preparation	Impurity concentration, at. %		Multiple
	Oxygen	Carbon	bonds
Silane decomposition in glow discharge (oilless evacuation)	<0.1	≈0.1	Yes
Electron-beam evaporation	1.7	1.3	No
Ion-plasma sputtering	1.1	2.3	No
Vacuum sublimation of silicon	≈0.1	0.3	Yes
Silane decomposition with oilless evacuation	1.8	2.1	No

voids and bound hydrogen. Hydrogen atoms are known to have a lower electron scattering efficiency than silicon atoms, so that a high density of Si–H bonds and especially Si–H_2 bonds can affect the value of the first coordination number. The values of the valence angle $\varphi=(113\pm6)^\circ$ and the interatomic spacing $r_1=(2.34\pm0.04)$ Å are close to the ideal tetrahedral and indicate that the silicon atoms have four ordinary, almost-ideal, tetrahedral bonds.

Annealing at 350 °C leads to restoration of the structure of amorphous silicon up to typical values of the short-range order parameters for *a*-Si:H films prepared at high (250 − 300 °C) substrate temperatures. With a further increase in the anneal temperature, the character of the structural transformation and the parameters of the short-range order structure of the amorphous films repeat our previous data,[1] within the experimental error limits, for the case $T_s=250\,^\circ$C; in other words, after annealing at 500 °C we have observed a sharp decrease in k_1 to (2.1 ± 0.2) Å and (2.08 ± 0.04) Å, along with an increase in the valence angle to almost 180°, $\varphi=(173\pm6)^\circ$. Annealing at 700 °C immediately results in partial recrystallization of the film.

We have also observed significant structural changes in hydrogen-free silicon. In this case *a*-Si films were prepared by the vacuum sublimation of silicon. The substrate temperature was 300 °C. Like *a*-Si:H, the films remained amorphous up to an anneal temperature of 700 °C, and at $T_a=500\,^\circ$C we observed a substantial change in the short-range order structure of the still amorphous material. At this anneal temperature k_1 decreases from (3.8 ± 0.2) Å to (2.8 ± 0.2) Å, and r_1 decreases to (2.15 ± 0.04) Å. The valence angle, however, undergoes a perceptibly smaller change than in *a*-Si:H films $[\varphi=(132\pm6)^\circ]$. Even though the variation of the short-range order parameters is less pronounced than in hydrogenated silicon, they cannot be attributed to experimental error.

As in Ref. 1, we attribute the above-described changes in the short-range order structure of *a*-Si:H and *a*-Si to the formation of silicon multiple bonds during annealing.

Measurements of the structure of hydrogen-free amorphous silicon films prepared by other methods do not reveal any appreciable variation of the parameters of the first coordination sphere in annealing up to the temperature of partial recrystallization.

Table I shows data from an Auger spectral analysis of our films and the capacity of silicon atoms in these films to form multiple bonds in annealing. Clearly, the phenomenon in question is observed only in silicon films prepared by a technique that yields a sufficiently low (<1 at. %) content of impurities such as oxygen and carbon. Unfortunately, the methods at our disposal for the preparation of amorphous silicon films do not allow separate controlled variation of the oxygen and carbon concentrations when the latter are lower than 1 at. %. Consequently, to discern the role of each of these impurities, we have conducted experiments to study the short-range order structure of *a*-Si:H irradiated with carbon, oxygen, and neon ions.

The application of ion implantation for the injection of impurities is accompanied by the formation of a high density of radiation defects; our neon irradiation experiments therefore required that we take into account the influence of such defects on possible anneal-induced structural transformations of the films irradiated with carbon and oxygen ions.

The results of structural modifications with the annealing of previously irradiated *a*-Si:H films are shown in Figs. 2 and 3. The energy of the ions was chosen to match their range with the thickness of the irradiated film. It is a fairly simple matter in this case to estimate the average concentration of the injected impurity, which is uniquely determined by the irradiation dose alone. At the maximum dose it is of the order of 2 at. %, which is at least an order of magnitude higher than the natural concentration of impurities in the as-prepared silicon film.

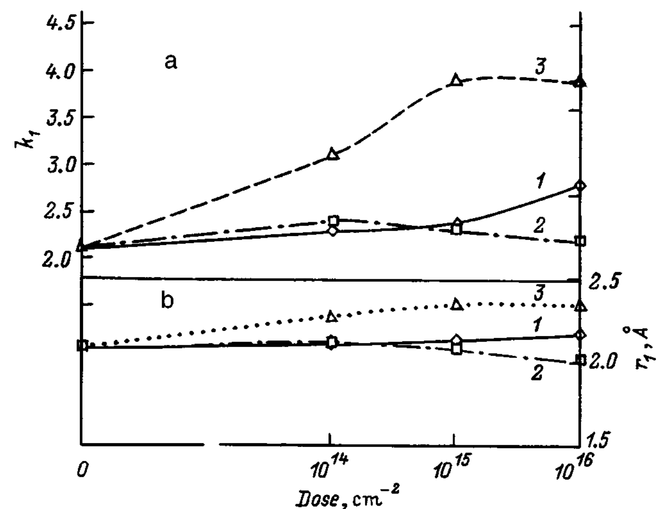

FIG. 2. Influence of irradiation dose on the first coordination number (a) and interatomic spacing (b) in *a*-Si:H films. Anneal temperature 500 °C. Ions: (*1*) neon; (*2*) carbon; (*3*) oxygen.

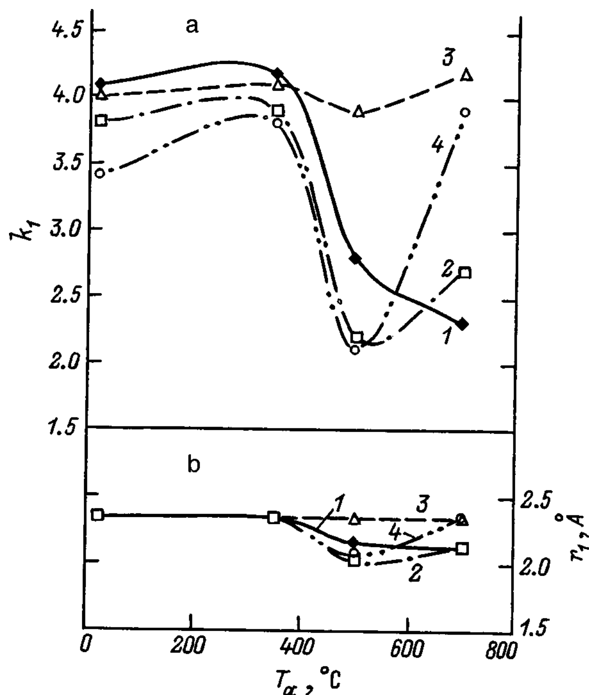

FIG. 3. Influence of irradiation on the variation of the first coordination number (a) and interatomic spacing (b) in *a*-Si:H films during annealing. Irradiation dose 1×10^{16} ions/cm^2. Ions: (*1*) neon; (*2*) carbon; (*3*) oxygen; (*4*) nonirradiated sample.

It is evident that the introduction of radiation defects during the irradiation of *a*-Si:H with neon ions is conducive to restoration of the tetrahedral structure of silicon (Fig. 2, curve *1*). In particular, we have observed that the first coordination number increases from 3.4 in nonirradiated silicon to 4.0 in silicon irradiated with neon at a dose $>10^{15}$ ions/cm^2. Neon partially accumulates in the voids, displacing hydrogen. The latter moves out into the bulk of the film, where it forms new Si–H bonds or escapes the film. Annealing at 350 °C can be regarded as a postimplantation treatment, which induces structural transformations that lower the free energy of the disordered *a*-Si:H network by creating a more uniform distribution of neon and by lowering the density of voids and other defects. According to secondary-ion mass spectroscopy data, implanted neon stays in the irradiated layer up to anneal temperatures ~1000 °C, and its initial evaporation temperature is 700 °C (Ref. 9). In our range of anneal temperatures, therefore, neon stays in the films, where it influences the diffusion and evaporation of hydrogen and, accordingly, influences the possible structural transformations in annealing. In particular, this is how we explain the lag of the recrystallization of amorphous silicon films at irradiation doses above 10^{15} cm^{-2}. They remain amorphous even at the highest anneal temperature used in our work. On the other hand, it should be noted that the presence of radiation defects and neon in the films does not eliminate the reduction of the first coordination number and the interatomic spacing after annealing, but merely raises the necessary temperature.

After carbon and oxygen implantation, the onset of radiation defects is accompanied by the embedding of atoms of these impurities in the disordered network and the formation of corresponding chemical bonds. Having an ionic component, such chemical bonds are stronger than the silicon-silicon bond.

It is evident from Figs. 2 and 3 that k_1 and r_1 are also observed to decrease after the irradiation of amorphous silicon films with carbon, even at the maximum dose. Moreover, the observed decrease in the average interatomic spacing is more pronounced. Here the maximum implanted carbon concentration (≈2 at. %) is higher than the carbon concentration in *a*-Si films prepared by methods in which the phenomenon in question has not been observed. It is a well-known fact that the carbon atom, having a smaller covalent radius than the silicon atom, is responsible for the onset of additional tensile stresses and dangling bonds in silicon. In addition, it can form multiple bonds with silicon. The presence of the ionic component together with the possible formation of a π-component of the silicon-carbon bond makes this bond noticeably shorter than the silicon-silicon bond. However, the carbon concentration in films irradiated even at the maximum carbon dose is still not sufficient to account for our observed decrease in the average distance between atoms (to 2.01 Å instead of 2.10 Å).

Finally, it is evident from Figs. 2 and 3 that the introduction of approximately 0.2 at. % (irradiation dose $\sim10^{15}$ cm^{-2}) oxygen atoms in *a*-Si:H films is sufficient to completely suppress the influence of annealing on the perceptible structural transformations of the disordered network. With this fact in mind, we can state unequivocally that the main reason for the absence of any reduction in k_1 and r_1 during annealing in the majority of amorphous silicon films (Table I) is the presence of a high concentration (in excess of 1 at. %) of oxygen atoms.

Consequently, when quantum-chemical methods are used in calculations of possible nontetrahedral silicon structures, allowance must be made for the fact that real films contain, together with silicon atoms, a small concentration of hydrogen in the form of Si–H bonds and (or) Si–H_2 bonds, as well as silicon-bound carbon and oxygen atoms. In theoretical calculations we have analyzed two models of the silicon chain structure. The first model rests on the assumption that silicon atoms can form only linear (one-dimensional) chains. The length of such chains is varied from 2 to 12 silicon atoms. Based on the experimental results, hydrogen, oxygen, or carbon atoms are situated at the ends of the chains. The object of the theoretical calculations is to look for stable linear silicon structures and to determine their parameters. The confinement to a linear structure alone can be fully justified, because in experiment restructuring takes place in a material comprising a rigid body, so that significant constraints are imposed on the movement of atoms during annealing.

Quantum-chemical calculations taking into account the correlation energy by second-order Mφller–Plesset perturbation theory [MP2/6-311G(d)] are cumbersome and technically difficult. As a result, we have managed them successfully only for clusters with a relatively small number of silicon atoms. The length of the chains of silicon atoms can be increased significantly by using the simpler Hartree–Fock

TABLE II. Optimized bond lengths (Å) and bond orders in linear silicon cluster structures.

Computational method	Cluster	Bond length, Å: Short Si–Si	Bond length, Å: Long Si–Si	Bond length, Å: Si–X	Bond order: Short Si–Si	Bond order: Long Si–Si	Bond order: Si–X
	Si_2H_2	1.939	⋯	1.453	2.916	⋯	0.956
	Si_4H_2	1.951	2.213	1.454	2.802	0.973	0.955
	Si_6H_2	1.965	2.210	1.454	2.665	0.994	0.957
	Si_8H_2	1.966	2.207	1.453	2.633	1.019	0.958
	$Si_{10}H_2$	1.968	2.206	1.453	2.599	1.024	0.959
RHF/6–311G(d)	$Si_{12}H_2$	1.968	2.205	1.453	2.595	1.027	0.960
	Si_2H_4	2.126	⋯	1.471	1.936	⋯	0.943
	Si_4H_4	2.071	2.112	1.467	1.934	1.849	0.941
	Si_6H_4	2.069	2.075	1.466	1.885	1.805	0.941
	Si_8H_4	2.066	2.072	1.466	1.830	1.799	0.942
	Si_2H_6	2.367	⋯	1.483	0.970	⋯	0.936
	Si_2H_2	1.984	⋯	1.463	2.916	⋯	0.954
	Si_4H_2	2.010	2.166	1.465	2.802	1.009	0.952
	Si_6H_2	2.044	2.152	1.466	2.665	1.045	0.954
	Si_2H_4	2.141	⋯	1.478	1.933	⋯	0.942
	Si_4H_4	2.084	2.134	1.476	1.936	1.841	0.940
MP2/6–311G(d)	Si_2H_6	⋯	2.346	1.488	⋯	0.971	0.936
	$Si_2C_2H_2$	⋯	2.165	1.626	⋯	0.971	2.830
	$Si_4C_2H_2$	2.038	2.154	1.631	2.643	1.003	2.788
	$Si_2C_2H_4$	2.068	⋯	1.722	1.974	⋯	1.873
	$Si_4C_2H_4$	2.074	2.089	1.720	1.898	1.805	1.856
	$Si_2C_2H_6$	1.985	⋯	1.880	2.918	⋯	0.916
	$Si_4C_2H_6$	2.010	2.170	1.878	2.764	0.996	0.928

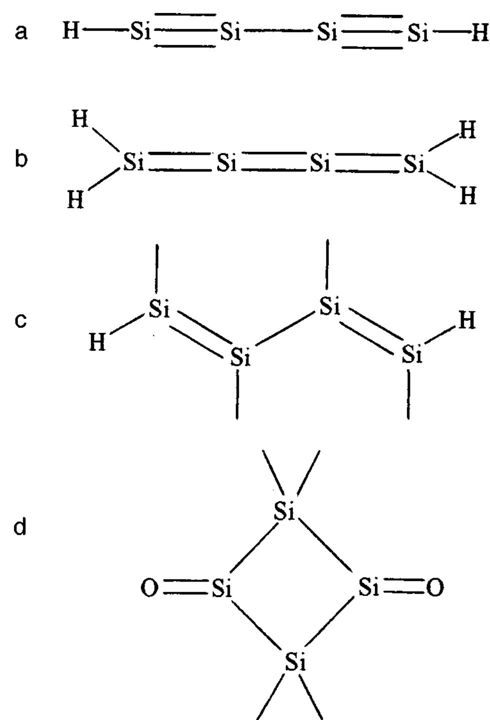

FIG. 4. Final structural geometries of silicon clusters after optimization.

method in basis 6-311G(d) [RHF/6-311G(d)]. Naturally, the results are less reliable in this approach. However, our calculations of comparatively small clusters by both methods do not yield fundamental differences in the results (Table II). This outcome encourages our expectation that the data of our calculations for large clusters without regard for the correlation energy will be equally trustworthy.

For example, Table II gives the parameters of the stable linear silicon clusters determined by us. If the chain of silicon atoms is terminated in oxygen atoms, we could not find a cluster structure with an energy minimum. The distances between silicon atoms in the table correspond to silicon-silicon bonds closest to the center. The symbol X in the Si-X column is interpreted everywhere as hydrogen atoms for a cluster of the Si_nH_m type, as carbon atoms for a cluster of the $Si_nC_kH_m$ type, and as oxygen atoms for a cluster of the Si_nO_k type. Clearly, if one hydrogen atom is situated at each end of the silicon chain, this kind of structure is optimized to a polyene form of the cluster with alternating triple and ordinary bonds (structure *a* in Fig. 4). The length of the silicon triple bond is determined by the length of the chain and in the cases investigated by us vary from 1.966 Å to 2.044 Å. The ordinary bond is shorter than in the ideal tetrahedral material and, depending on the length of the chain, varies from 2.152 Å to 2.213 Å. A similar shortening of a single bond in molecules with multiple bonds has been observed previously[10] for carbon. With the understanding that the electron diffraction method gives interatomic spacings averaged over the entire volume of the investigated material, the bond length (~2.08 Å) is in good agreement with the theoretical calculations. Consequently, the calculated stable linear chains of silicon atoms of the polyene type are fully capable of existing in *a*-Si:H films annealed at 550 °C.

In contrast, the existence of two hydrogen atoms at the ends of the chains imparts stability to a cumulene-structured cluster, which now consists of silicon atoms with double bonds (structure *b* in Fig. 4). Here, as in the case of the polyene chain, the bond length depends on the number of atoms in the cluster. It varies from 2.066 Å to 2.141 Å and correlates quite well with the experimental data.

When three hydrogen atoms are present at the ends of the chains of silicon atoms, as should be expected, we obtain a cluster structure with ordinary silicon-silicon bonds and interatomic spacings close to the ideal for a tetrahedral structure.

For the second cluster model used in the quantum-chemical calculations we have lifted the linearity restriction from the atomic structure. Some of the results are shown in Table III and in Fig. 4 (structures *c* and *d*). It is evident that for this model we again have clusters with stable chain structures. They are situated in one plane, but not along the same straight line. The optimized angles between silicon atoms vary from 115° to 127° for clusters of the Si_nH_2 type. It is

TABLE III. Optimized lengths (Å), angles (deg), and bond orders in nonlinear silicon cluster structures, method MP2/6-311G(d).

Cluster	Bond length, Å: Short Si–Si	Bond length, Å: Long Si–Si	Bond length, Å: Si–X	Bond order: Short Si–Si	Bond order: Long Si–Si	Bond order: Si–X	Angle, deg: Si1–Si2–Si3(X)
Si_2H_2	2.102	⋯	1.492	2.292	⋯	0.933	125.0
Si_4H_2	2.117	2.288	1.493	2.158	0.960	0.937	118.2
Si_4O_2	2.299		1.544	0.920		1.886	140.7

also interesting to note that the total order of the bonds per silicon atom is only 3 for these clusters. We can therefore assume that in a real amorphous silicon film each silicon atom has one unfilled bond, or it can be used to form a bond with another chain, thereby promoting the formation of a three-dimensional disordered network. The silicon atoms in this case exist in the sp^2 hybrid state and have ordinary and double bonds. The average distance between atoms is greater than for linear chains. It is interesting to note that, according to electron spin resonance (ESR) data, hydrogen-free amorphous silicon films annealed at 500 °C have a high density of uncompensated spins ($\approx 10^{19}\,\mathrm{cm}^{-3}$). The ESR signal has a g factor close to 2.0055, which is usually attributed to dangling bonds. In contrast with the first model, we have succeeded in finding a stable cluster form containing oxygen atoms. The results of calculations for Si_nO_2 are given in Table III and in Fig. 4 (structure *d*). We see that the silicon atoms are joined by ordinary bonds, and that the bond lengths are close to the tetrahedral values. The original linear chain of atoms is now twisted, and the increase in the number of silicon atoms results in the formation of a three-dimensional structure. This means that oxygen is an inhibitor for the formation of multiple bonds.

Consequently, stable chain forms exist for both of the cluster models discussed here. In the case of a linear cluster the existing minimum of the surface potential energy is conditional and is not preserved in transition to three-dimensional optimization. For the second cluster model, on the other hand, the resulting stationary point is a local minimum even in the case of total optimization. The data are further corroborated by calculations of the vibrational frequencies. The difference in the cluster energies for linear and nonlinear arrangements of the silicon atoms in the chains per Si atom is on the order of 8–10 kcal. This difference is not too large, so that the result of anneal-induced restructuring is significantly influenced by the properties of the as-prepared tetrahedral silicon films and the conditions under which the structural transformations take place. The distance between these local and global energy minima corresponding to a tetrahedral arrangement of atoms for the different cluster configurations is ~ 20 kcal per Si atom.

CONCLUSIONS

Based on our calculations, which exhibit good agreement with experiments, we can conclude that in nature there are no fundamental restrictions on the formation of long silicon chains of atoms existing in the sp or sp^2 hybrid state. The final result of structural transformation, like the process itself, depends on the properties of the as-prepared material and the presence of external influences. The use of hydrogen-saturated amorphous silicon as the basic material under certain conditions can lead to the production of linear amorphous silicon by annealing. At present, however, neither experiment nor calculations provide a straightforward answer to the question as to what type of linear chain of silicon atoms is formed (polyene, cumulene, or both together). When hydrogen-free amorphous silicon is annealed, the most likely product will be a chain material with silicon atoms existing in the sp^2 hybrid state. The presence of oxygen in the as-prepared silicon films is the primary obstacle to the formation of silicyne during annealing. The resulting material is amorphous. Unfortunately, this fact and frequent breakages make it difficult to observe long chains of silicon atoms directly.

This work has received support from the Russian Fund for Fundamental Research (Project Code 97-03-32428).

*)E-mail: mashin@phys.unn.runnet.ru

[1] A. F. Khokhlov, A. I. Mashin, and D. A. Khokhlov, JETP Lett. **67**, 675 (1998).
[2] A. I. Mashin, A. F. Khokhlov, I. V. Kol'chugin, and N. I. Mashin, in *Proceedings of the All-Russian Symposium on Amorphous and Microcrystalline Semiconductors* [in Russian], St. Petersburg (1998), p. 28.
[3] D. A. Khokhlov, D. A. Pavlov, and A. I. Mashin, in *Proceedings of the All-Russian Conference: ''The Sixteenth N. V. Belov Scientific Lectures''* [in Russian], Nizhny Novgorod (1997), p. 136.
[4] L. I. Tatarinova, *Electron Diffraction of Amorphous Materials* [in Russian], Nauka, Moscow, 1972.
[5] S. I. Ovsetsin, D. A. Khokhlov, E. A. Soldatov, and A. I. Mashin, in *Proceedings of the All-Russian Conference: ''The Sixteenth N. V. Belov Scientific Lectures''* [in Russian], Nizhny Novgorod (1997), p. 105.
[6] V. N. Gordeev, A. I. Popov, and V. A. Filikov, Izv. Akad. Nauk SSSR, Neorg. Mater. **16**, 1773 (1980).
[7] M. W. Schmidt, K. K. Baldridge, J. A. Boatz, S. T. Elbert, M. S. Gordon, J. J. Jensen, S. Koseki, N. Matsunaga, K. A. Nguyen, S. Su, T. L. Windus, M. Dupuis, and J. A. Montgomery, J. Comput. Chem. **14**, 1347 (1993).
[8] W. Beyer, in *Tetrahedrally-Bonded Amorphous Semiconductors*, edited by D. Adler and H. Fritzsche (Plenum Press, New York, 1985) p. 129.
[9] A. F. Khokhlov, A. I. Mashin, D. A. Pavlov, and D. A. Khokhlov, Fiz. Tekh. Poluprovodn. **28**, 1750 (1994) [Semiconductors **28**, 971 (1994)].
[10] A. F. Skryshevskiĭ, *Structural Analysis of Liquids and Amorphous Solids* [in Russian], Vyssh. Shkola, Moscow, 1980.

Translated by James S. Wood

Formation of optically active centers in films of erbium-doped amorphous hydrated silicon

M. M. Mezdrogina, M. P. Annaorazova, E. I. Terukov, I. N. Trapeznikova, and N. Nazarov

A. F. Ioffe Physicotechnical Institute, Russian Academy of Sciences, 194021 St. Petersburg, Russia
(Submitted December 25, 1998; accepted for publication February 25, 1999)
Fiz. Tekh. Poluprovodn. **33**, 1260–1263 (October 1999)

We have observed photoluminescence at 1.54 μm from *a*-Si:H films doped with erbium of various degrees of purity. It is shown that the additional introduction of oxygen activates the Er ions. The effect of silicides and defects in amorphous silicon *a*-Si:H films and in crystalline silicon *c*-Si is investigated. © *1999 American Institute of Physics.* [S1063-7826(99)02310-8]

The possibility of using erbium-doped amorphous hydrated silicon films (*a*-Si:H⟨Er⟩) to prepare photo- and electroluminescence devices appeared after luminescence at wavelength $\lambda = 1.54\ \mu$m was observed in them near room temperature.[1] The wide interest in research on single crystal (*c*-Si) and amorphous hydrated (*a*-Si:H) silicon doped with erbium is due to the possible applications of silicon technology for integrating devices, which are based on this material and which operate at a wavelength corresponding to minimum losses and minimum dispersion in fiber-optic communication lines. It is known that the technology for depositing *a*-Si:H⟨Er⟩ films does not impose any restrictions on the density of metallic and gaseous impurities.

It has been shown[2–4] that the photoluminescence (PL) intensity depends on the erbium concentration (C_{Er}), and it increases on annealing, with the additional introduction of oxygen when magnetron sputtering is used for film deposition, and with the use of ion implantation for introducing erbium into the disordered structural network of *a*-Si:H. When a multielectrode system was used to obtain the *a*-Si:H ⟨Er⟩ films, the additional introduction of oxygen decreased the PL intensity.[2]

On the basis of the data obtained in Ref. 5 it is believed that the emitting centers in *c*-Si, *a*-Si:H⟨Er⟩, and *a*-Si:H⟨Er⟩ subjected to high-temperature annealing are clusters of the erbium oxide Er–O. It has been shown by emission Mössbauer spectroscopy on ^{169}Er (^{169}Tm) that the optically active PL centers in *a*-Si:H⟨Er⟩ are clusters, whose structure, just as in *c*-Si, corresponds to the oxide Er_2O_3. It has also been shown that the nature of the clusters formed by erbium and oxygen atoms in *c*-Si and *a*-Si:H is different with respect to the local environment: In *c*-Si the structure is close to the crystal structure of Er_2O_3, while in *a*-Si:H films it is somewhat different. Cluster formation occurs in the amorphous phase, even despite high-temperature annealing. However, the process leading to the formation of optically active clusters of erbium oxide in the amorphous phase upon the introduction of erbium and oxygen during growth and upon the introduction of the same impurities by implantation in *c*-Si is unclear so far.

Our objective in the present work is to investigate the formation of optically active clusters in *a*-Si:H⟨Er⟩ films when using the method of magnetron sputtering of the target and with rf sputtering using a multielectrode system.

It has been shown[6] that the PL intensity in *a*-Si:H⟨Er⟩ films obtained by magnetron sputtering is always higher than in films obtained by rf sputtering. Moreover, it has been determined that the introduction of oxygen impurity in concentrations an order of magnitude higher than the erbium concentration increases the PL in *a*-Si:H⟨Er⟩ films obtained by magnetron sputtering, while a decrease of the oxygen concentration results in an environment around erbium ions that is characteristic of erbium silicide $ErSi_2$, which, as shown in Ref. 5, is an optically inactive center. At the same time, it is well known that when iron is introduced in *c*-Si PL is also observed at the wavelength $\lambda = 1.54\ \mu$m, and the optically active centers are, as inferred in Ref. 7, precipitates of iron silicide β-$FeSi_2$. The appearance of $FeSi_2$ precipitates has also been observed by Mössbauer spectroscopy when ^{57}Fe is introduced in *a*-Si:H films.[8] Photoluminescence at $\lambda = 1.54\ \mu$m in *c*-Si has been observed without the introduction of any impurities.[9] The authors attribute this observation to the presence of dislocations in the experimental samples. It has been shown[10] that when different rare-earth elements (REEs) (Dy, Cd, Tb, Nd, Eu) are introduced into the disordered structure of the *a*-Si:H network, it is observed that the elements strongly influence the spectrum of localized states of the tails of the allowed bands of the intrinsic structural defects with states of the type D^-, D^0, and D^+. Intracenter optical transitions associated with isolated charged REE centers have not been observed, which could attest to the formation of complicated complexes in the *a*-Si:H matrix by REE impurities. It has been shown that all REEs, except Eu, form acceptor levels in the mobility gap in *a*-Si:H films. At the same time, PL at 1.54 μm is observed in *a*-Si:H⟨Er⟩ films only in the case of *n*-type conductivity.

The kinetics of film growth in the magnetron sputtering process is different from that of *a*-Si:H film growth using rf sputtering with a multielectrode system. For magnetron sputtering, the growth mechanism leading to the appearance of a distinct columnar microstructure as a result of the high effective electron density in the plasma gap is the dominant mechanism. The outer surfaces of the ''columns'' have a high density of defects due to the presence of dangling

 © 1999 American Institute of Physics

TABLE I. The results of chemical analysis of Er according to metallic and gaseous impurities.

Metal impurity content, wt. %							Gas impurity content, wt. %			
Y	Dy	Cu	Tb	Yb	Fe	Total	N_2	O_2	H_2	Total
0.04	0.03	0.002	0.02	0.03	0.001	0.14	0.04	0.12	0.001	0.16

silicon–silicon, silicon–oxygen, and silicon–hydrogen bonds of the dihydrides SiH_2 (according to infrared spectroscopy data for the absorption bands at 1060 and 2100 cm^{-1}). The extended microstructure of the film surfaces is one of the determining factors for the formation of erbium oxides. When a multielectrode system is used during rf sputtering in a mixture of silane, argon, and hydrogen gases, according to these investigations, a columnar microstructure is not observed in either reflection or transmission, although inhomogeneities no greater than 200–300 μm in size are visible; the main type of bonds between silicon and hydrogen are the monohydride bonds SiH (according to infrared spectroscopy data, the 1060-cm^{-1} absorption band is absent, an absorption band is present at 2000 cm^{-1}, and the 2100-cm^{-1} band is weak).[11]

1. EXPERIMENT

The a-Si:H⟨Er⟩ films were obtained by magnetron sputtering of a mosaic target consisting of single-crystal silicon and erbium and by the method of rf sputtering in a multielectrode system. Erbium of various purities was used: repeatedly remelted in a suspended state in helium gas or in vacuum (type 1) and ultrapure erbium (type 2). As a rule, ultrapure erbium contains no less than 0.10–0.12% gaseous impurities and no less than 0.15–0.20% organic impurities (see Table I). Because of the high vapor pressure, most erbium oxides and organic impurities, their content decreases after the initial erbium is melted in a suspended state. The deposition temperature and the growth rate were constant and equal to 250 °C and 2 Å /s, respectively. Oxygen was introduced from water vapor in the process of deposition by rf sputtering and from the gas phase by magnetron sputtering.

Fused quartz and KEF-10 c-Si served as substrates for subsequent measurements of the electroluminescence and KDB-10 c-Si was used for infrared spectroscopy.

Measurements of the PL of a-Si:H⟨Er⟩ films were performed using a KSVU-23 automated setup in the synchronous detection mode. A cooled germanium photodiode was used as a detector. Photoluminescence was excited by the 4880-Å line of a 50-mW argon laser.

Spectral dependences of the PL intensity (at temperatures $T=77$ and 300 K) as a function of the erbium concentration in a-Si:H⟨Er⟩ films, obtained by magnetron sputtering using erbium (type 1) with introduction of oxygen (the flow rate was 0.03 cm^3/s), are shown in Figs. 1a and 1b. Photoluminescence is observed at $\lambda=1.54$ μm, and maximum intensity occurs at concentration $C'_{Er}=1.08\%$.

When type-1 erbium with the same concentration and without the introduction of oxygen is used, the $\lambda=1.54$-μm PL band is not observed. In Ref. 5, where Er without special purification was used, it is shown that the maximum PL intensity is observed with erbium concentration 10^{20} cm^{-3}, i.e., C''_{Er} is several percent. Note that $C'_{Er}=C''_{Er}$. The temperature dependences of the PL intensity of the experimental a-Si:H⟨Er⟩ films obtained using type-1 erbium with the addition of oxygen and using type-2 erbium are essentially identical.

The dependences of the PL intensity of a-Si:H⟨Er⟩ films obtained by rf sputtering with a constant erbium concentration and introduction of water vapor during the deposition process were investigated. It was found that the PL intensity decreases sharply when the water vapor, i.e., an oxygen-containing impurity, is introduced. As is well known, under the conditions of an rf discharge water dissociates into the components H and OH. The OH group is an active component, which participates in the heterogeneous reactions on the surface of the growing film and gives rise to the appearance of dihydride bonds of silicon with hydrogen (the absorption band at 2100 cm^{-1}). The reactions with participation of hydroxyl groups on the surface of the growing film seem to result in the formation of optically inactive centers: The PL intensity decreases. One of the questions arising in the study of the nature of optically active centers in not only a-Si:H⟨Er⟩ but also c-Si⟨Er⟩ is whether the appearance of erbium silicide is responsible for the dropoff of the PL (according to Mössbauer emission spectroscopy data, erbium silicide was observed in a-Si:H⟨Er⟩ films with a low PL intensity) or the spectrum of localized states in the mobility gap changes as a result of the formation of erbium silicide. An investigation of the effect of the oxgyen concentration on the PL intensity in GaN⟨Er⟩ gave a similar dependence: The PL intensity at $T=300$ K decreases for oxygen density $C_O<10^{19}$ cm^{-3} and increases rapidly only for $C_O>10^{20}$ cm^{-3} (Refs. 11–13).

When a multielectrode system is used, oxygen is introduced from water vapor, whose pressure should not exceed 10^{-4} Torr, which is probably too low for the formation of optically active centers in a-Si:H⟨Er⟩ films.

The formation of optically active centers when magnetron sputtering is used occurs as follows: When type-2 erbium is used, the Er–O complexes emerge directly from the mosaic target. The electron energy is too low for the complexes to dissociate, and the complexes Er–O reach the surface of the growing film. Heterogeneous reactions on the surface of the growing film do not play a large role, since the substrate temperature does not exceed 250–300 °C. When type-1 erbium is used, the mosaic target ensures that erbium atoms reach the surface of the growing film. When oxygen is not additionally introduced, most likely erbium silicide

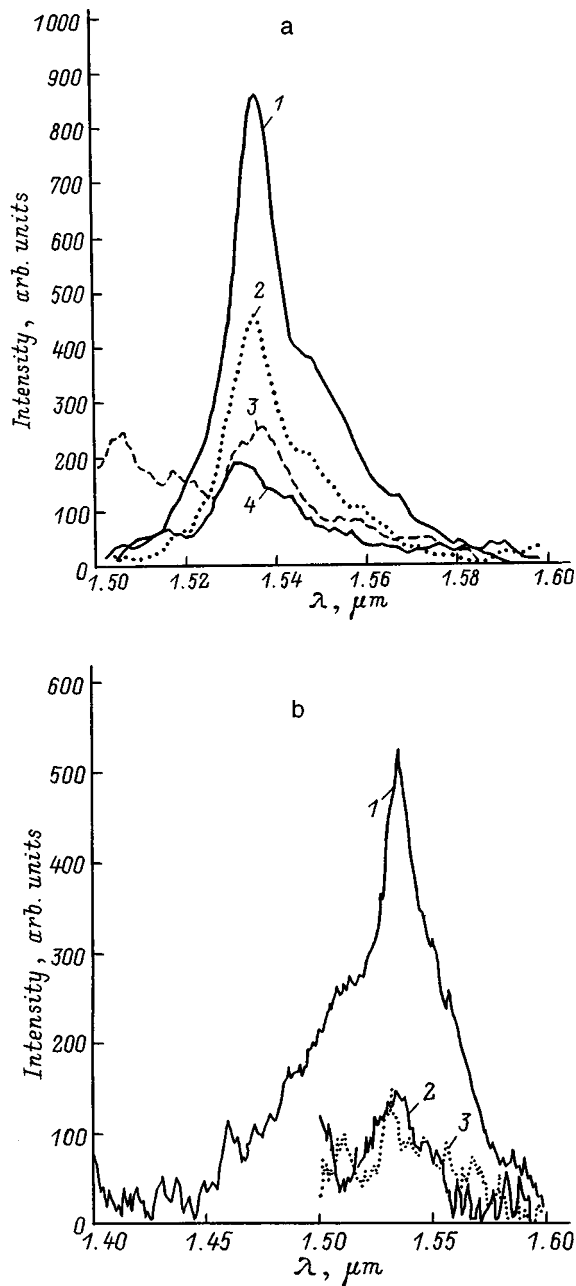

FIG. 1. Photoluminescence spectra of a-Si:H⟨Er⟩ films. a — Er (type 1); C_{Er}, %: *1* — 1.08, *2* — 0.79, *3* — 0.34, *4* — 1.42. $T=77$ K. b — Er (type 2); C_{Er}, %: *1* — 1.08, *2* — 0.79, *3* — 0.34; $T=300$ K.

forms — the $\lambda=1.54$-μm PL band is not observed with type-1 erbium concentration equal to the type-2 erbium concentration. The introduction of oxygen increases the PL intensity with Er concentration increasing to $C_{Er}=1.08\%$, and as the Er concentration continues to increase, the PL intensity decreases. The increase in the erbium concentration seems to result in larger nonuniformities, i.e., the charge state and the density of defects in the disordered structural network of a-Si:H change. In Refs. 10 and 14 it is shown that an increase in the REE concentration as a result of doping of a-Si:H films results in a nonmonotonic increase of the dark conductivity and decreases the activation energy of the temperature-dependence of the dark conductivity, although

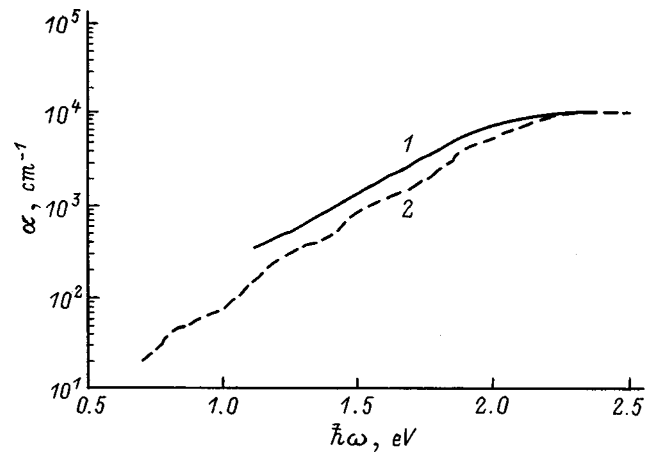

FIG. 2. Spectral dependence of the absorption coefficient $\alpha(\hbar\omega)$ of a-Si:H⟨Er⟩ (*1*) and a-Si:H⟨Fe⟩ (*2*) films at $T=300$ K.

the width of the optical band gap remains nearly constant. The question of the nature of the optically active centers remains open, even though existing data show the presence of erbium oxide in a-Si:H⟨Er⟩ films in which intense PL is observed at 1.54 μm.[5,8]

Comparing the data from optical transmission measurements on a-Si:H⟨Er⟩ and a-Si:H⟨Fe⟩ films (Fig. 2), it is evident that the absorption on defects in the films is essentially the same. As follows from Ref. 7, the optically active center is $FeSi_2$. In Ref. 14, light-emitting diodes operating at 1.54 μm were prepared on the basis of the Si–$FeSi_2$ structure. The assumption that the other silicide, $ErSi_2$, is optically inactive is based only on the fact that $ErSi_2$ has been observed in films showing weak PL.[15]

The additional introduction of ytterbium into an a-Si:H film did not change the PL spectra substantially: The $\lambda=1.04$-μm line characteristic of intracenter transitions of Yb was not observed, and no change was observed in the PL intensity at $\lambda=1.54$ μm.

2. CONCLUSIONS

In summary, the nature of the PL at $\lambda=1.54$ μm in a-Si:H⟨Er⟩ films remains in the research stage. Activation of erbium ions due to the formation of Er_2O_3 as a result of introduction of oxygen is substantial, as is characteristic of c-Si. In addition, the question of the role of the silicide ($ErSi_2$) and defects such as dangling Si–Si bonds remains open.

We wish to thank A. V. Medvedev and A. B. Pevtsov for performing the PL measurements.

[1] H. Ennen, J. Schneider, G. Pomkenke, and A. Axmann, Appl. Phys. Lett. **43**, 943 (1983).
[2] E. I. Terukov, V. Kh. Kudoyarova, M. M. Mezdrogina, V. G. Golubev, A. Sturm, and W. Fuhs, Fiz. Tekh. Poluprovodn. **30**, 820 (1996) [Semiconductors **30**, 440 (1996)].
[3] M. S. Bresler, O. B. Gusev, V. Kh. Kudoyarova, A. N. Kuznetsov, P. E. Pak, E. I. Terukov, I. N. Jassievich, and B. P. Zaharchenya, Appl. Phys. Lett. **67**, 3599 (1995).
[4] A. Polman, G. N. Van den Hoven, J. S. Custer, J. H. Shin, R. Serna, and P. F. A. Alkemade, J. Appl. Phys. **77**, 1256 (1995).
[5] V. F. Masterov, F. S. Nasredinov, P. P. Seregin, M. M. Mezdrogina, and

E. I. Terukov, Fiz. Tekh. Poluprovodn. **32**, 708 (1998) [Semiconductors **32**, 636 (1998)].
[6] T. Ostereich, C. Swiatkowski, and I. Broser, Appl. Phys. Lett. **56**, 446 (1990).
[7] D. N. Leong, M. A. Harry, K. J. Reeson, and K. P. Homewood, Appl. Phys. Lett. **68** (12), 1649 (1996).
[8] A. R. Regel', P. P. Seregin, F. S. Nasredinov, M. M. Mezdrogina, and M. S. Ablova, Fiz. Tekh. Poluprovodn. **22**, 162 (1988) [Sov. Phys. Semicond. **22**, 100 (1988)].
[9] S. Lanzerstorfer, M. Stepikove, J. Hartung, C. Skierbisz, and W. Jantch, Mater. Sci. Forum **258–263**, 1509 (1997).
[10] Zh. Ataev, V. A. Vasil'ev, I. A. Elizarov, and M. M. Mezdrogina, Fiz. Tekh. Poluprovodn. **29**, 1537 (1995) [Semiconductors **29**, 799 (1995)].
[11] M. M. Mezdrogina, P. P. Seregin, F. S. Nasredinov, A. F. Bardamid, and V. A. Khaĭdarov, Neorg. Mater. **27**, 1123 (1989).
[12] A. Ferrasi, G. Franzo, S. Coffa, F. Priolo, F. D. Acapito, and S. Mobilio, Appl. Phys. Lett. **79**, 1712 (1997).
[13] D. M. Hansen, R. Zhang, N. R. Perkins, S. Salfi, L. Zhang, K. L. Bray, and T. F. Kurch, Appl. Phys. Lett. **72**(10) (1998).
[14] D. Leong, M. A. Harry, K. J. Reeson, and K. P. Homewood, Nature (London) **387**, 686 (1997).
[15] A. M. Shmyreva, T. V. Semikina, M. G. Dusheĭko, and N. Bishena, in *Abstracts of Reports at the All-Russia Symposium on Amorphous and Microcrystalline Semiconductors* (St. Petersburg, 1998) p. 144.

Translated by M. E. Alferieff

Variation of the parameters and composition of thin films of porous silicon as a result of oxidation: ellipsometric studies

E. V. Astrova,*) V. B. Voronkov, A. D. Remenyuk, and V. B. Shuman

A. F. Ioffe Physicotechnical Institute, Russian Academy of Sciences, 194021 St. Petersburg, Russia

V. A. Tolmachev

S. I. Vavilov State Optical Institute, 199034 St. Petersburg, Russia

(Submitted April 13, 1999; accepted for publication April 15, 1999)
Fiz. Tekh. Poluprovodn. **33**, 1264–1270 (October 1999)

The variation of the optical characteristics of thin films of oxidized porous silicon as a function of the preparation regime and subsequent heat treatment is investigated by ellipsometry. It is shown that the refractive index, optical thickness, and extinction coefficient of porous silicon films decrease monotonically, but the film thickness increases as the degree of oxidation of the silicon base layer increases. An analysis of the film thickness as a function of the degree of oxidation shows that it differs very little from the same dependence for the nonporous film. The composition of the films is determined from the measured refractive index at a wavelength $\lambda = 632.8$ nm by means of curves calculated on the basis of the three-component Bruggeman model of the effective medium for layers with different initial porosities.
© *1999 American Institute of Physics.* [S1063-7826(99)02410-2]

Porous silicon has recently begun to find applicationsr the production on silicon of thin films having predetermined optical constants (refractive index n and extinction coefficient k).[1,2] The applications of porous silicon with various indices n range from ''superlattice'' interference filters[3] to waveguides and brighteners.[1,4,5] The need to stabilize the optical parameters of porous silicon films and to enhance their transparency in the short-wavelength region of the visible spectrum requires additional processing of the material, for example, oxidation or nitridization.[6,7] The initial values of the optical constants of porous silicon are changed by these operations. The predictable realization of the necessary film parameters requires knowledge of how the latter depend on the technological preparation regime, i.e., on the silicon composition: its porosity and oxide concentration. In the past, the laws governing the oxidation of porous silicon have been of interest in regard to the solution of such practical problems as the preparation of silicon-on-insulator (SOI) structures[8] and the stabilization of photoluminescence and electroluminescence.[9,6] In the first case the porous Si had to be converted into a sufficiently thick and dense oxide, and the primary objective in the second case was to passivate the surface of crystallites in porous Si. Consequently, high-temperature oxidation ($T > 1000\,^\circ$C) has been used predominantly for the production of insulation, and only short-time pulsed annealing ($T = 800 - 900\,^\circ$C) has been used for passivation.

It is difficult to trace the variations of the porosity p and the thickness d of thin ($d < 1\ \mu$m) porous silicon films by the usual gravimetric method[10] and profilometry,[11,12] because the variations of the weight and thickness of the sample are too small. In the majority of papers on porous Si the refractive index has been determined from reflection measurements,[2,13] although ellipsometry has also been used in some studies.[14–16] For calculations of the refractive index in this case the film is regarded as an effective two-component medium consisting of silicon and voids, and with oxidized layers it is regarded as a three-component medium with the oxide as the third component.[13,17]

The objective of the present study is to investigate by ellipsometry the optical characteristics, porosity, and composition of thin films of porous silicon in various stages of oxidation. The primary concern is to investigate porous silicon layers prepared on an n^+-silicon surface by chemical etching (stain-etched films). This undertaking is motivated both by the feasibility of using the layers as brighteners for solar cells[5] and by the fact that the oxidation of such films has not been investigated previously.

EXPERIMENTAL

The porous films were prepared by the chemical or electrochemical etching of single-crystalline wafers of n^+-type and p-type silicon. The film preparation regimes are given in Table I. Sample 1 in the table actually refers to a series of samples prepared under conditions differing only in the etch time. Some of the as-prepared silicon wafers were subjected to preliminary diffused alloying with phosphorus at a surface density $N_s = 2 \times 10^{20}\,\text{cm}^{-3}$. The depth of the n^+-layer (1.4 μm) was much greater than the thickness of the porous film obtained from it. The chemical etching of n^+-Si in HF containing a small quantity of $NaNO_2$ oxidant[18] permits the reaction to take place without the liberation of hydrogen bubbles and produces uniformly stained thin films, whose thickness depends on the reaction time. The chemical etching process used in the preparation of porous silicon is extremely sensitive to the surface state of the silicon and takes place

 © 1999 American Institute of Physics

TABLE I. Preparation regimes and as-prepared parameters of porous silicon films.

No.	Type of silicon	Doping level, cm^{-3}	Substrate orientation	Electrolyte composition	Current density j, mA/cm^2	Etch time t, s	Depolarization, % [b]	F	d, nm	n	k	p, %
1 [a]	n-Si(Sb)	5×10^{18}	(111)	0.01% $NaNO_2$ soln. in HF	Chem. etch	60–300 [a]	2–17	3.5–90 [a]	57.6–86.3 [a]	2.450–2.847 [a]	0.010–0.015 [a]	46–34 [a]
2	n-Si(P)	2.5×10^{17}	(100)	0.01% $NaNO_2$ soln. in HF	Same	180	1–6	81	97.6	2.344	0.013	50
3	p-Si(B)	1.5×10^{16}	(100)	HF: H_2O: C_2H_5OH =2: 1: 1	2.1	60	1–2	48	106.2	2.044	0.006	58
4	p-Si(B)	4×10^{14}	(100)	HF: H_2O: C_2H_5OH =1: 1: 2	10	25	4–22	227	128.7	1.486	0.000	75
5	n-Si(P)	2×10^{20}	(111)	Same	2	45	2–4	29	76.8	1.858	0.003	63

[a]The values are given for a series of samples.
[b]The depolarization is given for angles of incidence $\varphi=55°, 60°, 65°$.

only on a hydrophilic surface. To prevent contamination and simplify the preparation of the wafers prior to the formation of the chemical porous Si film, they were subjected to thermal oxidation (thickness of the oxide layer 0.4 μm). When immersed in the solution for preparation of the porous Si, the oxide was dissolved in it for $\sim$30 s, and then the formation of the stained film began after a certain time had passed.

It is important to note that the oxidation of porous silicon calls for certain precautions to avoid encrustation of the surface and the buildup of elements of the base layer.[19] Oxidation is therefore usually carried out in two stages: a preliminary low-temperature stage, when the surface hydrogen layer is replaced by an oxide film, and a final high-temperature stage aimed at complete oxidation of the Si base layer and subsequent consolidation of the porous SiO_2. The samples of series 1 were subjected to the first oxidation stage in air at 300 °C or in water vapor (90–100 °C); the second stage was carried out at $T=500-700$ °C. All other samples were annealed in a single stage. Sample 2 was divided into parts having identical characteristics of the as-prepared porous Si, and each part was annealed for one hour at a specific temperature in the range $200-800\,°C$.

Multiple-angle ellipsometry was used to determine the parameters of the film. The ellipsometric analysis of porous Si films has its own special characteristics due to imperfection of the interface between the porous Si and the substrate and inhomogeneities in the film itself due to the high sensitivity of the etching rate to defects and fluctuations of the substrate alloying level. As a result, the total reflected light beam is made up of beams with different polarization characteristics, and this creates certain difficulties even during the measurement stage and is manifested, for example, as incomplete extinction of the signal in the null ellipsometer. It should be noted that the issue of depolarization of the beam by the porous Si film has never been discussed in the publications known to us, probably because ellipsometers with a nonnull signal recording scheme (e.g., incorporating a rotating analyzer) were used. In the case of a null ellipsometer the influence of the depolarization component (as long as it is not too pronounced) is more likely expressed merely in an increase of the uncompensated component at the signal minimum and, as a result, in a certain loss in the accuracy of determination, rather than in the actual values of the evaluated ellipsometric parameters Δ and ψ (Ref. 20). It is important to note that optical imperfection of the porous Si films can also introduce errors in the subsequent calculations. As a rule, these data and the values of the error function F are not indicated in ellipsometric studies of porous silicon, with the exception of Ref. 21.

The measurements in the present study have been carried out by means of an LÉF-3M null ellipsometer (wavelength $\lambda=632.8$ nm). The instrument has the following configuration: polarizer–compensator–sample–analyzer–photodetector.[22] The measure of depolarization of the beam was the deviation of the signal on the photodetector recording system of the LÉF-3M instrument from the zero (noise) level, expressed as a percentage of the total scale in the maximum sensitivity regime. The choice of angles of incidence of the light beam $\varphi=55°, 60°, 65°$ was dictated by the criterion of minimum beam depolarization.

After the ellipsometric parameters had been measured, the following model was used for subsequent calculations: environment–homogeneous isotropic film–substrate. The refractive index n, the extinction coefficient k, and the thickness d of the film were calculated by searching for the unknown parameters with error function F calculated by the least-squares method, taking into account the error of the parameters.[22,23] The film thicknesses were measured within $1-2$-nm error limits, and the error of determination of n did not exceed $\delta n=0.002$, but for k it was larger: $\delta k=0.004$. The optical constants of the substrate were determined with allowance for the natural oxide surface film and were close to data in the literature: $n_{Si}=3.862$ and $k_{Si}=0.023$.

MODEL OF THE EFFECTIVE MEDIUM

The analysis of the values obtained for the optical constants is based on the isotropic Bruggeman model.[24] It is assumed that the partially oxidized porous silicon consists of three components: silicon, silicon dioxide, and voids, with refractive indices n_{Si}, n_{SiO_2}, and $n_v=1$, respectively. The dependence of the degree of oxidation and porosity on the effective refractive index is calculated with allowance for the fact that the oxidized porous silicon film is not an arbitrary

mixture of the three components, but the content of each one varies during oxidation as a result of the other. In the wavelength interval where k is small, the condition $\mathrm{Re}\langle N^2\rangle = \mathrm{Re}[(n+ik)^2] \simeq n^2$ holds, where N is the complex refractive index. Let the volume fraction of silicon in the as-prepared, unoxidized film be $f=1-p_{\mathrm{in}}$, where p_{in} is the initial porosity. As a result of oxidation, a fraction x of the silicon is converted into SiO_2. The porous silicon then has the new composition

$$\text{volume fraction of Si} \quad f-x, \tag{1}$$

$$\text{volume fraction of SiO}_2 \quad g=2.27x, \tag{2}$$

$$\text{Porosity} \quad p=1-f-1.27x. \tag{3}$$

The combination of silicon with oxygen increases the volume occupied by the solid base of the film, i.e., decreases its porosity. It follows from the ratio between the gram-atomic weight of Si (28 g) and its density 2.33 g/cm^3 that the volume occupied by one gram-atom of Si is $v_{\mathrm{Si}}=28/2.33 = 12.02\,\mathrm{cm}^3$, and one gram-molecule of silicon dioxide, taking into account the gram-molecular weight of 60 g and density of 2.20 g/cm^3, is $v_{\mathrm{SiO_2}}=60/2.20=27.27\,\mathrm{cm}^3$; i.e., the oxidation of each Si atom increases the volume of the solid phase associated with it by a factor of 2.27.

The Bruggeman equation can be written in the form

$$\mathrm{F}(f-x)+\mathrm{G}2.27x+\mathrm{V}(1-f-1.27x)=0, \tag{4}$$

where

$$\mathrm{F}=\frac{n_{\mathrm{Si}}^2-n^2}{n_{\mathrm{Si}}^2+2n^2}, \tag{5}$$

$$\mathrm{G}=\frac{n_{\mathrm{SiO_2}}^2-n^2}{n_{\mathrm{SiO_2}}^2+2n^2}, \tag{6}$$

$$\mathrm{V}=\frac{1-n^2}{1+2n^2}, \tag{7}$$

and n is the effective refractive index of the film.

The determination of n by means of Eq. (4) calls for the solution of a cubic equation. It is far simpler to solve the inverse problem of finding x for known values of n:

$$x=\frac{f\mathrm{F}+(1-f)\mathrm{V}}{\mathrm{F}-2.27\mathrm{G}+1.27\mathrm{V}}. \tag{8}$$

It is convenient to characterize the degree of oxidation as the fraction of oxidized Si base layer:

$$s=(x/f)\cdot 100\%. \tag{9}$$

Calculated curves relating the degree of oxidation of the silicon base layer to the refractive index at $\lambda=632.8$ nm for films with various initial porosities are shown in Fig. 1. Figure 2 shows how the porosity of the layer varies as n decreases because of oxidation. The ranges of variation of n and p are bounded by two-component porous systems: The upper dot-dashed curve describes a medium consisting of silicon and voids ($\mathrm{Si}+V$), and the lower curve characterizes the porous oxide ($\mathrm{SiO_2}+V$). It is evident from Fig. 2 that porous Si films with different initial porosities behave differently. Films with $p_{\mathrm{in}}>56\%$ after complete oxidation of the Si base layer remain porous, whereas in porous Si with a lower porosity the voids vanish well before the Si base layer is completely oxidized, producing another two-component system $\mathrm{Si}+\mathrm{SiO_2}$ (see Fig. 1). Attention should be called to the fact that for all such films, beginning with a certain degree of oxidation dictated by the point of intersection with the $\mathrm{Si}+\mathrm{SiO_2}$ curve, the function $n=f(s)$ is identical and does not depend on p_{in}.

VARIATION OF THE POROUS SILICON FILM THICKNESS DURING OXIDATION

The foregoing considerations are based on the fact that the voids are small and distributed uniformly in the film. Accordingly, the porosity has not become equal to zero until now, and the volume of porous silicon should not increase. However, the true picture most likely departs from this idealized version, and the voids in the film come in a wide range of sizes. The smaller ones quickly fill up with SiO_2 and begin to push the silicon crystallites apart. This behavior can cause the film thickness to increase long before the condition $p=0$ is satisfied.

The fraction of solid phase in the porous silicon before oxidation is determined entirely by the silicon component and is equal to f. The volume occupied by the solid phase is therefore equal to $f v_0$, where v_0 is the volume of unoxidized porous Si. Let the volume now be equal to v_x as a result of oxidation. The solid phase then consists of Si and SiO_2, and its fraction is $f+1.27x$. Assuming that the minimum void diameter is equal to 0, we can find the new volume of the solid phase $v_x(f+1.27x)$. The relative increase in volume is then

$$v_x/v_0=(f+1.27x)/f=1+1.27s, \tag{10}$$

and the linear scale is given by the cube root of this quantity. Consequently, the thickness of the film will increase with increasing degree of oxidation according to the relation

$$d/d_0=\sqrt[3]{1+1.27s}, \tag{11}$$

where d_0 is its initial thickness. The maximum increase in the thickness due to complete oxidation ($s=1$) is $d/d_0 = 1.31$.

EXPERIMENTAL RESULTS AND DISCUSSION

The results of determining n, k, and d from the measured ellipsometric parameters on the porous silicon films before oxidation are given in Table I. Also shown in Table I are the percentage depolarization and the error function. The thickness of the chemical porous Si films (samples 1 and 2) before oxidation were $d_0=(57.6-97.6)$ nm, $n=2.344-2.847$, and the thickness of the electrochemical films (samples 3–5) were $d_0=(77-129)$ nm, and $n=1.486-2.044$. We assumed that the film is oxide-free immediately after preparation, and we determined its initial porosity p_{in} from the measured refractive index with the aid of the $\mathrm{Si}+V$ curve in Fig. 2. This assumption is valid for films prepared on p^+-Si (Ref.

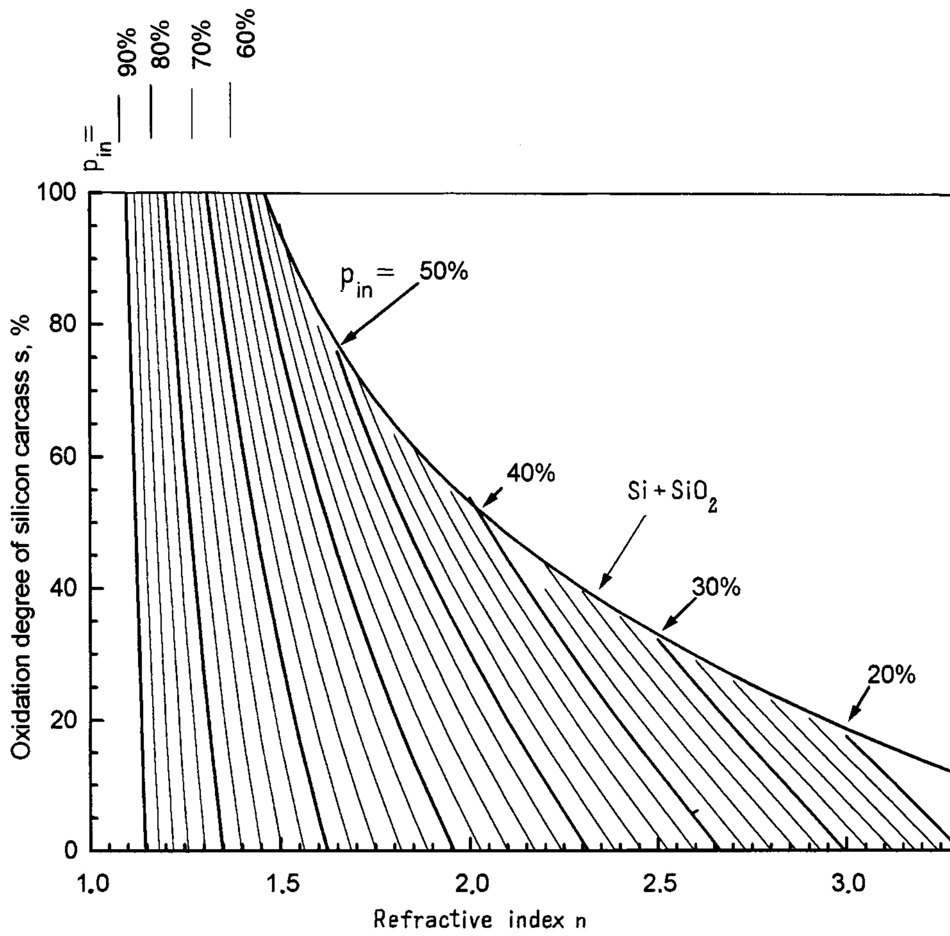

FIG. 1. Calculated curves characterizing the relation between the refractive index of oxidized porous silicon and the degree of oxidation of the silicon base layer, $\lambda = 632.8$ nm. The $Si+SiO_2$ curve corresponds to a film in which no voids are left after oxidation; p_{in} is the initial porosity of the unoxidized film.

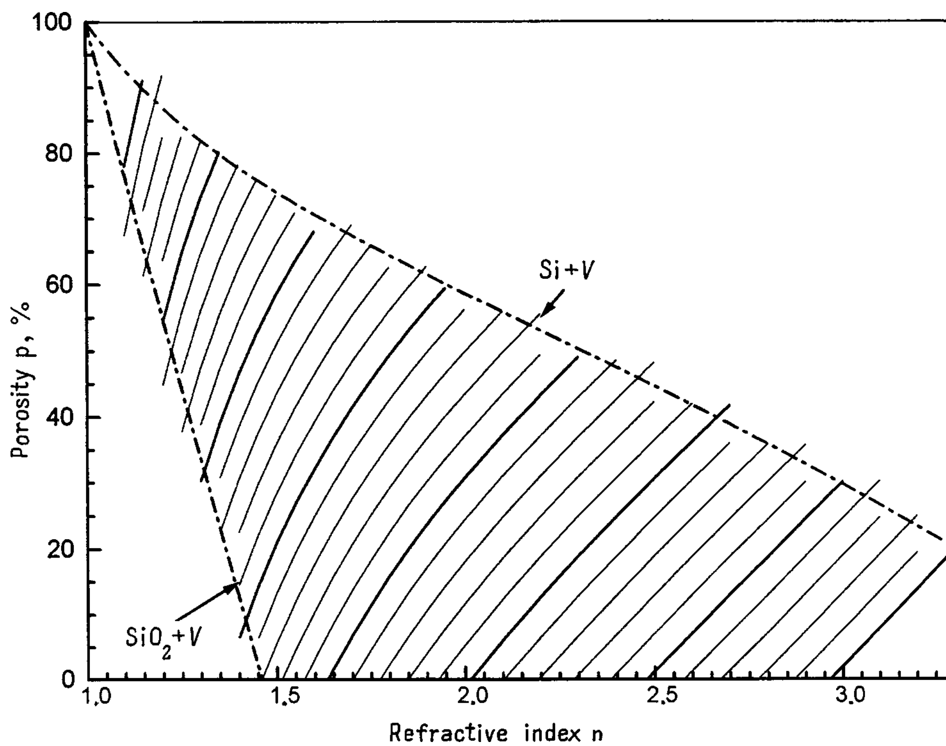

FIG. 2. Relation between the porosity and the refractive index of oxidized porous silicon, calculated for various initial porosities p_{in} of the unoxidized film, $\lambda = 632.8$ nm. The dot-dashed curves representing $Si+V$ (porous silicon) and SiO_2+V (porous oxide) bound the region of values having physical significance; p_{in} is determined from the point of intersection of the $p-n$ curve with the $Si+V$ curve.

TABLE II. Parameters of porous silicon layers after oxidation.

Sample No.	Oxidation regime Stage I	Stage II	Thickness d, nm	Refractive index n	Porosity p, %	Degree of oxidation
1a [a]	As-prepared film,		72.2	2.590	41.8	0
	300 °C, 17 min		74.4	2.320	24.8	23
		700 °C, 60 min	84.5	1.737	0	69
	100 °C, H_2O, 10 min		84.0	2.105	12.3	40
		500 °C, 60 min	89.8	1.776	0	67
	90 °C, H_2O, 90 min		73.2	2.081	11	42
		600 °C, 60 min	80.8	1.746	0	68.5
3 [b]	Stored in air, 25 °C, 12 days		111	1.818	42.8	28.6
4 [b]	600 °C, 60 min		122.1	1.294	52	73
5 [b]	700 °C, 60 min		76.9	1.650	48	33

[a]Sample 1a is one of the samples in series 1; it is divided into three parts, each subjected to two-stage oxidation in its own regime.
[b]The parameters of the as-prepared layers are given in Table I.

13) and n^+-Si (Ref. 25) and is corroborated by our measurements of the infrared reflection spectra of thicker films prepared under like conditions.

It follows from the values obtained for n, k and d (Table II) that oxidation by annealing in air at 90−800 °C produces a significant drop in n. After each oxidation stage n was measured by the ellipsometric method to determine the degree of oxidation s and the porosity p from the curves in Figs. 1 and 2 for the corresponding p_{in}. The initial porosity was in the interval 34−50% for the chemical porous Si films and 58−75% for the electrochemical films. For either type of film the degree of oxidation and the new porosity determined under the same heat treatment condition depend strongly on the substrate material and can fluctuate from $s=33\%$ to $s=84\%$ after heat treatment at $T=600$ °C for $p_{in}=63\%$ and 84%, respectively.

The oxidizing atmosphere is found to have a significant influence. Oxidation of the chemical films in water vapor at 90 °C and boiling in deionized water (100 °C) produced a greater reduction in n and, accordingly, a higher degree of oxidation than heat treatment in air at the higher temperature $T=300$ °C ($s=42\%$ and 40% as opposed to 23%). The thickness of the porous Si film always increases after heat treatment, consistent with the results obtained for thicker films in Refs. 11 and 12. The coefficient k exhibits considerable scatter, as it does in Ref. 26 for this spectral range.

We now analyze the main patterns of oxidation-induced variation of the parameters of chemical porous Si films in the example of sample 2 with an initial porosity $p_{in}=50\%$ (see Figs. 3–6). As oxidation progresses, the refractive index decreases from $n=2.34$ to $n=1.48$, signaling almost complete oxidation of the film after annealing at 800 °C and its conversion to SiO_2 without voids (porous SiO_2 would have $n<1.46$). Accordingly, the extinction coefficient drops essentially to zero (Fig. 3). From the calculated data in Figs. 2 and 1 we determine that the voids in this porous silicon sample must vanish at $n=1.64$, which corresponds to $s=78\%$. Indeed, in Figs. 3 and 5 a decrease in the rate of change of the refractive index and the oxidation rate is observed for $n<1.64$ and $s>78\%$, respectively, in the range $T\geq 530$ °C, which can be attributed to closing of the voids. Figure 4 shows the temperature dependence of the film thickness d and its optical thickness nd. The latter is of primary interest in regard to the fabrication of interference devices and coatings. It is evident that d, which initially increases almost linearly with the anneal temperature, also exhibits a tendency to saturation at higher temperatures. Nonetheless, the decrease in n during oxidation prevails over the increase in d, causing the optical thickness to decrease on the whole.

The dependence of the relative thickness of the porous silicon layer d/d_0 on the degree of oxidation of the silicon base layer is plotted in Fig. 6, where it is compared with the curve calculated from Eq. (11). Clearly, the simplified model, which completely does away with the role of the voids, fairly well describes the experimental dependence. The final value $d/d_0=1.33$ resulting from 98% oxidation of the silicon base layer agrees satisfactorily with the expected value of 1.31 for a monolithic film. This result is consistent with the earlier notion that the change in volume of porous silicon during oxidation in dry oxygen agrees qualitatively with the change in volume during the oxidation of single-crystalline silicon.[27] Such an increase in the film thickness during oxidation is possibly attributable to the predominantly columnar structure of porous silicon. Upon becoming oxi-

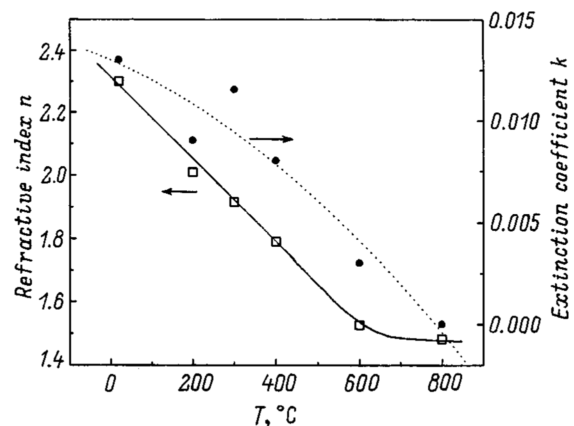

FIG. 3. Dependence of the optical parameters of a porous silicon film on the temperature of a one-hour anneal in air (chemical film 2 on n^+-silicon.

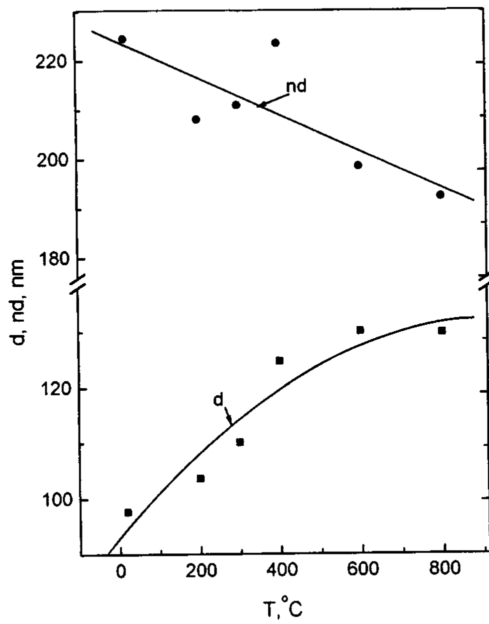

FIG. 4. Variation of the thickness d and optical thickness nd of a porous silicon film as functions of the temperature of a one-hour anneal in air.

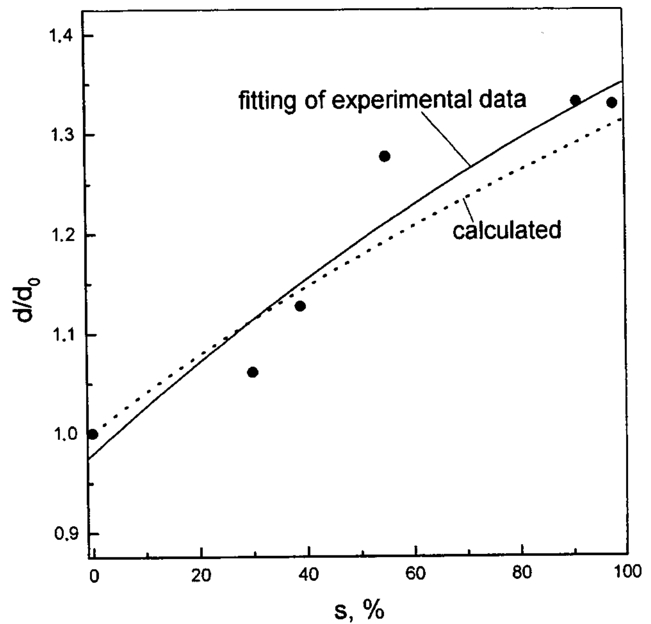

FIG. 6. Dependence of the dimensionless thickness d/d_0 of a porous Si film on the degree of oxidation. The solid curve approximates the experimental data, and the dotted curve is calculated according to Eq. (11).

dized, every such column causes the thickness to increase by an amount roughly consistent with the oxidation of monolithic silicon.

CONCLUSIONS

We have demonstrated the possibility, by means of ellipsometric measurements at one light wavelength, of investigating the variation of the optical constants and the thickness of porous silicon films as functions of the preparation regime and subsequent heat treatment and then using these data to determine the film composition (porosity and SiO_2 content).

Preliminary studies of the laws governing the oxidation of porous silicon films prepared by chemical etching have shown that their refractive index and the extinction coefficient decrease monotonically, whereas the film thickness increases as the anneal temperature and, accordingly, the degree of oxidation increase. The variation of the thickness follows approximately the same pattern as should occur for an oxidized nonporous silicon film.

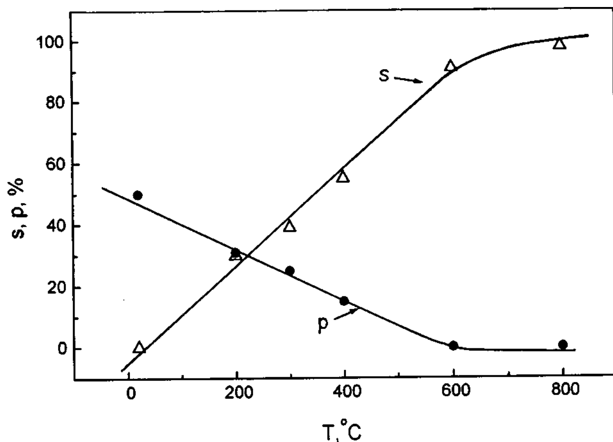

FIG. 5. Variation of the degree of oxidation of the silicon base layer and porosity of the porous Si film as functions of the anneal temperature (one hour in air). The film contains no voids at $T > 530\,^{\circ}\mathrm{C}$.

This work has received support from the programs ''Physics of Solid State Nanostructures'' and ''Promising Trends in Microelectronic and Nanoelectronic Technology.''

*)E-mail: east@pop.ioffe.rssi.ru

[1] A. Loni, L. T. Canham, M. G. Berger, R. Arens-Fisher, H. Munder, H. Luth, H. F. Arrand, and T. M. Benson, Thin Solid Films **276**, 143 (1996).
[2] C. Mazzoleni and L. Pavesi, Appl. Phys. Lett. **67**, 2983 (1995).
[3] M. J. Berger, R. Arens-Fischer, St. Frohnhoff, C. Dieker, K. Winz, H. Munder, H. Luth, M. Arntzen, and W. Theiss, Mater. Res. Soc. Symp. Proc. **358**, 327 (1995).
[4] G. Maiello, S. L. Monica, A. Ferrari, G. Masini, V. P. Bondarenko, A. M. Dorofeev, and N. M. Kazuchits, Thin Solid Films **297**, 311 (1997).
[5] L. Schirone, G. Sotigiu, and F. P. Califano, Thin Solid Films **297**, 296 (1997).
[6] M. J. Berger, R. Arens-Fischer, M. Thonissen, M. Kruger, S. Billat, H. Luth, S. Hibrich, W. Theiss, and P. Grosse, Thin Solid Films **297**, 237 (1997).
[7] L. Stalmans, J. Poortmans, H. Bender, S. Jin, T. Conard, J. Nijs, L. Debarge, and A. Slaoui, in *International Conference on Porous Semiconductors, Scientific and Technical Materials* (Mallorca, 1998), Abstr. 0-14.
[8] G. Bomchil, A. Halimaoui, and R. Herino, Microelectron. Eng. **8**, 293 (1988).
[9] J. L. Batstone, M. A. Tischler, and R. T. Collins, Appl. Phys. Lett. **62**, 2667 (1993).
[10] A. Halimaoui, in *Porous Silicon. Science and Technology (Winter School, Les Houches, 1994)*, edited by J.-C. Vial and J. Derrien (Springer-Verlag, Berlin-Heidelberg, Les Edition de Physique Les Ulis, 1995) p. 33.
[11] K. Barla, R. Herino, and G. Bomchil, J. Appl. Phys. **59**, 439 (1986).
[12] Y. Arita, K. Kuranari, and Y. Sunohara, Jpn. J. Appl. Phys. **15**, 1655 (1976).
[13] C. Pickering, M. I. J. Beale, D. J. Robbins, P. J. Pearson, and R. Greef, J. Phys. C Solid State Phys. **17**, 6535 (1984).

[14] P. M. Faushet, L. Tsybetskov, S. P. Duttagupta, and K. D. Hinsehman, Thin Solid Films **297**, 254 (1997).
[15] L. T. Canham, M. R. Houlton, W. Y. Leong, C. Pickering, and J. M. Keen, J. Appl. Phys. **70**, 422 (1991).
[16] M. Fried, H. Wormeester, E. Zoethout, T. Lohner, O. Polgar, and I. Barsony, Thin Solid Films **313/314**, 459 (1998).
[17] L. V. Belyakov, T. L. Makarova, V. I. Sakharov, I. T. Serenkov, and O. M. Sreseli, Fiz. Tekh. Poluprovodn. **32**, 1122 (1998) [Semiconductors **32**, 1003 (1998)].
[18] B. B. Loginov and V. P. Gaĭdenko, Zh. Prikl. Khim. **50**, 1683 (1977).
[19] L. Dolgyi, N. Kazuchits, V. Yakovtseva, N. Vorosov, M. Balucani, V. Bondarenko, L. Franchina, G. Lamedina, and A. Ferrari, in *International Conference on Porous Semiconductors: Science and Technology* (Mallorca, Spain, 1998) Abstr. 0-70.
[20] R. M. A. Azzam and N. M. Bashara, *Ellipsometry and Polarized Light* (North-Holland Publ. Co., Amsterdam; Elsevier North-Holland, New York, 1977).
[21] R. B. Bjorklund, S. Zangooie, and H. Arwin, Appl. Phys. Lett. **69**, 3001 (1996).
[22] V. A. Tolmachev, Proc. SPIE **3094**, 281 (1997).
[23] V. A. Tolmachev, Opt. Commun. **153**, 39 (1998).
[24] D. E. Aspnes and J. B. Theeten, J. Appl. Phys. **50**, 4928 (1979).
[25] R. Zanoni, G. Righini, G. Matogno, L. Shirone, G. Sotgiu, and F. Rallo, in *E-MRS* (Strasbourg, 1998) B-I/P. 16.
[26] F. Ferrieu, A. Halimaoui, and D. Bensahel, Solid State Commun. **84**, 293 (1992).
[27] V. A. Labunov, V. P. Bondarenko, and V. E. Borisenko, Zarub. Élektron. Tekh., No. 14(185) (1978).

Translated by James S. Wood